Rational design of SERS active silica coated silver nanoparticles as a versatile platform for semi-quantitative bio-imaging

Louise Rocks

December 2012

A thesis presented to the University of Strathclyde, Department of Pure and Applied Chemistry in fulfilment of the requirements for degree of Doctor of Philosophy.

This thesis is the result of the author's original research. It has been composed by the author and has not been previously submitted for examination which has led to the award of a degree.

Signed: Date:

Acknowledgements

Firstly, I would like to thank my project supervisors Professor Duncan Graham and Dr. Karen Faulds for their support, encouragement and guidance. I would also like to thank the Raman group in general for their scientific advice and emotional support when things have not gone to plan. I would particularly like to thank Sara Rooney, Gerry McAnally and Rachel Brown for providing chemical materials, Dr. Zeljka Krpetic and Dr. Iain Larmour for electron microscopy analysis, and Maartje Goebers for performing cell culture and incubation.

I extend my gratitude to my collaborators at the University of Glasgow, in particular Tovah Shaw and the School of Veterinary Medicine, for providing tissue culture and sectioning services.

Anna, words cannot convey my appreciation for all your help in the final stages of this thesis. Special thanks also to my Glasgow family at the GU Catholic Chaplaincy - I wouldn't be here without your love and prayers. You have strengthened my faith in God and myself. To my family and close friends, your love and encouragement are responsible for who, and where, I am today. I am truly blessed to have you all in my life.

Abstract

In recent years there has been an increased demand for real-time detection of specific biological species and interactions within a meaningful environment. Surface enhanced Raman scattering (SERS) from metallic nanoparticles represents an approach under development with added advantages over fluorescence. One such benefit is the narrower vibrational bands in SERS compared to fluorescence which increases potential for simultaneous detection of more than one species.

The use of metallic nanoparticles in Raman enhancement is hindered by non-specific adsorption of contaminating species and uncontrolled aggregation *in vivo*. Silica encapsulation of the nanoparticles results in a biocompatible and robust substrate with consistent surface chemistry. While gold nanoparticles have been shelled in silica by many different methods, transfer of encapsulation methods to silver has not been possible due to the reduced chemical stability of silver. New surface chemistries are therefore required to achieve reproducible, silica encapsulated silver nanoparticles.

Tri-functional molecules were synthesised which stabilise the silver nanoparticle core, act as (resonance) Raman reporters and provide suitable precursors for subsequent silica encapsulation. Subsequent bio-functionalisation of these nanoparticles, by covalent attachment of proteins, generates SERS active bio-imaging nanoparticles. Raman mapping of biological samples has been used for *ex vivo* detection and imaging of the inflammatory marker tumour necrosis factor. Semi-quantitative discrimination, of cerebral tissue sections, was achieved between mice infected with experimental cerebral malaria and uninfected controls. These results were produced using both 632.8 nm and 514.5 nm excitation wavelengths.

In this work, a sensitive SERS based approach to biomolecule imaging has been developed. Successful targeting of TNF using silver nanoparticles, and excitation wavelengths in the visible region, may provide advantages over the use of gold in a wide range of SERS based applications.

Abbreviations

2D	two dimensional
3D	three dimensional
4-NBT	4-nitrobenzenethiol
λ_{max}	absorption maximum
ACI	average component intensity
AgNP	silver nanoparticles
APTMS	3-aminopropyl trimethoxysilane
AuNP	gold nanoparticles
BRCS AgNP	borohydride reduced, citrate stabilised silver nanoparticles
BSA	bovine serum albumin
BT	benzotriazole
BT-COOH	carboxyl-terminal benzotriazole
BT-NH_2	amino-terminal benzotriazole
BT-OH	hydroxyl-terminal benzotriazole
BT-SiO_2	alkoxysilyl-terminal benzotriazole
CARS	coherent anti-stokes Raman spectroscopy
CCD	charge-coupled device
CdSe / ZnS	cadmium selenide / zinc sulfide core / shell
CR AgNP	citrate reduced silver nanoparticles
DCLS	direct classical least squares
dH_2O	de-ionised water
DIPEA	N,N-diisopropylethylamine
DLS	dynamic light scattering
DMF	dimethylformamide
DMSO	dimethyl sulfoxide
DPX	distyrene-plasticiser-xylene
DNA	deoxyribose nucleic acid
ECM	experimental cerebral malaria
EDTA	ethylene-diaminetetraacetic acid
EDTA AgNP	ethylene-diaminetetraacetic acid reduced silver nanoparticles

EMEM	eagle minimum essential medium
EtOH	ethanol
F_{ab}	antigen-binding fragment
F_c	crystallisable fragment
FWHM	full width at half maximum
GFP	green fluorescent protein
HEPES	4-(2-hydroxyethyl)-1-piperazineethanesulfonic acid buffer
HER2	human epidermal growth factor receptor 2
ICAM-1	intracellular adhesion molecule 1
IgG	immunoglobulin G
IHC	immunohistochemical
iPrOH	isopropanol
IL-1/ 6	interleukin 1 / 6
IR	infrared
kDa	kiloDaltons
KHD	Kramer Heisenberg Dirac
LUT	lookup table
M	molar
mAb	monoclonal antibodies
MBA	4-mercaptobenzoic acid
MeOH	methanol
MPTMS	mercaptopropyl trimethoxysilane
NIR	near infrared
OCT	optimum cutting temperature
PAGE	polyacrylamide gel electrophoresis
PBS	phosphate buffered saline
PDB ID	protein databank identification
PDDA	poly(diallyldimethylammonium)
PEG	polyethylene glycol
pfa	paraformaldehyde
pM	picomolar
QD	quantum dot

RFP	red fluorescent protein
ROS	reactive oxygen species
RRS	resonance Raman spectroscopy
SDS-PAGE	sodium dodecyl sulfate polyacrylamide gel electrophoresis
SEM	scanning electron microscopy
SERS	surface enhanced Raman spectroscopy
SERRS	surface enhanced resonance Raman spectroscopy
SORS	spatially offset Raman spectroscopy
sTNF	soluble tumour necrosis factor
sTNFR	soluble tumour necrosis factor receptor
TACE	tumour necrosis factor - alpha converting enzyme
TAMRA	carboxytetramethylrhodamine
TBE	tris Borate EDTA buffer
TEA	triethylamine
TEM	transmission electron microscopy
TESPIC	3-(triethoxysilyl)propyl isocyanate
TEOS	tetraethyl orthosilicate
TIBA	triisobutylamine
TMA	trimethylamine
tmTNF	transmembrane tumour necrosis factor
TNFα	tumour necrosis factor – alpha
TNFR	tumour necrosis factor receptor
TOAB	tetraoctylammonium bromide
UV-Vis	ultraviolet-visible

Contents

Table of Contents

1 Introduction

Spectroscopy pertains to the study of the exchange between electromagnetic radiation and matter. Spectroscopic techniques that utilise different regions of the electromagnetic spectrum can be employed to yield a multitude of molecular information, determining chemical composition and physical properties. The application of spectroscopy to monitor transitions between various states is summarised in Table 1.1.

Table 1.1 Summary of spectroscopic techniques used to monitor transitions within different energy levels of a molecule.

Excited state	Spectroscopic technique
Electronic	Ultraviolet-visible (UV-Vis) Fluorescence Nuclear magnetic resonance (NMR)
Vibrational	Infrared (IR) Raman
Rotational	Rotational Raman (gases)

Light is considered to possess both wave-like and particle-like characteristics. The wavelength and frequency of light are related to a quantum of energy, known as photons. The frequency (ν) is known to be proportional to changes in energy (E) (equation 1.1); the wavelength (λ) exhibits an inversely proportional relationship to these properties (equation 1.2).

$$\Delta E = h\nu \qquad 1.1$$

$$\nu = \frac{c}{\lambda} \qquad 1.2$$

Where: h = Planck's constant (6.626068×10^{-34} m^2 kg s^{-1})

c = speed of light (2.998×10^{8} m s^{-1})

According to quantum mechanics, photons have specific energies and are defined as quantised. Likewise, the energy levels of electrons in an atom or molecule are also quantised. The Born-Oppenheimer approximation is the assumption that the electronic and nuclear (vibrational and rotational) motion in molecules can be separated:

$$E = E_e + E_{vib} + E_{rot} \qquad 1.3$$

The vibration of a molecule can be described using a simple harmonic oscillator model where the force on each nucleus is proportional to the displacement (Figure 1.1a). The vibrational energy levels are equally spaced within a potential energy well. However, this model does not take bond dissociation energy into consideration. The Morse potential model accounts for the anharmonicity of real bonds. The relative motion of both nuclei, their displacement from the centre of mass of the molecule, and dissociation energy are both taken into consideration. The stretched parabola indicated in Figure 1.1b illustrates the uneven spacing between vibrational energy levels.

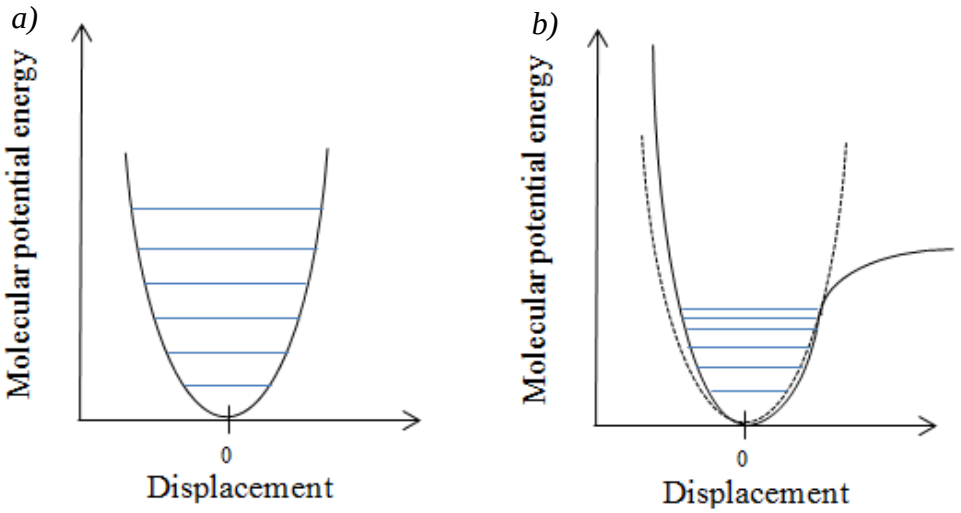

Figure 1.1a) Harmonic oscillator potential and b)Morse potential (harmonic oscillator potential curve is shown in dash for illustrative purposes) of a diatomic molecule.

A heteronuclear diatomic molecule can absorb or emit photons whose energy corresponds to the change in vibrational states according to the selection rule:

$$\Delta v = \pm 1 \qquad 1.4$$

Vibrational spectroscopy can be monitored by both Infrared (IR) and Raman spectroscopy. IR spectroscopy involves absorption of light; Raman is a scattering process. Molecules require a permanent dipole to be IR active and thus the observed signal from asymmetric vibrations are most intense. The strength of Raman scattering is dependent upon the polarisability of the molecule with symmetric vibrations producing the strongest signals.

Unlike in absorption processes, the incident photons involved in scattering do not need to be tuned to a specific transition within the electronic structure of the molecule. When light interacts with a molecule it causes the electron cloud surrounding the nucleus to become polarised for a brief period of time creating a virtual state. Virtual states are higher in energy than the molecule's ground state; the

actual level of energy will be dependent on the frequency of incident light. When the distorted electron cloud relaxes scattering occurs. The interaction of photons with the electron cloud, without inducing nuclear motion, results in minimal changes in the frequency of the scattered photon. This elastic process, referred to as Rayleigh scattering, is the predominant scattering process. Inelastic scattering of the photons is known as Raman scattering.[1]

1.1 Raman Theory

Raman scattering is a relatively weak process; only one in every 10^6 photons are Raman scattered.[1] Scattering is a result of a change in the polarisability of a molecule. Incident excitation induces a dipole in the molecule, separating the electrons from the nucleus. The strength of dipole induced is dependent upon both the polarisability of the molecule and the applied electric field (equation 1.5).

$$\mu_{IND} = \alpha E \qquad 1.5$$

where: μ_{IND} is the induced dipole (C m^{-1})

α is the polarisability of the molecule (m^3)

E is the electric field (C m^{-2})

Raman scattering can be further broken down into two subsections: Stokes and anti-Stokes scattering. Interaction with a photon can result in absorption of energy by the molecule, causing the molecule to relax into a higher energy vibrational state – this is Stokes scattering. Thermal energy can result in some molecules being in a higher energy vibrational state before interaction with a photon. On scattering, energy is transferred from the molecule to the photon resulting in the molecule returning to a lower energy vibrational state – this is anti-Stokes scattering.

As stated by the Boltzman distribution (equation 1.6), most of the molecules within a sample will be in the lowest energy vibrational level of the ground state at room temperature. Under ambient conditions, Stokes scattering has increased intensities

when compared to anti-Stokes. The co-occurrence of other emissive processes, including fluorescence, may mask the Stokes scattering. In these instances, the measurement of anti-Stokes scattering is preferable.

$$\frac{N_1}{N_0} = \frac{g_1}{g_0} e^{\left[-\frac{\Delta E}{kT}\right]} \qquad 1.6$$

A summary of the transitions occurring during scattering and adsorption processes is illustrated in Figure 1.2

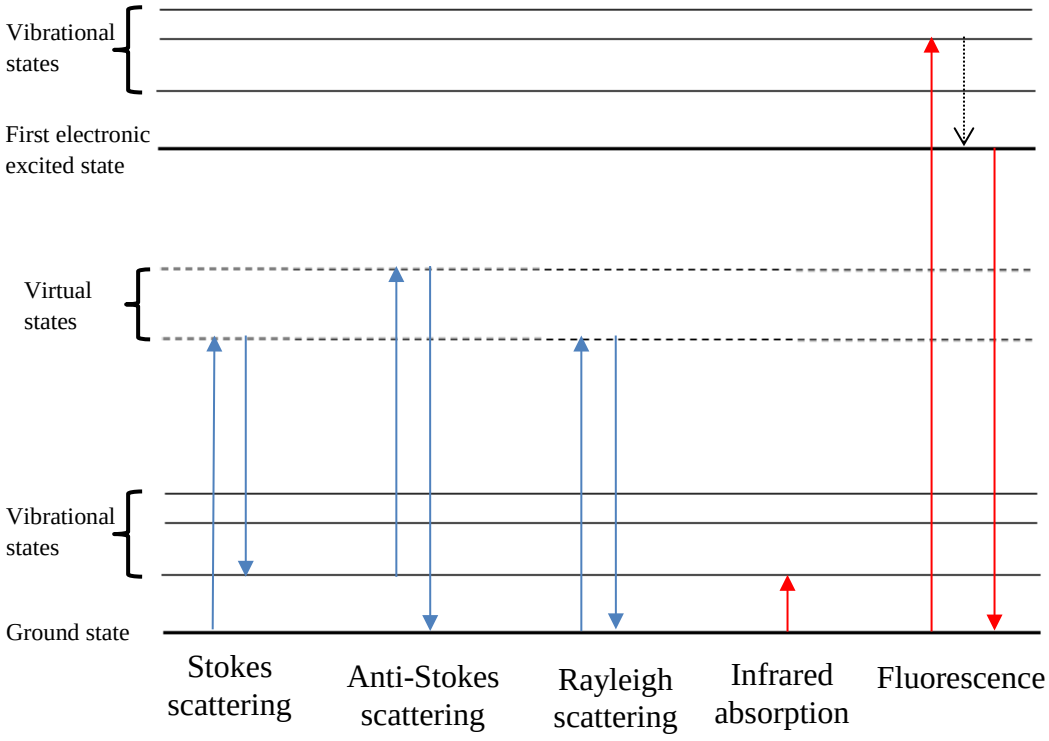

Figure 1.2 A Jablonksi representation of transitions between energy levels in scattering and absorption processes.

The intensity of Raman scattering is related to the 4th power of the excitation frequency (equation 1.7). Therefore, shorter excitation wavelengths produce more

intense Raman scattering. However, at higher energy ultraviolet-visible (UV-Vis) radiation sample degradation, including burning, and fluorescence can occur.

$$I = KI_L \alpha^2 \nu^4 \qquad 1.7$$

where: K is constant

I_L is the intensity of the laser

α is the polarisability of the molecule

ν is the frequency of the laser

The Kramer Heisenberg Dirac (KHD) expression is used to describe the polarisability of the molecule (equation 1.8).[1]

$$\alpha^2 = k\sum_I \left[\frac{\langle F|r_\rho|I\rangle\langle I|r_\sigma|G\rangle}{V_{G\to I} - V_L - i\Gamma_I} + \frac{\langle I|r_\rho|G\rangle\langle F|r_\sigma|I\rangle}{V_{I\to F} + V_L - i\Gamma_I} \right] \qquad 1.8$$

Where: α is the molecular polarisability

ρ and σ are the incident and scattered polarisation directions

∑ is the sum over all vibronic states of the molecule

G, F and I are the ground, final and intermediate states of the Raman scattering process

$\nu_{G\to I}$ is the frequency of transition from G to the I vibronic states

ν_L is the frequency of the incident radiation and

$i\Gamma_I$ is a dampening term, accounting for the lifetime of the intermediate vibronic states of the molecule.

The KHD expression essentially describes the excitation process. The numerator is a summation of all the possible states of the molecule. The dampening term of the denominator, although minor, is significant. Without this term, the frequency of incident light would be equal to that of an electronic transition resulting in infinite scattering.[1]

To further understand the selection rules of Raman scattering the Born-Oppenheimer approximation can be applied to the KHD expression. Splitting of the states into electronic (θ) and vibrational (ϕ) components is possible due to differences in timescales (10^{-13} and 10^{-9} of a sec respectively).[1] The rotational component is usually negated. The vibrational component depends entirely on the nucleic co-ordination and thus does not involve the operator. Due to the speed of the Raman process the electronic component can be approximated to the occurrence when the nuclei are at rest (with a correction to permit change in electronic structure when the nuclei move).[1]

$$\langle F|r_\rho|I\rangle = \langle \theta_F \phi_F |r_\rho| \theta_I \phi_I \rangle = \langle \phi_F |\phi_I\rangle \langle \theta_F |r_\rho| \theta_I \rangle = M_{FI}(R) \langle \phi_F |\phi_I\rangle \qquad 1.9$$

The Born-Oppenheimer solution to the KHD expression is defined as:

$$\alpha^2 = \left[kM_{R0}{}^2 \sum_I \frac{\langle \phi_F |\phi_G\rangle \langle \phi_I |\phi_G\rangle}{V_{G\to I} - V_L - i\Gamma_I} \right] \quad \text{Term A} \; +$$

$$\left[M_{R0} M'_{R0} \sum_I \frac{\langle \phi_F |R_\varepsilon|\phi_I\rangle \langle \phi_I |\phi_G\rangle + \langle \phi_F |\phi_I\rangle \langle \phi_I |R_\varepsilon|\phi_G\rangle}{V_{G\to I} - V_L - i\Gamma_I} \right] \quad \text{Term B} \qquad 1.10$$

As no operators are contained within the A term, closure theorem dictates that the final value will be zero; no Raman scattering is obtained from the A term. Raman scattering is obtained from the B term where R_ε prevents the occurrence of overtones. In the case of resonance Raman scattering, the closure theorem does not apply so A term scattering is also obtained and overtones are allowed and can be intense. Even with B term enhancement, weaker overtones can often be observed. [1]

1.1.1 Resonance Raman Spectroscopy (RRS)

Resonance Raman scattering occurs when the incident line of the laser has an energy corresponding to an electronic transition within a chromophore present in the sample

molecule. A as previously stated, here closure theorem no longer holds true. A and B term scattering is observed and overtones can occur.[1]

The intensity of Raman bands resulting from the chromophore of interest are reportedly amplified in the order 10^3 when contrasted to Raman scattering.[2] As a result, Raman spectroscopy becomes a more sensitive method of detection and also selective for the chromophore of interest.

Distinct from Raman scattering, absorption of a photon no longer results in the excitation of the molecule to a virtual excited state. Absorption of a photon from the incident laser induces the chromophore molecules to be promoted into the vibrational energy levels of the first excited state. The difference between resonance Raman scattering and fluorescence is largely related to the time scales involved (10^{-12} and 10^{-9} s). The scattering process is fast and occurs before the nuclei reach equilibrium position in the excited state, though the co-occurrence of fluorescence is a significant issue in resonance Raman spectroscopy.

Fluorescence interference may be reduced through use of a pulsed laser or alternatively by monitoring anti-Stokes scattering.[3, 4] Additionally, due to the intensity of the laser at wavelengths close to the absorption maximum of the molecule, sample degradation can occur. This may be reduced by spinning the sample or flowing the sample past the laser.[5, 6]

The drawbacks relating to RRS do not detract from the positive aspects of the technique. Of particular significance, due to the relatively weak Raman scattering observed from substances such as water and proteins, selective molecules can be monitored by resonance Raman scattering within biological systems with minimal background interference.[7, 8]

1.1.2 Surface enhanced Raman scattering (SERS)

Further enhancement of Raman scattering intensities was reported by Fleischman *et al.* in 1974.[9] In this work, the enhancement of Raman signals from a pyridine sample was reported when the pyridine was adsorbed onto a roughened silver electrode; similar enhancement was not observed when a smooth silver electrode was employed. This work was repeated subsequently by independent researchers who proposed that the increase in intensity was too large to be attributed to an increase in surface area of the electrode.[10, 11] Both groups attributed the increase in Raman scattering intensities to a surface enhancement from the silver electrode. Moskovits proposed that this enhancement was a result of excitation of the surface plasmon.[12] The mechanism by which excitation is translated into enhancement of the Raman scattering has been categorised as a combination of electromagnetic and chemical enhancement.

The electromagnetic enhancement effect is related to the surface plasmon of the material. Analysis of the electromagnetic field of an isolated, spherical, metallic nanoparticle is useful for illustrating the criteria necessary for surface enhanced Raman spectroscopy (SERS). The field at the surface of the sphere in the presence of an applied electric field is defined in equation 1.11.

$$E_r = E_0 \cos\theta + g\left(\frac{\alpha^3}{r^3}\right)E_0 \cos\theta \qquad 1.11$$

Where: E is the total electric field at a distance (r) from the surface

α is the radius of the sphere

θ is the angle relative to the direction of the electric field

g is a constant related to the dielectric constants (equation 1.12)

$$g = \left(\frac{\varepsilon_1(\nu_L) - \varepsilon_0}{\varepsilon_1(\nu_L) + 2\varepsilon_0}\right) \qquad 1.12$$

ε_0 and ε_1 are the dielectric constants of the surrounding medium and the sphere respectively and ν_L is the frequency of the incident radiation.[1] At the plasmon resonance frequency, excitation of the surface plasmon significantly increases the local field experienced by molecules adsorbed at the surface of the sphere. The polarisability of the molecule becomes more intense, amplifying the Raman scattering. The electric field, at any point on the surface, can be described by a perpendicular component and a parallel component. From equation 1.12, for metallic spheres with a dielectric constant of approximately 1, it can be deduced that the electric field at the metal surface is greater in the direction perpendicular to the surface. Thus, if a molecule lies with polarisability perpendicular to the surface the enhancement will be greater. Furthermore, since the field has an inversely proportional relationship to r^3, SERS enhancement of a molecule diminishes with distance from the surface.[1]

Chemical enhancement, or charge transfer enhancement, assumes that a chemical bond is formed between the analyte and the surface allowing for charge transfer between the two. It is proposed that the incident radiation is absorbed by the metal, not the surface plasmon, and the charge subsequently transferred to the analyte molecule. Polarisability of the molecule would be greatly increased due to the added electrons available from the bond to the metal.

It is generally accepted that both of these mechanisms have a part to play in explaining the enhancement of Raman scattering observed when a molecule is absorbed onto a surface.

One approach that can be exploited to further improve the sensitivity of SERS is to make use of the resonance contribution from an adsorbed dye molecule. This is known as surface enhanced resonance Raman scattering (SERRS). SERRS is considered to be a combination of resonance Raman and surface enhanced Raman scattering. Although the mechanism behind the enhancement is still unclear, it is adequate to consider the enhancement to be the sum of the two events. Sensitivity of

this detection system is excellent and in some cases can rival that of fluorescence.[13, 14]

1.2 Metallic Nanostructures

Metallic nanoparticles, especially the coinage metals, have proven to be useful substrates for SE(R)RS analysis. Variation in the numerous features of the nanoparticle, including morphology, size, dispersion medium and state, chemical composition and surface modification generates a diverse catalogue of substrates. The unique chemical, physical and biological properties are attributed to the nanoscale size and the relatively high surface area to volume ratio of the particles. Decreasing the size of the particles to the nanometre range results in significant absorption in the near UV-Vis range which can influence the optical properties both near field and far field.[15]

1.2.1 Plasmonic properties

The surface plasmon band is a strong, broad band observed in the extinction spectra of metallic nanoparticles whose diameter is greater than 2 nm.[16] This is a result of the coherent oscillation of valence electrons on the surface of the nanoparticle as a result of an applied electric field (Figure 1.3). The frequency of oscillation is dependent upon the shape, size and monodispersity of the nanoparticles in addition to the dielectric constants of the metal and the surrounding medium. Metals such as gold, silver, copper and the alkali metals possess surface plasmon bands in the visible region. The intense colour produced, a combination of the adsorption and scattering properties of the nanoparticle, can be monitored by extinction spectroscopy.[17]

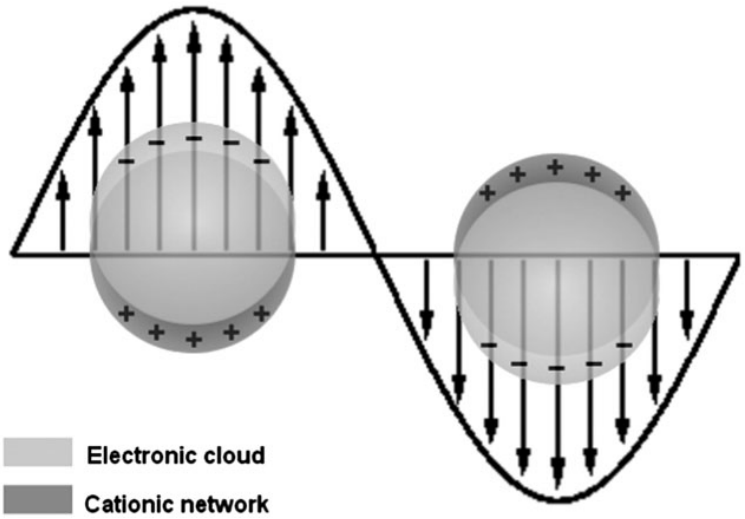

Figure 1.3 Schematic description of displacements in the electron cloud of metallic nanoparticles under the influence of an applied electromagnetic field.[16]

1.2.2 Synthesis and Characterisation

Faraday first described metallic gold colloids in 1857.[18] A colloidal system is comprised of two separate phases: a dispersed phase and a continuous phase. In relation to colloidal nanoparticles, the nanoparticles are evenly dispersed in a solution without precipitation. In general, gold nanoparticles are produced *via* reduction of tetrachloroauric acid ($H[AuCl_4]$). Citrate reduction of $H[AuCl_4]$ in an aqueous environment was first described by Turkevich [19, 20] and later refined by Frens.[21] Organic phase gold nanoparticles were subsequently synthesised using the phase transfer catalyst tetraoctylammonium bromide (TOAB).[22]

Citrate-reduced silver[23] and gold colloids are frequently used for surface enhancement effects. The citrate reducing agent is also believed to act as a surface capping agent, providing monolayer coverage of negatively charged citrate ions which aids the monodispersity of the solution. For this reason citrate solutions are often added to sodium borohydride reduced silver colloids to increase the stability of the colloid.[24] Ethylenediaminetetraacetic acid (EDTA) is another common reducing agent used in the preparation of aqueous silver colloids.[25]

The shape, size and monodispersity of the colloid affect the surface plasmon band of the nanoparticles. Mie theory, used to describe the scattering properties of metallic

nanoparticles, can be applied to interpret the extinction spectra of colloidal solutions.[26, 27] Nanoparticles with increased diameter are detected as a "red-shift" in the surface plasmon band.[28]

1.2.3 SERS reporters

Metallic nanoparticles have been utilised as substrates for intrinsic SERS detection of deoxyribose nucleic acid (DNA), proteins, cellular components and prohibited substances.[29-32] However, this technique often suffers from reduced reproducibility and sensitivity. Extrinsic SERS detection of biomolecules, as a result of the conjugation of Raman reporter molecules to the surface of the nanoparticle, can improve sensitivity.[33]

Aryl sulfides, including 4-mercaptobenzoic acid (MBA) and 4-nitrobenzenethiol (4-NBT), have commonly been employed as SERS reporter molecules.[34, 35] Dye molecules have also been incorporated as resonant Raman reporters to further improve the sensitivity of the technique.

Benzotriazole (BT) dyes have previously been synthesised to complex directly to the surface of silver nanoparticles.[36] While surface enhancement of Raman reporters can occur through the electrostatic attraction of the molecule to the surface of the nanoparticle, the BT dye can form covalent bonds through its triazole moiety. The orientation of the molecule on the surface is thereby fixed, reducing variability in the signal due to desorption and orientation effects. BT dyes are known to form irreversible polymeric complexes with the silver surface, remaining attached in a range of experimental conditions, making them ideal Raman reporters.[37-41]

While BT dyes are resonant in the green (≈ 500 nm), they are also considered effective SERRS reporters in the red.[42] However, cyanine dyes are also applicable as extrinsic SERRS reporters at biologically compatible wavelengths.[43] Near infra-red (NIR) dyes, such as crystal violet, offer suitable Raman reporters at longer excitation wavelengths.[44] This is an advantage in the analysis of cellular components due to the reduced background intensity of biological species in the NIR region.

Additionally, squaraine dyes have also been synthesised for conjugation to metallic nanoparticles.[42] The unique band observed, due to the usually weak Raman carbonyl vibration, is advantageous for multiplex analysis. The narrow bands of the molecularly specific SERS spectra permit simultaneous identification of different reporters within a mixture.[45, 46]

1.2.4 Nanoparticle assemblies / aggregates

Single metallic nanoparticles have a surface plasmon that resonates over a small range of wavelengths. If the plasmon is considered as a wave of free oscillating electrons, when two of these nanoparticles come into close proximity the electrons from one nanoparticle are free to combine with those from the second nanoparticle. This creates a new surface plasmon over many metallic nanoparticles. The frequency of the surface plasmon of a single nanoparticle decreases as the size of nanoparticle increases. This is also true for dimers and larger aggregates whose surface plasmon band lies further into the visible region.

Monomeric 35 nm silver nanoparticles ($\lambda_{max} \approx 400$ nm) are not in resonance with 514.5 nm excitation and therefore should not produce a large enhancement of Raman scattering. Surface enhancement has been achieved using single colloidal particles however a dramatic increase in Raman scattering intensity is observed when aggregation is induced. Khan and co-workers elucidated that only 2.3 % of single particles were SERRS active; the minimum percentage of SERRS active dimeric species was significantly higher (28 %).[47] "Hot spots" of intense Raman scattering are observed in samples of aggregated silver colloid adsorbed on a surface; these are thought to occur at points where two nanoparticles touch.[48] At the junction of two particles the surface plasmon significantly increases in energy however the bulk plasmon does not. The resultant increase in electromagnetic enhancement observed at these junctions has been employed in the single molecule detection of proteins.[49]

Induced agglomeration of nanoparticles, using aggregating agents such as sodium chloride (NaCl) and spermine, is commonly employed as a means of increasing the sensitivity of SERS detection.[50, 51] Alternatively, the assembly of nanoparticles by specific molecular recognition events has been employed to "turn on" the SERS effect. Nanoparticle assembly has been successful in monitoring DNA hybridisation events and protein-peptide interactions.[52, 53]

1.2.5 Core / shell nanostructures

The need for water-soluble SERS substrates for analysis within biological environments has led to the development of core / shell systems. The choice of shell is determined by the property or combination of properties the shell is to afford to the hybrid nanomaterial: optical transparency, stabilisation of the core and the amenability to further functionalisation.[54] The use of nanoparticles functionalised with polyethylene glycol (PEG) shells has been shown to be widely applicable in cellular analysis.[55, 56] Similarly, silica is being used increasingly for the shelling of nanoparticles to provide a robust substrate with consistent surface chemistry.

1.2.5.1 PEG encapsulation

PEG has been shown to be a suitable biocompatible material, resistant to non-specific binding and compatible with aqueous environments. Hydrophobic colloids have been rendered hydrophilic *via* monolayer coverage of ethylene glycol- and carboxyl acid- terminated thiols.[57, 58] The two alkanethiolate ligands shown in Figure 1.4 are composed of a hydrophobic and a hydrophilic block; this allows absorption onto the hydrophobic surface of the metallic nanoparticles whilst providing a hydrophilic outer shell. Smaller thiolated ethylene glycol molecules may be preferable to the use of PEG chains as the longer chains form coils whose conformation and packing will vary depending on the solvent used. Smaller chains will form a more organised, dense, protective shell around the nanoparticles.[59]

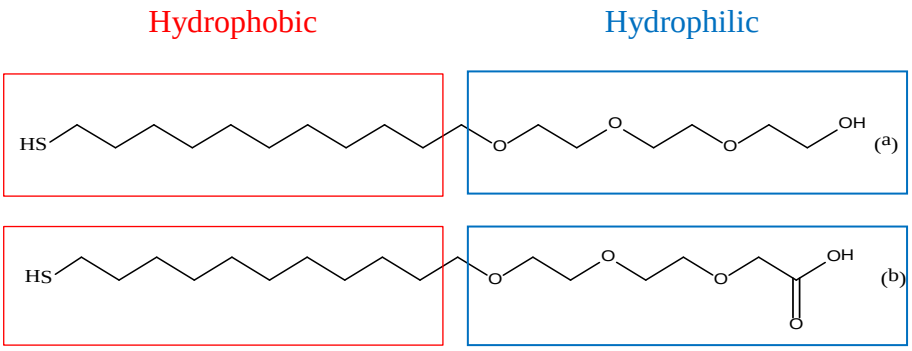

Figure 1.4: Illustration of (a) polyethylene glycol and (b) carboxyl acid terminated thiols for use in modifying surfaces of metallic nanoparticles

Gold nanoparticles capped with thiol terminated PEG ligands are prominent in investigations at biological interfaces due to their high dispersion stability and reduced non-specific protein binding. PEGylated nanoparticles are not reported to cause adverse toxicological effects in mice after a period of 28 days.[60] Presence of the PEG shell is also reported to reduce uptake of the nanoparticles by the liver.[61, 62] Exposed terminal functional groups from the PEG monolayer are important to afford further functionalisation of the core / shell nanoparticles.[63]

1.2.5.2 Silica encapsulation

Ung *et al.* report advantages of silica encapsulation, as a source of stabilisation of metallic nanoparticles, as opposed to organic stabilisers.[64] Firstly, the silica shell is optically transparent allowing the monitoring of chemical reactions spectroscopically. Secondly, silica is chemically inert, providing a mere physical blockage to the surface of the core and not affecting redox reactions occurring at the core surface. It should be noted that the silica does not render the core resistant to chemical degradation but rather acts as a selectively permeable membrane, controlling the rate of reactions occurring at the metal core. A decrease in the rate of reaction or complete inhibition can be achieved depending on the thickness of the silica layer. The silica layer also prevents aggregation of the nanoparticles.[64]

The high acidity of silanols, in comparison to carbinols, coupled with the relatively high basicity of the group means that silanols have a strong tendency to form

hydrogen bonds to themselves and other species containing suitable hydrogen bonding sites.[65] Silanol groups also have a strong propensity to self-condense and form compounds containing siloxane (Si-O-Si) linkages. Silica nanoparticles and thin films are commonly prepared by methods exploiting this property, namely the well-established Stöber method.[66] This is defined as the poly-hydrolysis and condensation of alkoxysilanes in low molecular weight alcohols. The reaction scheme is illustrated in Figure 1.5.

$$Si(OR)_4 + nH_2O \rightarrow Si(OR)_{4-n}(OH)_n + nROH$$

$$\equiv Si - OH + HOSi\equiv \rightarrow \equiv Si - O - Si\equiv + H_2O$$

$$\equiv Si - OH + ROSi\equiv \rightarrow \equiv Si - O - Si\equiv + ROH$$

Figure 1.5: Reaction scheme for Stöber condensation of alkoxysilanes.[67]

The main limitation in the silica encapsulation of metallic nanostructures is the inherent vitreophobic nature of noble metals. The relative chemical instability of silver, in comparison to gold, poses an additional obstacle in the silica coating of silver nanoparticles. Ammonium hydroxide readily oxidises silver to form soluble complex ions resulting in the formation of excess core-free silica particles.[64] Furthermore, transferring metallic nanoparticles into an alcohol / water solution, as per the Stöber method, may result in multiple silver cores within the silica shell due to the reduction in dielectric constant. For this reason vitreophilising agents, namely mercapto and amino functionalised silane coupling agents, have been employed to facilitate the silica-coating of both silver and gold nanoparticles.[68, 69] Self-assembled monolayer coverage of silane coupling agents enhances the stability of the core in the harsh conditions necessary for silica growth and provides a vitreophilic surface for growth of a silica shell *via* alkoxysilane condensation.

Pioneering work into the synthesis of nanosized gold / silica core / shell particles was reported by Liz-Marzán *et al.* in 1996.[69] The surface of the gold nanoparticles was rendered vitreophilic by the addition of a silane coupling agent, 3-aminopropyl trimethoxysilane (APTMS). It was proposed that APTMS displaced the citrate capping molecules adsorbed on the nanoparticle surface forming monolayer

coverage. Addition of active silica produced a thin layer of silica on the gold nanoparticles and additional silica growth was achieved using a modified Stöber method.

PEG molecules can also be used to cap the surface of the citrate stabilised nanoparticles before performing Stöber condensation of alkoxysilanes; this affords stabilisation to the colloid on transfer to ethanolic solutions.[70]

An alternative route to the fabrication of silica encapsulated silver nanoparticles is to produce solutions of $[Ag(NH_3)_2]^+$-doped silica particles prior to addition of a reducing agent, such as sodium borohydride, to form stable spherical nanoparticles.[71] Furthermore, silica encapsulated nanoparticles can be synthesised via water-soluble nanoparticle micelles under basic conditions[72] and by reverse microemulsion.[73]

1.2.5.2.1 Inclusion of Raman reporter within silica shells

Inclusion of a Raman reporter molecule within the silica shell allows for SE(R)RS detection of the core / shell nanoparticles whilst leaving the surface free for conjugation to biomolecules. That is to say that the Raman signals come from a reporter embedded in the silica shell and not from the target molecule. Pioneering work in this area was performed by the Natan group with success using both gold and silver nanoparticles.[68] Doering and Nie reported a similar but "improved" method for use with gold nanoparticles (by controlling Raman reporter and silane coupling agent concentrations) that indicated the compatibility of isothiocyanate dyes with silica encapsulation.[74] Further work in this area suggested that, in the case of gold nanoparticles, the need for a silane coupling agent could be removed from the synthetic route, removing the competition for reporter molecule binding to the surface of the metal and thus improving the intensity of the Raman signals.[75]

The aforementioned methods, based in alkaline conditions, are not suitable for use with NIR fluorophores; pre-functionalising the NIR dye with a siloxyl group has overcome this problem.[76] Furthermore, addition of the Raman reporter can induce inadvertent aggregation of nanoparticles; this is exaggerated by the timescale needed

for the silica coating procedure. Brown. *et al.* propose that controlled aggregation of the nanoparticles prior to addition of the Raman reporter can overcome this setback.[77, 78]

1.2.6 Functionalisation

Functionalisation of nanoparticles with biomolecules is of growing interest for use as biosensors. Firstly, the nanoparticles are to be soluble in aqueous environments and secondly the organisation of biomolecules on the surface of the nanoparticle, whilst retaining their bioactivity, needs to be controlled in order to preventing non-specific adsorption of other biological molecules.

The functionalisation of nanoparticles with proteins can be achieved through four central linking chemistries.[79] Electrostatic adsorption onto the surface of the nanoparticle is the simplest, requiring no chemical reaction. This in an inherently non-specific interaction with the result being reduced control of protein orientation on the nanoparticle surface. Direct covalent attachment of the protein to the nanoparticle surface can be achieved utilising gold-thiol chemistry. This requires an available cysteine residue close to the protein surface. However, due to the presence of capping agents or Raman reporters on the nanoparticle surface, steric crowding may prevent the protein from reaching the nanoparticle surface.

Alternatively, cofactors with a specific affinity for a protein can be exploited. The most common of these is biotin. The strength of the biotin binding to streptavidin is strong enough to almost be considered covalent.[80] Antibodies and aptamers also display specific affinity for proteins. A number of proteins may be tethered to the nanoparticle surface *via* specific interactions with these cofactors.

Another method for the formation of nanoparticle-protein conjugates is *via* covalent linkage. This utilises the functional groups present of the nanoparticle surface, many of which are capable of forming covalent bonds with protein residues. By

controlling the number of reactive groups on the nanoparticle surface, the number of protein molecules on the surface can be regulated.

1.3 Spectroscopic imaging of biological systems

In recent years there has been an increase in demand for real-time detection of specific biological species and interactions within a meaningful environment. As described in section 1.2, metallic nanoparticles have shown great promise for imaging in biological systems. At present, magnetic resonance imaging and positron emission tomography dominate the field of spectroscopic bio-imaging. However, combining microscopy with spectroscopic techniques has the potential to enhance the spatial resolution of optical imaging. Advances in this field have been achieved using fluorescence and Raman bio-imaging.

1.3.1 Fluorescence bio-imaging

Fluorescence has been the leader in tagging technology for many years whose applications include forensics, DNA sequencing and medical diagnostics.[81-83] Fluorescence is the occurrence of the absorption of a photon to produce an excited state and the subsequent emission of a photon of lower energy. Due to the high sensitivity of this technique, it is increasingly being used for molecular and cellular imaging.[84] Fluorescent imaging can reveal information regarding the localisation of intracellular molecules, occasionally down to the level of single molecule detection.[85]

Fluorophores commonly employed in bio-imaging include naturally occurring fluorescent proteins such as green fluorescent protein (GFP) and red fluorescent protein (RFP), organic molecules such as fluorescein and semi-conductor nanocrystals.[86-92] Molecules such as GFP and RFP can suffer from disadvantages such as steric hindrance, whilst organic molecules including fluorescein are liable to photobleaching.

Semi-conductor nanocrystals, more commonly referred to as quantum dots, have been pivotal in advancing the sensitivity and photostability of both biosensors and fluorescent imaging agents in biological detection systems.[55, 93] Their colour-tunable properties render them attractive cell-imaging reagents.[94] They are also resistant to photo-bleaching and offer significant potential for simultaneous detection of multiple analytes.[95]

1.3.1.1 Fluorescence bio-imaging *via* Quantum dots

Quantum dots (QD) can be synthesised from a number of semi-conductors but are considered to be a unique class of semi-conductors due to their size which ranges from 2-10 nm; the size and shape of the QD can be carefully controlled during synthesis by altering the temperature and the ligands employed. The absorption and emission of QD are determined by their size and composition. In comparison to organic fluorophores, quantum dots have longer fluorescent lifetimes and narrower emission profiles. However, oxidation and other chemical reactions can occur on the surface of the quantum dots, reducing the quantum yield i.e. the ratio of emitted to absorbed photons. To prevent such reactions, a shell can be grown on the nanocrystal. This shell, usually a couple of atomic layers, is composed of a compound with a larger band gap than that of the nanocrystal.[96]

In vitro and *in vivo* investigations confirm cellular uptake of silica encapsulated cadmium selenide / zinc sulphide core / shell (CdSe / ZnS) QD; localisation within intracellular vesicles was observed.[97] Surface functionalisation further increases the potential of these nanocrystals for biological investigations. The preparation of biocompatible quantum dots, using bifunctional mercaptoacetic acid, was pioneered by Nie *et al.*[98] Surface ligands containing amine or carboxyl groups can be cross-linked to various biomolecules such as proteins and peptides.[98, 99] Functionality can also be achieved through electrostatic interactions between quantum dots and proteins.[100, 101] Surface coverage using proteins is an extremely attractive option due to the production of biological, soluble and protected QD suitable for further functional manipulation.

Wu *et al.* demonstrated successful cellular targeting with quantum dots whose photostability was significantly improved in comparison to previously employed organic dyes.[95] Further to this, quantum dots have been applied to the analysis of pathological tissue samples.[102, 103]

Passive and active targeting of prostate tumours in mice was reported *via* fluorescent imaging (*ex-vivo* and *in-vivo)* using PEG encapsulated nanocrystals (Figure 1.6). [55, 104] Lipid encapsulated quantum dots have also been employed as *in vivo* imaging agents due to their remarkable stability and biocompatibility.[105]

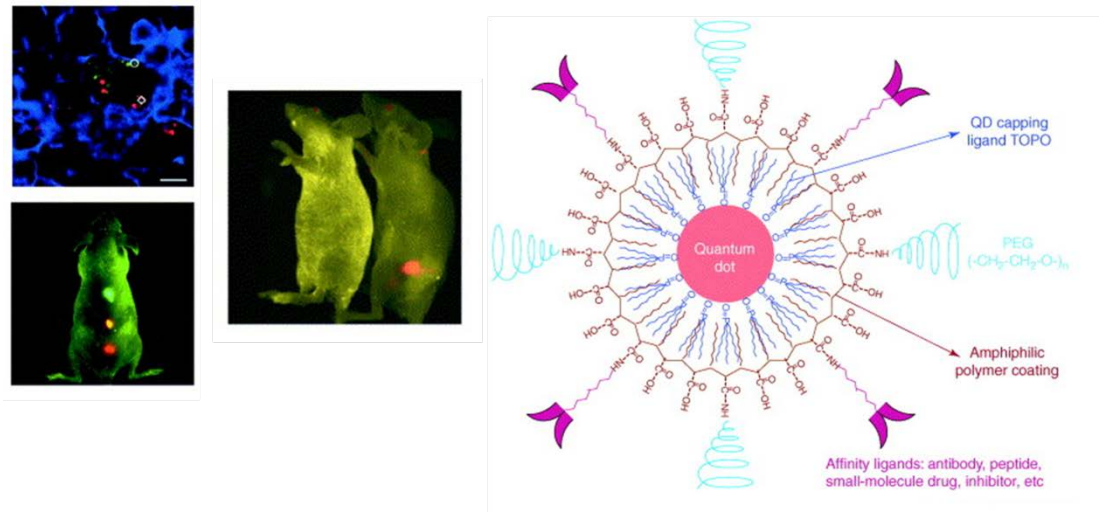

Figure 1.6 Passive and active targeting of prostate tumours in mice via *fluorescent imaging (*ex-vivo *and* in-vivo) *using PEG encapsulated nanocrystals. Adapted from* "In vivo *molecular and cellular imaging with quantum dots", by Xiaohu Gao* et al.

However, there are many disadvantages associated with quantum dots including non-specific adsorption of substrates and aggregation. Previous studies indicate that, although cell uptake of nanocrystals is successful, large aggregate formation can occur within cells.[106] Similar aggregation problems have also been observed during *in vivo* fluorescence in *in situ* hybridisation.[107]

The intrinsic fluorescence of many biological species in the visible region also poses a problem for bio-imaging. It has been suggested that an "optical window" exists in the NIR region where the major contributors to autofluorescence, water and haemoglobin, possess local minima.[108] Quantum dots with emission tuned to this "NIR window" prove effective as bio-imaging reagents.[109, 110]

Raman spectroscopy provides an alternative to the use of fluorescent microscopy for the detection and imaging of biological targets.

1.3.2 Raman bio-imaging

The non-invasive diagnostic potential of Raman spectroscopy has been exploited in the probing of biological tissue, allowing discrimination between normal and neoplastic tissue.[111] Due to the diffuse scattering nature of tissue, the penetration depth of this technique is limited to only several hundred microns.[112] Spatially offset Raman spectroscopy (SORS) overcomes this limitation, providing effective Raman analysis of sub-surface tissue samples.[113] The low Raman cross-sections of many biological species can also hinder the analysis of cell and tissue samples. Coherent anti-Stokes Raman spectroscopy (CARS), is uninhibited by autofluorescence and can achieve signal enhancements of up to 4 orders of magnitude. CARS thus provides a powerful variant of Raman spectroscopy for use in cell and tissue analysis.[114] Alternatively, enhancement effects can be utilised to improve the signal to noise ratio of Raman spectroscopic techniques. Selective analysis of haemozoin *via* RRS has proven to be effective in Raman-based malaria diagnostics.[115, 116]

As previously discussed, further enhancement effects are observed when the analyte is held in close proximity to the surface of a metallic nanoparticle. Utilising SERS from metallic nanoparticles provides narrower bands of information rich spectral output. Sensitivity of this detection system can be further increased by combination with RRS resulting in SERRS.

1.3.3 SE(R)RS bio-imaging

Detection limits as low as single molecule are reported using SERRS.[117, 118] The impressive sensitivity renders the technique particularly suitable to ultrasensitive analysis in living biological systems.[119] Metallic nanoparticles can be utilised in both label free detection of analytes and "targeted research with SERS labels".[120] Direct detection of analytes relies on the characteristic SERS spectrum of the analyte itself. Indirect detection utilises the distinctive SERS spectrum of a Raman reporter, held in close proximity to a nanoparticle surface, to identify the target analyte.

SERS measurements resulting from cellular uptake of gold nanoparticles demonstrate the direct identification of "physiologically relevant molecules".[31] The formation of aggregate structures over time highlights the reduced stability of "bare" nanoparticles in biological environments. However, the formation of these nanoaggregates was subsequently utilised in the mapping of local pH within cells.[121, 122] Protein detection incorporating nanoparticles largely involves the interaction of antibody functionalised nanoparticles with a target protein.[34, 123] Antibody-conjugated hollow gold nanospheres were employed in the indirect cellular imaging of human epidermal growth factor receptor 2 (HER2), demonstrating their viability in the imaging of cancer markers in live cells.[124]

Metallic nanoparticles face similar disadvantages to quantum dots i.e. uncontrollable aggregation and thus lack of reproducible enhancement of Raman scattering.[125] Another major challenge is the lack of selectivity for surface sites on the nanoparticles with potentially hundreds of competing adsorbates possible in a biological environment.[126] While the cytotoxic effect of metallic nanoparticles (and nanoparticles in general) is still unknown, it is suggested that efforts should be made to reduce the possible adverse effects of nanoparticles that may occur *in vivo*.[127] Core / shell nanomaterials may provide an opportunity to exploit the advantages of SERS while avoiding the aforementioned limitations.

1.3.3.1 SERS imaging *via* core / shell nanoparticles

Chemisorption of Raman reporters onto gold nanoparticles has proven to be preferable to physisorption, with respect to intensity and stability of SERS signal.[128] Encapsulated nanoparticles offer the attractive prospects of avoiding desorption of reporter molecules and preventing undesirable adsorption of competing molecules at the nanoparticle surface. PEGylated metallic nanoparticles have exhibited substantial success in monitoring biological functions and interactions whilst antibody conjugated gold / PEG nanoparticles have been successful in the *in vivo* targeting of cancers cells.[56] In the latter study, spectroscopic detection using a 784.6 nm excitation wavelength allowed for subcutaneous and muscular tumour targeting using SERS (Figure 1.7).

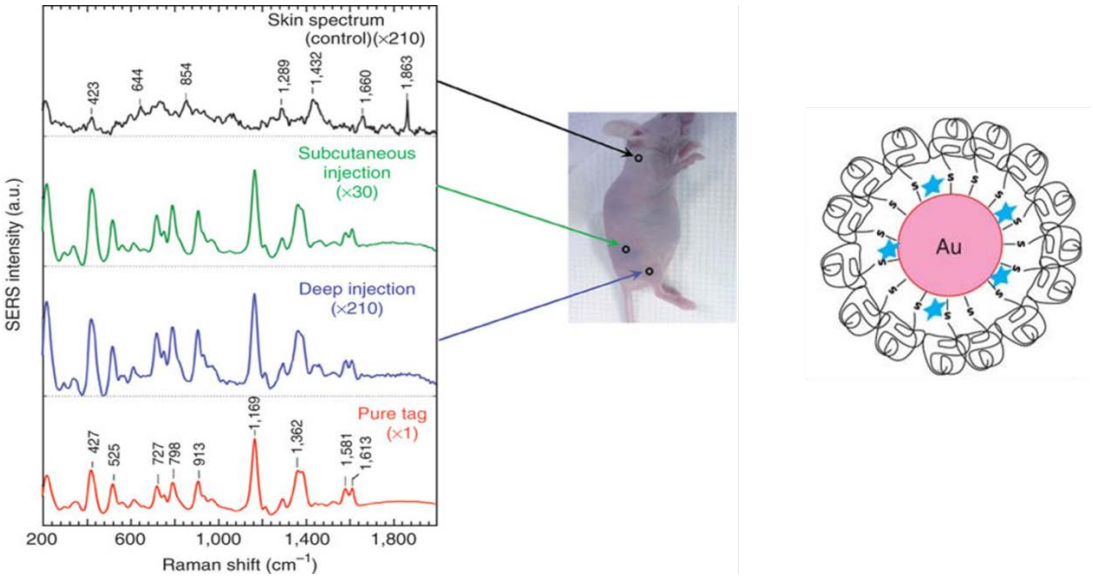

Figure 1.7 Passive targeting of prostate tumours in mice via *SERS imaging (*in-vivo) *using PEG encapsulated gold nanoparticles. Adapted from "*in vivo *tumour targeting and spectroscopic detection with surface-enhanced Raman nanoparticle tags", by Ximei Qian* et al.

Synthesis of tri-functional linkers, capable of complexing to the nanoparticle surface and conferring excellent stability, offers an alternative to PEG encapsulation.[129] These core / shell nanoparticles have demonstrated potential for deep tissue imaging at depths of 15 - 25 mm.[130] More recently, bovine serum albumin (BSA) has been

used for the shelling of SERS active nanoparticles in the targeted detection of tumours in mice.[131]

Silica encapsulation of nanoparticles is particularly attractive due to its mechanical stability.[120] Silica shell SERS active particles were pioneered by two separate groups in 2003.[68, 74] Their successful biological applications include the detection of tumour cells in the presence of whole human blood and the classification of renal tumours.[132, 133] Non-invasive *in vivo* detection of such nanoparticles has been reported at picomolar sensitivity (at limited depths) highlighting the capability for Raman imaging of biological events in living subjects.[134]

The ability to detect more than 1 biomarker simultaneously using nanoparticles has the potential to increase the effectiveness of screening methods. The narrow bands of information rich spectral output from Raman spectroscopy highlight the multiplexing capabilities of this technique, making it ideal for multiple biomarker detection. The multiplexing potential of silica encapsulated gold nanoparticles was demonstrated *via* passive targeting in mice (Figure 1.8).[54] Detection of five distinct SERS markers from deep tissue, after *intra venous* injection, underpins their applicability for the simultaneous interrogation of multiple biomarkers in biological samples.

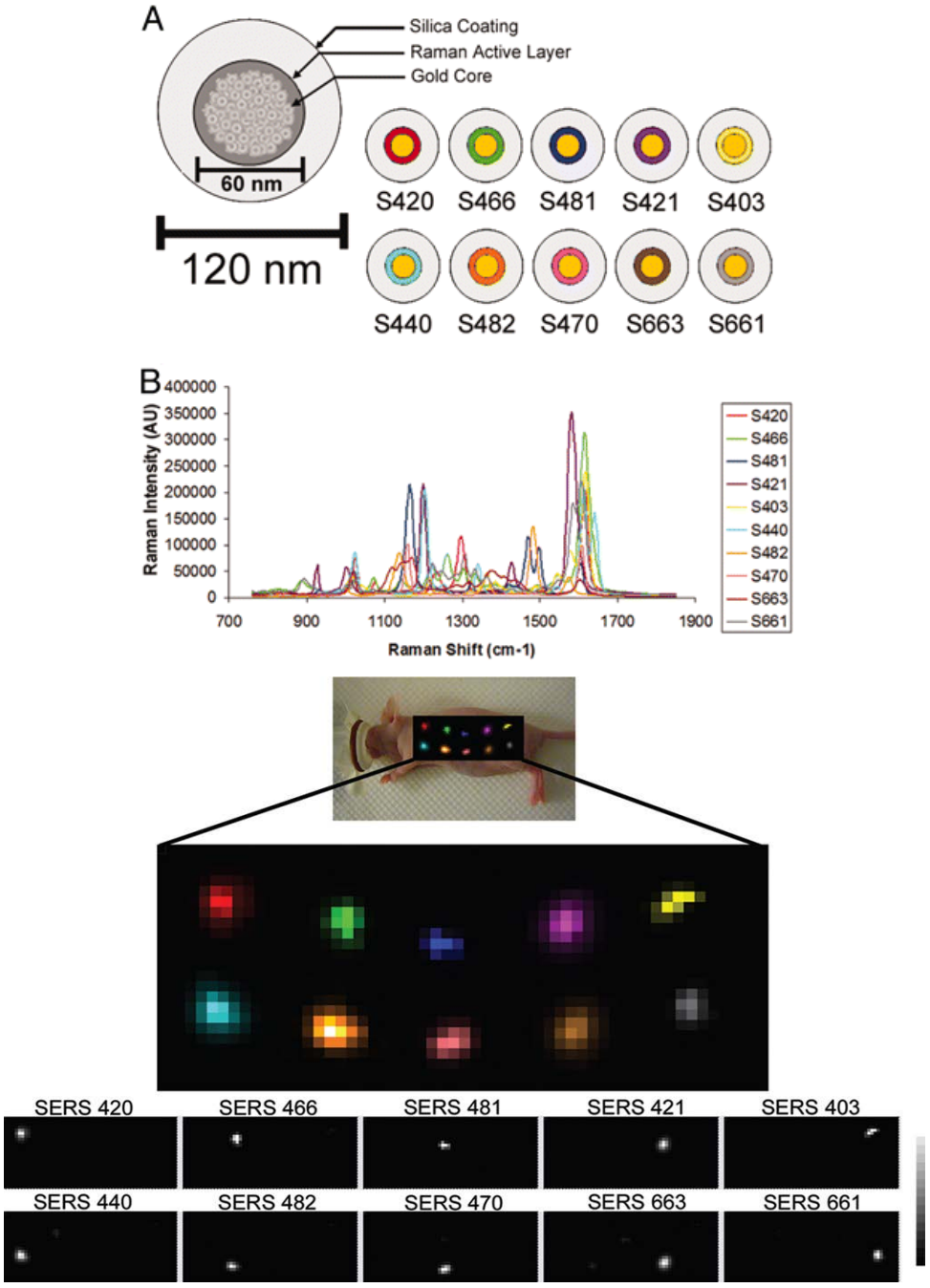

Figure 1.8 Multiplexing potential afforded by SERS active nanoparticles. Adapted from "Multiplex imaging of surface enhanced Raman scattering nanotags in living mice using non-invasive Raman spectrsocopy", by Christina Zavaleta et al.

1.4 Inflammation

As discussed, nanoparticles have shown huge potential for imaging biological systems. The work presented in this thesis aims to further develop silica encapsulated silver nanoparticles for use in biological applications, particularly involving the inflammatory system and related diseases. This section describes the particular systems that will be investigated.

Inflammation is part of a complex biological response to injury, infection or irritation. Chronic inflammation can lead to host of other diseases including rheumatoid arthritis, inflammatory bowel disease, eczema and diabetes. Inflammation is mediated by a host of secreted polypeptides known as cytokines. It is proposed that Tumour Necrosis Factor – alpha (TNFα) is the apical pro-inflammatory cytokine in an extensive protein signalling network.[135] The success of anti-TNFα therapies in the treatment of inflammatory conditions underpins this proposition.

1.4.1 Cytokines

Cytokines play a critical role in numerous host defence mechanisms such as T- and B-cell immune responses, inflammation, tissue damage, tissue repair and haematopoiesis.[136] Synergies, antagonism and natural inhibition occur between cytokines which can further complicate the cytokine network. Whilst being clinically distinct, all autoimmune diseases involve the production of cytokines which specifically mediate an inflammatory response in the body. Cytokines, secreted by specific cells of the immune system, carry signals locally between cells. These signalling molecules are typically proteins, peptides or glycoproteins. The cytokine network of rheumatoid arthritis is one of the best studied in human autoimmune diseases.[137] Many pro-inflammatory cytokines are expressed in diseased joints including TNFα and interleukin 1 and 6 (IL-1, IL-6). Both TNFα and IL-1 are thought to up-regulate each other in a positive feedback loop to cause most of the pathological symptoms. Using cell cultures from diseased joints, the TNFα cytokine network was established.[135, 138]

1.4.2 Tumour Necrosis Factor

The TNF family is a group of cytokines that can be responsible for cell death in some instances. TNFα is the most common cytokine within this family and is often referred to as TNF. It is primarily produced as a pro-peptide, a transmembrane protein consisting of 233 amino acids (pro-TNF).[139] Soluble TNF is released by an enzyme catalysed reaction involving the TNF-converting enzyme (TACE) as depicted in Figure 1.9. This enzyme is a transmembrane protein containing a zinc-dependent catalytic region. The pro-region of the enzyme contains a cysteine residue that interacts with its catalytic domain; this must be displaced for the enzyme to become active.[140] The soluble form of TNF that is released, is a homotrimer consisting of 17 kilo Dalton (kDa) subunits (157 amino acids).[141] In their trimeric forms, both transmembrane and soluble TNF are biologically active.[46]

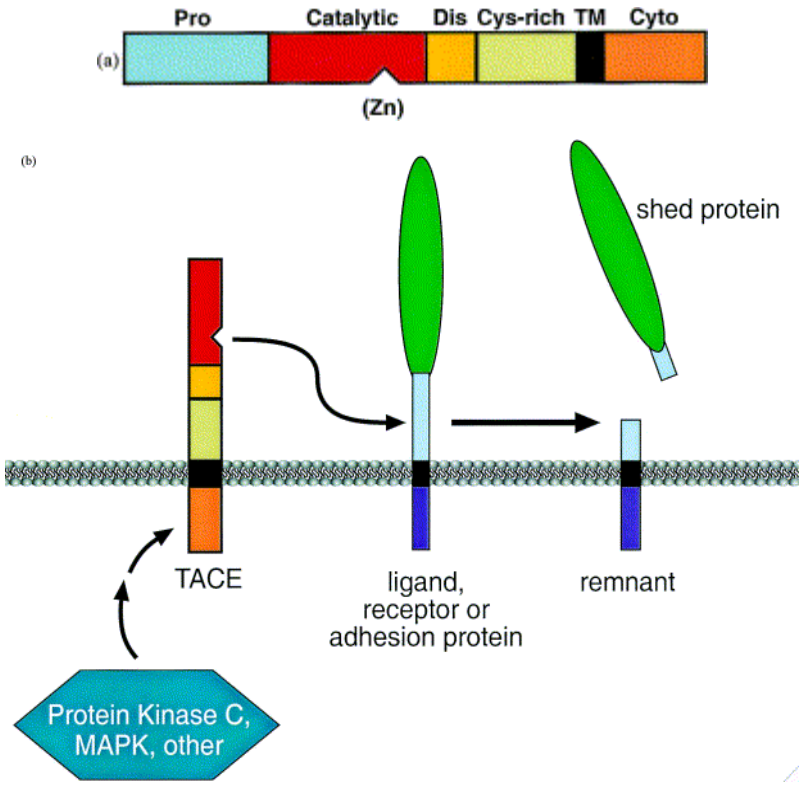

Figure 1.9: (a) Structure of tumour necrosis factor- alpha converting enzyme (TACE). Cysteine within the pro domain interacts with the active site zinc of the catalytic domain – this must be displaced to generate the active enzyme. (b) TACE cleaves the transmembrane form of TNF within the stalk (pale blue) shedding the soluble form including the functional extracellular domain (green). Adapted from "Tumour necrosis factor-alpha converting enzyme", by Roy Black.

1.4.3 Tumour necrosis factor receptors

Cytokine receptors are expressed on the surface of responsive cells. TNF binds to and activates its two receptors, tumour necrosis factor receptor 1 and 2 (TNFR1 and TNFR2), contributing to the stimulation of an immune response. The host defence functions resulting from these interactions are dependent on the receptor to which TNFα binds. Binding of TNF to either receptor results in trimerisation of that receptor.[142] The association and dissociation rates of TNF with TNFR2 are much higher than for TNFR1; it has been postulated that TNFR2 increases the

concentration of TNF at the cell surface, facilitating the binding of TNF to TNFR1.[143]

Figure 1.10 Solution to the structure of the TNF-TNFR2 complex (PDB ID:3ALQ)[144]

It has been proposed that it is an overproduction of TNF that causes various autoimmune diseases including rheumatoid arthritis.[145] Studies performed by various research groups indicate a noticeable benefit of the inhibition of TNF on collagen induced arthritis.[146-148] Thus inhibitors of TNF have become the primary method of treatment in rheumatoid arthritis patients.

1.4.4 TNF inhibitors

TNF inhibitors bind to soluble TNF in circulation in the human body, thereby preventing the cytokine from binding to TNF receptors on the surface of the cells. This reduces the immune response ordinarily signalled by TNF binding - illustrated in Figure 1.11. At present, the main therapeutics in use (both in clinical practice and trials) are biological, protein-based drugs. These include antibodies to TNFα or proteins similar in structure to the TNF receptors. The main advantage of these

drugs is their high specificity, however they do require repeated injections and their cost is much greater than that of smaller organic molecules. [149, 150]

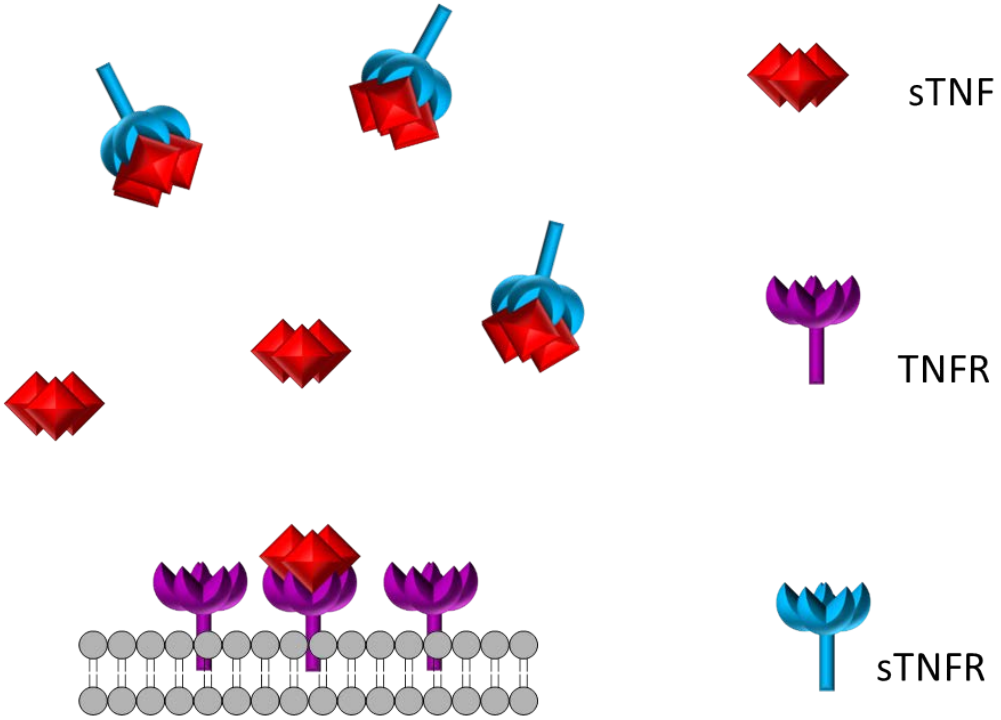

Figure 1.11: Use of biological, protein based drugs (sTNFR) to reduce the binding of soluble TNF to the TNF receptors (TNFR) on the surface of cells.

1.4.4.1 Monoclonal Antibodies

Monoclonal antibodies (mAb), as opposed to polyclonal antibodies, are produced by a particular clone of B-cells. They are the only truly monospecifc reagents i.e. react with a single antigenic determinant, making them an ideal candidate for therapeutic and diagnostic applications. Their structure is composed of two heavy and two light chains, forming an antigen-binding fragment (F_{ab}) and a crystallisable fragment (F_c).

Infliximab is an effective therapeutic in use for the treatment of rheumatoid arthritis. This was the first anti-TNF antibody used in rheumatoid arthritis therapy and is also used in the treatment of Crohn's disease.[151] It is a chimeric monoclonal antibody, comprised of the F_{ab} region of a mouse and the F_c region of a human immunoglobulin G (IgG1) antibody; chimeric monoclonal antibodies have reduced

immunogenicity when compared to murine equivalents. Consequent to the success of Infliximab, humanised monoclonal anti-TNF antibodies have been synthesised by various companies, though most of these are still in the early stages of development.[152] Humanised monoclonal antibodies, whilst having part of their complementarity determining regions from non-human origin, have been modified so that their protein sequence is of increased similarity to the antibodies produced naturally by humans. Consequently, they have even further reduced immunogenicity but the nature of the modifications can often result in reduce binding between the F_{ab} region and antigen.[153] Adalimumab, a fully humanised monoclonal anti-TNF antibody, is considered less immunogenic than infliximab.[47]

In contrast to the use of monoclonal antibodies as therapeutic agents for rheumatoid arthritis, the use of biological molecules based on the TNF receptor has proven most efficacious.

1.4.4.2 TNF Receptor based biological

As previously stated TNF binds to and activates its two receptors, TNFR1 and TNFR2. TNFR1 is a 55 kDa protein whilst TNFR2 is a 75 kDa protein. These cell membrane bound receptors interact with soluble TNF molecules, to prompt a cell signalling pathway thereby inducing inflammation. However, when cleaved from the cell surface these soluble receptor molecules act as physiological inhibitors; thus pharmaceutically engineered soluble TNFR molecules should also act as efficient inhibitors of the TNF signalling pathway.[154] Dimeric species, capable of bind two TNF molecules simultaneously, would be more effective in competing with cell-membrane bound receptors to prevent cell signalling; such was the basis for some of the most common rheumatoid therapeutics in use today.

Lenercept, is a TNFR1 dimer linked to the Fc region of an IgG antibody. Whilst initial results from animal testing proved to be successful, similar results were not observed in the transfer to clinical testing.[155] *Etanercept*, similarly, is a TNFR2 dimer linked to the Fc region of an IgG antibody. This TNF receptor based molecule

proved successful in animal testing and subsequently in human clinical trials.[156] To produce a fusion protein such as Etanercept, the human gene for the p75 TNF receptor is fused with the gene for the F_c region of an IgG antibody. Translation of this fusion gene produces a single protein.

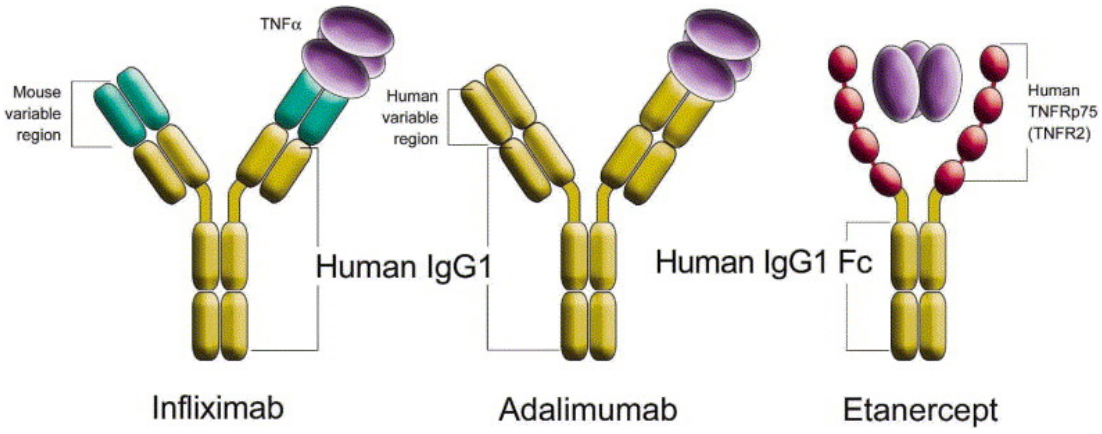

Figure 1.12 Anti-TNF molecules bind to and neutralize the activity of TNFα. From "Tumour necrosis factor inhibitors: Clinical implications of their different immunogenicity profiles", by Paul Anderson.

Recent SERS detection of inflammation has been reported *via* targeting of intercellular adhesion molecule-1 (ICAM-1). The observed signal to noise of this technique, using antibody-functionalised, SERS active, gold / silica, core / shell nanoparticles, was twice that of conventional fluorescence.[157] An analogous method to detect inflammation is investigated herein, by targeting TNF. The development of silver / silica particles provides an alternative spectroscopic substrate, potentially enabling bio-imaging using lower excitation wavelengths.

2 Aims

Chapter 3 aims to develop a method for the fabrication of silica encapsulated silver nanoparticles. This includes an evaluation of existing methodologies. Efforts will be undertaken to stabilise the silver nanoparticle cores, thus controlling the resultant particle size distribution of the core shell nanomaterials. Incorporation of a Raman reporter molecule will render the particles amenable to SERS; the reproducibility of the resultant SERS signal will be monitored. A brief assessment of the stability of the hybrid nanoparticles will also be performed.

The aim of the work in chapter 4 is to render the synthesised core / shell nanoparticles bio-functional. Optimisation of the synthetic route will be required to produce silver core particles with reproducible SERS outputs at biologically relevant excitation wavelengths. Furthermore, a method for the conjugation of biomolecules, specifically proteins, to the silica shell will be developed.

Chapter 5 investigates the potential for imaging inflammation markers, namely TNF, using the aforementioned bio-functionalised core / shell particles. This work aims to highlight areas of inflammation in biological samples.

3 Synthesis of silver / silica core / shell nanoparticles

3.1 Introduction

The application of nanoparticles within biotechnology is extensive, encompassing sensing, recognition, delivery and imaging. The emergence of core / shell nanoparticles in recent years has largely dominated the field of bio-imaging. The choice of core material in these nanoparticles is dependent on the detection technique employed. The choice of shell composition is determined by the property, or combination of properties, the shell is to afford to the hybrid nanomaterial: optical transparency, stabilisation of the core and amenability to further functionalisation.

The coating of metallic and inorganic nanostructures with silica shells is becoming increasingly prominent in the development of biologically compatible nanomaterials. Silica is considered to provide a "chemically inert" surface in biological environments, physically isolating the nanostructure whilst allowing exploitation of the catalytic, electrical, and optical properties of the core.

Sol-gel methods are commonly used for the fabrication of core / shell nanomaterials. Colloidal solutions (sol) act as precursors for integrated networks (gel) through poly hydrolysis and condensation reactions. Typical precursors for such reactions include metal alkoxides. Hydrolysis of tetraethyl orthosilicate (TEOS) under acidic conditions was observed to yield silicon dioxide (SiO_2) in the form of a "glass-like material".[158] Exploitation of this phenomenon led to the fabrication of monodisperse silica nanoparticles.[66] This "Stöber method" has since found wide-spread application in the construction of silica shells on the surface of inorganic, magnetic and metallic nanoparticles.[159-161]

The main limitation to the silica coating of metallic nanostructures is the inherent vitreophobic (little affinity for silica) nature of noble metals. Furthermore,

transferring metallic nanoparticles into an alcohol / water solution, as per the Stöber method, may result in clustering within a single silica shell due to the reduction in dielectric constant. For this reason vitreophilising agents, namely mercapto and amino functionalised silane coupling agents, have been employed to facilitate the silica-coating of both silver and gold nanoparticles.[68, 69] Self-assembled monolayer coverage of the silane coupling agents enhances the stability of the core in the harsh conditions necessary for silica growth. This monolayer also provides a vitreophilic surface for the growth of a silica shell *via* alkoxysilane condensation, thus resulting in the formation of a complete shell around the metallic core.

The work in this chapter presents the design and synthesis of reproducible SERS "active" silver / silica core / shell nanoparticles.

3.2 Silica encapsulation of silver nanoparticles

Preliminary efforts to encapsulate silver nanoparticle cores in silica shells investigated the reproducibility of previously published methods. The application of silica encapsulated gold nanoparticles is extensive but the literature regarding their preparation is limited to a few heavily cited references.[69, 162, 163] In contrast, the majority of literature regarding silica encapsulated silver nanoparticles pertains towards their preparation as opposed to application. There are also a small number of methods reporting the synthetic routes for general silica encapsulation of colloidal nanoparticles.[162] However, due to the inconsistencies in surface chemistry it would be unlikely that one method could be transferable between a number of different particles. Notably, the reduced stability of silver nanoparticles in comparison to gold and other commonly encapsulated nanoparticles poses a synthetic challenge.

Kobayashi and co-workers demonstrated the direct silica encapsulation of borohydride reduced, citrate stabilised silver nanoparticles (BRCS AgNP) using optimised modifications of the Stöber method.[164] Efforts to reproduce this work were unsuccessful (Figure 3.1a). Extinction spectra of the AgNP exhibit complete loss of the surface plasmon band post silica encapsulation. Stabilisation of the AgNP

cores was not achieved, resulting in either the oxidation of the silver nanoparticles or coagulation and subsequent precipitation of the colloid. Ung *et al.* proposed the use of silane coupling agents such as 3-aminopropyl trimethoxysilane (APTMS) to minimise coalescence of the silver nanoparticles during silica encapsulation.[64] In this methodology, silica deposition was achieved *via* precipitation of supersaturated sodium silicate solutions. Once again, efforts to reproduce the reported method to prepare silica coated silver nanoparticles were unsuccessful (Figure 3.1b). In this instance, the surface plasmon band has not been completely extinguished suggesting that the silane coupling agent affords nominal stabilisation of the silver nanoparticles.

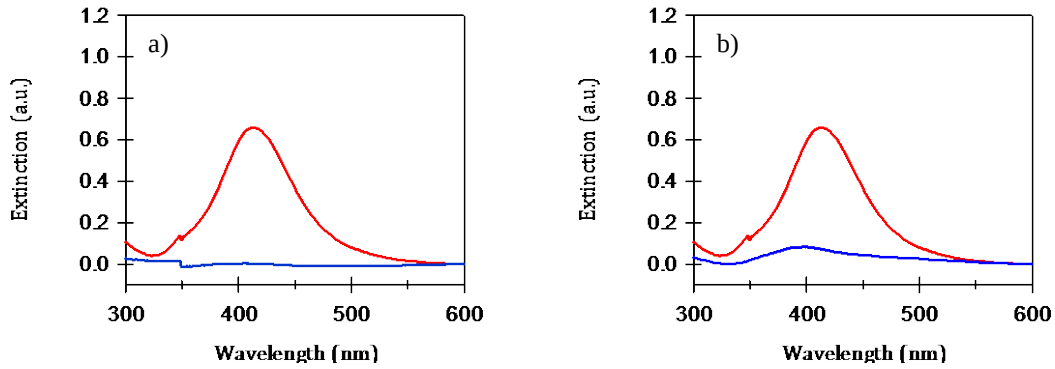

Figure 3.1 Extinction spectroscopy analysis of AgNP pre (red) and post (blue) silica encapsulation via previously published methods by a) Kobayashi and b) Ung.[64, 164]

The latter method is constructed around the idea that BRCS AgNP at pH 5 are optimal for "priming of the silver surface". Organofunctional silane agents, such as APTMS, prepared in aqueous solutions rapidly hydrolyse to silane triols. The composition of aqueous organosilanes is pH dependent; at pH 5 APTMS should be zwitterionic as depicted in Figure 3.2.[64]

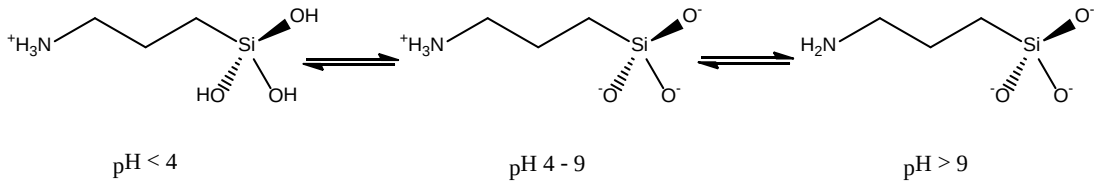

Figure 3.2 pH dependent composition of aqueous APTMS.

Dilute acids such as hydrochloric and acetic acid are capable of reducing the pH of BRCS AgNP solutions; however this compromised the integrity of the sample as indicated in Figure 3.3. Chloride ions are commonly used to induce aggregation within silver nanoparticle suspensions, thus hydrochloric acid would be an unsuitable choice for pH adjustment. Acetic acid did not induce aggregation to the same extent as hydrochloric acid; however broadening of the surface plasmon band in extinction spectroscopy indicated a broader distribution of particle size (i.e. increased polydispersity) within the pH adjusted samples. This could be a result of the acid molecules interacting with the nanoparticle surface, either electrostatically or displacing the stabilising citrate ions. The surface plasmon band was blue-shifted inferring a change in the refractive index of the particles; this pointed to alterations in the surface chemistry. A method of pH adjustment that did not alter the surface chemistry of the nanoparticle would therefore be preferable.

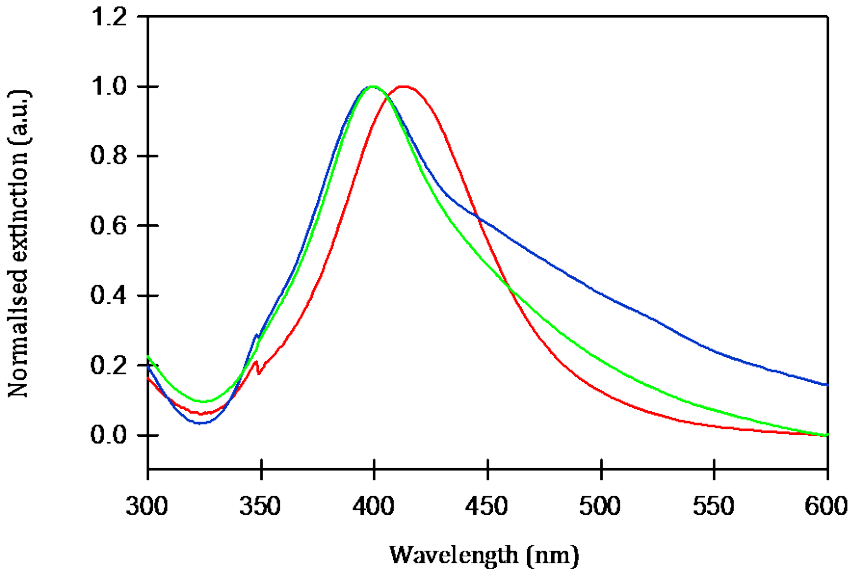

Figure 3.3 Extinction spectra of BRCS AgNP at pH 9 (red) and adjusted to pH 5 using dil. hydrochloric acid (blue) and dil. acetic acid (green).

The prescence of excess small molecules, remaining from the colloid synthesis process, may influence the pH of the resulting colloidal suspesnsion. Post-synthetic purification of colloids can be performed to remove excess borohydride ions from BRCS AgNP sols. Aliquots of colloid were purified by boiling, centrifugation and dialysis. pH and extinction spectroscopy measurements were recorded (Table 3.1). Full width at half maximum (FWHM) of the surface plasmon band provided a measure of the the particle size distribution of the colloid.

Table 3.1 pH and extinction comparison of AgNP prior to and after processing by boiling, centrifugation and dialysis.

Sample	pH	λ_{max} (nm)	FWHM (nm)
BRCS Ag (unprocessed)	9.0	407	76
Boiled	9.4	408	74
Centrifuged	8.4	403	71
Dialysed (t=48hr.)	6.6	397	155

Dialysis of BRCS AgNP, against doubly distilled deionised water over a period of 48 hr., was found to be the most effective method of reducing colloid pH. However, the monodispersity of the colloid was greatly diminished, as illustrated by the significant increase in FWHM of the surface plasmon. This is clearly demonstrated in Figure 3.4. The increased polydisperisty of the sample was most likely due to removal of "stabilising" ions as well as the presence of excess ions and small molecules. Boiling BRCS AgNPs for a period of 1 hour, to remove excess borohydride ions, resulted in an increase in pH.[24] However, changes observed in extinction spectroscopy were nominal. Removal of excess molecules by centrifugation did lower the pH of colloid. The associated reduction in FWHM value of the surface plasmon band was attributed to a narrower distribution in particle size in the suspension, commonly observed after centrifugation. Centrifugation also led to a reduction in nanoparticle concentration, demonstrated by a reduction in the surface plasmon band in extinction spectroscopy. The blue-shift in absorption maximum (λ_{max}) may have been due to an increase in borohydride ions adsorbing on the nanoparticle surface or other changes in the capping ions.[165]

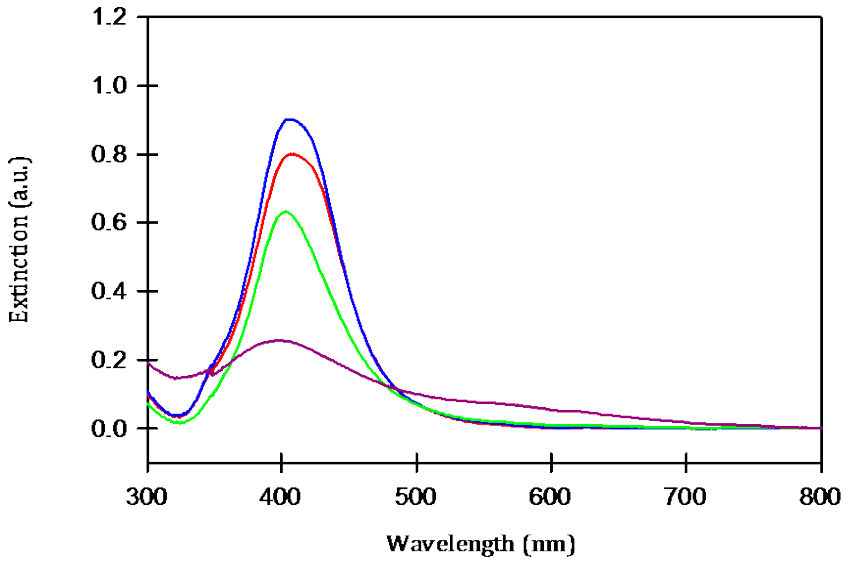

Figure 3.4 Extinction spectra of unadjusted AgNP (red) and after processing by boiling (blue), centrifugation (green) and dialysis (purple).

Whilst centrifugation did not bring the pH of the colloidal solution to pH 5, it did take the pH below the pKa of the amine moiety. Thus the organosilane should exist in the "optimal" zwitterionic state, allowing APTMS to complex with the nanoparticle surface. Subsequent silica encapsultion following the "Ung method" outlined in 8.2.2 was performed and triplicate samples analysed by extinction spectroscopy (Figure 3.5).

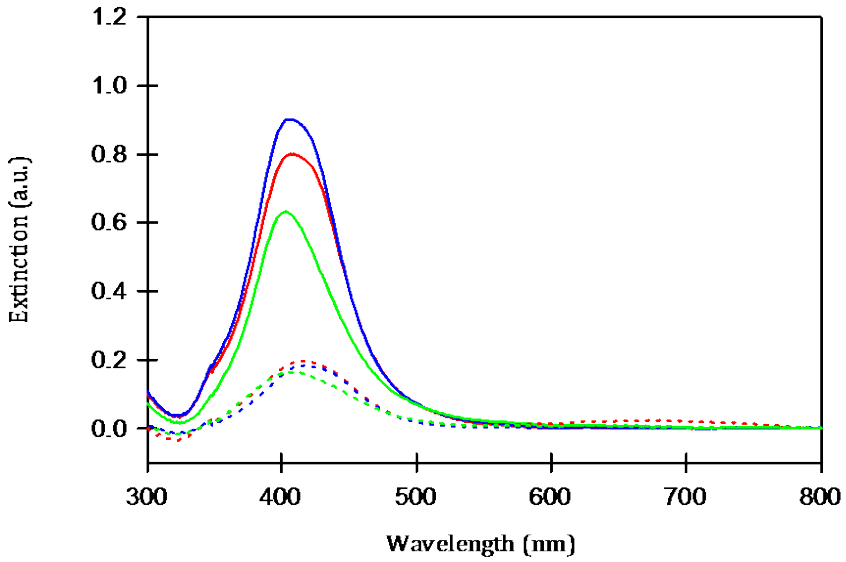

Figure 3.5 Extinction spectra of BRCS AgNP pre (solid) and post (dashed) silica encapsulation. Unprocessed BRCS AgNP (red) and BRCS AgNP purified by boiling (blue) and centrifugation (green) were subjected to silica encapsulation as outlined in 8.2.2.

Unprocessed BRCS AgNP and those purified by boiling and centrifugation with pH values of 9.0, 9.4 and 8.4 respectively (Figure 3.5) exhibited greater stability following silica encapsulation than those with an "optimal" pH value of 5 (Figure 3.1b). Lowering the pH of the starting suspension, promoting the amine to a positively charged state, did not appear to be conducive to particle stabilisation. It was proposed that the positively charged amino functionality may have induced flocculation of the negatively charged, citrate capped nanoparticles. Moreover, it is expected that the amine functional silane coupling agent co-ordinates to the nanoparticle surface *via* dative bonding into vacant d-orbitals and would therefore be unprotonated when adsorbing. Colloidal suspensions with pH measurements above pH 9 would potentially provide improved APTMS conjugation, increasing the stabilising effect.

Additionally, an internal cyclic structure may form in the zwitterionic APTMS, preventing co-ordination with the nanoparticle surface (Figure 3.6).[166] The lone pair of electrons from the unprotonated amino moiety may also form an internal 5

membered ring with the silicon atom, although this is less likely to occur due to the increased strain in the 5 membered ring.[167]

Figure 3.6 Internal cyclic structures formed by 3-amino substituted organic silanols in aqueous solution.

It is possible to combine the two aforementioned methods. Firstly, the surface of the silver nanoparticles is rendered vitreophillic by the addition of a silane coupling agent. This permits the growth of a silica shell using a modification of the Stöber method, adding TEOS and an amine catalyst. Silica formation by Stöber condensation can proceed *via* acid or alkali mediated catalysis. Weakly branched polymeric networks of silica are observed following acid-catalysed hydrolysis of alkoxysilanes. Conversely, highly branched "colloidal" particles are produced as a result of base-catalysed hydrolysis.[67, 168] In alkaline conditions, the rate of condensation of TEOS is faster with respect to the rate of hydrolysis.[169] Increasing the basicity of the nanoparticle suspension should therefore promote amine-catalysed condensation of TEOS onto the vitreophilised surface. Accordingly, this would reduce the exposure of the silver cores to reaction conditions, minimising their coalescence prior to and during silica encapsulation.

Aqueous suspensions of silver nanoparticles prepared by ethylene-diaminetetraacetic acid (EDTA) reduction have, on average, a higher pH than those prepared by borohydride reduction. Aqueous suspensions of citrate reduced silver nanoparticles (CR AgNP) have a similar pH to BRCS AgNP due to the citrate capping layer present on the surface of both colloids. Whilst the reproducibility between batches of BRCS AgNP is much higher than that of CR AgNP, BRCS AgNP are considered to be less stable than CR AgNP.[170] These properties are summarised in Table 3.2.

Table 3.2 Summary of average data obtained by extinction spectroscopy, dynamic light scattering (DLS), Zeta potential and pH measurements of triplicate samples of BRCS, CR and EDTA AgNP. DLS measurements are not reported for BRCS AgNP as the particle size falls outside the limits of the instrument. An approximate diameter for BRCS AgNP is reported. CR AgNP was provided by Sara Rooney.

	λ_{max} (nm)	FWHM (nm)	Diameter (nm)	Zeta potential (mV)	pH
BRCS AgNP	406	109	10 [64]	-24.2	9.0
CR AgNP	403	93	35.67	-44.0	8.7
EDTA AgNP	421	94	41.99	-33.6	11.4

Zeta potential measurements were employed to assess the stability of the particles in solution. The sign and magnitude of the zeta potential is directly proportional to the sign and magnitude of the particle surface charge density.[171]

APTMS was conjugated to the surface of BRCS AgNP (pH 9.0), CR AgNP (pH 8.7) and EDTA AgNP (pH 11.4). A modified base-catalysed Stöber method was used in efforts to silica encapsulate these nanoparticles (see 8.2.3). Extinction spectroscopy was used to analyse samples pre and post silica encapsulation (Figure 3.7).

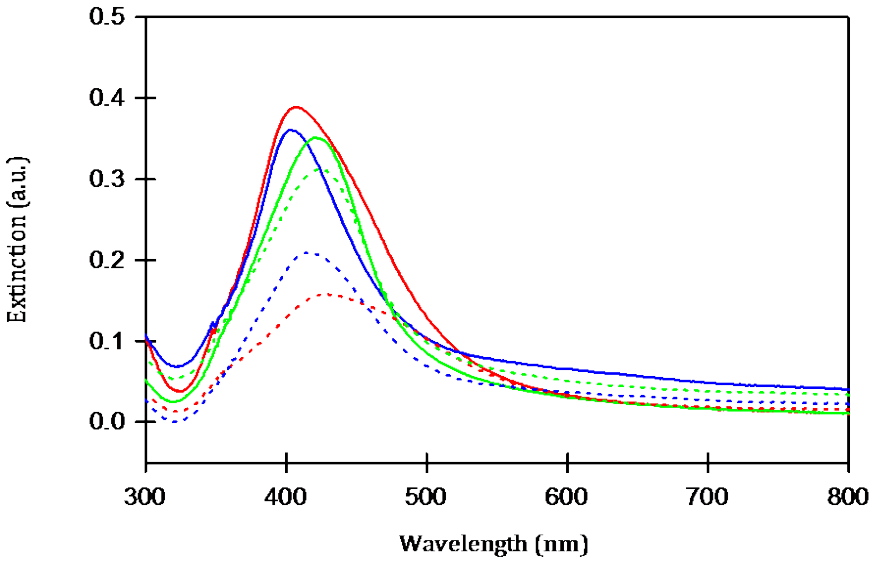

Figure 3.7 Extinction spectra of AgNP pre (solid) and post (dashed) silica encapsulation. AgNP were prepared using borohydride (red), citrate (blue) and EDTA (green) reduction methods with resulting pH values of 9.0, 8.7 and 11.4 respectively.

Nanoparticle suspensions with increased basicity are shown to have increased stability during silica encapsulation, illustrated by a narrower particle size distribution in the resultant silver / silica core / shell nanocomposities. Dampening and broadening of the surface plasmon was observed in the post encapsulation extinction spectroscopy measurements of BRCS AgNP and CR AgNP; these effects were much reduced in the encapsulation of EDTA AgNP. At higher pH values, base-catalysed Stöber condensation of TEOS occurred at a faster rate. Under these conditions, the silver nanoparticle cores were exposed for shorter time periods, reducing the aggregation of particles prior to and during silica encapsulation. These results also are in agreement with previous findings that report increased stability of CR AgNP compared with BRCS AgNP.[170]

EDTA AgNP were used in all subsequent efforts towards silica encapsulation of silver nanoparticles *via* Stöber condensation.

3.3 Silica encapsulation of SERS "active" silver nanoparticles

3.3.1 A comparison of mixed monolayer designs

The fabrication of silica encapsulated silver nanoparticles that are detectable by surface enhanced Raman spectroscopy presents an additional requirement; a Raman active molecule must be held in close proximity to the surface of the nanoparticle. Natan and co-workers have developed extremely successful gold analogues.[54, 68, 132, 172, 173] The synthesis of such particles utilises mixed monolayer coverage of the aforementioned silane coupling agents and Raman active molecules on the nanoparticle surface.

The silica encapsulation method outlined in 8.2.3 was further developed to incorportate a mixed monolayer. Aliquots of a Raman active benzotriazole dye (at sub monolayer concentrations) and silane coupling agent were simultaneously added to EDTA AgNP. APTMS and the mercapto analogue (MPTMS) were compared for use as competitive vitreophilising precursors. The extinction spectra of EDTA AgNP with complete monolayer coverage of dye and mixed monolayers of APTMS / dye and MPTMS / dye are shown in Figure 3.8a. Silica encapsulation of these nanoparticle conjugates was achieved using base-catalysed Stöber condensation of TEOS (see 8.2.3). The samples were re-analysed using extinction spectrsocopy post silica encapsulation (Figure 3.8b).

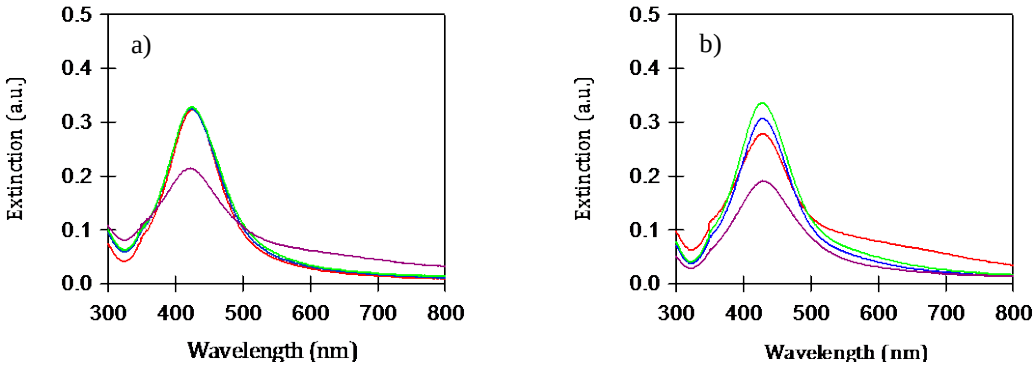

Figure 3.8 Extinction spectra a) pre-encapsulation and b) post-encapsulation of "bare" EDTA AgNP (red), EDTA AgNP with monolayer coverage of dye (blue) and EDTA AgNP with mixed monolayer coverage of dye and silane precursor APTMS (green) and MPTMS (purple).

Addition of dye molecules to the surface of the nanoparticles did not significantly affect the observed surface plasmon band in extinction spectroscopy. Similar results were observed when aliquots of APTMS and dye were simultaneously added to the colloidal suspensions. Conversely, after concurrent additions of MPTMS and dye, the surface plasmon band was noticeably dampened and broader, indicating an increased nanoparticle size distribution. Furthermore, increased extinction at longer wavelengths indicated the presence of nanoparticle aggregates. Due to the high affinity of thiols for silver surfaces, dense coverage of MPTMS is expected to form quickly on the metal surface. However, in order to minimise defects in self-assembled monolayers of alkane thiols, a period allowing for re-organisation is often required.[153] Optimisation of the conjugation conditions for MPTMS / dye mixed monolayers may improve the stability of the resultant conjugates.

Post silica encapsulation, the surface plasmon band observed from "bare" silver nanoparticles in solution was dampened and there was an increase in the extinction at longer wavelengths. These results show that the modified Stöber method induced aggregation of nanoparticles in the absence of dye or silane precursor. Increased particle size distribution was less evident in silica encapsulated nanoparticles synthesised from particles exhibiting monolayer dye or APTMS / dye mixed monolayer coverage. Contrary to "bare" nanoparticles, the surface plasmon band for

nanoparticle-conjugate suspensions post silica encapsulation exhibited increased similarities to the pre encapsulation extinction spectra. No further dampening of the surface plasmon band was induced by subjecting nanoparticles with MPTMS / dye mixed monolayer coverage to silica encapsulation. These data give an indication that the presence of dye and / or silane couple agents on the surface of the nanoparticle afforded stabilisation during silica encapsulation *via* the modified Stöber method.

The samples were also anlaysed using SERS with a 514.5 nm excitation wavelength (Figure 3.9). Three SERS meaurements of three replicate samples were recorded and the average peak height of the most prominent peak at 1615 cm^{-1} was calculated. As the pre and post silica encapsulation samples were measured at different times, recorded data was standardised with respect to the Raman intensity of cyclohexane at 800 cm^{-1}. 35 nm EDTA AgNP, as monomers, are not in resonance with the incident laser at this frequency, therefore they should not produce large electromagnetic enhancements of the Raman signal. The presence of dimers and trimers are known to create “hotspots” of electromagnetic enhancement; significant local field enhancements up to the order of 10^5 can be observed at the gap between two metallic spheres. Larger aggregates, whose surface plasmon is more closely in resonance with the excitation wavelength, are also known to produce large enhancements. Thus, an increase in SERS intensity can often be attributed to an increase in the particle size distribution of a colloidal suspension.

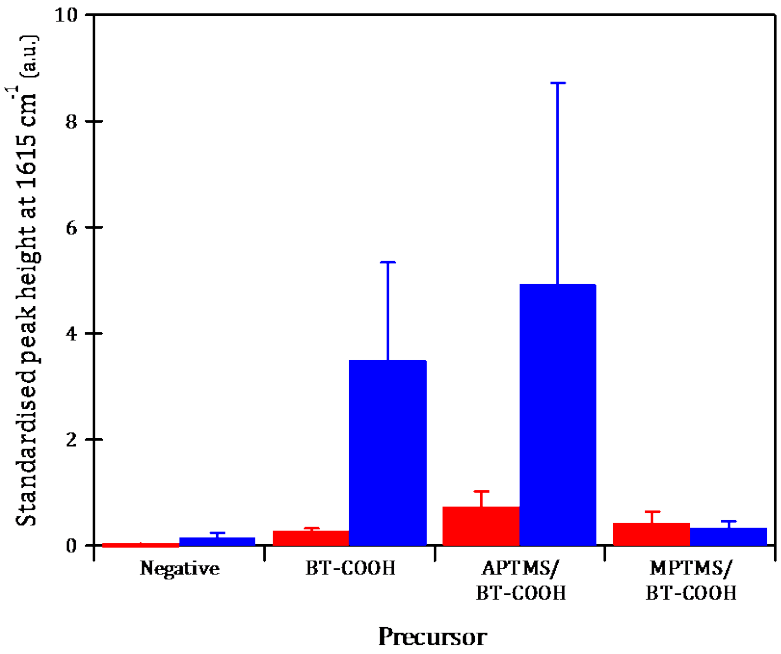

Figure 3.9 SERS analysis, using 514.5 nm excitation wavelength, of silver nanoparticles pre (red) and post (blue) silica encapsulation. Core / shell particles were synthesised using monolayer coverage of dye (BT-COOH) and mixed monolayers of APTMS or MPTMS with dye. Error bars indicate 1 standard deviation of the average peak height.

Prior to silica encapsulation, the relative SERS intensities observed for mixed monolayers of APTMS / dye was approximately 2.5 times greater than that observed for monolayers of dye. However, no significant differences were observed in the extinction spectra of the two samples. The variability in the SERS intensities of dye monolayers and mixed monolayers of APTMS / dye, prior to silica encapsulation were 18.7 % and 39.9 % R.S.D respectively. It was proposed that this was a result of increased variability in the number of dye molecules on the surface of the nanoparticles in mixed monolayer systems.

The relative SERS intensity resulting from monolayer dye and mixed monolayers of APTMS / dye was significantly increased post silica encapsulation. The extinction spectra (Figure 3.8) did not indicate the occurrence of extensive aggregation of the silver nanoparticle cores. The presence of dimers and trimers, generating “hotspots” of electromagnetic enhancement, may not significantly alter the appearance of the

surface plasmon band in extinction spectroscopy. The increased SERS intensities observed post silica encapsulation were thus attributed to an increase in dimer / trimer population within the samples. These data suggested that both monolayer surface coverage of dye molecules or mixed monolayers of dye and APTMS do not afford complete stabilisation of the nanoparticle core during silica encapsulation, under these conditions. As the aggregation observed here is not controlled, the variability in SERS intensity of the samples is high (R.S.D 53.0 % and 77.2 % for silver / silica nanoparticles synthesised from monolayers of dye and mixed monolayers of APTMS / dye respectively). Optimisation of the silica shelling protocol may improve the variability in SERS intensities observed post encapsulation.

The observed SERS intensity of MPTMS / dye mixed monolayer samples post silica encapsulation was greatly reduced, compared to APTMS / dye samples. With regard to the APTMS / dye mixed monolayer, complexing of both molecules to the nanoparticle surface utilises the available lone pair of electrons from a nitrogen atom. Conversely, the nitrogen of the dye and the sulfur from the MPTMS compete for co-ordination with the nanoparticle surface. Preferential binding of sulfur results in reduced binding of the dye and provides an explanation for the lower SERS intensity observed even in aggregated nanoparticle populations, as indicated by the extinction spectra (Figure 3.8).

These data indicated that avoiding mixed monolayers is preferential for the development of reproducible SERS detectable silica encapsulated silver nanoparticles. Successful silica encapsulation of gold nanoparticles has previously been achieved via covalent attachment of silane precursors to complete monolayers of Raman reporters.[45] Further to this, the authors were able to demonstrate the effectiveness of terminal alkoxysilane Raman reporters for similar purposes.[174] A molecule that could function as both vitreophiling precursor and Raman reporter should thus increase the reproducibility of the observed SERS signal. Due to the relative instability of silver, in comparison to gold, transfer of these methods to the silica encapsulation of silver nanoparticles was unsuccessful. Thus a series of

precursors were designed for the specific encapsulation of Raman active silver nanoparticles within a silica shell.

3.3.2 Tri-functional benzotriazole precursors

To that end, an appropriate precursor for the successful silica encapsulation of Raman active silver nanoparticles must:

- have significant affinity for the silver surface
- be (resonant) Raman active
- provide a vitreophilic surface on the nanoparticle

A series of trifunctional linkers based on benzotriazole (BT) dyes were synthesized for conjugation to the surface of silver nanoparticles (Figure 3.10).[38]

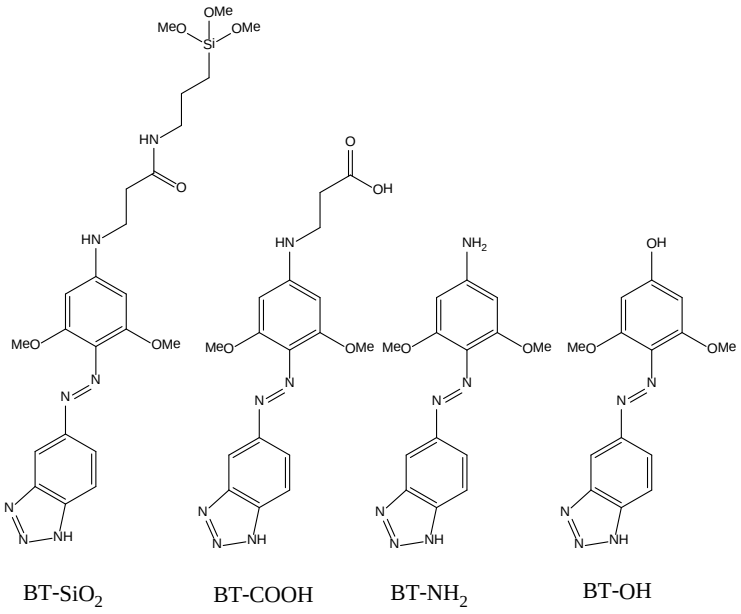

Figure 3.10 Four trifunctional precursor dyes for the synthesis of silica encapsulated silver nanoparticles.

BT dyes have previously been designed to complex directly to the surface of silver nanoparticles through the benzotriazole moiety.[36] Surface attachment of Raman reporters can occur through the electrostatic attraction of the molecule to the surface of the nanoparticle. Alternatively, the molecule can form a covalent attachment,

fixing the orientation of the molecule on the surface. This reduces variability in Raman signal intensities due to desorption and orientation effects. BT dyes are known to form irreversible polymeric complexes with the silver surface, remaining attached in a range of experimental conditions, making them ideal precursor candidates.[36, 37]

The BT molecule itself is Raman active and the azo chromophore offers an electronic transition close to the excitation frequency of lasers commonly employed in spectroscopy. This property can be exploited to improve the sensitivity of the technique. Full SERS spectra of the nanoparticle-precursor conjugates using a 514.5 nm excitation wavelength are shown in Figure 3.11.

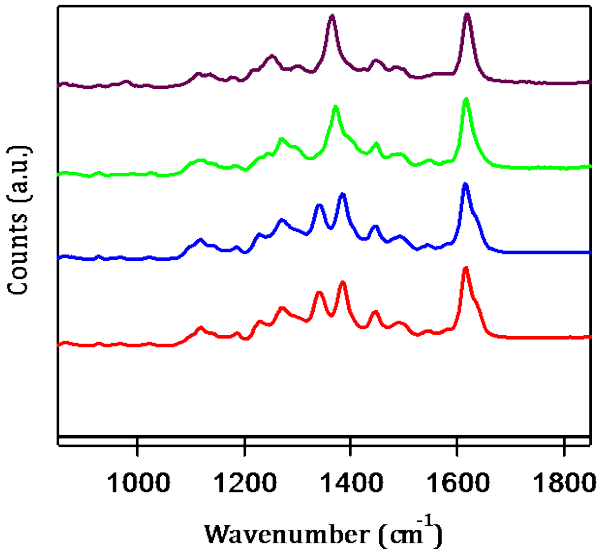

Figure 3.11 Normalised SERS spectra of EDTA AgNP (black) and the resulting precursor conjugates: BT-SiO_2 (red), BT-COOH (blue), BT-NH_2 (green) and BT-OH (purple) using a 514.5 nm excitation wavelength. Spectra were collected using a 514.5 nm excitation wavelength and are offset for illustrative purposes.

Terminal functionality was introduced to the BT molecules to provide a vitreophillic exposed nanoparticle surface. This functional group should be capable of forming bonds with oxide components, such as TEOS, commonly used in Stöber condensation reactions. Four different functionalities were selected, each capable of

undergoing condensation with TEOS. Thus, they can be considered to act as precursors for the development of an integrated network of siloxane linkages *via* the Stöber method. BT-SiO_2, with terminal alkoxysilyl functionality was synthesised from BT-COOH (carboxyl terminal). BT-NH_2 (amino terminal) and BT-OH (hydroxyl terminal) were previously synthesised by Gerry McAnally and Rachel Brown respectively.[36, 38]

Whilst the surface-seeking moiety of the four precursors is identical, the charge of terminal functionality can also influence co-ordination of the precursor with the nanoparticle surface. Negatively charged terminal groups will be repelled by the negatively charged EDTA species on the nanoparticle surface. Conversely, positively charged terminal groups may form electrostatic interactions and co-ordinate to the surface of adjacent nanoparticles, thus potentially inducing aggregation of the nanoparticles prior to silica encapsulation. At pH 11.5, the average pH of EDTA AgNP, BT-NH_2 ($pK_a \approx 9.3$) will be unprotonated. BT-COOH will be negatively charged ($pK_a \approx 4.9$) as will BT-OH ($pK_a \approx 9.95$). The terminal methoxy silyl group is not considered to be stable, readily hydrolysing to form organosilanol. Isolated silanols are considered to have pK_a similar to that of carboxylic acids ($pK_a \approx 4.9$).

The four precursor molecules (50 μL, 10 μM) were individually added to aliquots of AgEDTA (1 mL, 100 pM) and silica encapsulation achieved as outlined in 8.3.3. The conjugates and their silica encapsulated analogues were analysed by extinction spectroscopy and Raman spectroscopy using an excitation wavelength of 514.5 nm.

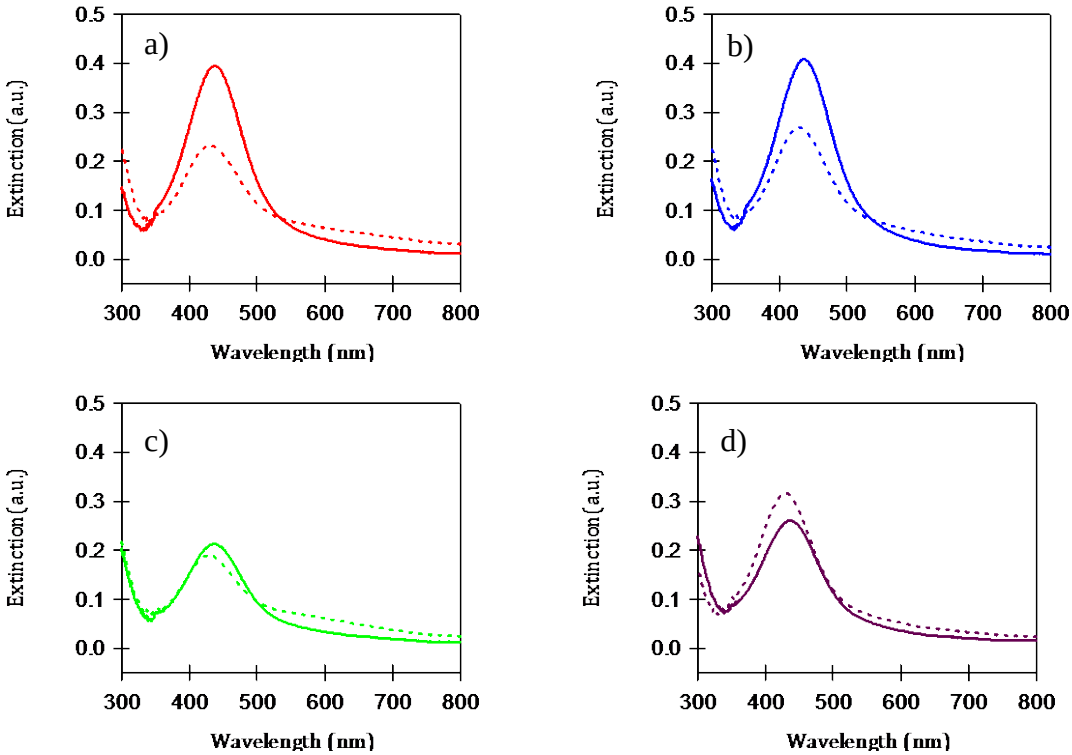

Figure 3.12 Extinction spectra of NP-precursor conjugates (solid) and their resulting silica encapsulated colloids (dashed). Precursors BT-SiO_2 (red), BT-COOH (blue), BT-NH_2 (green) and BT-OH (purple) (50 µL, 0.1 µM) were added to EDTA AgNP (1 mL, 100 pM)

Extinction spectroscopy analysis of conjugates, and their corresponding silica encapsulated colloids, synthesised using BT-SiO_2 and BT-COOH demonstrated similarities. The overall absorbance recorded from the samples post-silica encapsulation was diminished. This may have been due to loss of sample through repeated washing of the colloids. Alternatively, the dampening of the surface plasmon band coupled with increased absorbance at longer wavelengths could imply aggregation of the nanoparticles. These effects were observed to a greater extent with regards to the BT-SiO_2 nanoparticle conjugates compared with other NP-precursor conjugates. These data demonstrated that BT-SiO_2 did not afford sufficient stabilisation to the nanoparticle core during the encapsulation protocol. This nanoparticle instability was attributed to premature siloxane bridging between precursor molecules on adjacent nanoparticles.

Indications of aggregation were present pre-encapsulation in the BT-NH_2 conjugates. This suggested that the amino functionality of the precursor induced nanoparticle clustering prior to silica encapsulation. This observed aggregation may have been a result of interactions between the amine of the precursor with the surface of the EDTA AgNP. The colloid underwent further agglomeration during silica encapsulation; this was observed in increased extinctions at longer wavelengths.

Nanoparticles conjugated to BT-OH did not appear to experience aggregation prior to or during the silica encapsulation process. In fact, post silica encapsulation, the surface plasmon band in extinction spectroscopy was amplified compared to pre-encapsulation. This would infer that the terminal hydroxyl group of the precursor may not be as stabilising as the encapsulating silica shell. Unfunctionalised silver nanoparticles are stabilised against coagulation by the repulsive force of the negatively charged surface capping agents. The relatively high pKa of the hydroxyl group would reduce the surface charge of the nanoparticle conjugates, reducing their stabilising effect. This was confirmed by measuring the zeta potential of the colloids (Figure 3.13).

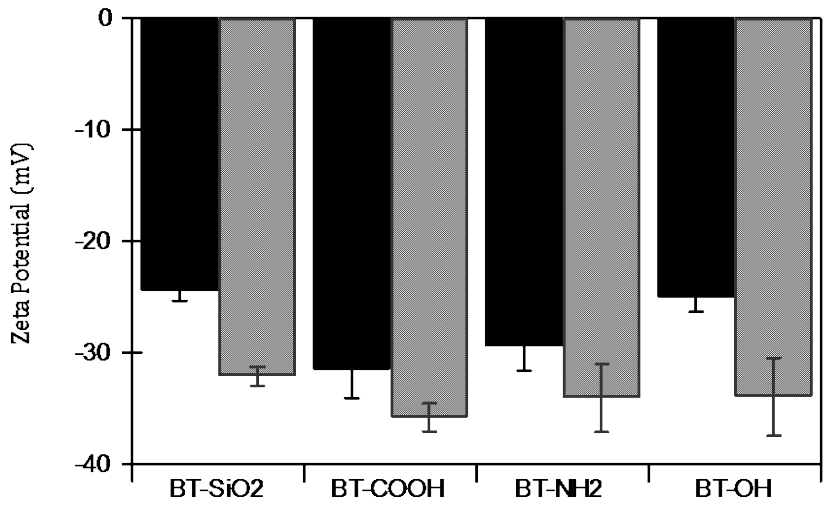

Figure 3.13 Zeta potential of nanoparticle-precursors conjugates pre (black) and post (grey) encapsulation. Error bars indicate one standard deviation.

SERS measurements of the colloids post encapsulation were also carried out using three different excitation wavelengths (Figure 3.14). The colloids showed optimal Raman activity when a 514.5 nm excitation wavelength was used. This is the wavelength most closely in resonance with the silver nanoparticles and the azo chromophore of the precursors. Progressively red-shifted excitation wavelengths resulted in a reduction in the SERS activity of silver nanoparticle suspensions. Aggregated nanoparticles, such as the BT-SiO_2 and BT-NH_2 conjugates, displayed sufficient SERS activity with 632.8 nm wavelength excitation. This was attributed to increased resonance of aggregated nanoparticles with the excitation laser and the generation of hotspots of electromagnetic enhancement. In samples prepared using BT-OH, where agglomeration of nanoparticles was minimal, the observed SERS signal intensity was reduced. Nominal SERS activity was observed in all samples when using a 784.6 nm excitation wavelength due to negligible resonance with the nanoparticles.

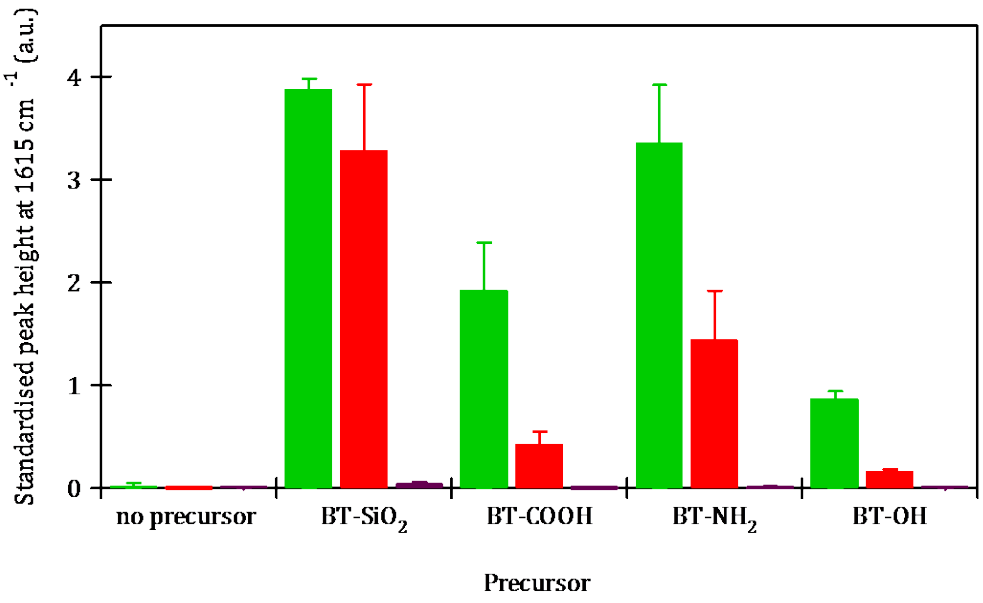

Figure 3.14 Standardised peak height at 1615 cm^{-1} observed in the SERS spectra of silica encapsulated NP-precursor conjugates. Precursors (50 µL, 0.1 µM) added to EDTA AgNP (1 mL, 100 pM) and silica encapsulated as per section 6.3.3. SERS measurements recorded using 514.5 nm (green), 632.8 nm (red) and 784.6 nm (purple) excitation wavelengths. Error bars indicate one standard deviation of 5 measurements of triplicate samples.

The presence of the silica shells around nanoparticles was visualised using scanning electron microscopy (SEM, Figure 3.15). SEM images were provided by Dr. Iain Larmour, University of Strathclyde. SEM was carried out on silica encapsulated nanoparticles deposited onto poly(diallyldimethylammonium) (PDDA) coated silicon wafers. PDDA was employed to reduce surface-induced aggregation artifacts observed when applying nanoparticles to silicon wafers. Differences in polydispersity of silica encapsulated silver nanoparticles fabricated using the four precursors were evident in SEM images (See Appendix I); this correlated with the results obtained in extinction spectroscopy and SERS analysis.

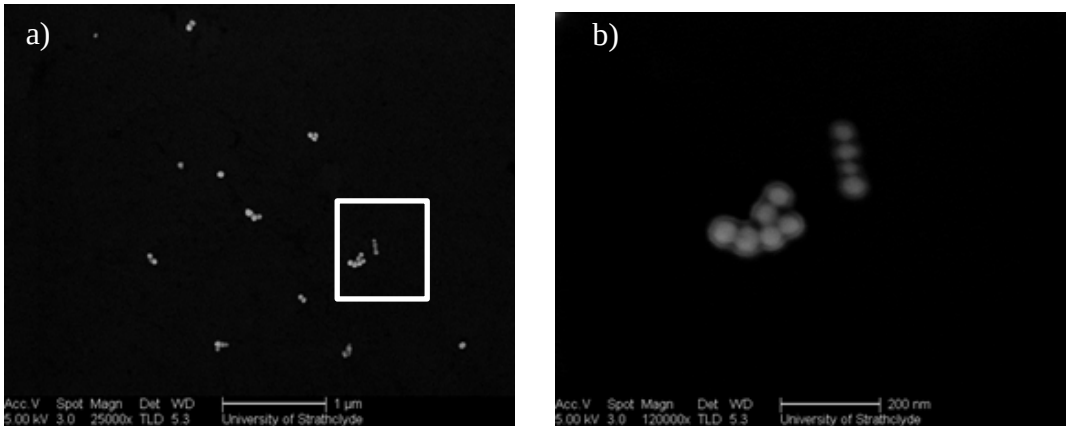

Figure 3.15 SEM images of silica shell, silver core nanoparticles constructed from BT-SiO_2 precursor (in the absence of silane coupling agents) at a) 25000x magnification and b) inset area at 120000x magnification.

All four BT-molecules were successful as precursors for the silica encapsulation of silver nanoparticles. The terminal functional groups were found to play a role in determining the particle size distribution of the encapsulated particles. It was proposed that this effect may be minimised by optimising the precursor addition to the silver nanoparticles.

The concentration of precursor that should be added to silver colloid to achieve optimal stabilisation of the nanoparticles was investigated. Serial dilutions of precursor were added to 1 mL EDTA AgNP resulting in final concentrations of

10^{-6} M to 10^{-9} M. Triplicate samples were prepared and analysed by extinction and Raman spectroscopy. The results are shown in Figure 3.16 (full extinction spectroscopy data is available in Appendix I).

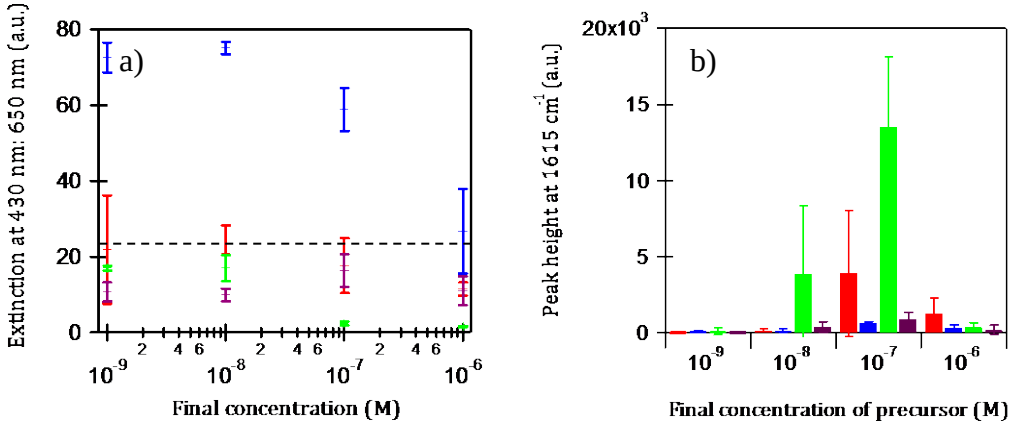

Figure 3.16 a) Extinction and b) SERS analysis of EDTA AgNP conjugates prepared with increasing concentration of precursors: BT-SiO_2 (red), BT-COOH (blue), BT-NH_2 (green) and BT-OH (purple) in 1 mL AgNP. Error bars indicate one standard deviation. Dashed black line indicates the extinction at 430 nm: 650 nm of unconjugated EDTA AgNP.

The ratio of the extinction of the surface plasmon band at 430 nm (the average extinction maximum) to that at 650 nm was calculated. This provided a measure of the aggregation induced by the precursors as larger particles and aggregates have a higher extinction at longer wavelengths. A decrease in the ratio of the extinction of the surface plasmon at 430 nm to 650 nm indicated an increase in the polydispersity of nanoparticles in solution. The average peak height of the most prominent Raman band at 1615 cm^{-1} was also calculated. This is assigned to the quadrant stretching mode of the benzotriazole and aromatic ring systems present in all four precursors.[38] Significant increases in Raman signal can be indicative of polydisperisity within samples.

A decrease in extinction ratio was observed with increasing final concentrations of BT-COOH. However, even at the highest precursor concentrations the extinction ratio was not significantly lower than unconjugated silver nanoparticles (23.9 ± 4.1).

No significant increase in SERS intensity was observed with increasing BT-COOH concentration, potentially due to the perceived stability of these nanoparticle conjugates.

BT-OH did not significantly alter the surface plasmon band with increasing final concentrations and similarly, no significant change in SERS activity was observed. Thus it was assumed that increasing the BT-OH concentration did not affect the particle size distribution of the conjugates. This confirmed previous findings where BT-OH was considered to be a non-aggregating Raman reporter.[175]

On increasing the concentration of BT-SiO_2, a reduction in the extinction ratio of the surface plasmon was observed in extinction spectroscopy. The SERS intensity accordingly increased but at final concentration of 10^{-6} M a drop in SERS activity was seen. This may have been due to possible siloxane bridging of the precursor molecules. Additional layers of precursor co-ordinating to the monolayer that are not removed after centrifugation may absorb some of the scattered light thus reducing that detected by the spectrometer. The result of this would be a reduction in the observed SERS intensity, as was seen for samples with a BT-SiO_2 concentration of 10^{-6} M.

The addition of increasing concentrations of BT-NH_2 to the nanoparticle suspensions led to a significant reduction in extinction ratio of the surface plasmon. It was proposed that the terminal amine moiety of nanoparticle-conjugated BT-NH_2 interacted with the surface of an adjacent silver nanoparticle resulting in aggregation and the emergence of "hot spots" of electromagnetic enhancement. As with BT-SiO_2, the SERS intensity of BT-NH_2 nanoparticle-precursor conjugates was decreased at final concentrations of 10^{-6} M. Due to extensive aggregation observed at this concentration of BT-NH_2 precursor (Figure 3.16a), nanoparticles precipitated out of solution forming a black sediment post centrifugation. As demonstrated by the extinction ratio of BT-NH_2 conjugates at final concentrations 10^{-7} M and 10^{-6} M, with extensive aggregation there is a fine line between high SERS intensities and nanoparticle sedimentation (Figure 3.16b).

All these data considered, a final concentration of 10^{-7} M was considered optimal for precursors BT-SiO_2, BT-COOH and BT-OH and 10^{-8} M for BT-NH_2. Further investigation was performed to assess the optimum volume of precursor that should be added to 1 mL EDTA AgNP to provide the predetermined final concentration. Triplicate samples were prepared and analysed by extinction and Raman spectroscopy. The results are shown in Figure 3.17. The particle size distribution was investigated using both the ratio of extinction maximum (430 nm) to the extinction at 650 nm and to a lesser extent the FWHM of the surface plasmon band in extinction spectroscopy.

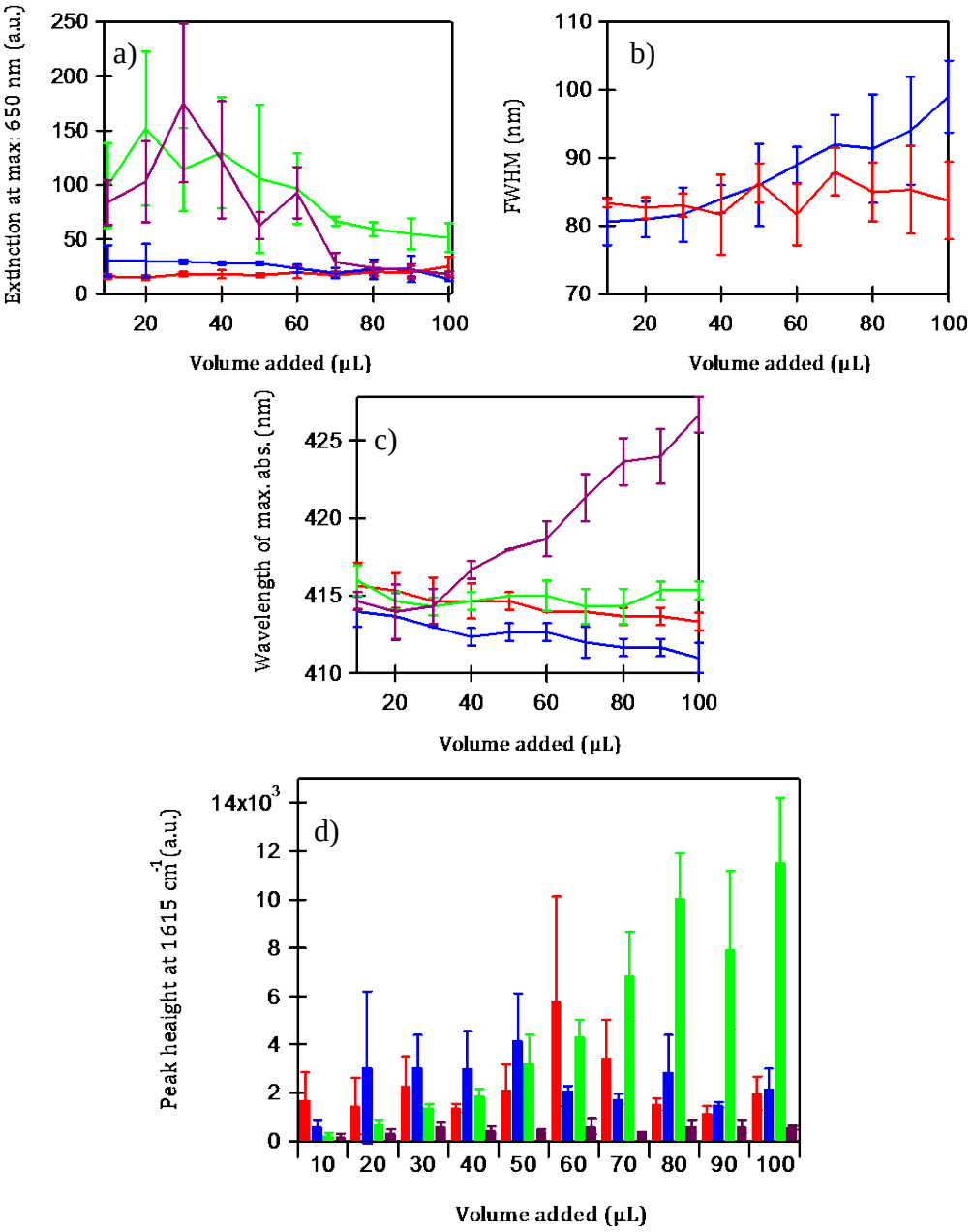

Figure 3.17 Extinction and SERS analysis of nanoparticle conjugates prepared using increasing volumes of precursors: $BTSiO_2$ (red), BTCOOH (blue), $BTNH_2$ (green) and BTOH (purple) at optimised final concentration in 1 mL AgNP.

The results from BT-SiO_2 and BT-COOH precursor-nanoparticle conjugates displayed similar trends. No significant increase in size distribution of the nanoparticles was observed from the extinction ratio in Figure 3.17a. The FWHM of the surface plasmon band increased with increasing volumes of BT-COOH, indicating partial aggregation, but the wavelength of the extinction maximum was

constant within instrumental error. The SERS intensity of the conjugates did not significantly increase with increasing volumes of BT-SiO_2 and BT-COOH. The variability in FWHM of the surface plasmon band increased with increasing volumes of BT-SiO_2. As was proposed for an increasing concentration of BT-SiO_2, this may have been a result of siloxane bridging between precursors on adjacent nanoparticles.

Extinction spectroscopy results for BT-NH_2 and BT-OH indicated an initial stabilisation effect on the surface plasmon band with increasing volumes of precursor. This was quickly followed by a continual decrease in ratio of extinction maximum: extinction at 650 nm, thus suggesting an increase in size distribution of the particles. This positively correlated with the rise in SERS intensity observed from nanoparticle conjugates with increasing volumes of BT-NH_2 (Figure 3.17d).

The same cannot be said for the SERS intensity of BT-OH conjugates which remained relatively constant over the investigated conditions. This may be explained by the continual rise in the wavelength of the extinction maximum with increasing volumes of BT-OH. It was proposed that the precursor itself was contributing to the extinction spectra of the conjugates. On examining the extinction spectra of the EDTA AgNP after addition of 100 μL BT-OH, the spectra can be considered as the sum of an EDTA AgNP and unconjugated BT-OH spectra (Figure 3.18). Increasing the volume of BT-OH added to the colloidal suspension resulted in residual BT-OH remaining in solution; this was not seen to increase the amount of precursor on the surface of the nanoparticles.

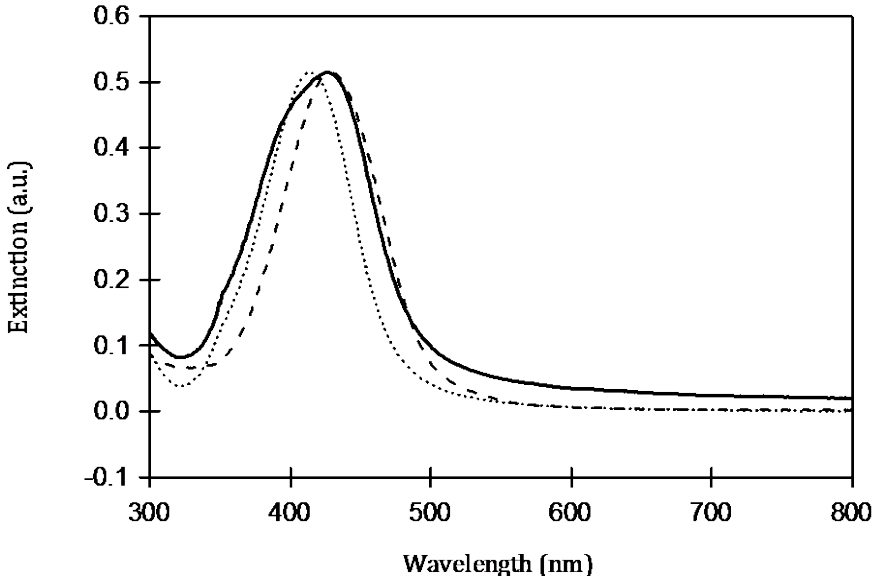

Figure 3.18 Extinction spectra of BT-OH conjugates after 100 µL addition and the corresponding component spectra of bare EDTA AgNP(dotted) and unconjugated BT-OH at 1.5 x 10^{-5} M (dashed).

To assess the ability of the precursors to act as stabilising agents for the nanoparticles during the silica coating process, the pre-determined optimal conditions were selected for addition to 1 mL aliquots of EDTA AgNP at 100 picomolar (pM):

- BT-SiO_2 - 40 µL, 1 x 10^{-5} M
- BT-COOH - 30 µL, 1 x 10^{-5} M
- BT-NH_2 - 20 µL, 1 x 10^{-6} M
- BT-OH- 30 µL, 1 x 10^{-5} M

Minimal aggregation was caused by these conditions. Therefore any increase in size distribution of the nanoparticles could be attributed to the silica coating process. The precursor-nanoparticle conjugates were silica encapsulated following a modification of the Stöber method as outlined in 6.3.3. The samples were analysed by extinction spectroscopy and DLS to assess any changes in particle size distribution.

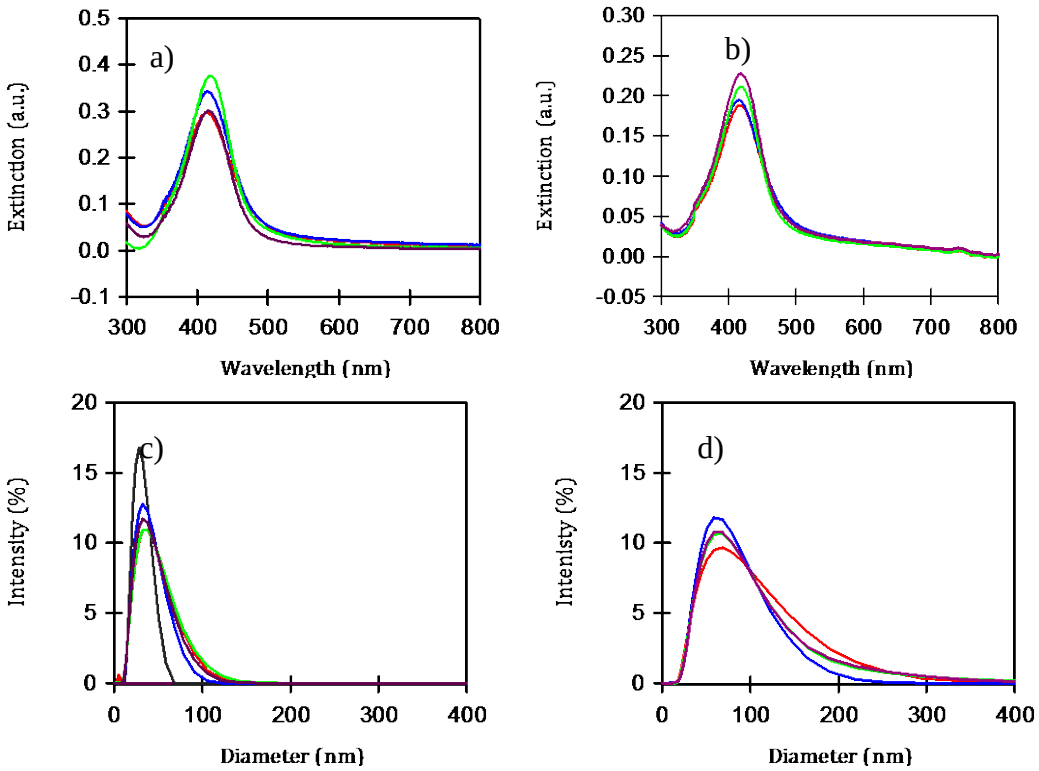

Figure 3.19 Extinction spectra of optimised EDTA AgNP (black) and AgNP-precursor conjugates BT-SiO_2 (red), BT-COOH (blue), BT-NH_2 (green) and BT-OH (purple) a) pre and b) post silica encapsulation. The corresponding DLS measurements c) pre and d) post silica encapsulation. Reported measurements are the average of triplicate samples.

Prior to silica encapsulation there were minor differences in extinction spectra recorded for the nanoparticle-precursor conjugates. The particle size distribution, as measured by DLS, was similar for all nanoparticle-precursor conjugates. Post silica encapsulation the extinction spectra of the conjugates remained similar whilst the DLS measurements display significant differences. When comparing the extinction spectra of samples pre and post encapsulation, a loss in overall extinction was observed. It was therefore proposed that the concentration of nanoparticles was reduced during washing of the particles after Stöber condensation. It is also possible that there was some oxidation of the silver nanoparticles, even in the presence of near monolayer coverage of precursor. Dampening of the surface plasmon band may also be attributed to partial aggregation. The DLS measurements indicated that the size

distribution of the silver nanoparticles was also greater in silica encapsulated particles compared to their nanoparticle-precursor conjugates. The smallest particle size distribution was observed from the silica coated particles synthesised using the BT-COOH precursor. This indicated that the BT-COOH precursor offers the most stabilisation of silver nanoparticles during silica coating *via* the outlined Stöber method in 6.3.3. The largest particle size distribution was observed from the silica coated particles synthesised using the BT-SiO_2 precursor. This is attributed to premature siloxane bridging between precursors on adjacent nanoparticles.

Figure 3.20 illustrates the average SERS intensity of optimised EDTA AgNP-precursor conjugates pre and post silica encapsulation. Triplicate measurements of triplicate samples were recorded using 514.5 nm excitation wavelength.

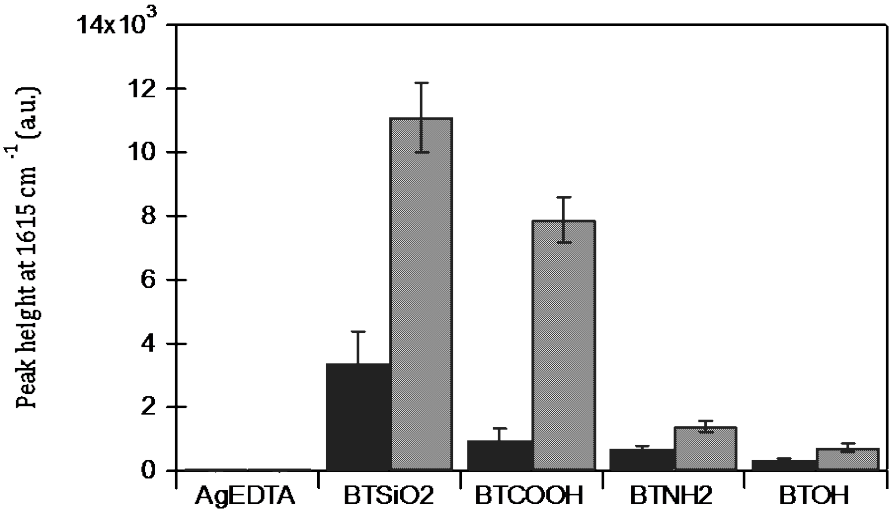

Figure 3.20 SERS comparison of the optimised AgNP-precursors conjugates pre (black) and post (grey) silica encapsulation using an excitation wavelength of 514.5 nm. Error bars indicate one standard deviation.

In all instances, SERS activity of the nanoparticle-precursor conjugates was increased post silica encapsulation. This was due to the perceived increase in polydispersity of the nanoparticles during the silica coating process (Figure3.19d). It was proposed that by introducing ethanol to the colloidal suspension, as per the

Stöber method, the nanoparticles may agglomerate due to the reduction in dielectric constant. However, monolayer coverage of the precursor on the surface of the nanoparticle should reduce the extent of the aggregation. The stabilising presence of BT-SiO_2 on the surface is most likely out-weighed by the tendency of the precursors to self-condense. Thus, more extensive aggregation of the cores provided more electromagnetic "hotspots" and increased the observed SERS intensities of the samples explaining.

The SERS intensity with respect to BT-NH_2 and BT-OH samples was also increased post silica encapsulation, but to a lesser extent. Extinction spectroscopy and DLS data did not indicate that increased monodispersity of the sample was the cause of reduced SERS.

The increase in SERS intensity post silica encapsulation was largest for the precursor BT-COOH. However, the DLS measurements of these samples indicated the smallest particle size distribution. It is possible that the precursor BT-COOH is capable of controlling the aggregation of nanoparticles to some degree, thus limiting the cluster size to dimers, trimers and small aggregates.

3.3.3 Optimisation of modifications to the Stöber method

The Stöber method refers to ammonium hydroxide-catalysed hydrolysis and condensation of alkoxysilanes in low molecular weight alcohols. Modifications of this well-established method are common in silica encapsulation of Raman-tagged nanoparticles. Some experimental factors were investigated to assess the optimal conditions for the synthesis of reproducible SERS active silver / silica core / shell nanoparticles using the precursor BT-COOH.

The first reports of silica condensation *via* the base-catalysed Stöber mechanism utilised ammonium catalysts. Ammonium hydroxide readily oxidises silver to form soluble complex ions resulting in the formation of excess core-free silica particles.[64] A more sterically hindered amine would be more compatible for the fabrication of silica coated silver nanoparticles. Even one methyl substituent on ammonium

hydroxide is sufficient at reducing the rate of oxidation at the silver nanoparticle surface.[164] The choice of amine catalyst in the modified Stöber method was investigated. In this study, triethylamine (TEA), triisobutylamine (TIBA) and N,N-diisopropylethylamine (DIPEA) were investigated as catalysts. 1 % volume / volume (v/v) solutions of the catalysts were prepared in both de-ionised water (dH_2O) and ethanol (EtOH). Following Stöber condensation, triplicate nanoparticle samples were analysed using extinction spectroscopy (Figure 3.21).

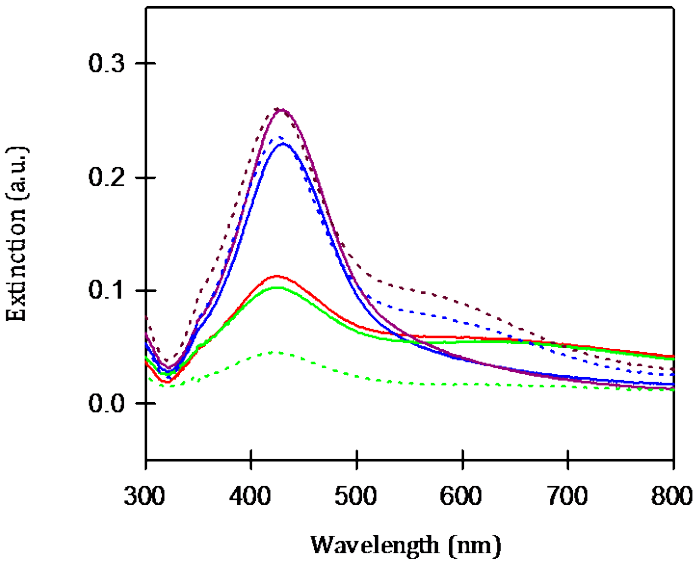

Figure 3.21 Extinction spectra comparing silica encapsulated silver nanoparticles synthesised from AgNP-precursor conjugates in the absence of an amine catalyst (red) and in the presence of TEA (blue), TIBA (green) and DIPEA (purple). Amine catalysts were dissolved in dH_2O (solid) and EtOH (dashed).

In samples prepared in the absence of an amine catalyst, the surface plasmon band of the silver nanoparticles was broadened and depleted. Increased extinction at longer wavelengths was also observed. This indicated extensive aggregation of the nanoparticles had occurred. It was proposed that in the absence of an amine catalyst, the rate of condensation of TEOS onto the surface of the nanoparticles was greatly reduced. The nanoparticles were exposed to the organic medium for longer periods of time, in which they became unstable. Aqueous solutions of TEA and DIPEA were efficient catalysts for Stöber condensation under these conditions. Ethanolic

solutions of these amines were not as effective. This may be due to the reduced solubility of the amines in organic solvents. TIBA did not prove to be an effective catalyst for the condensation of TEOS. TIBA is insoluble in water and provides nominal catalytic properties under these experimental conditions.

The concentration of ethanol used for the reaction solvent was also considered. Ethanol and ethanol / water mixtures were used to provided monomeric silica to facilitate homogenous growth of silica.[66] Previous studies have shown that high water concentrations can result in inhomogeneous surfaces.[176] 1:4 v/v water/ ethanol ratios are therefore often employed in the silica encapsulation of metallic nanoparticles.[69]

Nanoparticle conjugates were centrifuged in 1 mL aliquots and resuspended in small volumes of dH_2O. Ice-cold ethanol was added to the aliquots resulting in 1:1, 1:2, 1:3 and 1:4 v/v ratios of water / ethanol. TEOS and TEA were added and the reaction was allowed to proceed overnight. The samples were washed and resuspended in 1 mL dH_2O. The average extinction spectra of triplicate samples are displayed in Figure 3.22

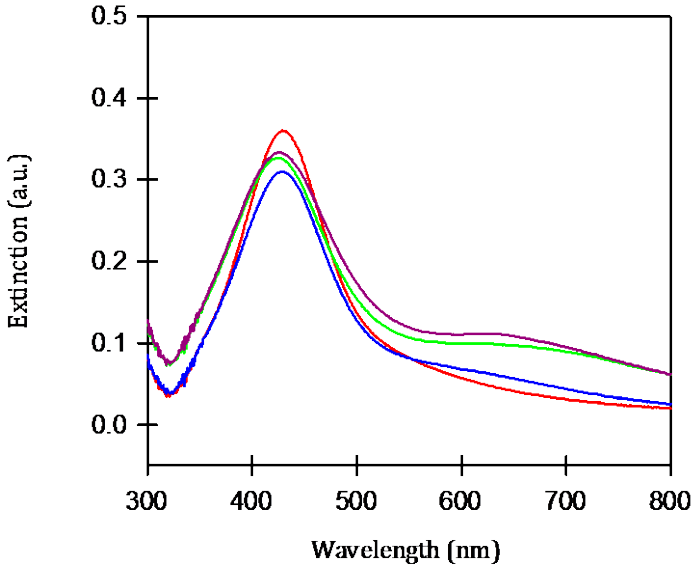

Figure 3.22 Extinction spectroscopy comparison of silica encapsulated silver nanoparticles synthesised in increasing dH_2O: EtOH concentrations 1:1 (red), 1:2 (blue), 1:3 (green) and 1:4 (purple).

Extinction spectroscopy measurements indicated aggregation of the silver nanoparticles was induced at higher ethanol concentrations. Increasing the concentration of ethanol in the reaction mixture reduced the overall polarity of the solvent system. This rendered the dispersive medium less effective at shielding the Van de Waals forces between adjacent nanoparticles, resulting in agglomeration of the nanoparticles.

In order to maintain stability, sufficient coverage of the nanoparticles must be obtained prior to the introduction of higher ethanol concentration. It was proposed that an initial silica layer grown in 1:1 v/v water / ethanol mixtures would be adequate at shielding the inter-particle Van der Waals forces. Additional layers of homogenous silica could then be grown at higher ethanol concentrations.

The effect of increasing ethanol concentration prior to and after an initial growth of 12 hours was investigated. The average extinction spectra and particle size distribution (as measured by DLS) of triplicate samples are illustrated in Figure 3.23.

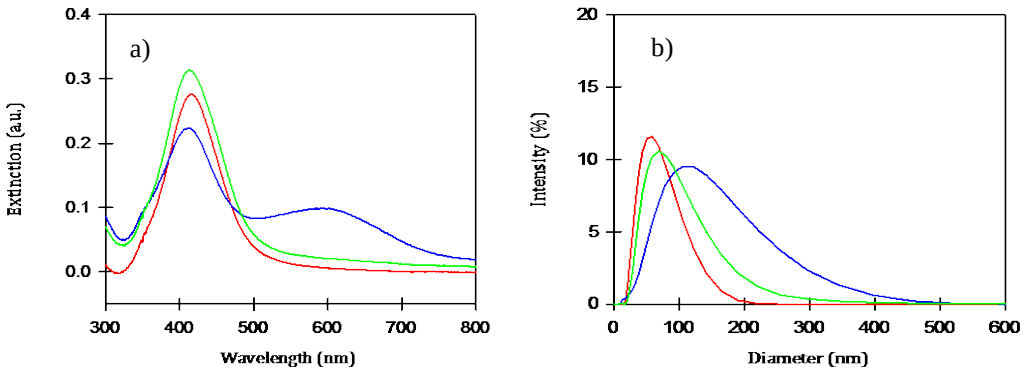

Figure 3.23 a) Extinction spectra of silica encapsulated silver nanoparticles synthesised in 1:1 dH_2O:EtOH (red) and 1:4 dH_2O:EtOH where EtOH concentration was increased during (blue) and after (green) initial silica growth and b) particle sizing data recorded by DLS.

As previously observed, increasing ethanol concentrations prior to silica growth induced aggregation of the nanoparticles. This effect was greatly reduced when silica growth was allowed to proceed in 1:1 v/v water: ethanol mixtures for 12 hours before increasing this ratio to 1:4 (water:ethanol). The shape of the surface plasmon band, observed in extinction spectroscopy, was not significantly affected when the ethanol concentration was increased after an initial growth period. However, a small blue-shift in the average wavelength at the extinction maximum was evident. The additional silica may have altered the refractive index of the particles, though one would expect that the increased silica deposition would increase the nanoparticle diameter and thus result in red-shift. The 4 nm shift may be considered a summation of these two effects. The DLS measurements indicated a greater particle size distribution with increased silica deposition. This was substantially reduced in comparison to increasing ethanol concentration prior to initial silica growth, suggesting that the initial layer of silica sufficiently shielded the attractive Van der Waals forces of adjacent particles and reduced coagulation.

Further to studies with ethanol, the choice of alcohol used to promote silica condensation was examined. Methanol (MeOH), ethanol (EtOH) and isopropanol (iPrOH) were compared as solvents used in a 1:1 v/v ratio with dH_2O. The resulting

suspensions were washed and resuspended in dH_2O. The average extinction spectra of triplicate samples are shown in Figure 3.24.

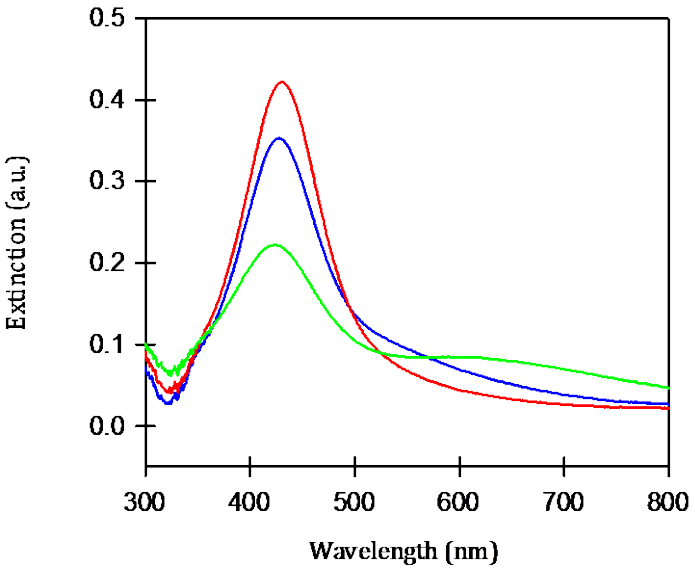

Figure 3.24 Extinction spectroscopy comparison of silica encapsulated silver nanoparticles synthesised in methanol (red) ethanol (blue) and iPrOH (green) in a 1:1 v/v ratio with dH_2O.

Extinction spectroscopy analysis indicates that the perceived stability of silver nanoparticles was negatively correlated with the length of the alkyl chain of the organic solvent. The dielectric constant of alcohols also decreases with increasing length of alkyl chain. The reported values at 25 ^{o}C for methanol, ethanol and isopropanol are 30, 24.3 and 18.23 respectively. Reducing the dielectric constant of the solvent significantly increases the Coulombic coupling between charge species.[177] It was therefore proposed that agglomeration of silver nanoparticles occurred due to the reduction in dielectric constant of the dispersive medium. Thus for reproducible silica encapsulation of silver nanoparticles, methanol is the preferred solvent for Stöber condensation of TEOS.

3.4 Assessment of silica encapsulation

The shelling of nanoparticles is finding increasing application in the design of bio-imaging reagents. Silica encapsulation is proposed to stabilise the nanoparticle cores against aggregation and control their chemical reactivity without interfering with their detectable read-out. The chemistry of the silica surface has been well-studied and is therefore amenable to a variety of attachment protocols. This aids functionalisation of the nanoparticles to permit interaction with biological species (see Chapter 4). The aforementioned properties of the silica shell are assessed herein.

3.4.1 Optical transparency of the silica shell

On the previously encapsulated nanoparticles (section 3.3.2) the optical transparency of the silica shell was investigated. SERS spectra of the AgNP-precursor conjugates were recorded prior to and after silica encapsulation. Five measurements were recorded for triplicate samples using a 514.5 nm excitation wavelength. The average spectra were normalised with respect to the 1615 cm^{-1} band to account for variations in observed signal strength. The signal from the encapsulated conjugates was subtracted from that recorded for the pre-encapsulated conjugates to create a difference spectrum (Figure 3.25).

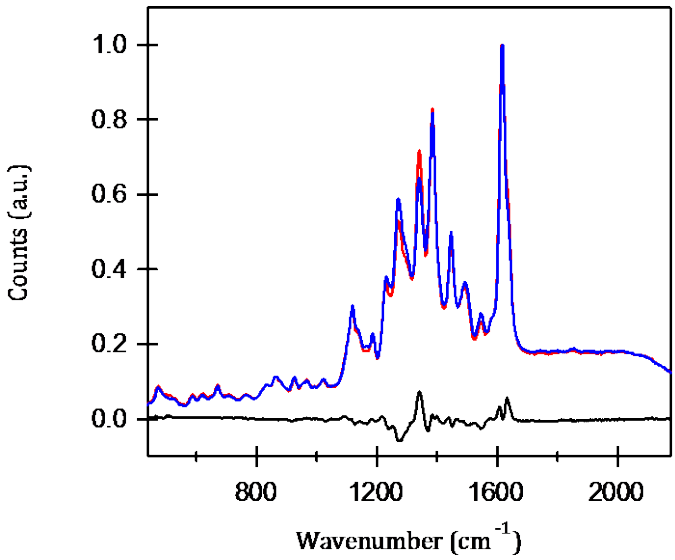

Figure 3.25 A comparison of the SERS spectra of AgNP-BT-SiO_2 conjugates pre (red) and post (blue) silica encapsulation. A difference spectrum (black) was constructed by subtracting the post-encapsulation spectrum from the pre-encapsulated spectrum. Spectra shown are average of 5replicate measurements of triplicate samples using a 514.5 nm excitation wavelength.

On initial inspection, few differences were observed between the SERS spectra pre and post silica encapsulation. However, the difference spectrum illustrated these differences more clearly. The emergence of new spectral bands post encapsulation was not evident; however there were some changes in the existing peak ratios.

Fluctuations in both spectral shape and intensity are a common feature in SERS measurements. This may be a result of dynamics of the SERS substrate i.e. Brownian motion of the particles through the focus of the exciting laser beam. Other effects concerning the polydispersity of the SERS substrate may also be applicable. The formation of small clusters alters the plasmon resonance of the substrate and its associated electromagnetic enhancement. As these enhancements are wavelength dependent, the peaks in the spectrum may be affected to different extents.[178] Therefore it was concluded that the silica shell was optically transparent but that changes in the polydisperity of the samples induced fluctuations in the SERS spectra, such as those observed for BT-SiO_2 nanoparticle conjugates.

3.4.2 Core Stability

The silica shell is also considered to afford stabilisation to the relatively unstable silver core. In this case, the protective ability of the silica shell against both aggregation and dissolution of the silver core was investigated. Sodium chloride (NaCl) is commonly employed as an aggregating agent for metallic nanoparticles.[179] The silica shell should ideally prevent aggregation of the silver nanoparticle core induced by NaCl, which is present in many biological buffers. To that end, extinction spectra of AgNP-precursor conjugates and their silica encapsulated equivalents were recorded immediately after addition of NaCl and again after 24 hr. (Figure 3.26).

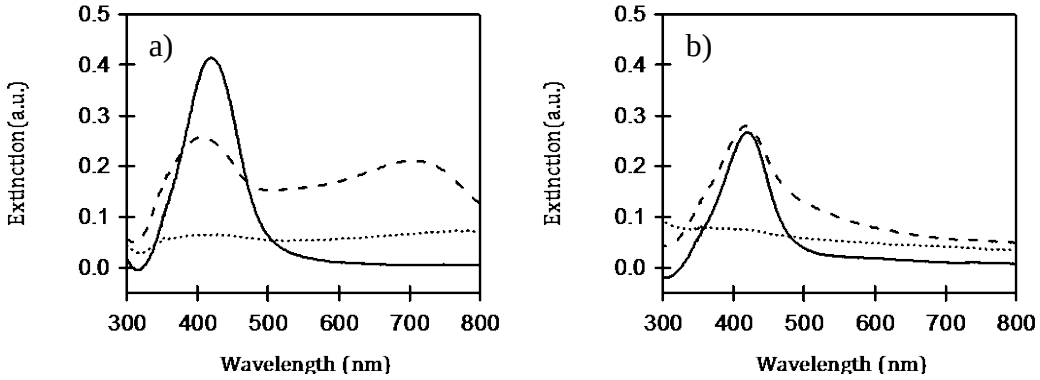

Figure 3.26 Extinction spectroscopy analysis of AgNP(BT-COOH) conjugates a) pre and b) post silica encapsulation on addition of NaCl (50 µL, 2 M) at t = 0 hr. (dashed) and t = 24 hr. (dotted).

Immediately after addition of NaCl, the pre-encapsulated conjugates displayed signs of aggregation (Figure 3.26a). Partial aggregation was also observed in the post-encapsulated samples though not to the same extent (Figure 3.26b). After 24 hr. extensive aggregation resulted in precipitation of larger particles and negligible extinction in the UV-Vis range for conjugates both pre and post silica encapsulation. It was proposed that the silica shell does not act as physical barrier to the silver core, but serves as a selectively permeable membrane, controlling the rate of reaction at the nanoparticle surface.

A similar investigation was designed to assess the shell's capability at preventing chemical oxidation of the silver core. Nitric acid (HNO_3) is employed in the cleaning of glassware used for colloid preparation due to its oxidative properties. Extinction spectra of AgNP-precursor conjugates and their silica encapsulated equivalents were recording immediately after addition of HNO_3 and again after 24 hr. (Figure 3.27).

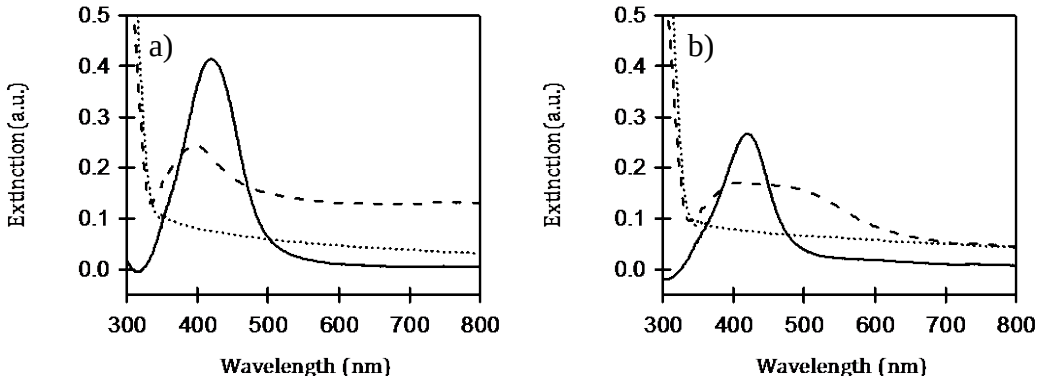

Figure 3.27 Extinction spectroscopy analysis of AgNP(BT-COOH) conjugates a) pre and b) post silica encapsulation on addition of HNO_3(50 µL, 10 %v/v) at t = 0 hr. (dashed) and t = 24 hr. (dotted).

Similar to the effect of the addition of NaCl, in the presence of HNO_3 the surface plasmon band was altered for AgNP-conjugates both pre and post silica encapsulation. This effect was observed to a greater extent in pre-encapsulated samples. However, after 24hr. the surface plasmon band in both samples was negligible. This emphasises the selective permeability of the silica shell and its effects on the reduction of kinetics at the nanoparticle surface.

3.4.3 Reporter Stability

Encapsulation of nanoparticle-reporter conjugates is anticipated to prevent desorption of Raman reporters from the nanoparticle surface and also prevents absorption of competing molecules from the biological environment. The covalent nature of the bonding between the four synthesised precursors and the metal should

negate desorption or even displacement of these reporter molecules from the nanoparticle surface. However, the ability to prevent adsorption of other molecules onto the surface will be investigated. The fluorescent dye carboxytetramethylrhodamine (TAMRA) was added to the nanoparticle-BT-COOH conjugates pre and post silica encapsulation. The non-fluorescent, non-aggregating dye BT-OH was also added to Ag-BT-COOH nanoparticle suspensions. This molecule has a similar Raman cross section to BT-COOH but also has sufficient spectral variance to allow discrimination. Extinction spectroscopy analysis of the pre-encapsulated samples is illustrated in Figure 3.28.

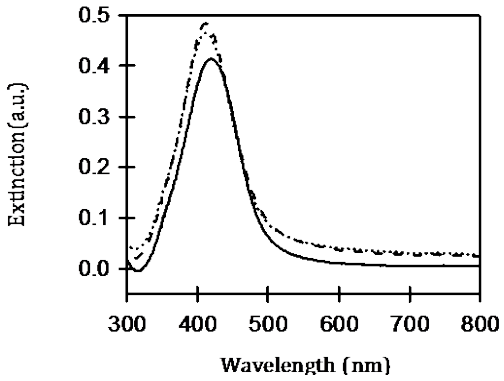

Figure 3.28 Extinction spectroscopy analysis of AgNP(BT-COOH) conjugates pre silica encapsulation (solid) and after addition of TAMRA (50 µL, 10 µM, dashed) and BT-OH (50 µL, 10 µM, dotted).

The local maximum observed in extinction spectra of the pre-encapsulated BT-COOH nanoparticle conjugates, after addition of TAMRA and BT-OH, appeared slightly shifted, but changes to the shape of the surface plasmon band were minimal.

The average SERS spectrum of the pre-encapsulated nanoparticles after the addition of TAMRA (Figure 3.29i) exhibited significant fluorescence. This background masked the Raman peaks of the SERS active BT-COOH conjugated to the nanoparticle surface. This fluorescence background can be attributed to the presence of TAMRA molecules. TAMRA is also SERS detectable; the fluorescence of the dye is largely quenched when in close proximity to the silver surface. As no

TAMRA Raman peaks were observed, superimposed on the fluorescent spectrum, it was suggested that TAMRA molecules were not directly attached to the nanoparticle surface. It was thus concluded that the TAMRA molecules were associated with the nanoparticle *via* the chemisorbed BT-COOH molecules.

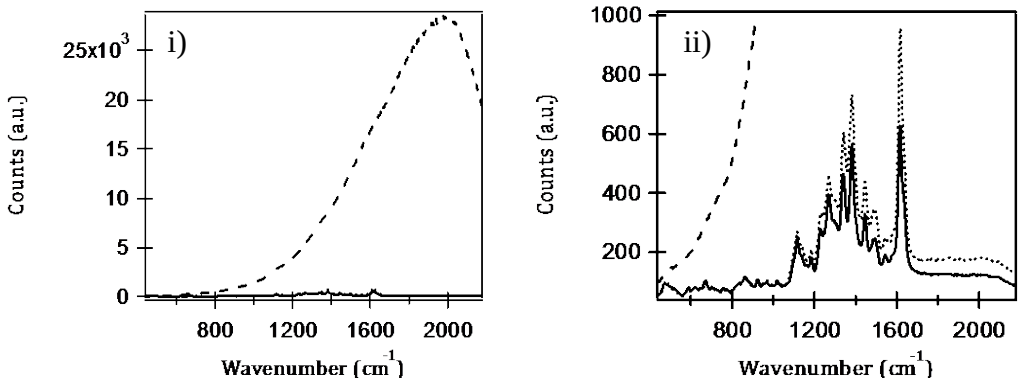

Figure 3.29 SERS analysis of AgNP(BT-COOH) conjugates pre silica encapsulation on addition of TAMRA (50 µL, 10 µM, dashed) and BT-OH (50 µL, 10 µM, dotted).

The addition of BT-OH to the pre-encapsulated BT-COOH conjugated nanoparticles did not appear to significantly alter the overall shape of the SERS spectral output (Figure 3.29ii). A difference spectrum was calculated to facilitate the determination of spectral changes after the addition of BT-OH (Figure 3.30). The average spectra pre and post addition of BT-OH were normalised with respect to the intensity maximum to minimise variations in signal intensity. The spectrum obtained from analysis of unadulterated AgNP-BT-COOH was subtracted from the BT-OH augmented complement to produce a difference spectrum. The spectral differences observed after TAMRA addition were clear, thus no difference spectrum was produced for these samples.

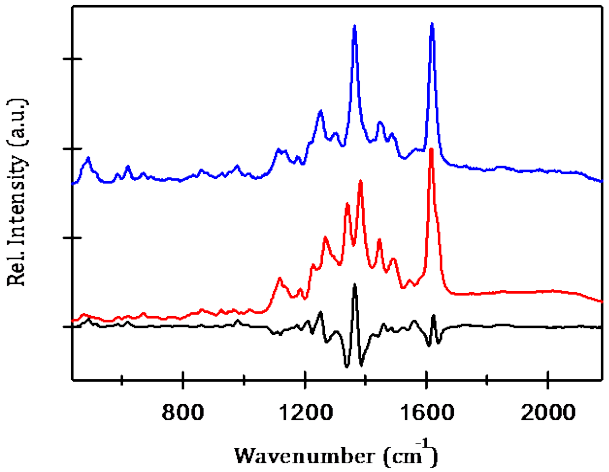

Figure 3.30 The difference spectrum (black) calculated by subtracting the spectrum of unadulterated Ag-BT-COOH nanoparticle conjugates (red) from the spectrum of the nanoparticles post addition of BT-OH. The SERS spectrum of BT-OH is also illustrated (blue).

After the addition of BT-OH, minor reductions were seen in the relative intensities of certain peaks associated with the BT-COOH SERS spectrum when using an excitation wavelength of 514.5 nm. This was co-incident with the emergence of a peak at 1370 cm^{-1}, common to the BT-OH SERS spectrum seen when employing the same excitation wavelength. These data indicated that BT-OH experienced enhancement from the silver nanoparticles and was therefore in close proximity to the nanoparticle surface. It was proposed that, under these conditions, BT-COOH molecules are at sub-monolayer coverage and BT-OH molecules are capable of aligning alongside BT-COOH on the surface.

Extinction spectroscopy and SERS analysis of the post-encapsulated samples are illustrated in Figure 3.31. Extinction spectra of the BT-OH and TAMRA adulterated samples indicate that aggregation of the nanoparticles had occurred. This was not observed in the analysis of pre-encapsulated samples.

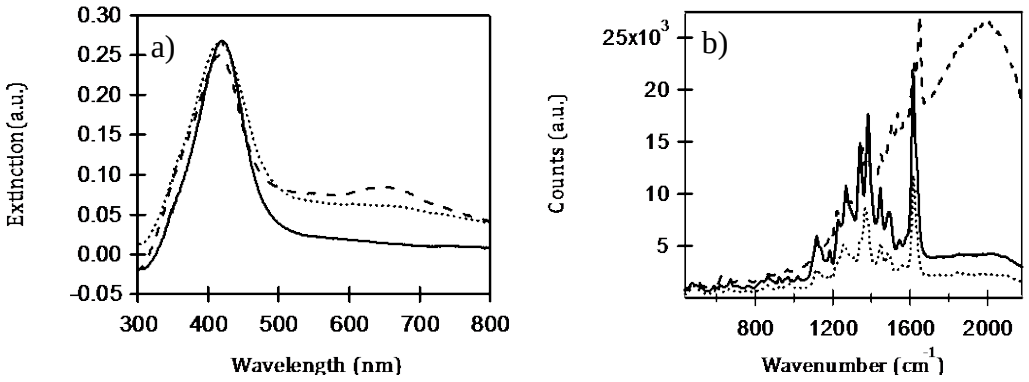

Figure 3.31 a) Extinction spectroscopy and b)SERS analysis of AgNP(BT-COOH) conjugates post silica encapsulation on addition of TAMRA (50 µL, 10 µM, dashed) and BT-OH (50 µL, 10 µM, dotted).

Overall, SERS spectra of the BT-OH and TAMRA adulterated post encapsulated samples exhibit more significant differences compared to the pre encapsulated samples in Figure 3.29. The average SERS spectrum of the post-encapsulated nanoparticles after the addition of TAMRA also exhibited significant fluorescence. However, unlike the pre-encapsulated complement, SERS peaks were prominent superimposed on the fluorescent background. A general reduction in the intensity of the BT-COOH spectral peaks was most likely due to the masking effect of the fluorescent background. The appearance of one of the more prominent peaks of the TAMRA spectrum were also evident although, significant fluorescence observed suggests that the TAMRA was not close enough to the silver surface to experience efficient quenching. The observed SERS spectrum of silica encapsulated BT-COOH conjugated nanoparticles following the addition of BT-OH also displayed significant similarities to the BT-OH spectrum.

Increased spectral variations were perceived in the encapsulated particles compared to the pre-encapsulated samples. This was attributed, not to the permeability of the silica shell but, to the aggregation induced by the additives (Figure 3.31a). If the adulterants were located in the emergent hotspots, the electromagnetic enhancement experienced would be significant. Thus, further stabilisation of the nanoparticles is

required to prevent contaminant SERS signals being detected though agglomeration of the silica encapsulated colloid.

3.5 Conclusions

Previously reported successful encapsulation of silver nanoparticles was assessed as being non-reproducible. This was attributed to insufficient stabilisation of the silver nanoparticle cores. In efforts towards increasing the stability of silver nanoparticles to base catalysed Stöber condensation of silica, EDTA AgNP (average colloidal pH ≈ 11.5) provided optimal over both CR AgNP (pH≈ 8.7) and BRCS AgNP (pH ≈ 9).

Incorporation of a Raman reporter molecule into the fabrication process *via* mixed monolayer coverage of reporter and silane precursors exhibited reduced SERS reproducibility. This was due to inhomogeneous coverage of the reporter on the nanoparticle surface. Thus it was proposed that a molecule acting as both Raman reporter and vitreophilising precursor would increase the reproducibility of SERS analysis.

Four tri-functional molecules were designed to stabilise the silver nanoparticles, act as Raman reporters and provide a suitable precursors for an integrated network of silica polymers *via* Stöber condensation. The nature of the terminal functional group was found to affect the particle size distribution both prior to and during silica encapsulation. Interactions between terminal amino moieties and the nanoparticle surface are thought to be responsible for induced aggregation prior to silica coatings. Premature siloxane bridging between adjacent terminal alkoxysilane groups induced agglomeration of nanoparticle cores during the silica coating process. In the first situation, these effects could be minimised through optimisation of precursor to nanoparticle concentrations.

Modifications of the Stöber method were also investigated. Examination of the choice of tri-substituted amine catalyst employed revealed TIBA was an unsuitable

catalyst due to the reduced solubility. TEA and DIPEA were effective catalysts, their efficiency increasing with solubility.

The concentration of ethanol used for the reaction solvent was also considered. Ethanol / water mixtures, such as 1:4 v/v ethanol / water, are often used to facilitate homogenous growth of silica. However, increasing the ethanol concentration increased the particle size distribution of the silver nanoparticles. It is postulated that the reduced polarity of the solvent reduces the shielding capabilities against the inherent Van der Waals forces between adjacent nanoparticles. The use of higher ethanol concentrations can be achieved after an initial silica growth period.

Alcohols with shorter alkyl chains have a higher relative permissibility and thus do not lower the overall dielectric constant of the reaction solution to the same extent as alcohols with longer alkyl chains. Thus methanol is was found to be more efficient at shielding the Van der Waals forces between adjacent nanoparticles, reducing the observed particle size distribution.

The silica shell was deemed to be optically transparent, not contributing to or significantly altering the observed SERS spectrum. However, the presence of the silica shell does not act as a physical barrier, but rather acts as a selectively permeable membrane reducing the kinetics of reactions at the nanoparticle surface. The shell is also predicted to prevent desorption of Raman reporters and absorption of other molecules onto the core surface. The covalent nature of bond between the synthesised precursors and the nanoparticle surface sufficiently averts desorption. However a small number of molecules may be able to penetrate the shell and sub monolayer coverage. The interaction of the shell with Raman active contaminants may induce aggregation. The resultant electromagnetic enhancement experienced in the induced hotspots may contribute to the overall spectral output. Therefore further stabilisation of the silica encapsulated nanoparticles is necessary before introducing them into a bio-analytical environment. This may be provided by further functionalisation with proteins (See chapter 4).

3.6 Future work

SEM images were used to assess the particle size distribution of the silver / silica nanoparticles fabricating using the four precursors. While the silica shell was observed, an accurate measurement of the thickness of the shell could be made using this technique. Preliminary investigations were initiated, in collaboration with Dr. Zeljka Krpetic at the University of Liverpool, to further characterise the silica shell by transmission electron microscopy (TEM). Initial imaging suggested that the thickness of the silica shell was no more than 5 nm in diameter (see Appendix I). These experiments were performed prior to optimisation of the synthetic route. Further analysis of the optimised silver / silica nanoparticles by TEM would reveal an accurate measurement of the silica shell.

The silica shell was not observed to afford significant stabilisation of the silver nanoparticle cores. Efforts to increase the shell thickness may reduce the kinetics of reactions occurring at the silver core. TEM images could be employed to correlate the radius of shell to the stabilising effects.

4 Bio-functionalised silica encapsulated nanoparticles for bio-imaging

4.1 Introduction

Natan and co-workers have reported some very successful work on the development of biocompatible gold / silica core / shell SERS active nanoparticles.[54, 172] The impressive multiplexing capabilities demonstrated by these gold / silica particles, coupled with their biocompatibility, make them versatile reagents for biological SERS analysis. The development of reproducible SERS active silver / silica analogues will find use in a wide range of applications where gold has previously been used, with the advantage offering the alternative optical properties of silver. SERS detectable silica encapsulated silver nanoparticles were previously synthesised (chapter 3); efforts towards rendering these particles suitable for *in-vitro* imaging are investigated herein.

Fluorescent interference, when using excitation wavelengths in the visible region of the electromagnetic spectrum, can reduce the sensitivity of SERS analysis of biological samples. Operating at wavelengths in the near-Infrared (NIR) spectrum, namely 784.6 nm, largely reduces the background fluorescence. Further to this, adsorption from water and haemoglobin is minimal and penetration depths are higher, due to lower energy photons, with NIR excitation. Therefore, for *in-vitro* studies, silica coated silver nanoparticles require sufficient SERS detectability at NIR excitation wavelengths. Far-red excitation wavelengths, such as 632.8 nm, are also commonly employed for SERS bio-imaging studies.[128, 180]

Bio-functionalisation of nanoparticles is desirable, permitting active targeting of biomarkers. Conjugation of biomolecules, such as proteins and DNA, to the surface of nanoparticles has resulted in the use of SERS in numerous biological detection

systems.[181, 182] The surface chemistry of silica nanoparticles has been well-studied and is amenable to a variety of attachment protocols.[183-185] Thus the surface on silver / silica core/ shell nanoparticles can theoretically be engineered with functionality, allowing conjugation to biomolecules and thus, specific targeting of biologically relevant markers.

The stability of the core / shell nanoparticles must also be considered - coagulation of uncoated-metallic nanoparticles is a common observation in the presence of biological buffers.[186] The silica shell is considered to "physically sequester" the silver core allowing exploitation of the optical properties. As previously reported, "the shell does not render the core impervious to chemical degradation but rather acts as a semi-permeable membrane, controlling the rate of chemical reactions relating to the silver core" (see also chapter 3).[64] The stability of bio-functionalised silver / silica particles, in biological solutions, is assessed herein.

4.2 Increased SERS activity at 632.8 nm

The SERS detectability of the silver / silica core/ shell nanoparticles synthesised in chapter 3 was assessed using longer excitation wavelengths. Extinction spectra for the optimised silica encapsulated nanoparticles fabricated using the four precursors (Figure 3.10) are shown in Figure 4.1.

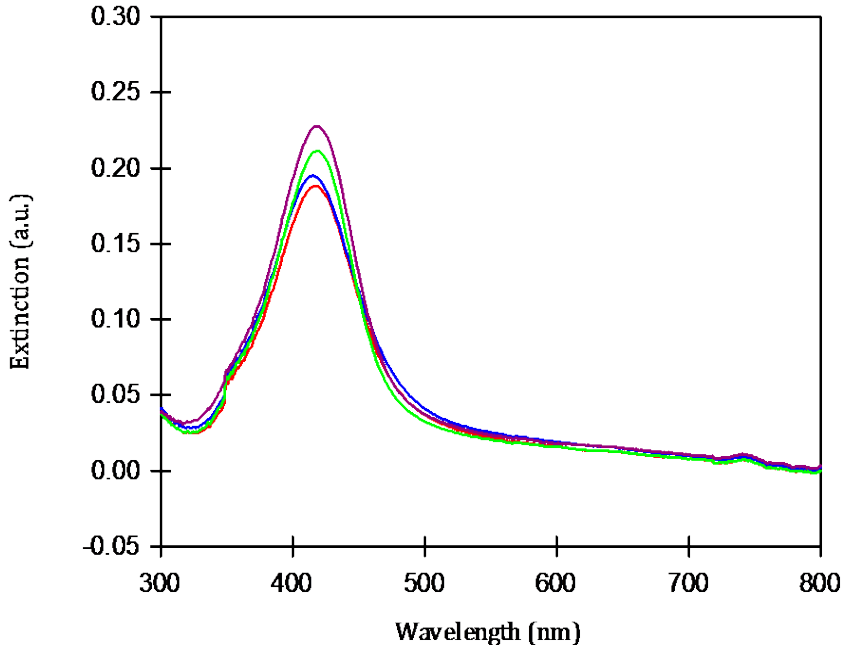

Figure 4.1 Extinction spectroscopy comparison of silver/ silica nanoparticles synthesised from the four trifunctional precursors: BT-SiO_2 (red), BT-COOH (blue), BT-NH_2 (green), and BT-OH (purple).

Extinction spectra demonstrate negligible plasmon resonance of the core / shell particles at 632.8 nm and 784.6 nm. Therefore, the expected SERS enhancement factors from these samples when using far red and NIR excitation wavelengths would be minimal. Efforts were undertaken to produce suitable core / shell nanoparticles, using the modified Stöber method outlined in chapter 3, exhibiting increased SERS "activity" with far red / NIR excitation wavelengths. The use of both nanoparticles and Raman reporters with increased resonance in these regions was investigated.

4.2.1 Transference of method to Au core

The application of gold nanoparticles (AuNP) and SERS within biological studies is extensive. This is a result of their perceived biocompatibility and their considerable "brightness" in the far red / NIR region. The silver nanoparticle core of silver / silica particles was replaced with 45 nm AuNP and the resulting SERS detectability, using far red excitation wavelengths, was investigated. The precursor BT-COOH was

conjugated to the surface of gold nanoparticles in triplicate and analysed by extinction spectroscopy (Figure 4.2) and SERS using 514.5 nm and 632.8 nm excitation wavelengths (Figure 4.3).

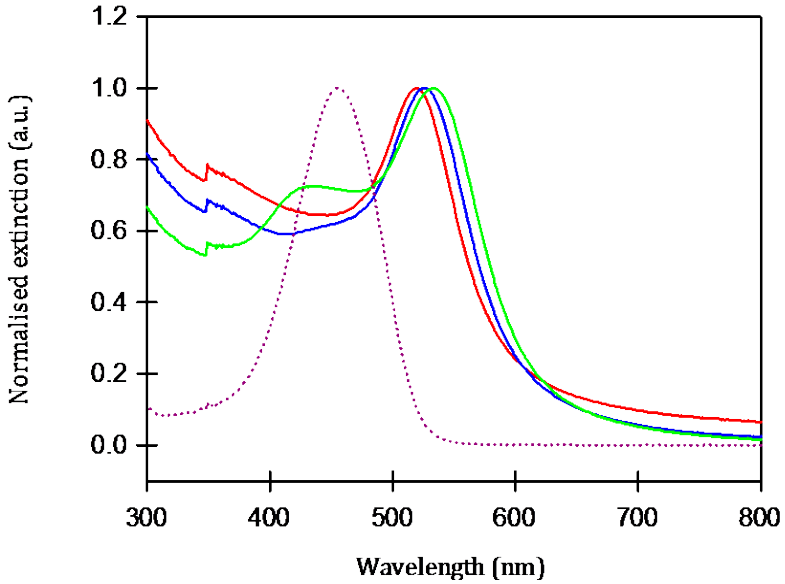

Figure 4.2 Extinction spectroscopy comparison of AuNP (red) conjugated to BT-COOH at final concentrations of 10^{-6} M (blue) and 10^{-5} M (green) and unconjugated BT-COOH (purple).

Minimal changes to the AuNP surface plasmon band were observed in the extinction spectra at final concentrations of up to 10^{-6} M of the BT-COOH precursor. At higher concentrations, the surface plasmon band broadened and a peak at approx. 450 nm emerged in the extinction spectrum. This wavelength is coincident with the absorption maximum of the unconjugated aqueous BT-COOH precursor. The emergence of this additional peak would suggest that excess precursor had not been sufficiently removed from the suspension and remained, unconjugated in solution.

The SERS intensity of the AuNP - precursor conjugates appeared to significantly increase at final concentrations of 10^{-5} M and 10^{-6} M BT-COOH, compared with lower concentrations of BT-COOH. However, the observed SERS responses were negligible for all AuNP conjugates analysed. A comparison of the SERS spectra obtained from unconjugated AuNP and BT-COOH conjugated AuNP clearly

illustrates the minimal SERS enhancements observed using 514.5 nm and 632.8 nm excitation wavelengths.

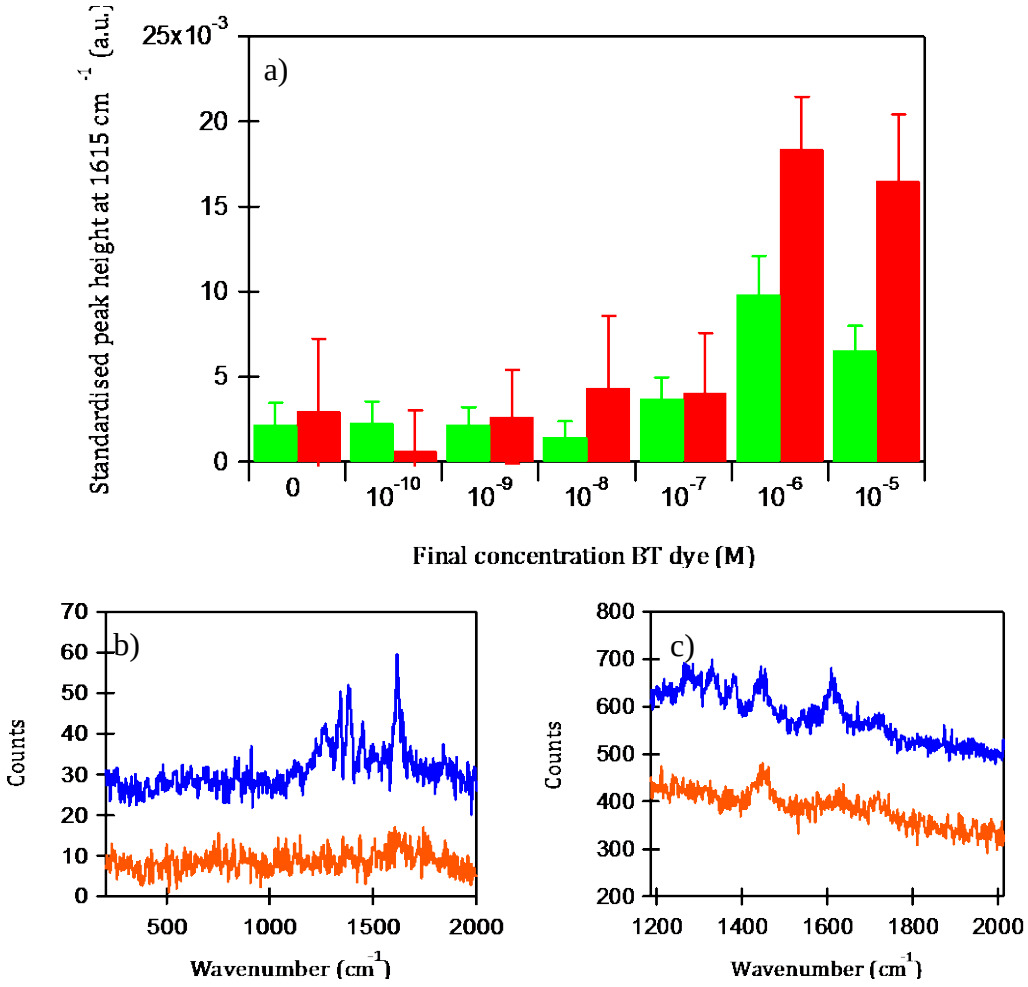

Figure 4.3a Standardised peak height at 1615 cm^{-1} recorded from SERS analysis of AuNP with increasing final BT-COOH concentrations using 514.5 nm (green) and 632.8 nm (red) excitation wavelengths. A spectral comparison of bare AuNP (orange) and AuNP-BT-COOH conjugates (blue) using b) 514.5 nm and c) 632.8 nm excitation wavelengths.

The low SERS enhancement was surprising as the surface plasmon of AuNP is close to the resonance of the excitation wavelengths used. It was proposed that the precursor did not efficiently coordinate with the AuNP surface. Gold is a softer Lewis acid than silver, due to its large diffuse outer orbitals. The two nitrogen donor atoms in the benzotriazole moiety of BT-COOH can be considered relatively hard bases and thus will have less affinity for gold than for silver. Therefore, it was

proposed that the developed method for silica encapsulation of silver nanoparticles, outlined in chapter 3, was not suitable for the use with gold nanoparticle cores.

4.2.2 NIR reporters

As an alternative to using nanoparticles in resonance with far red / NIR excitation wavelengths, it may be possible to incorporate NIR Raman reporters as the precursor for silica condensation on silver nanoparticles. The poor chemical stability of cyanine-based NIR dyes in acidic and basic conditions limits their compatibility with the Stöber condensation method.[76] Efforts to improve the photophysical and photochemical stability of these dyes include the attachment of various hydrophilic groups.[187, 188] The following NIR dye ($\lambda_{max} \approx 795$ nm) was selected for conjugation to gold and silver nanoparticles.

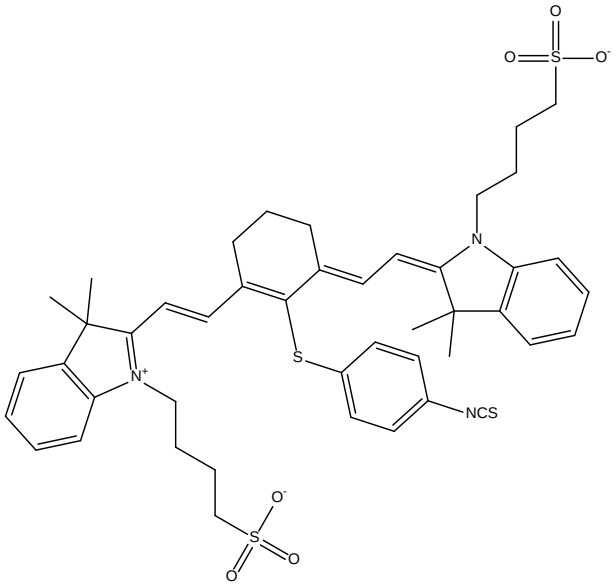

Figure 4.4. NIR dye used as a potential precursor for NIR detectable silica encapsulated silver and gold nanoparticles.

NIR dyes exhibit poor aqueous solubility, readily forming aggregates.[188] This reduces their compatibility with aqueous colloidal suspensions. The incorporation of sulfonate groups to the dye structure increases the solubility in aqueous solutions.[189] The NIR dye illustrated in Figure 4.4 was added to solutions of silver and gold nanoparticles at increasing concentrations. After washing, the samples were

analysed using an excitation wavelength of 784.6 nm. No significant peaks were observed in the resulting SERS spectra, suggesting that conjugation of the NIR dye to the nanoparticle surface was unsuccessful.

The absence of Raman peaks in SERS spectra obtained from nanoparticle-NIR conjugates was hypothesised to be a result of the poor solubility of the NIR reporter in aqueous colloidal suspensions. The hydrophilicity of the dye was therefore reconsidered. Even in the presence of two sulfonate groups, it is possible that the NIR dye may be forming aggregates in the aqueous suspension. This would prevent sufficient adsorption of the NIR on the nanoparticle surface. In an attempt to prevent aggregate formation of the NIR dye, ethanol was slowly added to colloidal suspensions of AgNP and AuNP to achieve 1:1 v/v ethanol:water suspensions. Solutions of the NIR dye were introduced to the suspensions. The washed samples were analysed by Raman spectroscopy using a 784.6 nm excitation wavelength (Figure 4.5).

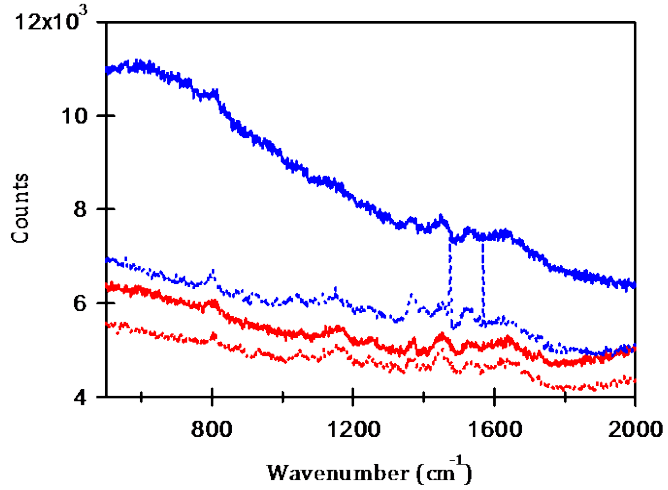

Figure 4.5. SERS spectra (using a 784.6 nm excitation wavelength) of AuNP (red) and AgNP (blue) after addition of the NIR dye (Figure 4.4) in aqueous conditions (solid) and in 1:1 ethanol:water v/v suspensions (dashed).

The use of increasing organic content of the nanoparticle suspensions was not seen to improve the recorded SERS spectrum of NIR using a 784.6 nm excitation wavelength. Similarly, no significant Raman peaks were identified in SERS spectra

using excitation wavelengths closer to the plasmon resonance of the nanoparticles (632.8 nm, Figure 4.6).

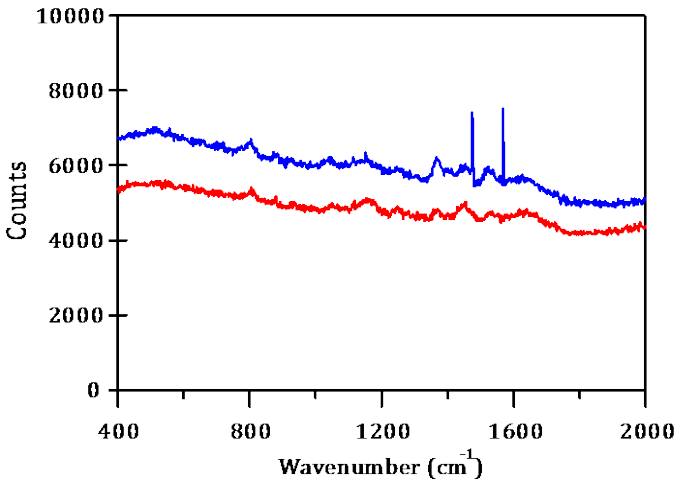

Figure 4.6 SERS spectra (using a 632.8 nm excitation wavelength) of Au (red) and Ag (blue) nanoparticles after addition of NIR dye (Figure 4.4) to nanoparticle suspensions in 1:1 v/v ethanol:water.

The NIR dye was seen to demonstrate little affinity for the nanoparticle surfaces and was deemed unsuitable for incorporation as a Raman reporter under these conditions.

4.2.3 "Controlled" aggregation of silver core

Agglomeration of nanoparticles creates "hotspots" of high electromagnetic enhancements, resulting in strong SERS signals. Further to this, suspensions of aggregated nanoparticles exhibit higher extinctions at longer wavelengths. This brings the surface plasmon band closer to resonance with far red excitation wavelengths. Therefore, while individual silver nanoparticles may not produce intense SERS signals with 632.8 nm excitation wavelengths, aggregated silver nanoparticles should demonstrate sufficient SERS activity.

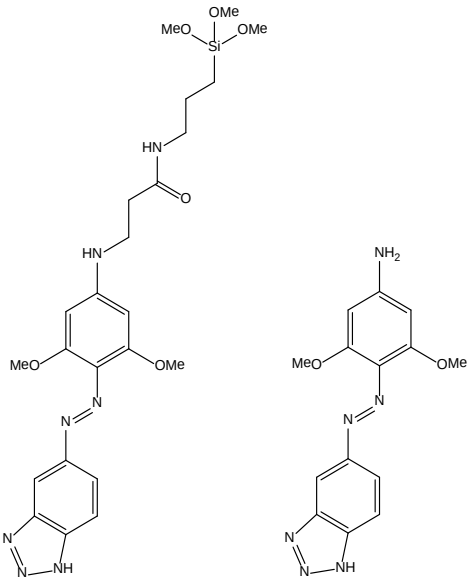

BT-SiO_2 BT-NH_2

Figure 4.7. "Aggregating" precursors for multi-core/ single shell nanoparticles.

It was previously observed in chapter 3 that two of the synthesised benzotriazole precursors (Figure 4.7) could induce aggregation of the silver nanoparticles. The terminal alkoxysilyl functionality of BT-SiO_2 was thought to be responsible for premature siloxane bridging between adjacent nanoparticles, during silica encapsulation. At increased concentrations of BT-NH_2, interactions between the amine moiety and the EDTA AgNP surface induced agglomeration prior to silica encapsulation. Extinction spectra of silver nanoparticles conjugated to the aforementioned Raman reporters and the resulting silica encapsulated colloids are represented in Figure 4.8.

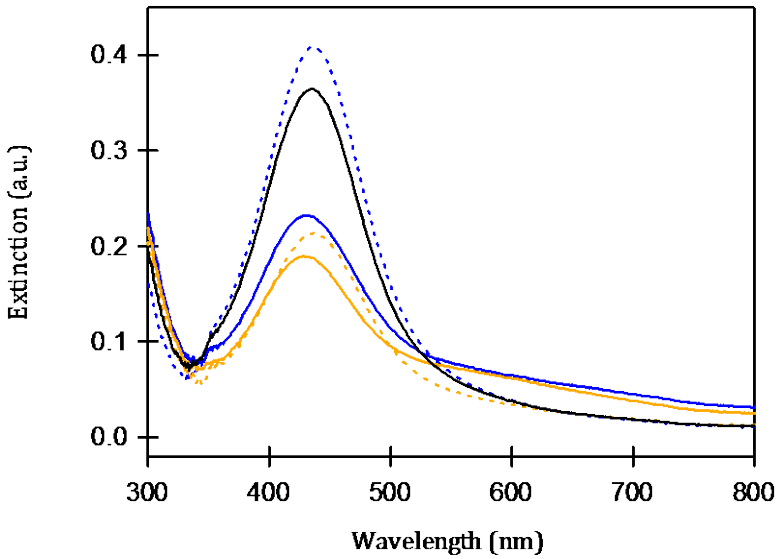

Figure 4.8. Extinction spectra of EDTA AgNP (black), AgNP-BTSiO$_2$ (blue) and AgNP-BTNH$_2$ (orange) conjugates pre (dashed) and post (solid) silica encapsulation.

SERS analysis of the AgNP – precursor conjugates was also carried out; the average peak height at 1615 cm^{-1} (the most prominent peak) was standardised against the peak height of a cyclohexane standard at 800 cm^{-1}. This was to facilitate comparison between the SERS intensities of the samples analysed using 514.5 nm and 632.8 nm excitation wavelengths (Figure 4.9).

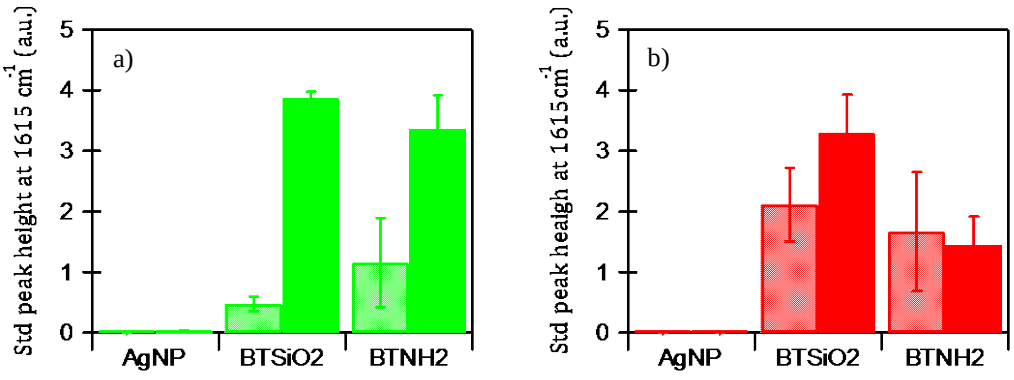

Figure 4.9. SERS analysis, using a) 514.5 nm and b) 632.8 nm excitation wavelengths, of EDTA AgNP, AgNP-BTSiO$_2$ and AgNP-BTNH$_2$ conjugates pre (dashed) and post (solid) silica encapsulation.

The observed SERS intensities of the samples pre-silica encapsulation were greater when using an excitation wavelength of 632.8 nm than 514.5 nm. This was unexpected, especially for the AgNP-BT-SiO$_2$ conjugates which exhibit minimal resonance at 632.8 nm. The increased extinction of the post–encapsulated AgNP-BT-SiO$_2$ conjugates at longer wavelengths suggested aggregation had occurred. This explained the increase in SERS intensities observed at both excitation wavelengths. The extinction spectrum of pre-encapsulated AgNP-BT-NH$_2$ conjugates depicted dampening of the surface plasmon band, compared to bare AgNP, but did not appear significantly broadened. Further dampening of the plasmon band was observed post-encapsulation, concurrent with higher extinction at longer wavelengths. These indications of increased particle size distribution were evident in the increased SERS signals using a 514.5 nm excitation wavelength, though less prominent at 632.8 m. The observed dampening of the surface plasmon band may be a result of reduction in particle concentration due to over-aggregation and precipitation of larger particles out of solution.

Silica encapsulated silver nanoparticles synthesised from BT-SiO$_2$ are seen to have more SERS activity than BT-NH$_2$ analogues, using a 632.8 nm excitation wavelength. The relative standard deviation of silica encapsulated particles

fabricated from BT-SiO_2 was also reduced in comparison to BT-NH_2 equivalents (19.5 % and 32.9 % respectively). Silver / silica particles synthesised using BT-SiO_2 precursors show potential to offer sufficient SERS activity at far red excitation wavelengths, allowing detection on incubation with biological samples.

4.3 Bio-functionalisation of silica encapsulated nanoparticles

4.3.1 Introducing surface functionality through silane coupling agents

As described in section 1.3.1 of the introduction, potential biological applications of silica encapsulated nanoparticles can be increased through further functionalisation with biomolecules. Silica encapsulation of silver nanoparticles provides a surface with consistent chemistry that is amenable to a number of attachment protocols. Silane coupling agents can be considered suitable linkers for the covalent attachment of proteins to a silica nanoparticle surface. Condensation of APTMS or MPTMS onto the surface of silica encapsulated nanoparticles introduces terminal amino or mercapto functionality respectively (Figure 4.10).

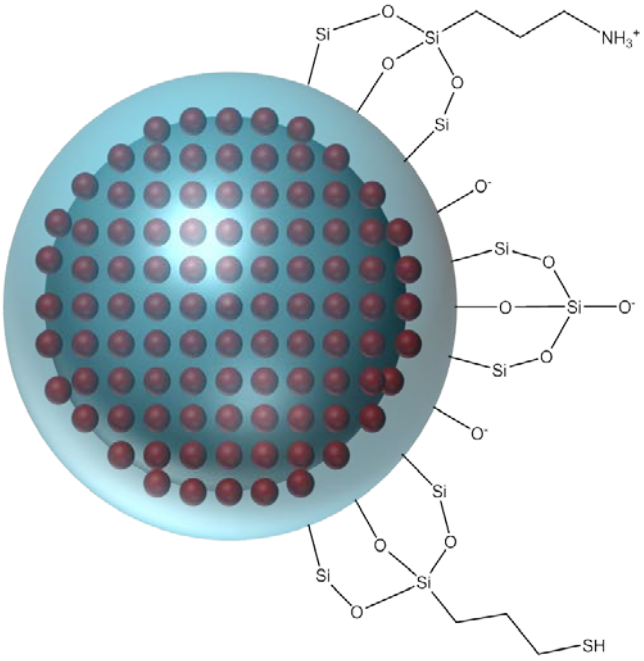

Figure 4.10 Representation of theoretical surface functionality of silver / silica nanoparticles, introduced by addition of silane coupling agents APTMS and MPTMS. Red spheres represent monolayer coverage of Raman reporters, conjugated to a silver nanoparticle, encapsulated in a silica shell.

The silica shell of silver / silica nanoparticles was synthesised from Stöber condensation of TEOS in ethanol / water mixtures. The fabricated silver / silica core / shell nanoparticles were washed prior to addition of APTMS and MPTMS. Further quantities of TEOS were added simultaneously, acting as spacer molecules to prevent over saturation of functional groups on the silica surface. Two solvent systems were investigated for this resuspension and functionalisation of the silica particles; water and 1:1 water / ethanol v/v. After condensation of the coupling agents, the nanoparticle samples were washed once more and analysed by extinction spectroscopy. The average spectra of triplicate samples are shown in Figure 4.11.

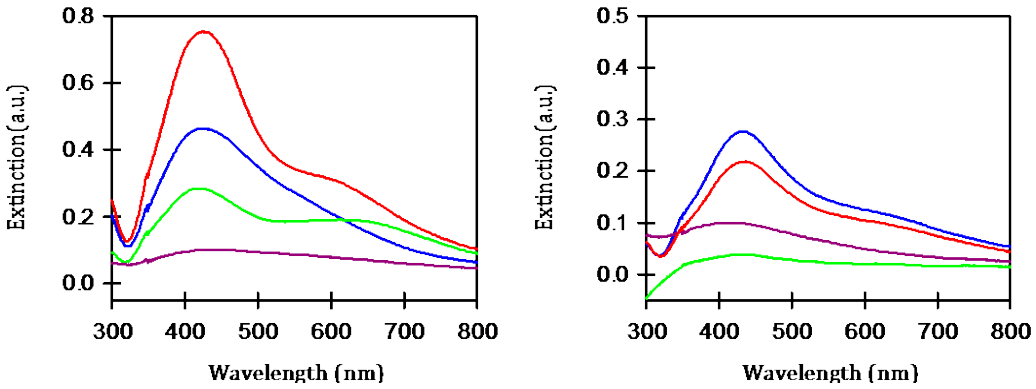

Figure 4.11 Extinction spectra of silica encapsulated silver nanoparticles, washed and resuspended in a) water and b) 1:1 water / ethanol v/v (red) prior to addition of TEOS (blue), APTMS (green), and MPTMS (purple).

Extinction spectroscopy analysis demonstrated dampening and broadening of the surface plasmon band of the nanoparticles post addition of APTMS and MPTMS (Figure 4.11). This effect was more prominent for the mercapto functionalised nanoparticles than for the amino analogues. However, the surface plasmon band of unfunctionalised silver / silica nanoparticles, and those resulting from the addition of further TEOS, also exhibited increased particle size distribution. It was proposed that silica encapsulated particles were not stable during multiple high speed washing steps. Repetitive centrifugation in water / ethanol solvent systems (Figure 4.11b) was seen to induce further aggregation of both functionalised and unfunctionalised silver / silica particles. This may have been a result of the reduced overall polarity of the dispersive medium, preventing effective shielding of inter-particle Van der Walls forces.

The potential for functionalising the silica encapsulated nanoparticles without inclusion of a wash step was investigated. APTMS, MPTMS and further quantities of TEOS were introduced to the encapsulated nanoparticles an hour after the previous TEOS aliquots had been added. After condensation of the coupling agents, the samples were washed and analysed by extinction spectroscopy. The average spectra of triplicate samples are shown in Figure 4.12.

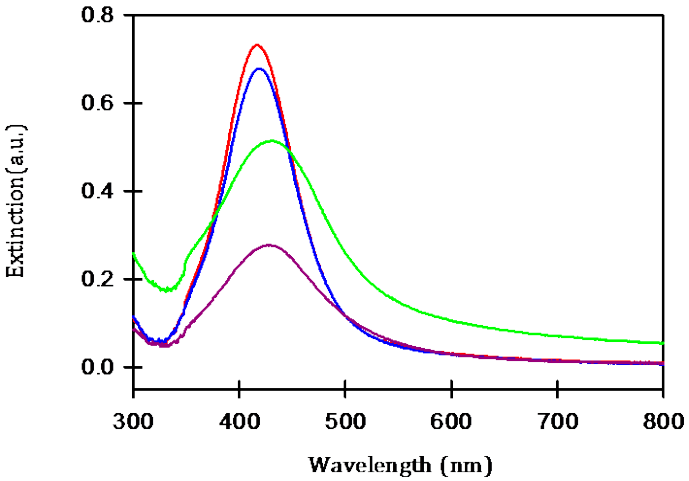

Figure 4.12 Extinction spectra of silica encapsulated silver nanoparticles (red) after addition of further TEOS (blue), APTMS (green) and MPTMS (purple)

Extinction spectroscopy indicated the stability of unfunctionalised silver / silica nanoparticles was increased when employing only one wash step. Addition of further quantities of TEOS to the silica surface did not significantly alter the surface plasmon band of the silver nanoparticles. Introduction of the amino moiety, through addition of APTMS, resulted in an increased the particle size distribution. This was indicated by broadening of the surface plasmon band and increased extinction at longer wavelengths. APTMS is capable of interacting with the silica surface *via* both alkoxysilane condensation and electrostatic interactions. The simultaneous occurrence of these interactions may have induced aggregation of the nanoparticles.

Post modification of the silica surface with MPTMS, the surface plasmon band was depleted but not significantly broadened. This may be an effect of the reduced solubility of thiols in aqueous solvents. Introducing terminal thiol groups onto the nanoparticle surface may thus induce precipitation, reducing the nanoparticle concentration in solutions. This would explain the reduction in extinction of the surface plasmon band.

All these data considered, it appears that terminal amino and mercapto functionalities were engineered on the surface of the nanoparticle. However, the resulting nanoparticles exhibited reduced stability. For this reason another silane coupling

agent was considered. 3-(triethoxysilyl) propyl isocyanate (TESPIC) was conjugated to silica encapsulated nanoparticles. TESPIC was added to unwashed silica encapsulated nanoparticles with and without further aliquots of TEOS to establish the effect of spacer molecules. The resultant samples were washed and analysed by extinction spectroscopy (Figure 4.13).

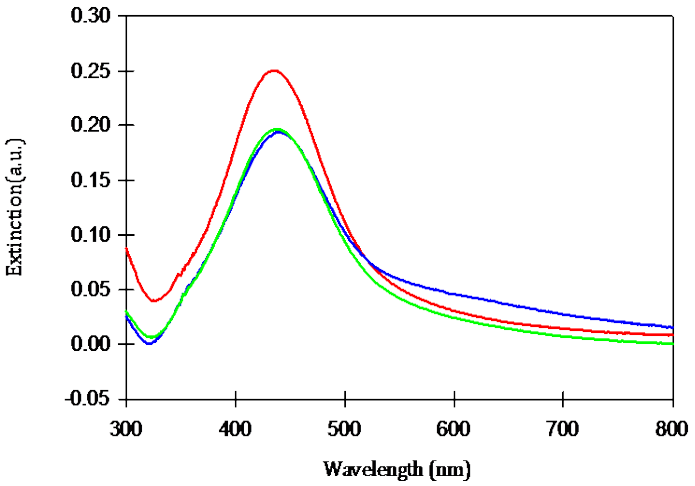

Figure 4.13 Extinction spectra of silica encapsulated silver nanoparticles (red) after addition of TESPIC only (blue) and TESPIC with the inclusion of additional TEOS (green).

In comparison to samples previously functionalised with APTMS and MPTMS, TESPIC functionalised nanoparticles were seen to have increased stability. This stabilisation was further evident when aliquots of TEOS were conjugated simultaneously. It is therefore probable that TEOS was performing as a spacer molecule, preventing over saturation of the silica surface with TESPIC.

4.3.2 Formation of nanoparticle-protein conjugates

Covalent attachment of protein molecules to the silica surface may occur *via* interaction of the engineered terminal isocyante moiety on the nanoparticle surface (provided by TESPIC) with a number of primary amine residues of proteins (Scheme 4.)

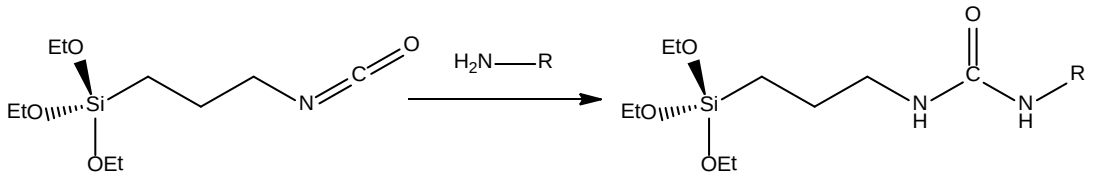

Scheme 4.1 Reaction of 3-(triethoxysilyl) propyl isocyante with primary amines

Isocyanates are susceptible to deterioration during storage and are considered to be unstable. Rapid hydrolysis, in the presence of water, produces 1, 3-disubstituted ureas.[190] Therefore, it is unlikely that the TESPIC functionalised nanoparticles will retain their functionality in aqueous solutions. For this reason it was considered to first react the isocyanate silane coupling agent with the protein, and then form the nanoparticle protein conjugate.

10 equivalents of TESPIC were reacted with the protein of interest under buffered conditions as outlined in 8.4.1. The crude product was added to unwashed aliquots of silver / silica nanoparticles (synthesised from BT-COOH, chapter 3) at least 30 min. after the last TEOS addition.

TESPIC modified protein, at increasing molar excesses, was added to the silica encapsulated nanoparticles. The stability of the resulting protein-nanoparticle conjugates, under buffered conditions, was determined by extinction spectroscopy (Figure 4.14). Molar excess ratios were calculated from the initial concentration of silver nanoparticles (pre-encapsulation) and the combined concentration of protein (modified and unmodified). The silver / silica nanoparticle – protein conjugates were washed and resuspended in three buffer systems for comparison:

1. 4-(2-hydroxyethyl)-1-piperazineethanesulfonic acid buffer (HEPES): 25 mM, 20 mM KCl, pH 7.25
2. Phosphate buffer : 60 mM, pH 7
3. Phosphate buffered saline (PBS): (10 mM, 0.3 M NaCl, pH 7)

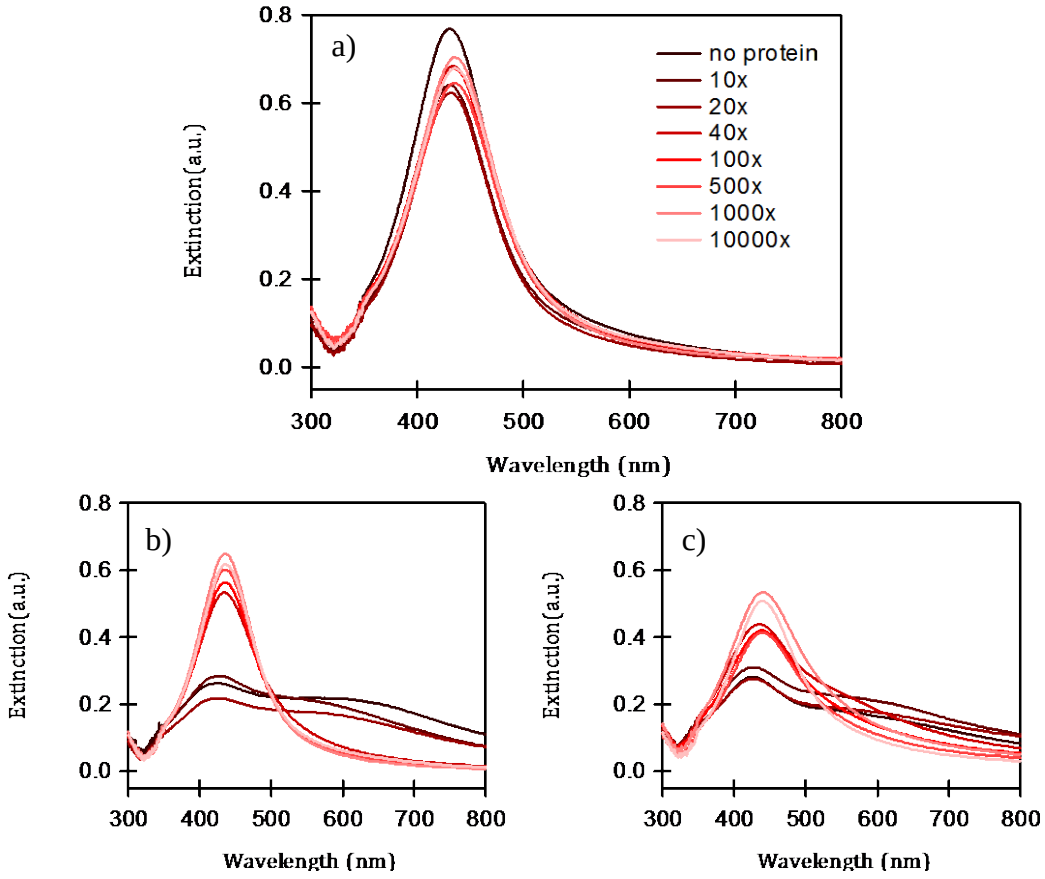

Figure 4.14 Extinction spectroscopy analysis demonstrating the stability of silica encapsulated AgNP and their protein conjugated equivalents with increasing protein molar excesses in a) HEPES b) phosphate buffer and c) PBS.

The unfunctionalised silver / silica nanoparticles were stable in HEPES and thus, no change was observed to the shape of the surface plasmon band in extinction spectroscopy following addition of protein. However, the extinction maximum of the surface plasmon was progressively red shifted with increasing protein concentration. Unfunctionalised silver / silica nanoparticles were not stable in phosphate buffer but became increasingly stabilised with higher molar excesses of protein. A 40 fold protein to nanoparticle molar excess was required to stabilise the silver / silica nanoparticles in phosphate buffer. However, this protein molar excess was not sufficiently stabilising in the presence of NaCl. A 1000 fold protein to silver / silica nanoparticle molar excess was required to stabilise the nanoparticles in PBS. From the extinction spectra illustrated in Figure 4.14 it was determined that the protein was successfully bound to the surface of the nanoparticles. The TESPIC

modified protein was not purified prior to incubation with silica nanoparticles. Due to the presence of modified and unmodified protein, it is possible that the unmodified protein, through electrostatic association with the nanoparticle's silica surface, also contributed to the stabilising effect observed. Unmodified and TESPIC modified proteins were added, at similar concentrations of 1000 fold molar excess, to unwashed silver / silica nanoparticle suspensions. The resultant conjugates were resuspended in PBS and analysed by extinction spectroscopy (Figure 4.15).

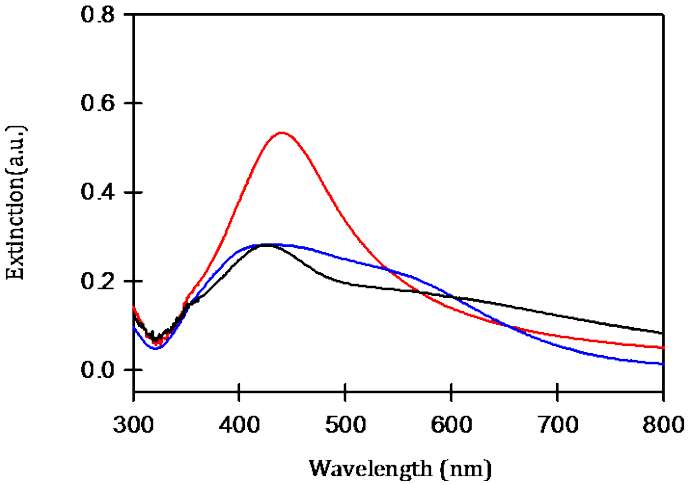

Figure 4.15 Extinction spectroscopy analysis showing a comparison of silica encapsulated nanoparticles (black) with unmodified (blue) and crude TESPIC modified protein (red) nanoparticle conjugates in PBS.

The extinction spectra observed indicated that electrostatic interaction of unmodified protein provided slight stabilisation of the silver / silica nanoparticles in PBS. Addition of TESPIC modified protein molecules provided additional covalent attachment to the silver / silica nanoparticles and thus, increased the stability of the conjugates under buffered conditions. Further characterisation of the protein on the nanoparticle surface was investigated.

4.3.3 Gel electrophoresis

Gel electrophoresis is a method used for the separation of proteins by size and charge. Polyacrylamide gel electrophoresis (PAGE) efficiently separates proteins

between 5 - 200 kDa. Control of the polymerisation of acrylamide and bisacrylamide produces uniform pore sizes within the gel. Protein mixtures may be separated based on the electrophoretic mobility of the folded protein (Native PAGE) or denatured protein (SDS-PAGE). Conversely, agarose gels do not possess uniform pores, thus allowing for separation of proteins larger than 200 kDa and larger molecules. Separation of metallic nanoparticles on agarose gels, based on size and shape, has been reported.[191] This extends to the purification of DNA-nanoparticle conjugates[192] and monitoring of protein nanoparticle binding.[193] It is therefore expected that the aforementioned nanoparticle-protein conjugates will migrate through agarose gels to a different extent than unfunctionalised silver / silica nanoparticles, confirming successful bio-functionalisation.

Protein-nanoparticle conjugates were prepared for analysis by gel electrophoresis (1 % agarose). Covalently bonded protein – nanoparticle conjugates were prepared using 1000 and 10,000 fold protein molar excess *via* TESPIC. The electrostatic interaction of unmodified protein with silica encapsulated nanoparticles was also assessed with 10,000 fold molar excess of protein to nanoparticle. Such high protein concentrations were selected to ensure maximum nanoparticle stability in the buffers required for electrophoretic analysis. Electrophoretic mobility of the nanoparticle – protein conjugates was compared to unfunctionalised silver / silica nanoparticles and unconjugated protein at 1 mg / mL. The concentration of unconjugated protein analysed was similar to that added to nanoparticles. Duplicate batches of nanoparticles and their conjugates were analysed

Post electrophoresis, visualisation of the protein bands was achieved using EZBlue™ staining reagent (Sigma-Aldrich).

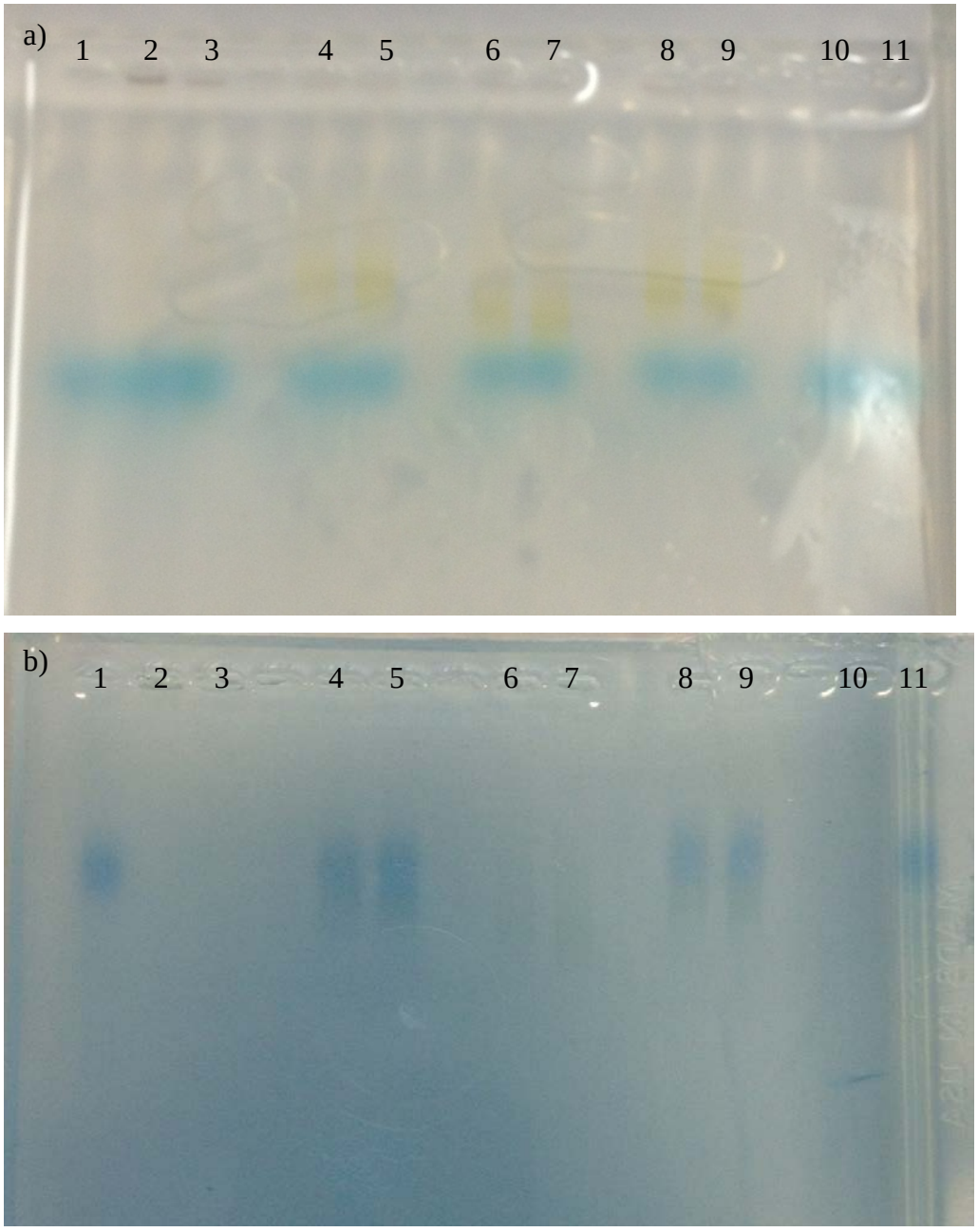

Figure 4.16a) Gel image and b) EZBlue™ stained gel image of protein binding assay. 10 µL of sample / loading buffer mixture was loaded onto a 1 % agarose gel and run for 30 min at 150 V. Lane 1 and 11: protein at 1 mg / mL, lanes 2 and 3: unfunctionalised silica encapsulated nanoparticles, lanes 4 and 5: covalently bonded protein-nanoparticle conjugates (10,000 fold protein molar excess), lanes 6 and 7: covalently formed protein-nanoparticle conjugates (1,000 fold protein molar excess), lanes 8 and 9: electrostatically formed protein-nanoparticle conjugates (10,000 fold protein molar excess). Lane 10: loading buffer only.

The blue bands observed in Figure 4.16a correspond to loading buffer; this negative control was run in lane 10. The unfunctionalised silver / silica nanoparticles failed to migrate through the gel; sedimentation was observed in the wells of lanes 2 and 3. This may have been due to minimal electrophoretic mobility of silica encapsulated nanoparticles, though this seems unlikely as the zeta potential of these unfunctionalised nanoparticles is reported as -34.02 ± 1.53 mV at neutral pH (see 3.3.2). Zeta potential is related to electrophoretic mobility by the Henrys equation (equation 4.1):

$$U_E = \frac{2\varepsilon\zeta F(ka)}{3\eta} \qquad 4.1$$

where: U_E is the electrophoretic mobility

ζ is the zeta potential

ε and η are the dielectric constant and viscosity respectively

$F(ka)$ is Henry's function.

Considering Henry's equation, it is doubtful that the unfunctionalised silver / silica nanoparticles exhibited no electrophoretic mobility. It was more probable that the unfunctionalised silver/ silica nanoparticles precipitated out of solution. As previously illustrated in Figure 4.14, unfunctionalised nanoparticles exhibited negligible stability in buffered conditions. Sedimentation of the nanoparticles in the wells prevented electrophoretic migration of the silver / silica nanoparticles through the gel.

Silica encapsulated nanoparticles functionalised with covalently bonded protein at 10,000 fold protein molar excess *via* TESPIC were seen to show similar electrophoretic mobility to those functionalised by electrostatic interaction of the unmodified protein at the same excess. The silica encapsulated silver nanoparticles were seen as yellow bands in lanes 4, 5, 8 and 9. Post staining with EZBlue™ these yellow band appeared blue. EZBlue stains only proteins, leaving the background relatively clean, allowing direct visualisation of the proteins during the staining

process. This confirmed the successful conjugation of protein to the surface of the nanoparticles. The protein bands of these nanoparticle – protein conjugates depicted similar mobility to that of unconjugated protein (lanes 1 and11) at a similar concentration. This suggested that the mobility of the nanoparticle – protein conjugates was largely determined by the mobility of the protein.

The observed bands from nanoparticle – protein conjugates synthesised *via* covalent attachment of the protein at a lower protein concentration (1000 fold molar excess) were seen to migrate further than those with a higher protein concentration (10,000 fold molar excess). Proteins are separated based on charge in agarose gels, as the pore sizes are generally too large to act as molecular sieves. It was proposed that varying the amount of protein on the nanoparticle impacts the packing on the surface. However surface coverage of protein may increase the exposure of the protein's surface charge, increasing the conjugates' electrophoretic mobility. The protein band from these lower concentration conjugates was not as visible when stained with EZBlue™ (Figure 4.16b). In this instance, the concentration of detectable protein on the nanoparticle surface may be below the limit of detection of the staining technique.

4.4 Conclusions

To perform as bio-imaging reagents, nanoparticles must be stabilised against aggregation, passivated to control their chemical reactivity, and functionalised to permit interaction with biological species. The first two specifications are achieved, to a certain extent, by the silica encapsulation of the nanoparticles as discussed in chapter 3.

Monitoring biological interactions within a meaningful environment by Raman spectroscopy / SERS is favoured with far red / NIR excitation wavelengths. This affords reduced fluorescent backgrounds from biological samples and minimal sample degradation due to lower energy photons.[44, 194, 195] The silver / silica nanoparticles synthesised in chapter 3 were optimised for use with 514.5 nm

excitation wavelengths. Efforts were made to increase their SERS activity at longer wavelengths, namely 632.8 nm, by altering the core and reporter components. The use of gold nanoparticle cores and NIR reporter molecules were both unsuccessful in creating SERS detectable nanostructures. This demonstrated the specificity of the core / shell synthetic route. Utilising the aggregating properties of the precursors BT-SiO_2 and BT-NH_2, sufficient SERS activity was induced using a 632.8 nm excitation wavelength. The introduction of increased particle size distribution in the samples is not ideal but good reproducibility of the SERS signal was reported (19.46 % rel. standard deviation).

Bio-functionalisation of the silver / silica nanoparticles was attempted by engineering specific surface functionality *via* silane coupling agents. APTMS and MPTMS were employed to create amino and mercapto functionalised silica encapsulated nanoparticles. However, the resulting particles suffered from aggregation and solubility issues respectively. These difficulties were overcome using the isocyante analogue, TESPIC. Proteins were conjugated to the surface of the nanoparticles *via* covalent attachment through the terminal isocyante moiety provided by TESPIC. Due to the instability of the isocyante moiety in aqueous conditions, the protein was first conjugated to the silane coupling agent (TESPIC). These conjugates were then tethered to the silica nanoparticle surface through the alkoxysilane moiety.

Stability of the protein nanoparticle conjugates was assessed in a variety of buffered conditions. Unfunctionalised silver / silica nanoparticles were stable in HEPES buffer (pH 7.25), however stability was not attained in phosphate buffer (pH 7) or PBS (pH 7). A 40 fold molar excess of protein to original nanoparticle concentration was required to provide stabilisation of the nanoparticles in phosphate buffer. A higher concentration (1000 fold molar excess) of protein was required to afford stabilisation to the nanoparticle core in PBS. The stabilisation afforded by covalent attachment of the protein at this concentration is greater than that provided by electrostatic interaction of unmodified protein with the nanoparticle surface.

Gel electrophoresis measurements were used to confirm the presence of the protein on the nanoparticle surface.

4.5 Future work

Attempts to quantify the amount of protein on the nanoparticle surface *via* fluorescently labelled proteins were unsuccessful; no fluorescence was observed from any of the samples. The possibility that this was a result of fluorescent quenching by the silver core was investigated. However, dissolution of the core by nitric acid did not improve the fluorescent read-out of the samples. It was proposed that the concentration of fluorescent probe was below the limit of detection of the fluorimeter.

Future work would investigate the use of an immunoassay, as a more efficient method of determining the amount of biologically active protein on the surface of the nanoparticle. Due to the increased particle size distribution induced by the aggregating precursors, the average degree of protein per nanoparticle may not be overly accurate.

Circular dichroism measurements can be used to determine the integrity of the secondary structures of proteins. While limited information regarding the tertiary structure of proteins is provided by circular dichroism, analysis could be used to indicate unfolding of the protein on the surface of the nanoparticle.[180]

5 Bio-imaging of TNF using bio-functionalised core / shell nanoparticles

5.1 Introduction

Inflammation is part of a complex biological response to injury, infection or irritation. Chronic inflammation can lead to host of other diseases including rheumatoid arthritis, inflammatory bowel disease, eczema and diabetes. Inflammation is mediated by a host of secreted polypeptides known as cytokines. It is proposed that numerous pro-inflammatory cytokines are involved in an extensive network with Tumour Necrosis Factor (TNF) at its apex.[135] The success of anti-TNF therapies in the treatment of inflammatory conditions underpins this proposition.

TNF binds to receptors on cell membranes leading to cell death via apoptosis. It is proposed that an overproduction of TNF causes various autoimmune diseases. TNF inhibitors, such as etanercept, bind to soluble TNF (sTNF) in circulation in the body, thereby preventing the cytokine binding to the TNF receptors on the cell surface. This reduces the immune response ordinarily signalled by the binding. TNF is also present in the transmembrane form (tmTNF) to which etanercept can also bind, however etanercept has less affinity for tmTNF, in comparison to sTNF.[196]

Functionalising the surface of the SERS detectable silver / silica nanoparticles with etanercept should permit detection of the inflammation biomarker TNF. Raman mapping of biological samples incubated with such particles could potentially indicate areas where the biomarker is present in excess.

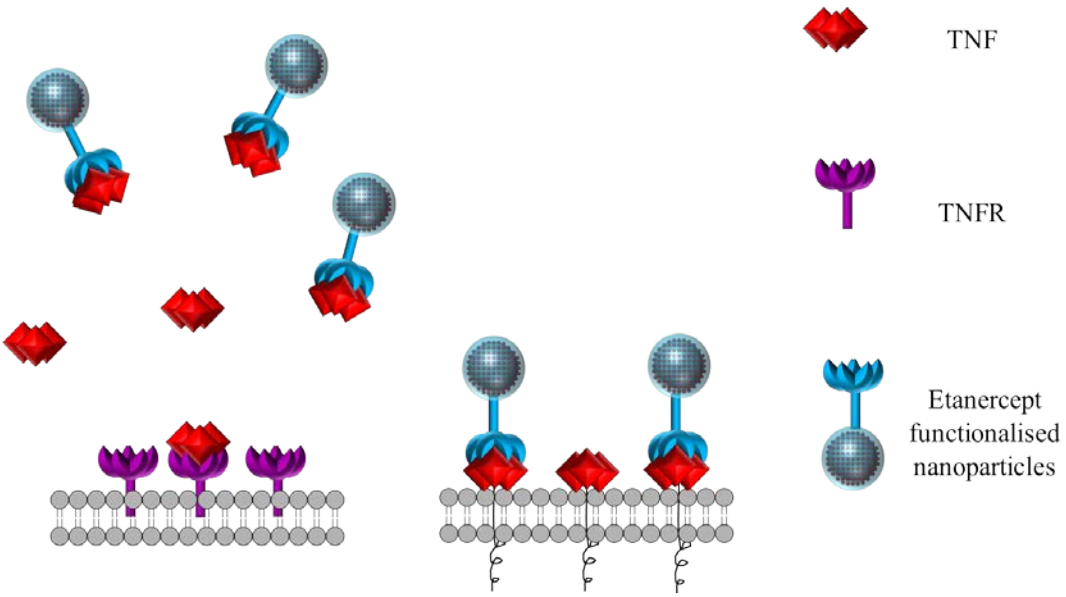

Figure 5.1Illustration of the interaction of etanercept functionalised nanoparticles with sTNF and tmTNF

SERS has proven to be an efficient detection technique for both cellular and *in vivo* studies.[197, 198] *In vitro* cellular studies should allow visualisation of tmTNF whilst *ex vivo* investigations should permit imaging of sTNF. As previously discussed in chapter 4, far red and NIR wavelengths are commonly employed for SERS analysis of biological tissues. However, higher energy excitation wavelengths are more closely in resonance with the nanoparticle probes. Excitation wavelengths of 632.8 nm and 514.5 nm were used throughout this chapter.

5.2 *In-vitro* analysis of tmTNFα

In-vitro studies were used for initial investigations into the imaging capabilities of etanercept functionalised nanoparticles (as prepared in chapter 4). HeLa cells were cultured for the imaging of tmTNF. All cell populations were prepared by Maartje Goobers (University of Strathclyde) as outlined in 8.5.1. tmTNF located on the surface of HeLa cells has been shown to interact with TNF receptor 2 (TNF-R2).[199] Etanercept, a fusion protein comprised of the extracellular domain of TNF-R2, also demonstrates efficient binding to tmTNF (K_D = 438 pM).[196] Assuming the fusion

protein retains biological activity, the etanercept functionalised SERS active nanoparticles should bind to tmTNF.

The cultured cells were incubated with etanercept functionalised nanoparticles for one hour. Following incubation, and in order to remove any extracellular matrix, the cells were washed four times with phosphate buffered saline (PBS). After fixation with paraformaldehyde (4 %) the cover-slips were washed consecutively with PBS and dH_2O and dried before mounting on slides.

Raman mapping of samples can be achieved by monitoring the observed intensity of signal at a particular wavenumber. Alternatively, the entire spectrum can be collected at each pixel. Direct classical least squares (DCLS) analysis was used to compare the recorded spectrum at each pixel to a reference spectrum (in this case a solution standard of unbound nanoparticles). This created an image with look up table (LUT) values between 0 and 1. Values close to 1 indicated pixels within the image whose spectral output was most similar to that of the reference spectrum. In these images, the blue trace refers to the reference spectra whilst the red trace is an isolated spectrum from the map whose LUT value falls within the outlined limits.

5.2.1 Detectability of functionalised nanoparticles in cell populations

The measureable SERS signal of cell-associated nanoparticles is reduced compared to unbound solution samples. This is due to a reduction in number of particles in the laser path and possible fluorescent interference from the biological samples. The scattered light from the SERS probes may also be absorbed by biological matter prior to reaching the detector. As previously discussed in chapter 4, monomeric silver nanoparticles probes are not SERS detectable at 632.8 nm. Partial agglomeration of the silver cores, using aggregating dye precursors (BT-NH_2 and BT-SiO_2), improves the measurable SERS signal. Nanoparticles of different particle size distributions were prepared and incubated with HeLa cells. Fabrication of silver / silica nanoparticles using the dye precursor BT-COOH (final concentration 10^{-7} M)

produced reasonably monodispersed suspensions (Figure 5.2). Similar concentrations of BT-NH_2 and BT-SiO_2 were expected to increase the particle size distribution of the resulting suspension. Extensive aggregation of the colloid was also induced through increased concentrations of BT-COOH. Extinction spectroscopy and SEM analysis was performed to assess the particle size distribution of the samples. The number of monomer, dimer, trimer and clusters of four or greater particles was ascertained by counting more than 100 particles from 4 representative images.

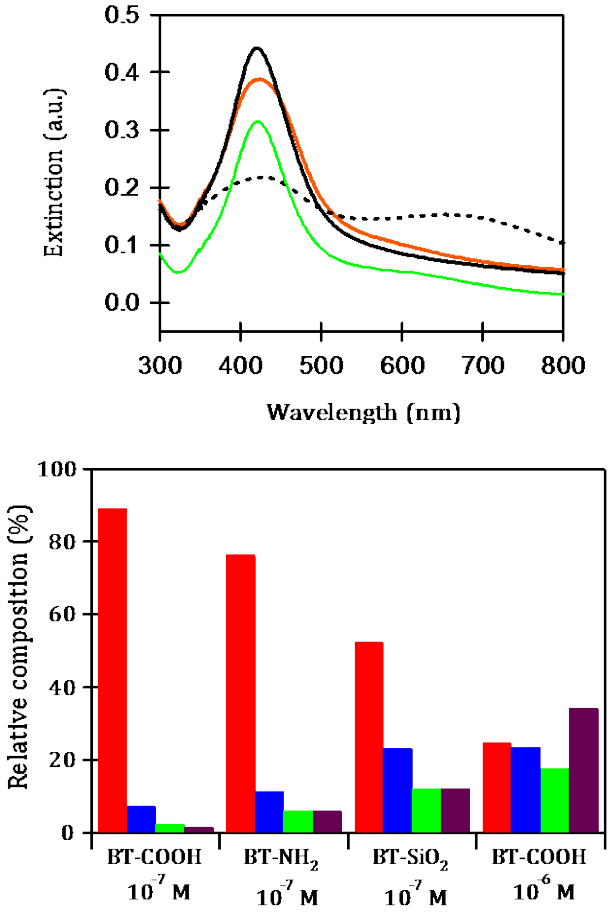

Figure 5.2a) Extinction spectra of unfunctionalised silver/silica nanoparticles synthesised from the precursors BT-COOH (black), BT-SiO_2 (orange) and BT-NH_2 (green) at final concentrations of 10^{-7} M (solid) and BT-COOH at a final concentration of 10^{-6} M (dashed). b) relative composition as determined by SEM: monomers (red), dimers (blue), trimers (green) and larger clusters (purple).

As expected, silver / silica suspensions produced from BT-COOH consisted of 90 % monomers. BT-SiO_2 successfully increased the percentage of larger particles; BT-NH_2 also increased the particle size distribution but to a lesser extent. Increasing the final concentration of BT-COOH employed in the synthetic route significantly increased the particle size distribution of the colloid. Aliquots of each of these populations were incubated with HeLa cells. The samples were mapped using a 632.8 nm excitation wavelength (50 % laser power, 10 sec accumulation). The spectra obtain at each pixel was compared to the solution spectra of the nanoparticles using DCLS. LUT values were set to $0.6 \leq x \leq 0.9$, indicating areas on the map which had between 60 - 90 % "fit" with the reference spectrum.

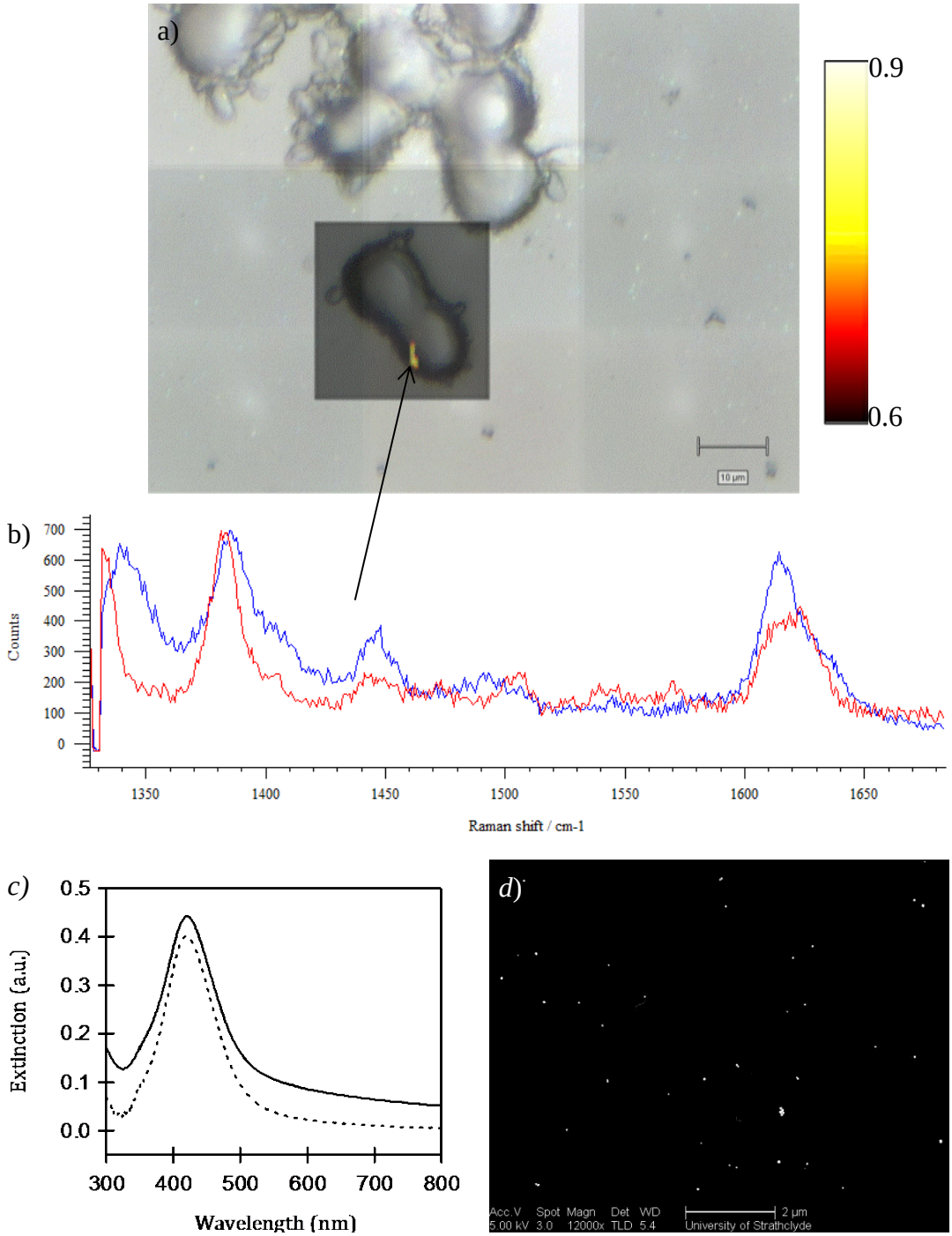

Figure 5.3a) SERS map observed from incubation of unfunctionalised (BT-COOH, 10^{-7} M) nanoparticles with HeLa cells. (632.8 nm excitation wavelength, 50 % laser power, 10 sec accumulation, LUT: $0.6 \leq x \leq 0.9$). b) A comparison of recorded spectrum at one pixel (red) to the reference spectrum (blue) c) Extinction spectra of the core / shell nanoparticles (solid) compared to EDTA AgNP (dashed) and d) SEM image of the pre-incubated particles.

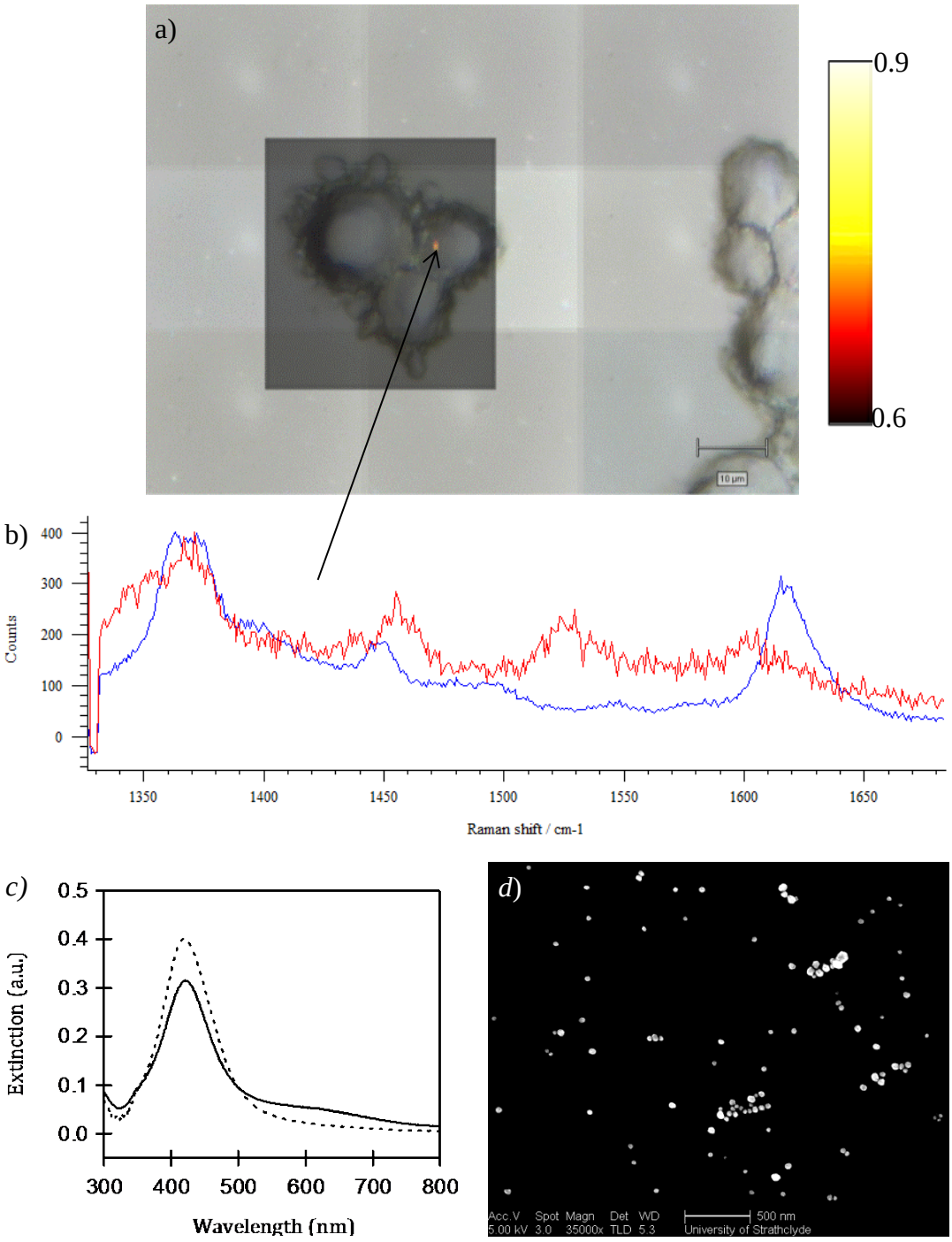

Figure 5.4 a) SERS map observed from incubation of unfunctionalised (BT-NH_2, 10^{-7} M) nanoparticles with HeLa cells. (632.8 nm excitation wavelength, 50 % laser power, 10 sec accumulation, LUT: $0.6 \leq x \leq 0.9$). b) A comparison of recorded spectrum at one pixel (red) to the reference spectrum (blue) c) Extinction spectra of the core / shell nanoparticles (solid) compared to EDTA AgNP (dashed) and d) SEM image of the pre-incubated particles.

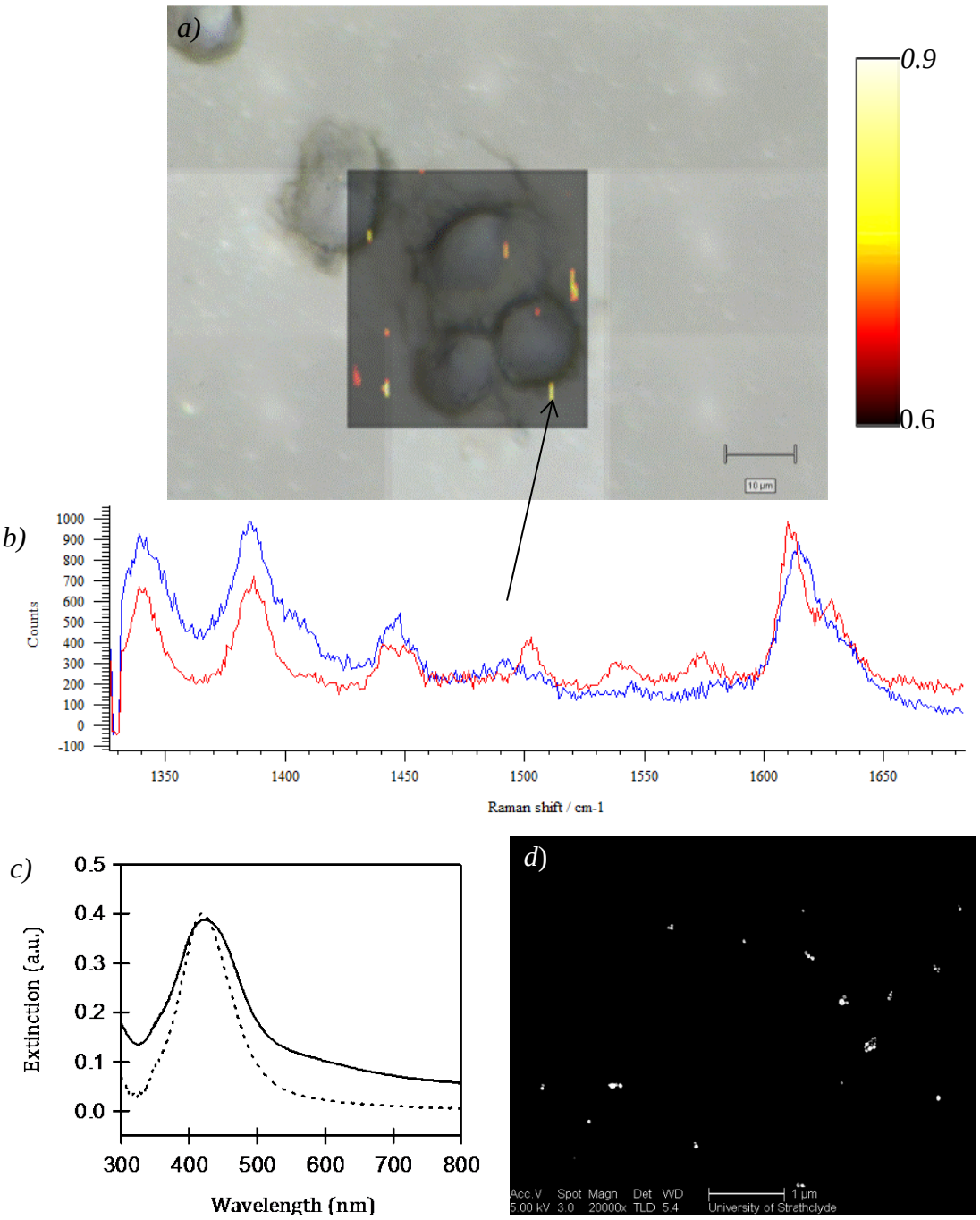

Figure 5.5 a) SERS map observed from incubation of unfunctionalised (BT-SiO_2, 10^{-7} M) nanoparticles with HeLa cells. (632.8 nm excitation wavelength, 50 % laser power, 10 sec accumulation, LUT: $0.6 \leq x \leq 0.9$). b) A comparison of recorded spectrum at one pixel (red) to the reference spectrum (blue) c) Extinction spectra of the core / shell nanoparticles (solid) compared to EDTA AgNP (dashed) and d) SEM image of the pre-incubated particles.

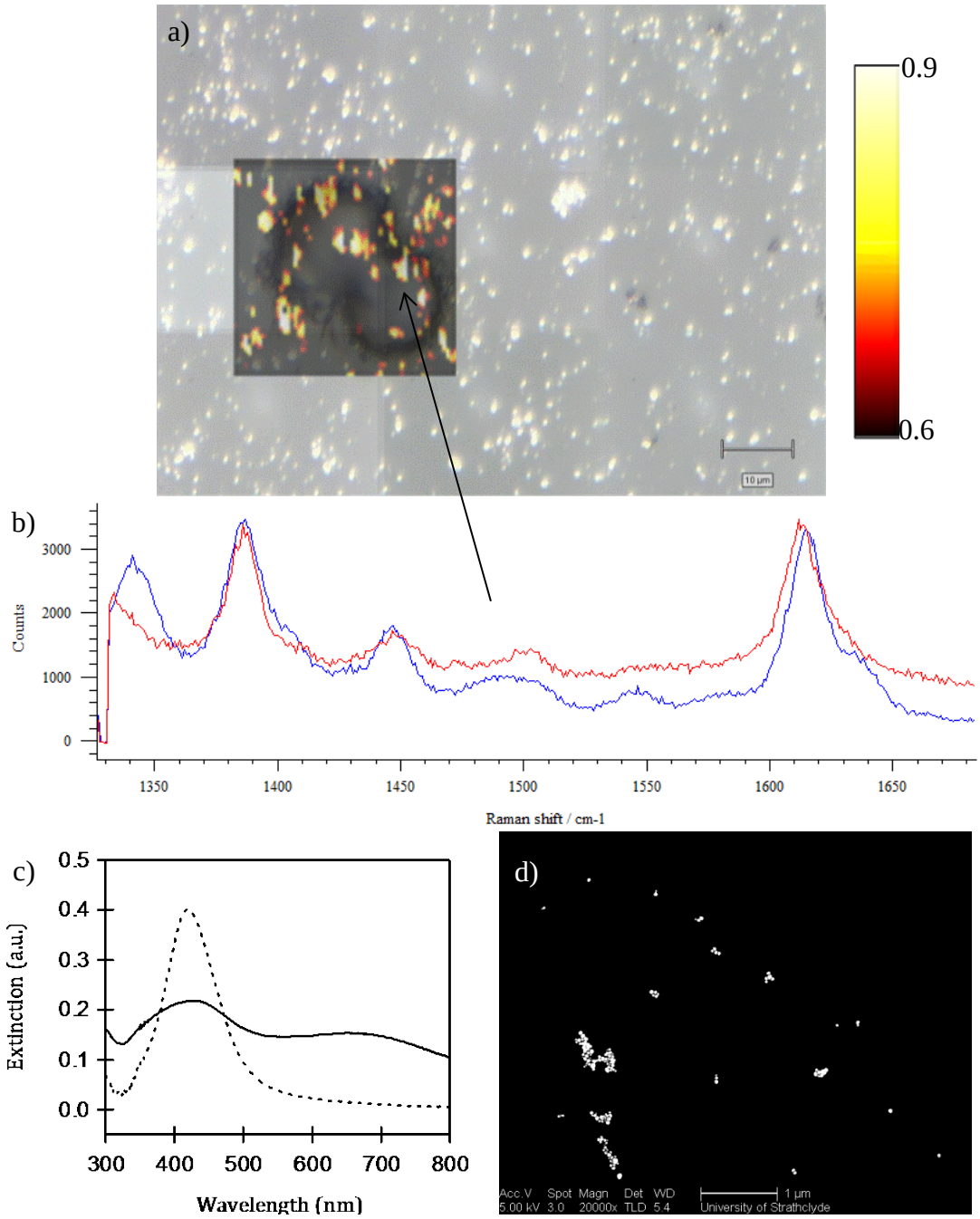

Figure 5.6 a) SERS map observed from incubation of unfunctionalised (BT-COOH, 10^{-6} M) nanoparticles with HeLa cells. (632.8 nm excitation wavelength, 50 % laser power, 10 sec accumulation, LUT: $0.6 \leq x \leq 0.9$). b) A comparison of recorded spectrum at one pixel (red) to the reference spectrum (blue) c) Extinction spectra of the core / shell nanoparticles (solid) compared to EDTA AgNP (dashed) and d) SEM image of the pre-incubated particles.

SERS signal was observed from all mapped populations. In the instance where largely monomeric nanoparticles were incubated with HeLa cells (Figure 5.3), few pixels whose spectra corresponded well with the reference spectrum were observed. This was attributed to reduced resonance of the nanoparticles with the excitation wavelength.

Increasing the particle size distribution of the colloid using BT-NH_2 as an aggregating precursor did not significantly increase the amount of signal observed from the sampled HeLa populations (Figure 5.4). It was proposed that the induced aggregation was not extensive enough to sufficiently increase the detectability of the particles. The spectra from the area highlighted in the false colour image displayed only slight correlation with the reference spectrum. This may have been a result of the low signal to noise ratio observed in the solution SERS spectra of these samples.

BT-SiO_2 is also capable of inducing partial aggregation of the nanoparticles. The relative composition of monomeric species was greater than 50 %, however the suspension now contained approx. 25 % dimers (Figure 5.2). This was evident in the extinction spectra, where the surface plasmon band was broader than the largely monomeric BT-COOH samples. Areas of large electromagnetic enhancement are created at the junction between two particles. The relatively high percentage composition of dimers was thought to be responsible for the increased signal observed from mapped cell populations (Figure 5.5).

High concentrations of “non-aggregating” precursors also induce agglomeration of the nanoparticles. The extent of coagulation was much greater than that observed from the “aggregating” precursors BT-SiO_2 and BT-NH_2 (Figure 5.2). Approximately 50 % of the particles were construed to exist in clusters or 3 or more particles. The extinction of these particles was mostly in resonance with the excitation wavelength thus, a significant increase in the quantity and intensity of signal was detected (Figure 5.6). However, a substantial amount of residual “debris” was observed in the white light image of the cells. This may be a result of the larger clusters having precipitated onto the surface of the glass slide that were not

efficiently removed with washing. Signal from these precipitated clusters may mask signal from cell bound or internalised nanoparticles.

Silver / silica nanoparticles synthesised from BT-SiO_2, with an average composition of approximately 25 % dimeric species, were deemed optimal for *in vitro* investigations at 632.8 nm.

The conditions used for collecting SERS data from cell populations were also investigated. Laser power was varied between 10, 50 and 100 % over accumulation times of 1, 5 and 10 seconds. Unfunctionalised silver / silica nanoparticles synthesised form BT-SiO_2 were incubated with HeLa cells and analysed using a 632.8 nm excitation wavelength. DCLS comparison with a solution of the unfunctionalised nanoparticles was used to create the false colour images in Figure 5.7. LUT values were set to $0.6 \leq x \leq 0.9$ for all samples.

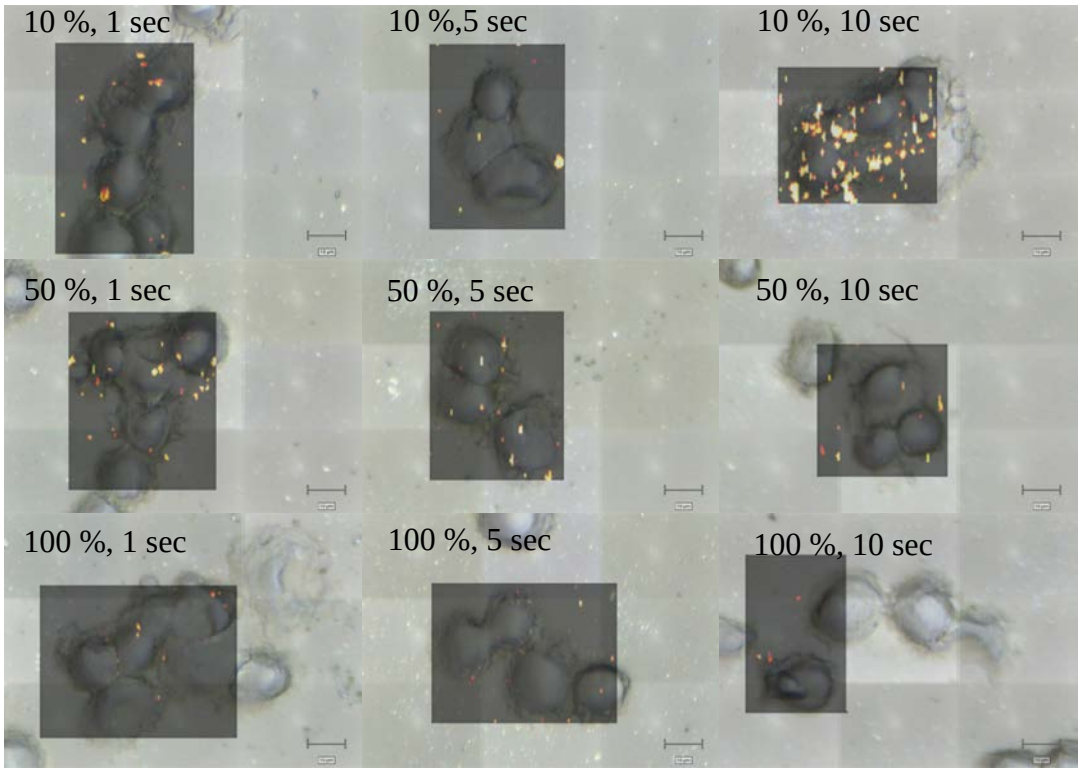

Figure 5.7 Raman map observed from incubation of unfunctionalised BT-SiO_2 fabricated core/ shell nanoparticles with HeLa cells. (632.8 nm excitation wavelength, increasing laser power and accumulation time, LUT values set between 0.6-0.9).

At lower laser power (10 %) more signal correlating to the reference spectrum was detected with increasing accumulation times. At 50 % laser power, decreasing accumulation time improved the detectability of the signal. Detectability of the SERS probes was reduced at 100 % laser power.

The integrity of the recorded signal was also examined. The average spectra from 5 pixels, of the aforementioned maps, showing good correlation with the reference spectrum were compared. Figure 5.8 depicts the improvement in signal to noise ratio observed with increasing accumulation time at 10 % laser power from 1 to 5 sec. While no further enhancement was observed at 10 sec. accumulation the quantity of signal detected was significantly larger.

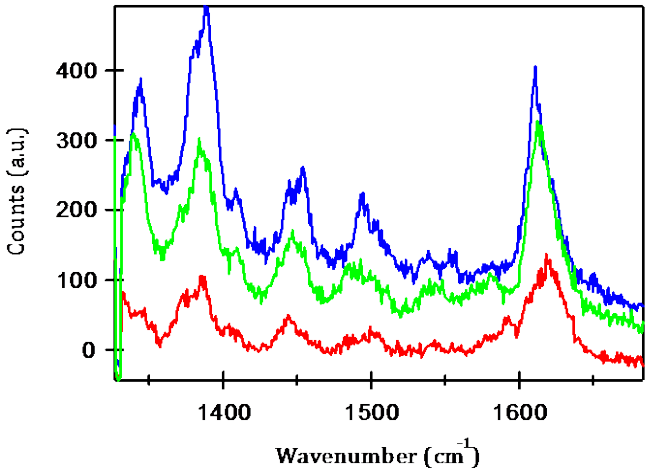

Figure 5.8 A comparison of Raman signals obtained using accumulation times of 1 sec. (red), 5 sec. (blue) and 10 sec. (green) at 10 % laser power (632.8 nm excitation wavelength). Average spectra of 5 pixels with LUT values $0.6 \leq x \leq 0.9$ observed from incubation of unfunctionalised BT-SiO_2 fabricated core/ shell nanoparticles with HeLa cells.

Similarly, the veracity of the detected signal with increasing laser powers was assessed at 1 sec. and 10 sec. accumulation

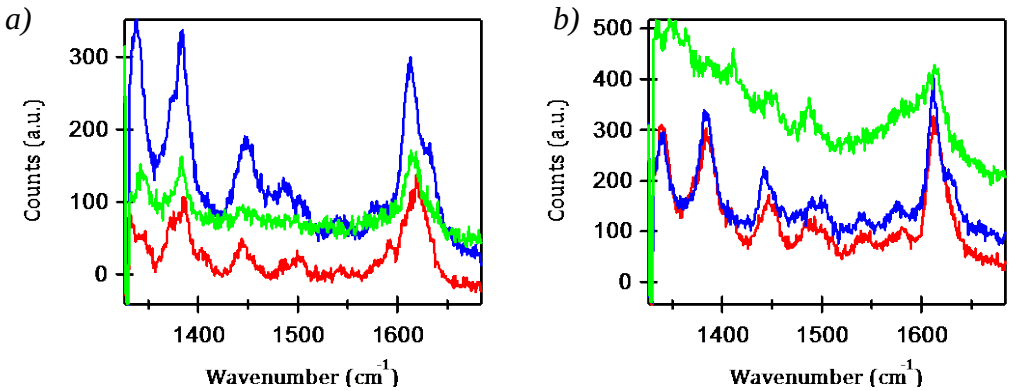

Figure 5.9 A comparison of Raman signals obtained using laser powers of 10 % (red), 50 % (blue) and 100 % (green) at a) 1 sec. and b) 10 sec. accumulation periods (632.8 nm excitation wavelength). Average spectra of 5 pixels with LUT values $0.6 \leq x \leq 0.9$ observed from incubation of unfunctionalised BT-SiO_2 fabricated core/ shell nanoparticles with HeLa cells.

The signal to noise ratio was enhanced when the employed laser power was increased from 10 % to 50 % at 1 sec. accumulation. This effect was nominal at extended accumulation periods. Maximising the excitation laser power had a negative effect on the detected signal. This occurred to a greater extent at longer accumulation times with an increase in background "noise". This was potentially due to fluorescent interference from the biological sample.

Therefore, for the purposes of *in vitro* investigations at 632.8 nm excitation wavelength, 10 % laser power over an accumulation period of 10 sec. was optimal for quantity and integrity of signal.

Due to the strong resonance contribution of the nanoparticles at shorter wavelengths, the feasibility of using a 514.5 nm excitation wavelength was assessed.

5.2.2 Detectability at 514.5 nm

As previously discussed in chapter 4, fluorescent inference from biological samples poses an obstacle upon excitation in the visible region of the electromagnetic spectrum. Operating at wavelengths in the far red / NIR regions, namely 632.8 nm and 784.6 nm, largely reduces background fluorescence. However, under SERS conditions, a 514.5 nm excitation wavelength amplifies the relative intensity of the Raman signal by several orders of magnitude (compared to fluorescence).[178] It is therefore possible to distinguish Raman peaks on top of a fluorescent background. The samples previously analysed at 632.8 nm in section 5.2.1 were subsequently subjected to excitation at 514.5 nm. Due to the increased fluorescent "noise" the LUT values were set to $0.8 \leq x \leq 0.9$, indicating areas on the map which had between 80 - 90 % "fit" with the reference spectrum.

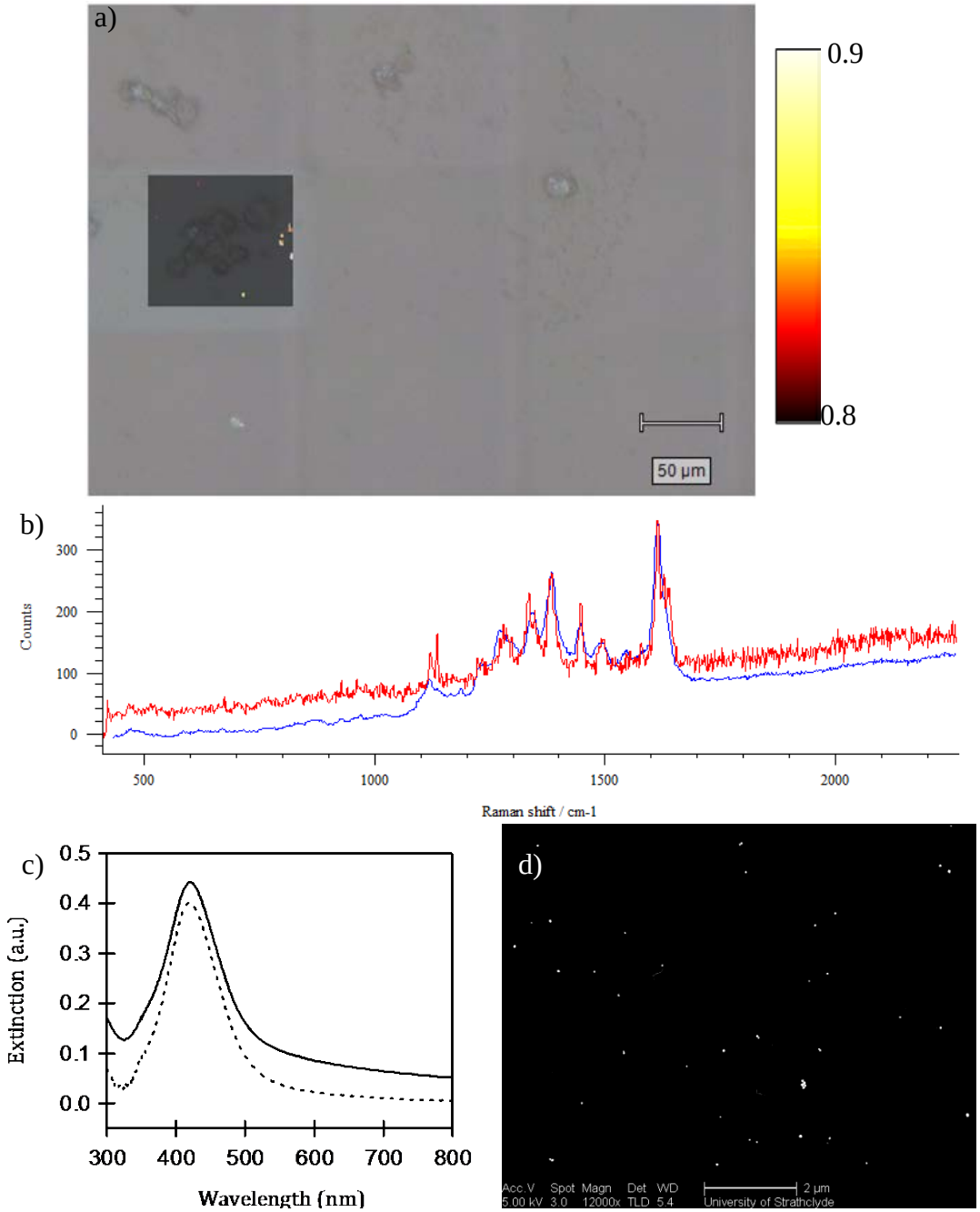

Figure 5.10 SERS map observed from incubation of unfunctionalised (BT-COOH, 10^{-7} M) nanoparticles with HeLa cells. (514.5 nm excitation wavelength, 10 % laser power, 10 sec accumulation, LUT: $0.8 \leq x \leq 0.9$). b) A comparison of recorded spectrum at one pixel (red) to the reference spectrum (blue) c) Extinction spectra of the core / shell nanoparticles (solid) compared to EDTA AgNP (dashed) and d) SEM image of the pre-incubated particles.

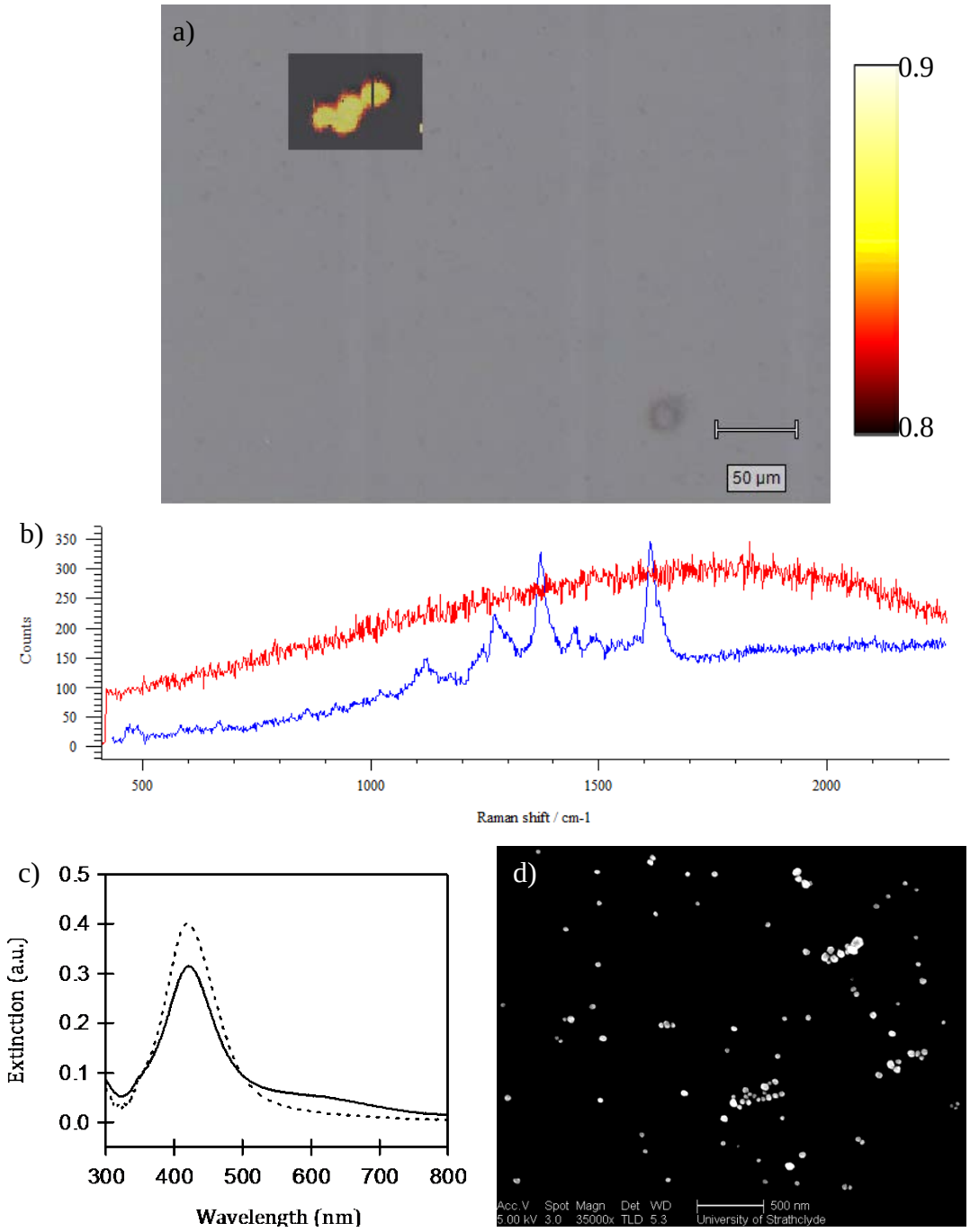

Figure 5.11 SERS map observed from incubation of unfunctionalised (BT-NH_2, 10^{-7} M) nanoparticles with HeLa cells. (514.5 nm excitation wavelength, 10 % laser power, 10 sec accumulation, LUT: $0.8 \leq x \leq 0.9$). b) A comparison of recorded spectrum at one pixel (red) to the reference spectrum (blue) c) Extinction spectra of the core / shell nanoparticles (solid) compared to EDTA AgNP (dashed) and d) SEM image of the pre-incubated particles.

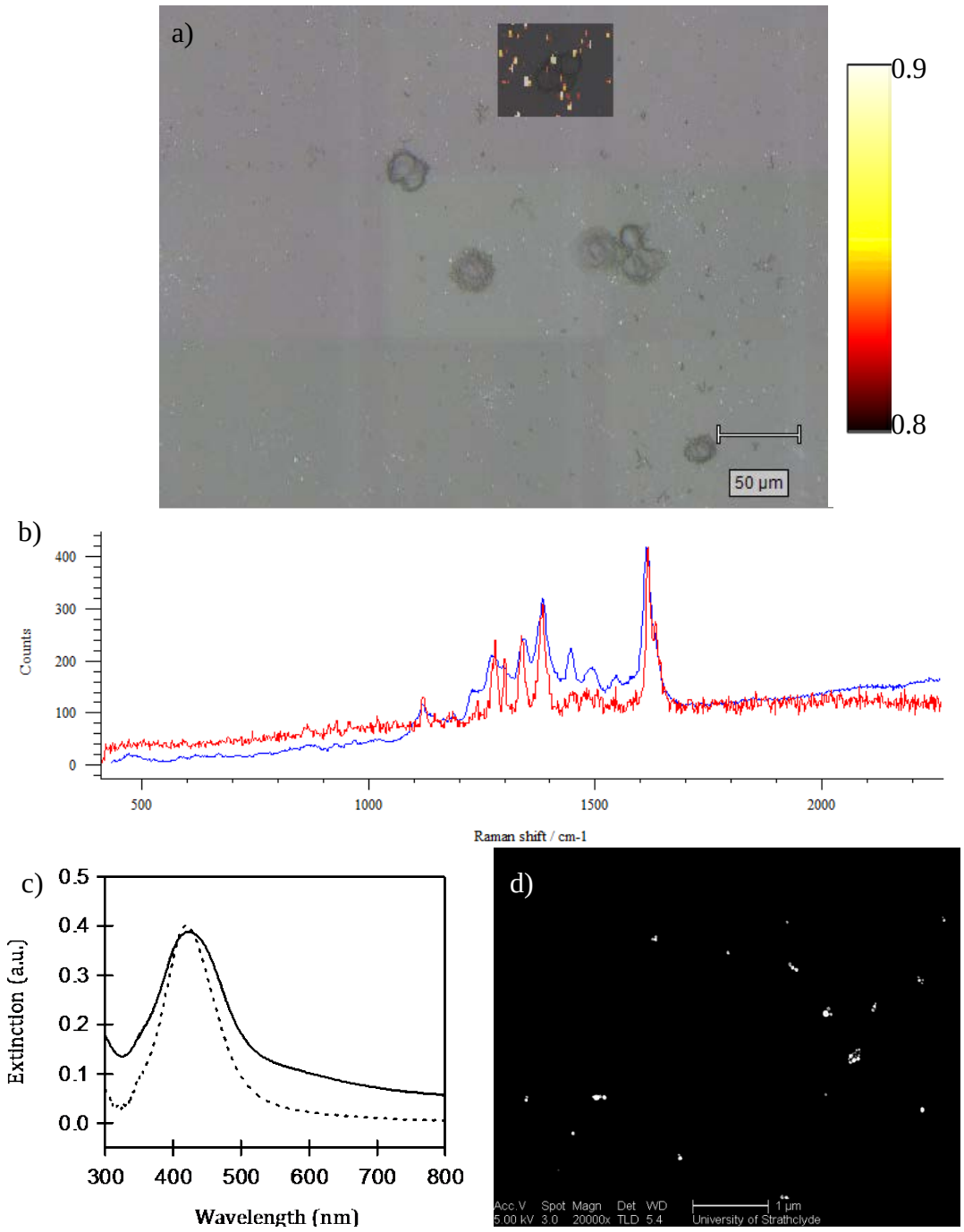

Figure 5.12 SERS map observed from incubation of unfunctionalised (BT-SiO_2, 10^{-7} M) nanoparticles with HeLa cells. (514.5 nm excitation wavelength, 10 % laser power, 10 sec accumulation, LUT: $0.8 \leq x \leq 0.9$). b) A comparison of recorded spectrum at one pixel (red) to the reference spectrum (blue) c) Extinction spectra of the core / shell nanoparticles (solid) compared to EDTA AgNP (dashed) and d) SEM image of the pre-incubated particles.

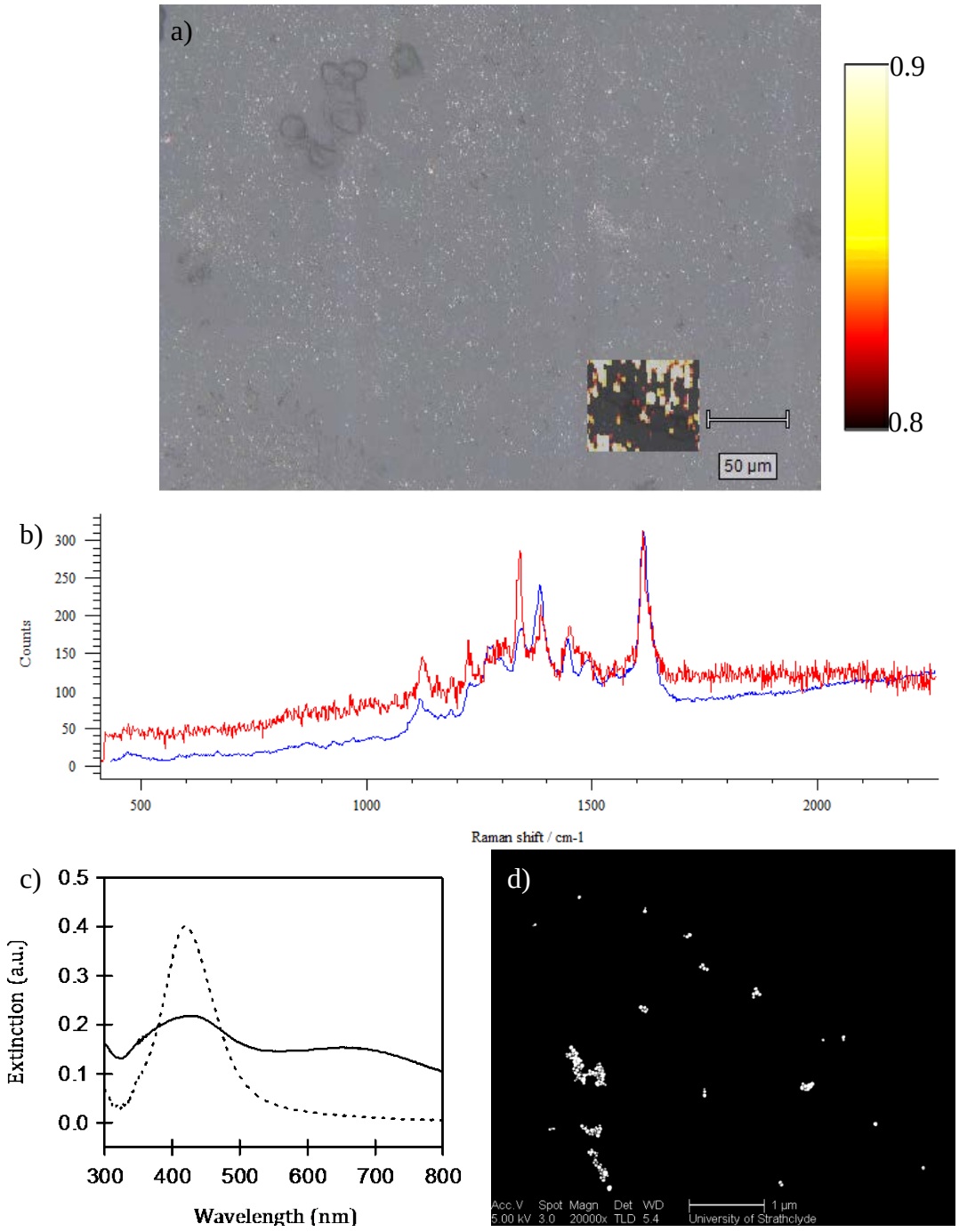

Figure 5.13 SERS map observed from incubation of unfunctionalised (BT-COOH, 10^{-6} M) nanoparticles with HeLa cells. (514.5 nm excitation wavelength, 10 % laser power, 10 sec accumulation, LUT: $0.8 \leq x \leq 0.9$). b) A comparison of recorded spectrum at one pixel (red) to the reference spectrum (blue) c) Extinction spectra of the core / shell nanoparticles (solid) compared to EDTA AgNP (dashed) and d) SEM image of the pre-incubated particles.

SERS signal was observed from populations of HeLa cells incubated with largely monomeric core / shell nanoparticles synthesised from BT-COOH (final concentration 10^{-7} M, Figure 5.10). As the LUT limits of the maps were increased to $0.8 \leq x \leq 0.9$, to reduce fluorescent interference, the collected spectra correlate well with the reference spectrum.

Increased particle size distribution was previously shown to amplify the observed signal at 632.8 nm excitation. However, BT-NH_2 induced aggregation was not sufficient to significantly increase the amount of signal detected from the sampled populations (Figure 5.11). At 514.5 nm excitation wavelengths, examination of the false colour image indicated blanket signal across the biological matter. This was a false positive as the collected spectra exhibited nominal correlation with the reference spectrum. No Raman peaks were identified, only intrinsic cellular fluorescence. This was unexpected due to the presence of small clusters with significant SERS activity. The extinction spectrum indicated a reduction in concentration compared to the BT-COOH samples. This may be responsible for the depleted signal. These probes did not offer sufficient SERS detectability at 514.5 nm.

BT-SiO_2 induced partial aggregation of the nanoparticles to a greater extent than BT-NH_2. The relatively high percentage composition of dimers increased the signal observed from the mapped cell population at both 632.8 nm and 514.5 nm (Figure 5.5Figure 5.12).

Extensive aggregation of the nanoparticles induced by high concentrations of “non-aggregating” precursors considerably increased the quantity of signal detected from mapped HeLa populations using a 514.5 nm excitation wavelength (Figure 5.13). However, as previously noted, precipitation of larger clusters may have resulted in excessive Raman signal. This uncontrolled, non-specific association may prove problematic when employing protein functionalised silver / silica particles for TNF targeting.

Silver / silica nanoparticles synthesised from BT-SiO_2 proved to be sufficient SERS probes for *in vitro* analysis at 514.5 nm. The extent and integrity of the recorded signal from BT-SiO_2 probes was explored at varying excitation conditions. The average spectra from 5 pixels showing good correlation with the reference spectrum, as determined by the LUT false colour image, were compared. Figure 5.14 depicts the average spectrum observed with increasing accumulation time at 10 % laser power from 1 to 10 sec. No significant spectral differences were noted as a result of extended accumulation times at 10 % laser power.

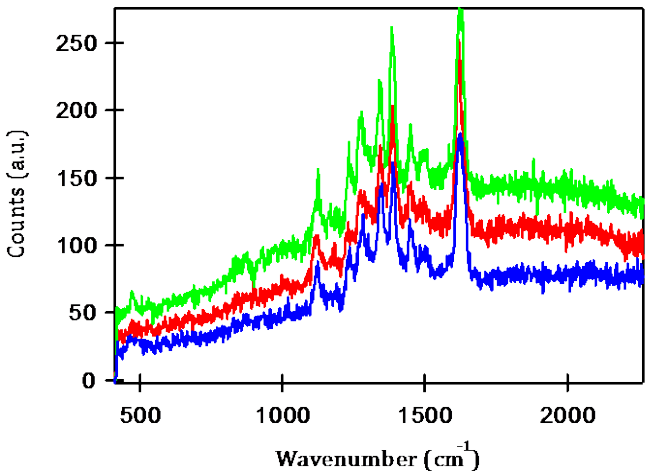

Figure 5.14 A comparison of Raman signals obtained using accumulation times of 1 sec. (red), 5 sec. (blue) and 10 sec. (green) at 10 % laser power (514.5 nm excitation wavelength). Average spectra of 5 pixels with LUT values $0.8 \leq x \leq 0.9$ observed from incubation of unfunctionalised BT-SiO_2 fabricated core/ shell nanoparticles with HeLa cells.

The effect of increasing laser power was investigated at 1 and 10 sec. accumulation periods (Figure 5.15). Similar results were observed for both data sets. Increasing laser power was negatively correlated with signal to noise ratio. Higher laser outputs were associated with an increase in fluorescent background and a reduction in spectral resolution of Raman peaks. These observations were heightened at longer accumulation intervals.

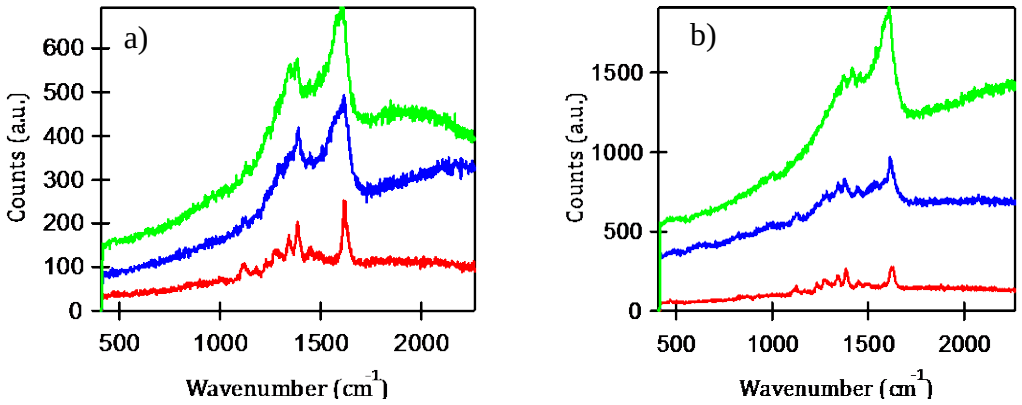

Figure 5.15 A comparison of Raman signals obtained using laser powers of 10 % (red), 50 % (blue) and 100 % (green) at a) 1 sec. and b) 10 sec. accumulation (514.5 nm excitation wavelength). Average spectra of 5 pixels with LUT values 0.8 ≤ x ≤ 0.9 observed from incubation of unfunctionalised BT-SiO_2 fabricated core/ shell nanoparticles with HeLa cells.

Thus 10 sec. accumulations at 10 % laser power output were deemed satisfactory for the *in vitro* interrogation of HeLa cells incubated with BT-SiO_2 fabricated silver / silica SERS probes.

Having determined the optimal probe and instrument conditions for the *in vitro* investigation of HeLa cells the ability to specifically target tmTNF was assessed. Samples were mapped using 632.8 nm (10 % laser power, 10 sec. accumulation) and 514.5 nm (10 % laser power, 5 sec. accumulation) excitation wavelengths.

5.2.3 Specificity of nanoparticle binding

BT-SiO_2 fabricated core / shell SERS probes were functionalised with the TNF marker, etanercept. The cell targeting nanoparticles were incubated with HeLa cells and analysed at 514.5 nm and 632.8 nm excitation wavelengths using the experimentally determined optimum conditions.

Etanercept was conjugated to the nanoparticles at a 100 fold and 200 fold molar excess. The extinction spectra depicted in Figure 5.16 illustrates the increased stability of the surface plasmon band with cumulative protein addition. This stabilising effect may reduce the SERS activity of the functionalised probes when using a 632.8 nm, and to a lesser extent 514.5 nm, excitation wavelength.

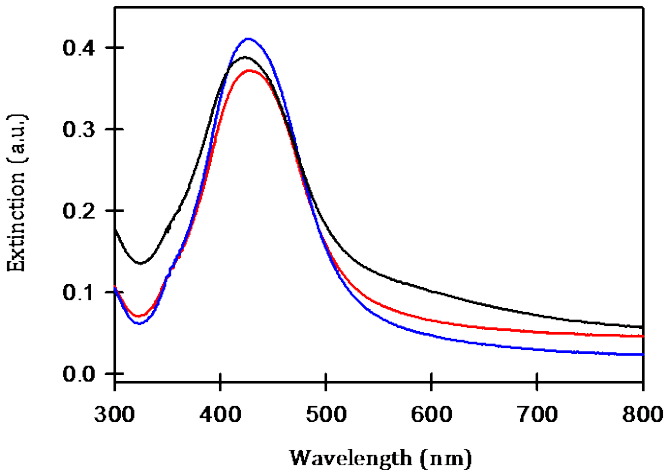

Figure 5.16 Extinction spectra of unfunctionalised silver / silica nanoparticles (black) and nanoparticles functionalised using 100 fold (red) and 200 fold (blue) molar excess of etanercept.

The samples were mapped using 632.8 nm (10 % laser power, 10 sec. accumulation) and 514.5 nm (10 % laser power, 5 sec. accumulation) excitation wavelengths. The spectra obtained at each pixel were compared to the solution spectra of the nanoparticles using DCLS. LUT values were set to $0.6 \leq x \leq 0.9$ and $0.8 \leq x \leq 0.9$ for 632.8 nm and 514.5 nm excitation wavelengths respectively. A representative map of each sample is illustrated in Figure 5.17.

As expected, the signal observed from incubation with functionalised nanoparticles was reduced compared to unfunctionalised nanoparticles. In the absence of a protein coating, the nanoparticles were less stable in buffered conditions resulting in increased extinction at longer wavelengths. Consequently the unfunctionalised nanoparticles were more closely in resonance with the excitation wavelength.

The majority of the signal observed following incubation with unfunctionalised nanoparticles, when using a 514.5 nm excitation wavelength, was outside the cells. This was also observed when using a 632.8 nm excitation wavelength, but to a lesser degree. The cells incubated with functionalised nanoparticles exhibited fewer detectable SERS signals, but the recorded signals were localised in the vicinity of the cells (Figure 5.17).

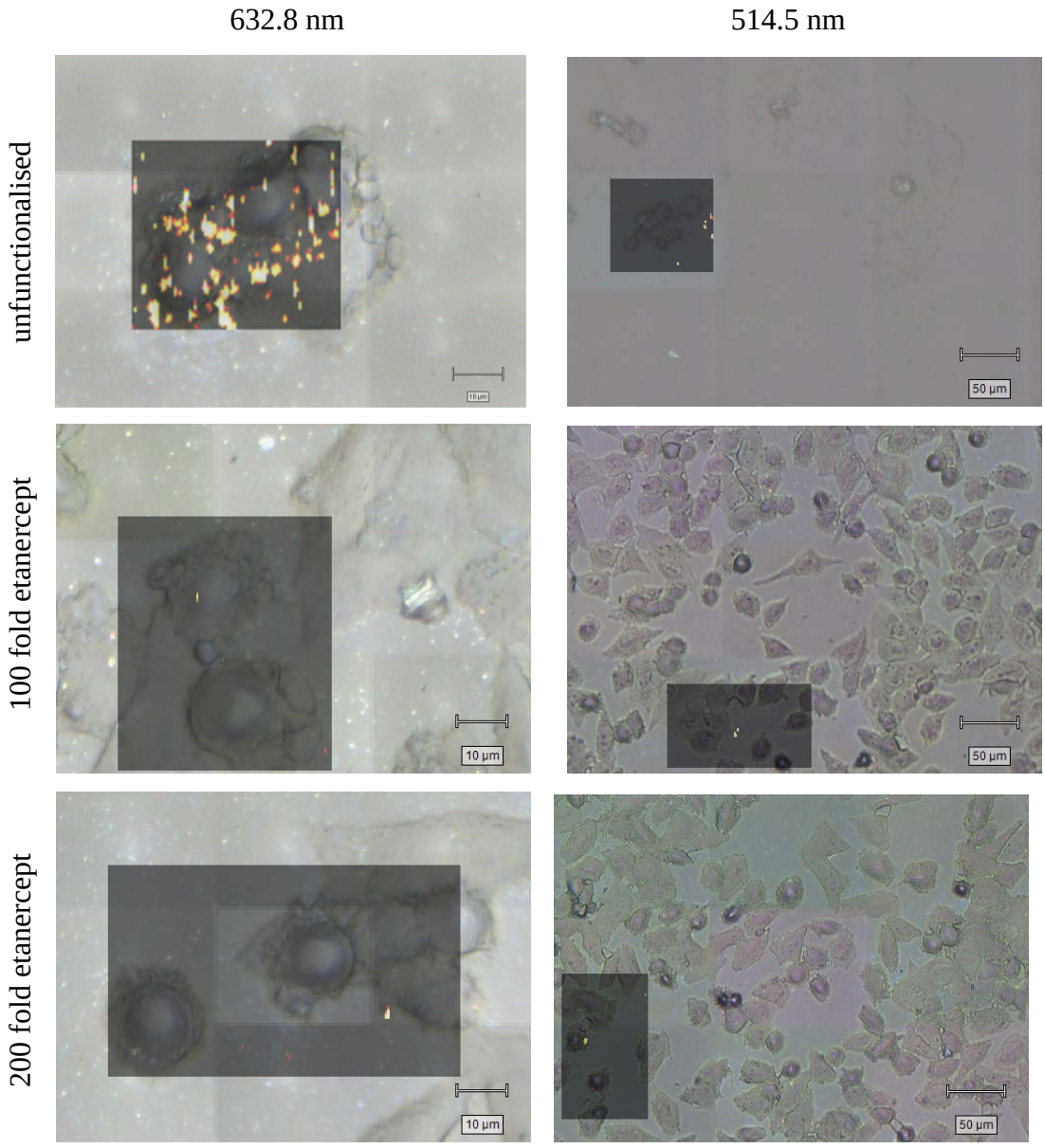

Figure 5.17 A comparison of observed signal from HeLa cells incubated with unfunctionalised silver / silica nanoparticles and nanoparticles functionalised using 100 fold and 200 fold molar excess etanercept. Samples analysed at 632.8 nm (LUT: $0.6 \leq x \leq 0.9$) and 514.5 nm (LUT: $0.8 \leq x \leq 0.9$).

However, due to the two dimensional (2D) nature of the SERS mapping it is not possible to determine whether the signal is a result of tmTNF- etanercept binding or cellular uptake. There is also a possibility that the results were due to non-specific binding. Further investigations will be necessary to probe the nature of the resultant signal. This would include three dimensional (3D) imaging or 2D mapping through

the z-plane. Functionalisation with non-membrane targeting proteins may aid discrimination between specific vs. non-specific interactions. The stability of the signal from the probes was also investigated.

5.2.4 Stability of signal

HeLa cells incubated with unfunctionalised silver / silica nanoparticles were analysed on day of preparation (t = 0) and again after a period of 1 week, 3 weeks and 1 month. The samples were mapped using a 632.8 nm excitation wavelength (10 % laser power, 10 sec. accumulation). The spectra obtain at each pixel was compared to the solution spectra of the nanoparticles using DCLS; LUT values were set to $0.6 \leq x \leq 0.9$ to create a false colour image. A representative map of each sample is illustrated in Figure 5.18.

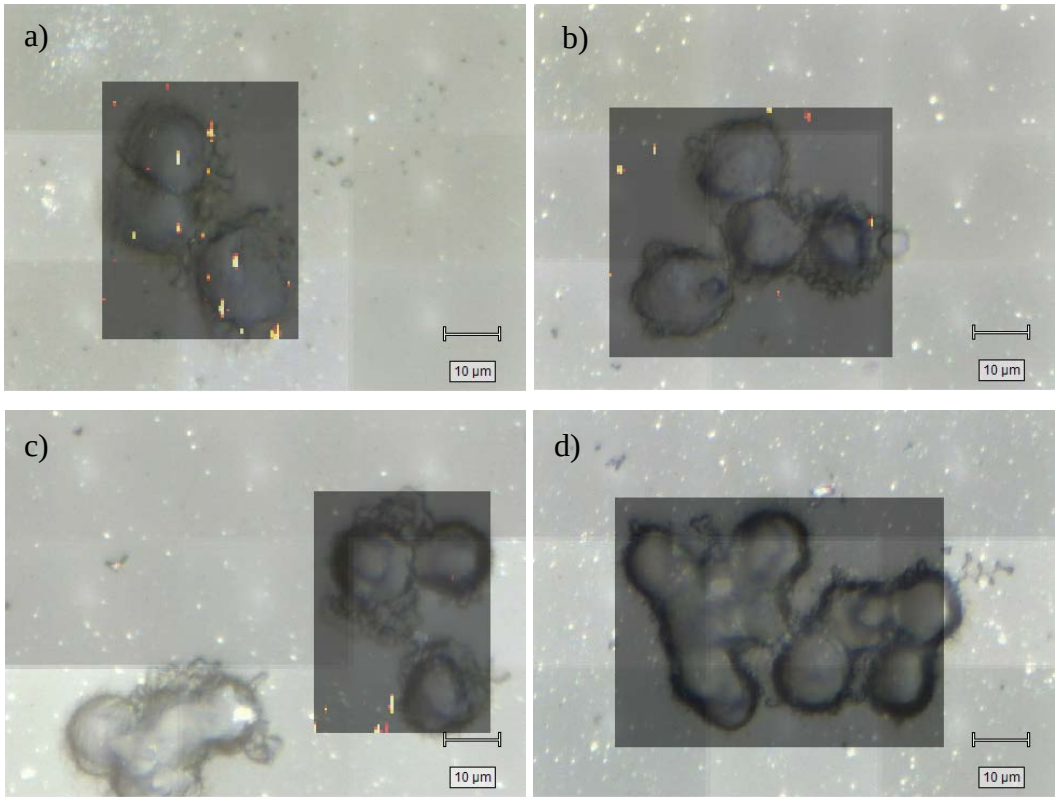

Figure 5.18 SERS signal observed from HeLa cells incubated with unfunctionalised silver / silica nanoparticles using a 632.8 nm excitation wavelength (LUT: $0.6 \leq x \leq 0.9$). Samples analysed a) on day of preparation (t = 0), b) t = 1 week, c) t = 3 weeks and d) t = 1 month.

The signal observed from the samples was seen to diminish over time. After a period of 1 month nominal signal is observed from the mapped cell populations. Dissolution of Stöber silica particles has been observed in biological media.[200] If the silver nanoparticle core had become exposed to the biological environment it may have been oxidised; this would have reduced the surface enhancement contributions on the Raman signal. This suggested that the unfunctionalised silica coated nanoparticles were not stable in biological media over a period of 1 month. Bio-functionalisation of silica surfaces has been proven to increase the stability against hydrolytic dissolution.[201] It follows that the stability of signal from protein functionalised nanoparticles may not be subject to the same deteriorating trend as the unfunctionalised nanoparticles. This requires further investigation to be conclusive.

5.3 *Ex-vivo* analysis of sTNFα

The avidity of etanercept binding to soluble sTNF is approximately 1000 fold greater than to the membrane bound analogue, tmTNF (K_D = 0.4 and 438 pM respectively).[196] It is proposed that both sTNF and tmTNF are biologically active in inflammatory signalling pathways.[202] Elevated serum levels of this cytokine are reported in both inflammatory and infectious diseases, with serum levels correlating to the severity of infection.[203, 204] Therefore, targeting of sTNF should permit discrimination between infected and uninfected samples. sTNF is contained within the extracellular matrix. During cell preparation, as outlined in 8.5.1, the extracellular matrix is removed prior to incubation with the etanercept functionalised nanoparticles. Therefore, *in vitro* cell investigations are not suitable for the comparison of infected and uninfected samples. *Ex vivo* imaging of tissue samples provides a suitable alternative.

Cerebral and spleen tissue samples were obtained from uninfected mice and mice infected with experimental cerebral malaria (ECM, samples provided by Tovah Shaw, University of Glasgow). Immunohistochemistry was performed on 15 μm tissue sections. The tissues were perfuse-fixed with acetone, cryopreserved in 30% sucrose, embedded in Tissue-Tek® OCT™, frozen in liquid Nitrogen and

cryopreserved at −70 °C. 4 % paraformaldehyde (pfa) was also considered as a fixation agent. 15 μm tissue sections were cut using a cryostat, mounted onto glass slides and washed with bovine serum albumin (3 % in PBS).

After fixation of tissues, antigen masking by solvents and fixatives may prevent many antibodies binding to their antigen. In particular, the formation of methylene bridges during fixation, which cross link proteins, mask antigenic sites. It was therefore necessary to include an antigen retrieval step, to break the protein cross-links and expose the antigenic binding site, in order to optimise immunohistochemical (IHC) staining. Tissue sections were incubated for twenty minutes at 96 °C in a water bath in Tris EDTA buffer (10mM EDTA, 0.25mM Tris, pH 9). All antigen retrieval steps were followed by a twenty minute cool down period. Silver / silica nanoparticles were incubated under a number of conditions (discussed in chapter 5) and the slides washed in buffer (0.1 M phosphate buffer, 0.1 % bovine serum albumin, 0.05 % sodium azide, 0.05 % Tween) prior to analysis.

5.3.1 Detection of Cerebral Malaria in mouse cerebral tissue

5.3.1.1 Optimisation of experimental parameters

In previous *in vitro* investigations, the laser power was attenuated to reduce fluorescent interference. The effect of laser power employed for interrogation of tissue samples was considered. Tissue sections were incubated with etanercept functionalised silver / silica particles, fabricated from BT-SiO_2, for 2 hours. The samples were washed and analysed at 10, 50 and 10 % laser output. The recorded spectra at 5 pixels whose DCLS comparison with the reference spectrum fell within the limits $0.7 \leq x \leq 0.9$ were averaged. The resulting maps and spectra are reported in Figure 5.19.

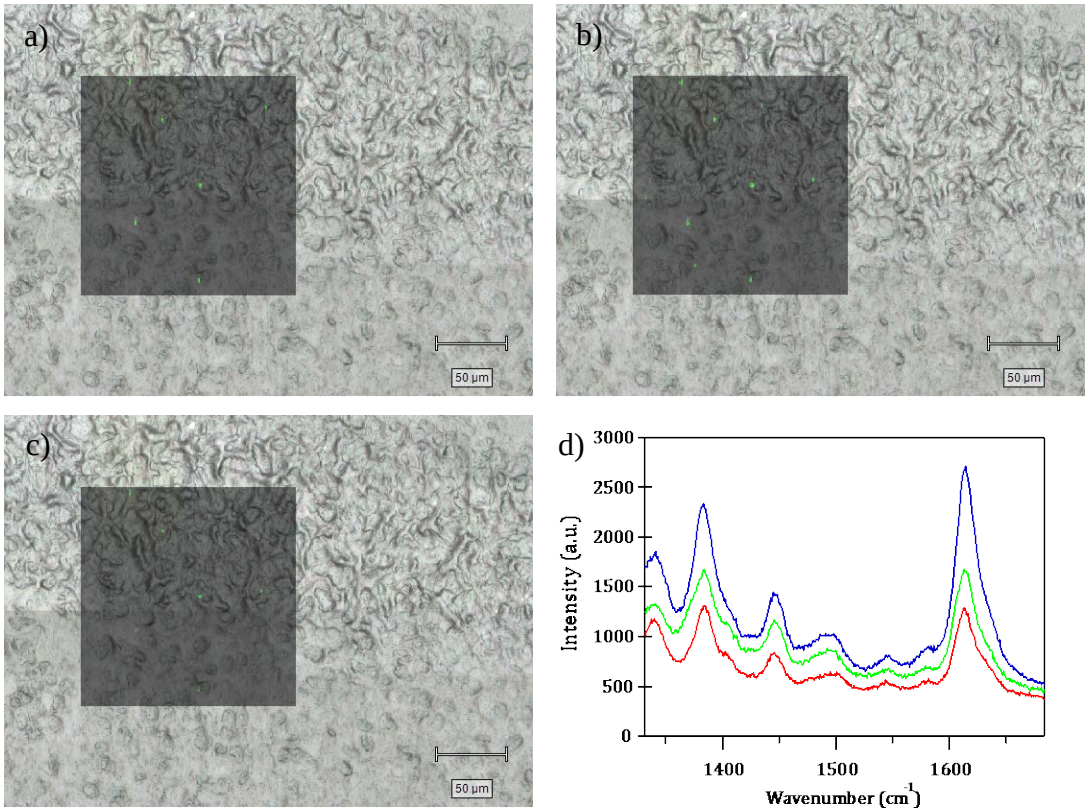

Figure 5.19 SERS map of acetone fixed, ECM infected cerebral tissue incubated with etanercept functionalised silver / silica particles, fabricated from BT-SiO_2, for 2 hrs. Samples analysed using a 632.8 nm excitation wavelength. Laser output was adjusted to a) 10 %, b) 50 % and c) 100 %. False colour images indicate pixels whose spectrum compares well with the reference spectrum (LUT: $0.7 \leq x \leq 0.9$). d) Average spectra collected from 5 pixels whose LUT value was within the aforementioned limits at 10 % (red), 50 % (blue) and 100 % (green) laser output.

From the SERS maps reported it was observed that repeated mapping of the tissue sample does not result in a deterioration of signal. There were nominal differences in both the quantity and integrity of SERS signal detected at increased laser outputs. However, the average signal to noise ratio of the spectra, when using a 632.8 nm excitation wavelength, was greatest at 50 % laser power. Therefore 50 % laser power was employed for all further SERS interrogation of tissue samples.

The affinity of the antigen normally determines the incubation interval in an IHC staining protocol. For monoclonal antibodies with high affinity, 30 minutes is

sufficient. Longer incubation periods are required for secondary antibodies and samples with low antigen density. Extensive staining periods can lead to undesirable non-specific binding. The binding of etanercept functionalised nanoparticles to the ECM infected cerebral tissue sections was monitored over incubation periods of 0.5 and 2 hours. The slides were washed with phosphate buffer and analysed using a 632.8 nm excitation wavelength. From Figure 5.20 it was observed that the incubation period was correlated with increased adhesion of the protein functionalised nanoparticles to the tissue sections.

The samples were also mapped at the interface between the glass slide and the tissue section (Figure 5.20c).

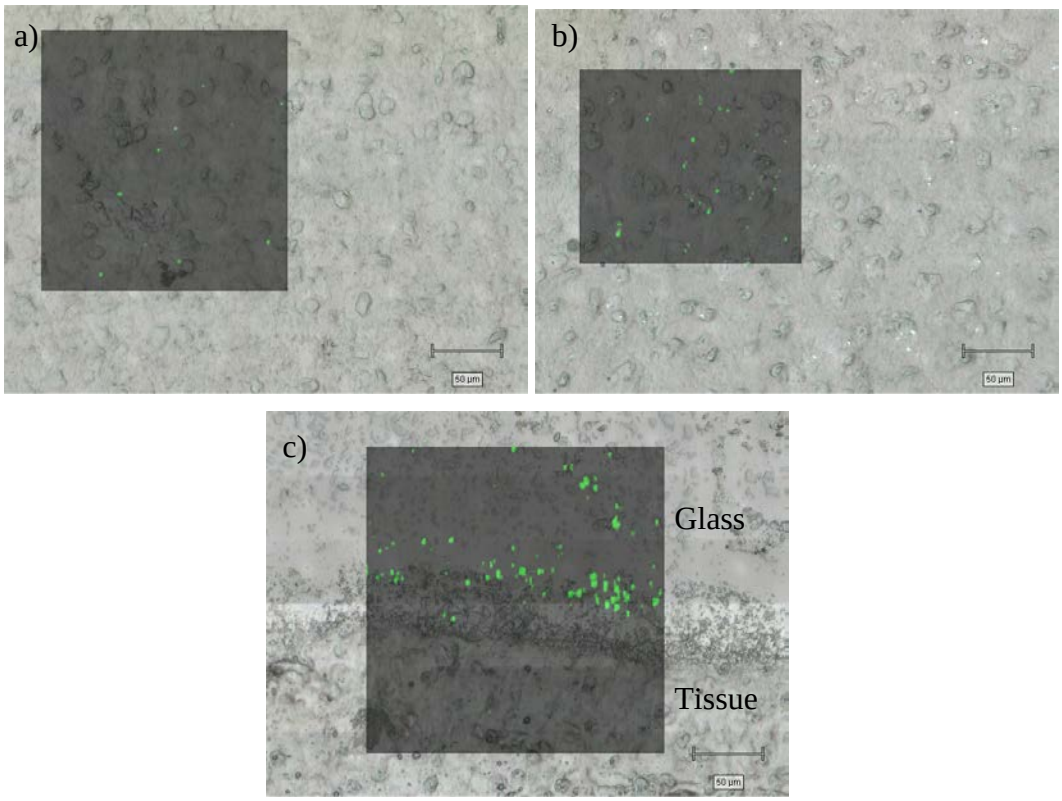

Figure 5.20 SERS map of acetone fixed, ECM infected cerebral tissue sections incubated with etanercept functionalised silver / silica particles, fabricated from BT-SiO_2, for a) 0.5 and b) 2 hr. and c) uninfected cerebral tissue incubated with etanercept functionalised nanoparticles for 2 hr. Samples analysed using a 632.8 nm excitation wavelength. False colour images indicate pixels whose spectrum compares well with the reference spectrum (LUT: $0.7 \leq x \leq 0.9$).

After washing, the nanoparticles remained bound to glass slide, but not to the surface of the tissue. This suggested that the protein-functionalised nanoparticles non-specifically bound to the glass slide but not to cerebral tissue sections. However, drying of the nanoparticle suspension onto the surface of tissue was also observed in some samples. This is illustrated in Figure 5.21.

Post incubation and washing, a coffee ring effect was observed where the nanoparticle droplet had formed on the tissue surface. This was a result of evaporation of the aqueous solvent throughout the incubation interval. Precipitation of the nanoparticles at the outer perimeter of nanoparticle droplet could be seen in the white light image. The detected signal of this mapped region was significantly greater than that at the centre of the droplet.

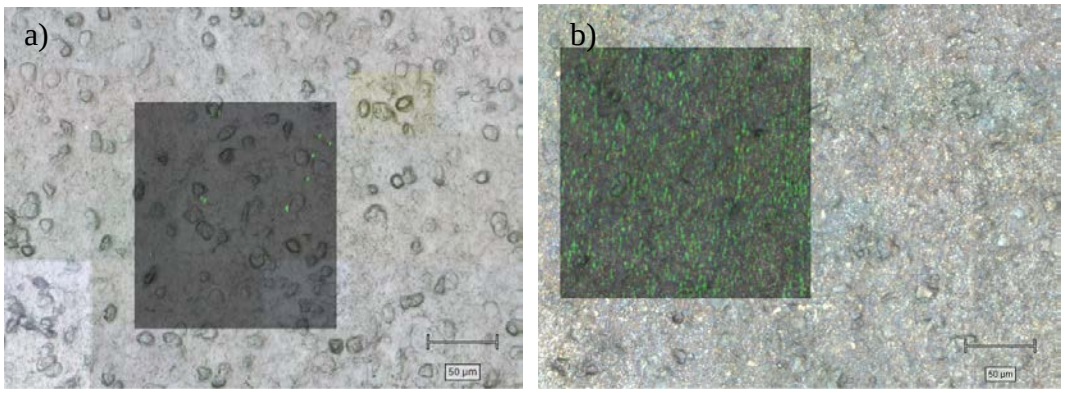

Figure 5.21 SERS map of acetone fixed, ECM infected cerebral tissue incubated with etanercept functionalised silver / silica particles, fabricated from BT-SiO_2, for 2 hr. at a) centre and b) outer perimeter of nanoparticle droplet. Samples analysed at 632.8 nm. False colour images indicate pixels whose spectrum compares well with the reference spectrum (LUT: $0.7 \leq x \leq 0.9$).

To avoid inconsistences associated with evaporation, and thereby reducing non-specific association of the nanoparticles during the incubation period, SecureSeal™ hybridisation chambers were purchased from Grace BioLabs. These enclosed chambers adhered to the glass slides, permitting incubation with approximately 0.5 mL nanoparticle suspensions whilst minimising evaporation of solvent.

Etanercept functionalised nanoparticles were incubated with ECM infected cerebral tissue samples in hybridisation chambers for 2 hr. The resulting SERS maps, using a 632.8 nm excitation wavelength, are illustrated Figure 5.22a.

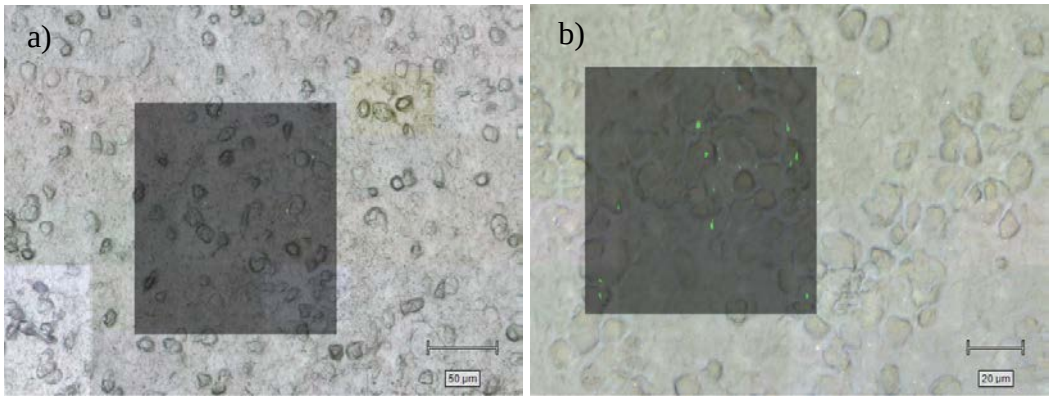

Figure 5.22 SERS map of acetone fixed, ECM infected cerebral tissue incubated etanercept functionalised silver / silica particles, fabricated from BT-SiO_2, in a SecureSeal™ chamber for a) 2 hr. and b)12 hr. Samples analysed using a 632.8 nm excitation wavelength. False colour images indicate pixels whose spectrum compares well with the reference spectrum (LUT: $0.7 \leq x \leq 0.9$).

The reported signal from etanercept functionalised nanoparticles was reduced compared to previously analysed samples. It was proposed that prolonged intervals may be required under the new incubation conditions. The incubation period was extended from 2 to 12 hr. and analysis was repeated (Figure 5.22b). Due to the protracted incubation, samples were kept at 4 °C. The detected signal correlating well with the reference spectrum was amplified over a 12 hr. incubation interval.

5.3.1.2 Specificity of nanoparticle binding

To ascertain the specificity of adhesion of the nanoparticles to the surface of the tissue sections, a blocking step was incorporated into the IHC protocol.

Following antigen retrieval, the exposed tissue sections were incubated with unconjugated etanercept (1 mg/ mL, PBS). Etanercept in its solution state mimics

soluble TNF receptors thereby, blocking all active TNF binding sites and preventing association with etanercept functionalised nanoparticles. The samples were washed and incubated for a further period with etanercept functionalised nanoparticles. The adhesion of the nanoparticles to ECM infected cerebral tissue samples was compared in the absence of and with the inclusion of the aforementioned etanercept blocking step (Figure 5.23)

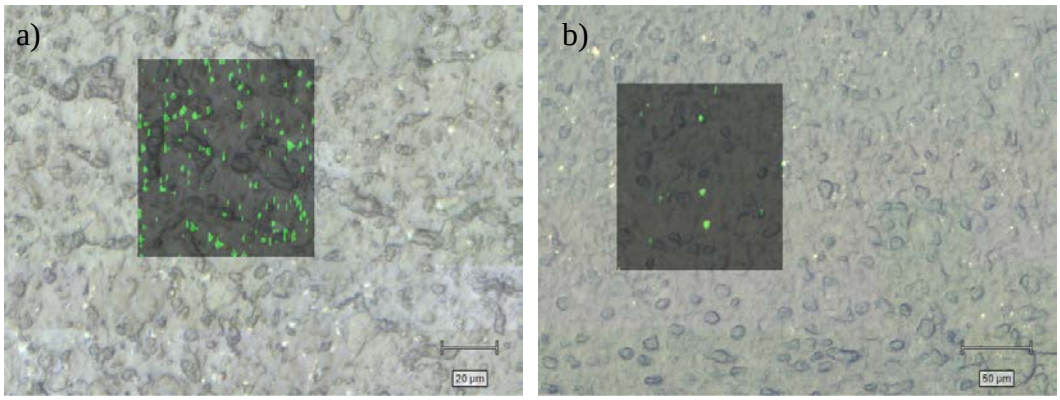

Figure 5.23 SERS map of acetone fixed, ECM infected cerebral tissue a) in absence of blocking step and b) etanercept blocked, incubated with etanercept-functionalised silver / silica nanoparticles, fabricated from BT-SiO_2, for 2 hrs. False colour images indicate pixels whose spectrum compares well with the reference spectrum (LUT: $0.7 \leq x \leq 0.9$).

Employing an etanercept blocking step significantly reduced the detected signal from the functionalised nanoparticles. The reduced availability of active TNF sites correlated with reduced output in the SERS map, thereby corroborating the specificity of binding of the etanercept functionalised nanoparticles with ECM infected cerebral tissue samples.

5.3.1.3 Assessing the integrity of the tissue samples

At this point, the morphology of the tissue samples was also examined. Previously analysed samples had been perfuse-fixed using acetone prior to freezing. This is considered to reduce the occurrence of artefacts formed when freezing fresh tissue samples. Fixation maintains the morphological integrity of the resultant samples.

The mechanism of fixation by acetone, a coagulating fixative, involved dehydration of proteins. This rendered the proteins insoluble, resulting in precipitation.[205] These precipitating fixatives are intrinsically denaturing, weakening hydrophobic interactions responsible for many secondary and tertiary structures.

Alternatively, cross-linking fixatives, such as paraformaldehyde, form covalent bonds within and between proteins. This primarily involves the formation of hydroxymethyl groups on lysine residues prior to condensation, resulting in methylene bridges between polypeptide chains. Fixation of tissues *via* paraformaldehyde was examined for preservation of chemical and morphological integrity.

ECM infected cerebral tissue sections, perfuse-fixed using acetone and alternatively pfa, were incubated with etanercept functionalised silver / silica nanoparticles. The samples were mapped using a 632.8 nm excitation wavelength and the recorded spectrum at each pixel compared to a reference spectrum using DCLS analysis. Pixels exhibiting greater than 70 % correlation are illustrated in the false colour images in Figure 5.24.

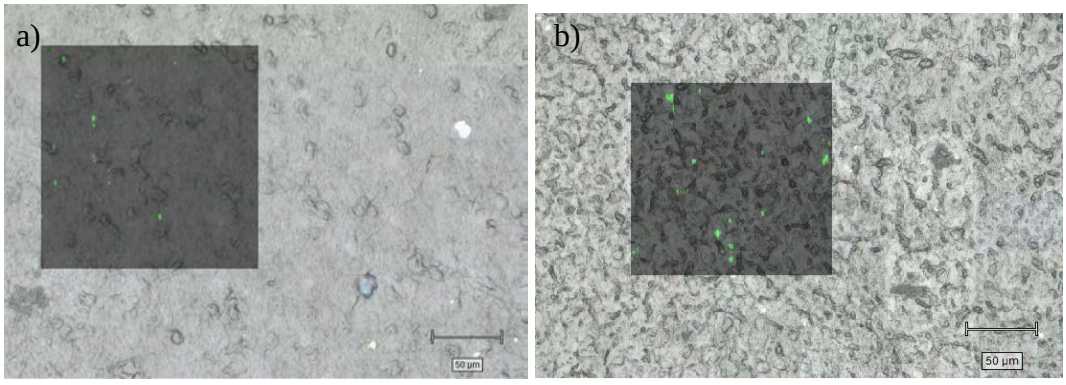

Figure 5.24 SERS map of a) acetone and b) 4 % pfa fixed ECM infected cerebral tissue incubated with etanercept functionalised silver / silica nanoparticles. Samples analysed using a 632.8 nm excitation wavelength. False colour images indicate pixels whose spectrum compares well with the reference spectrum (LUT: $0.7 \leq x \leq 0.9$).

The morphological integrity of the samples fixed with 4 % pfa was seemingly greater than those fixed by acetone. Samples fixed by pfa also demonstrates amplified signal from the functionalised nanoparticles. This may be attributed to improved chemical stability of pfa fixed cerebral tissue samples.

5.3.1.4 Analysis at shorter excitation wavelengths

As previously discussed in this chapter, excitation using far red and NIR wavelengths is preferable for spectral interrogation of biological samples. However, excitation using a 514.5 nm wavelength proved efficacious in the detection of tmTNF within HeLa cell populations. The compatibility of shorter excitation wavelengths with analysis of tissue samples was also investigated.

A second batch of ECM infected and uninfected cerebral samples were procured from the University of Glasgow. The samples were incubated with etanercept functionalised silver / silica nanoparticles using hybridisation chambers (incubation at 4 °C for 12 hr.) The samples were washed and analysed using 632.8 nm and 514.5 nm excitation wavelengths.

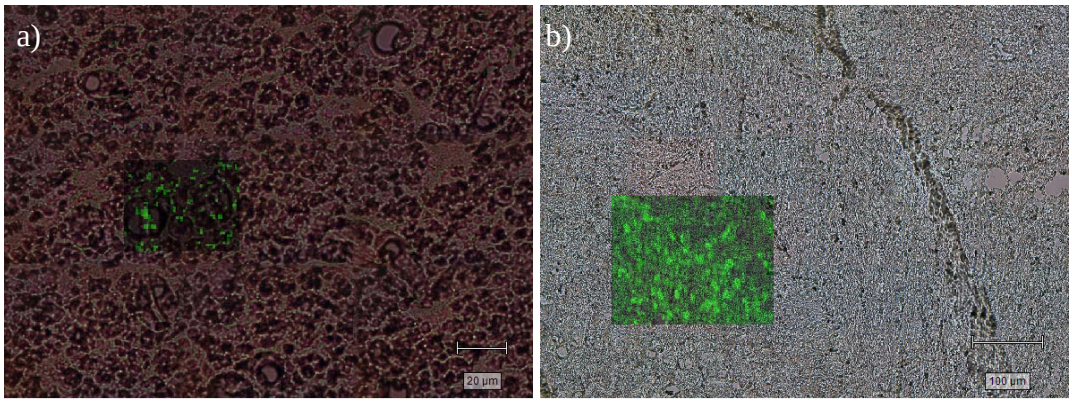

Figure 5.25 SERS map of 4 % pfa fixed, ECM infected cerebral tissue incubated with etanercept functionalised silver /silica nanoparticles, fabricated from BT-SiO_2, for 12 hrs. Samples analysed using a) 632.8 nm and b) 514.5 nm excitation wavelengths. False colour images indicate pixels whose spectrum compares well with the reference spectrum (LUT: $0.7 \leq x \leq 0.9$ and $0.8 \leq x \leq 0.9$ respectively).

The measured signal from the nanoparticles at 514.5 nm excitation was significantly greater; this was most likely a result of the shorter wavelength being closer to resonance with the SERS active nanoparticles. The density of the signal observed from the tissue samples using a 514.5 nm excitation wavelength was similar to that previously observed from coffee-ring precipitation however incubation was performed in SecureSeal™ chambers, minimising evaporation of the colloidal solvent. A section of the tissue sample exhibiting a distinctive glass/ tissue boundary was selectively mapped. If the density of signal was a result of drying or precipitation effects then signal will almost certainly be observed across the entire mapped area.

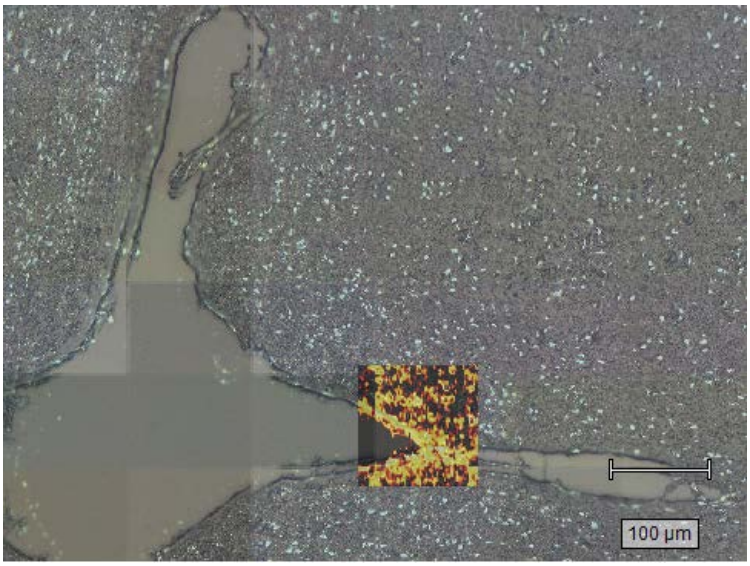

Figure 5.26 SERS map of 4 % pfa fixed, infected ECM infected cerebral tissue incubated with etanercept functionalised silver / silica nanoparticles, fabricated from BT-SiO_2, for 12 hrs. at 4 °C in a SecureSeal™ chamber. Sample analysed using a 514.5 nm excitation wavelength. False colour images indicate pixels whose spectrum compares well with the reference spectrum (LUT: $0.8 \leq x \leq 0.9$).

The signal detected from the etanercept functionalised nanoparticles correlated well with the white light image of the tissue section. Minimal signal was observed from pixels corresponding to the glass slide. It was proposed that the density of signal was not a result of non-specific adhesion or precipitation.

To determine if the density of signal at 514.5 nm excitation could be controlled, reduced incubation periods were explored. Further sections of this second batch of ECM infected and uninfected tissue samples were incubated with etanercept functionalised silver / silica nanoparticles using SecureSeal™ chambers (2 hr. incubation at room temp.). The detected signal at 514.5 and 632.8 nm is illustrated in Figure 5.27.

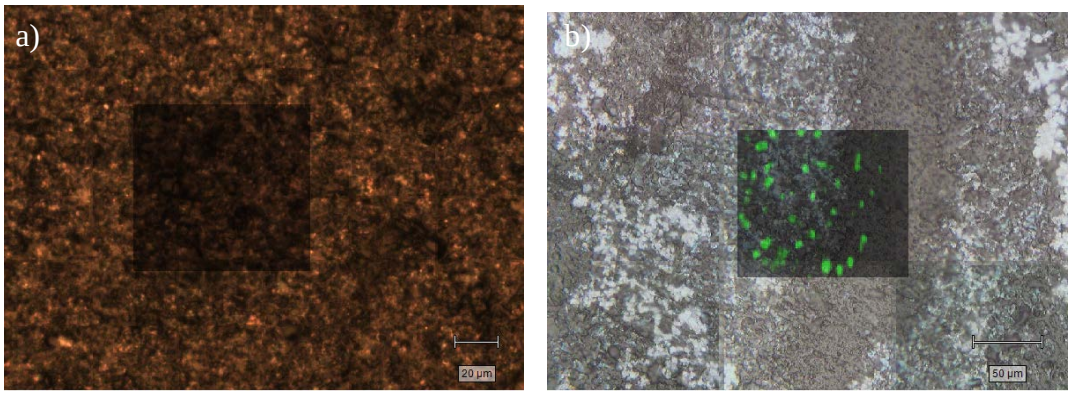

Figure 5.27 SERS map of 4 % pfa fixed, ECM infected cerebral tissue incubated with etanercept functionalised silver / silica nanoparticles, fabricated from BT-SiO_2, for 2 hrs. Samples analysed using i) 632.8 nm and b) 514.5 nm excitation wavelengths. False colour images indicate pixels whose spectrum compares well with the reference spectrum (LUT: $0.7 \leq x \leq 0.9$ and $0.8 \leq x \leq 0.9$ respectively).

The detected SERS signal from the nanoparticles was reduced at both excitation wavelengths when compared to longer incubation periods. The density of observed signal and localisation of the detected signal, using a 514.5 nm excitation wavelength, was improved. Therefore, for analysis of cerebral tissues using a 514.5 nm excitation wavelength, shorter incubation periods are recommended. However, nominal signal was observed using a 632.8 nm excitation wavelength, thus protracted incubation was required using hybridisation chambers.

Splenic tissue samples, removed from the same mice used to provide ECM infected cerebral tissue, were also provided. Similar conditions were employed to ascertain if TNF could be detected in splenic samples.

5.3.2 Detection of Cerebral Malaria in mouse spleen tissue

Splenic tissue samples from the sample mice used to provide the data collected in Figure 5.25 and Figure 5.27 were incubated with etanercept functionalised nanoparticles using hybridisation chambers (2 hr. incubation at room temp.). The samples were washed analysed using 632.8 nm and 514.5 nm excitation wavelengths.

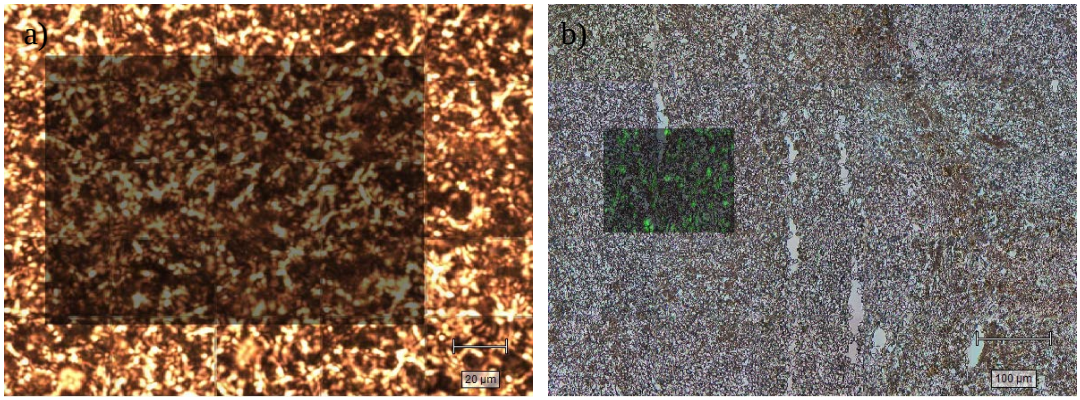

Figure 5.28 SERS map of 4 % pfa fixed, ECM infected splenic tissue incubated with etanercept functionalised silver / silica nanoparticles, fabricated from BT-SiO_2, for 2 hrs. Samples analysed using i) 632.8 nm and b) 514.5 nm excitation wavelengths. False colour images indicate pixels whose spectrum compares well with the reference spectrum (LUT: $0.7 \leq x \leq 0.9$ and $0.8 \leq x \leq 0.9$ respectively).

The etanercept functionalised nanoparticles were detected using a 514.5 nm excitation wavelength; nominal SERS output was reported using a 632.8 nm excitation wavelength. This was in agreement with the cerebral tissue samples previously analysed. Increased incubation periods were previously demonstrated to intensify the detected signal. The samples were incubated with etanercept functionalised nanoparticles using hybridisation chambers (incubation at 4 °C for 12 hr.)

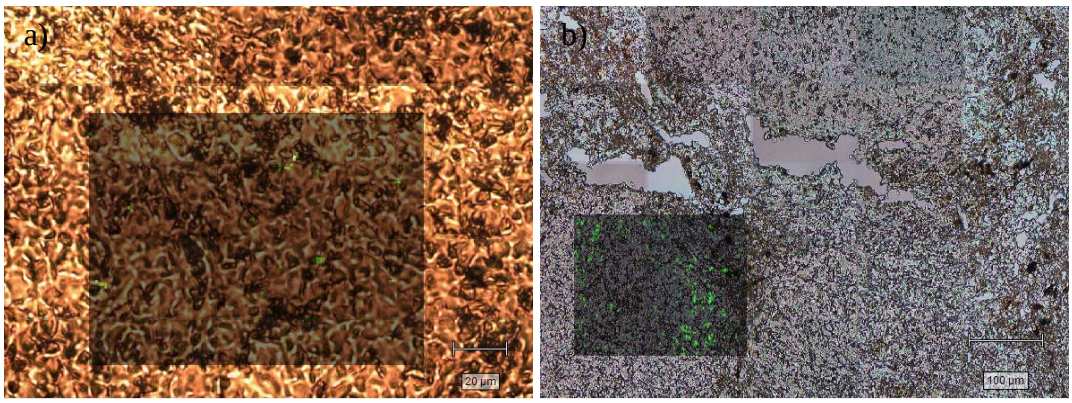

Figure 5.29 SERS map of 4 % pfa fixed, ECM infected splenic tissue incubated with etanercept functionalised silver / silica nanoparticles, fabricated from BT-SiO_2, for 12 hrs. Samples analysed using i) 632.8 nm and b) 514.5 nm excitation wavelengths. False colour images indicate pixels whose spectrum compares well with the reference spectrum (LUT: $0.7 \leq x \leq 0.9$ and $0.8 \leq x \leq 0.9$ respectively).

Protracted incubation amplified the reported signal using a 632.8 nm excitation wavelength, as formerly observed in cerebral tissue sections. Increased signal output was not observed using a 514.5 nm excitation wavelength over extended incubation periods.

The specificity of functionalised nanoparticle adhesion to cerebral tissue samples was previously established in section 5.3.1.2. The extension of this observation to splenic tissue samples was evaluated. Unconjugated etanercept was incubated with ECM infected splenic samples prior to incubation with functionalised nanoparticles. This was compared to samples where no blocking step was performed. SERS mapping of the samples using a 632.8 nm excitation wavelength was used to determine the amount of nanoparticles bound to the tissue surface (Figure 5.30).

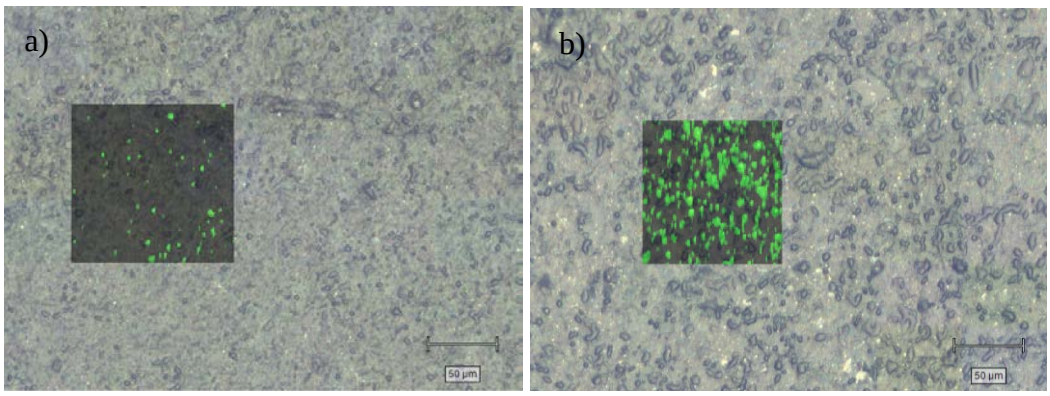

Figure 5.30 SERS map of pfa fixed, ECM infected 4 % pfa fixed spleen tissue a) in the absence of a blocking step and b) blocked with etanercept, incubated with etanercept-functionalised silver/ silica nanoparticles, fabricated from BT-SiO_2, for 2 hrs. False colour images indicate pixels whose spectrum compares well with the reference spectrum (LUT: $0.7 \leq x \leq 0.9$).

The etanercept blocking procedure, used to block all active TNF sites and thus reduce the binding of etanercept nanoparticles, was observed to increase the amount of nanoparticles detected on the splenic tissue surface. This implied that the adhesion of the nanoparticles to the splenic tissue surface was not solely the result of TNF-etanercept interactions. It was proposed that detection of increased TNF, expressed in mice infected with ECM, is not possible in splenic tissue samples.

5.4 Quantification of signal from tissue samples

5.4.1 Optimisation of DCLS parameters

Visual discrimination between infected and uninfected tissue samples is subjective. Additionally, more than one mapped area of the tissue sample is required to determine if the signal detected is representative of the whole tissue sample. Efforts were made towards quantification of the signal detected from tissue samples. This requires a technique that gives a positive value (proportional to intensity) from pixels where the reference spectrum is observed, and effectively zero contribution from elsewhere in the mapped region. Dividing the summation of these values by the

number of mapped pixels would result in an average value per pixel – the average component intensity (ACI).

DCLS analysis, which has been employed throughout this chapter, performs by definition the best least squares fit to the data so that even data with no features may contribute. To counteract this, baseline subtraction or differentiation of the raw data may be performed before fitting.

It is critical to avoid the background (negative) areas of the maps dominating the average value; ideally these areas should contribute zero to the result value. If this is true the result value will be a measure of the average SERS probe signal and therefore, be proportional to the average amount of biomarker in the mapped area. Any net contribution from the dark areas will reduce the discrimination between positive and negative samples.

The contribution from these dark areas of the map should therefore be quantified and minimised through adjustment of the DCLS analysis parameters. The signal observed from the (positive) areas, where nanoparticles are bound, should also be considered. The DCLS parameters affording maximum signal from the positive areas, whilst minimising contribution from the negative regions, were selected as optimal.

Cerebral tissue samples from uninfected samples in the absence of nanoparticles were analysed by SERS mapping using 514.5 nm and 632.8 nm excitation wavelengths.

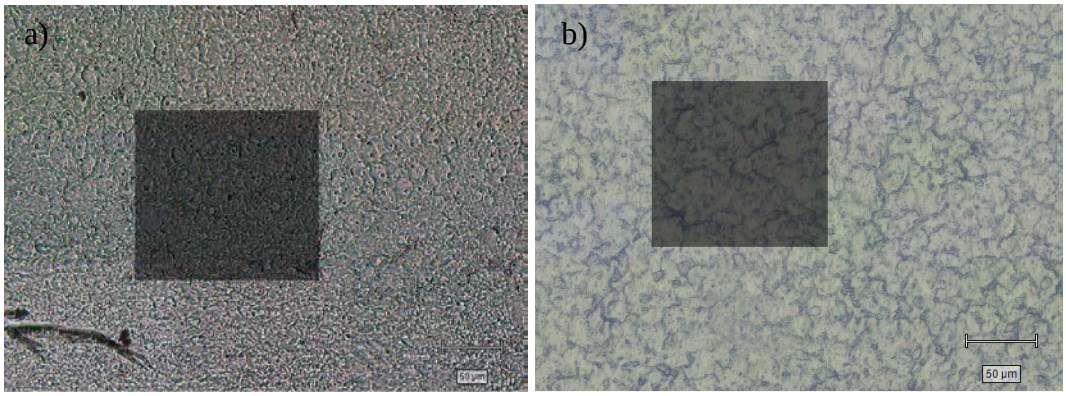

Figure 5.31 SERS map of 4 % pfa fixed, uninfected cerebral tissue in the absence of nanoparticles using a)514.5 nm and b) 632.8 nm excitation wavelengths. False colour images indicate pixels whose spectrum compares well with the reference spectrum (LUT: $0.8 \leq x \leq 0.9$ and $0.7 \leq x \leq 0.9$ respectively).

While no signal was observed visually from the tissue samples in the absence of nanoparticles, the contribution from the background (negative) areas was assessed under a variety of DCLS parameters. From Figure 5.32 it is noted that the data collected at both 514.5 and 632.8 nm excitation wavelengths exhibited an artefact at low wavenumbers. This was most likely a camera artefact which can be removed by reducing the charge-coupled device (CCD) area. Alternatively, the data set recorded at 514.5 and 632.8 nm excitation wavelengths can be truncated (500 – 2200 cm^{-1} and 1350 – 1670 cm^{-1} respectively).

a)

b)

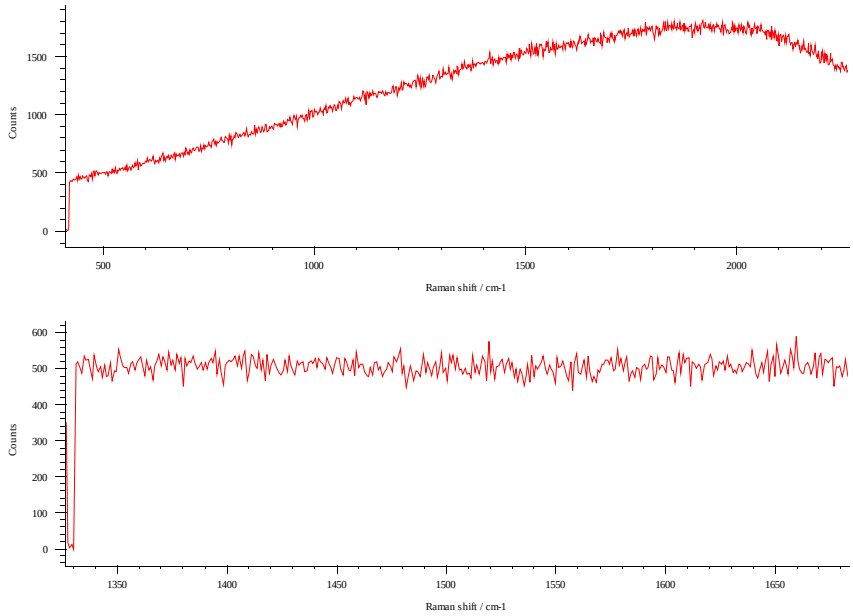

Figure 5.32 SERS spectra of 4 % pfa fixed, uninfected cerebral tissue in the absence of nanoparticles recorded using a)514.5 nm and b) 632.8 nm excitation wavelengths.

The recorded spectrum at each pixel was compared to that of the reference spectrum using DCLS across the data set (Figure 5.33). First order differentiation using the Savitsky-Golay method was selected to minimise background interference; polynomial regression (of a degree n) requires at least $n + 1$ data points. The polynomial order used for the differential was increased from 3° to 7°. The number of data points used to create the differential (scale) was also varied from $n + 1$ to $n + 4$.

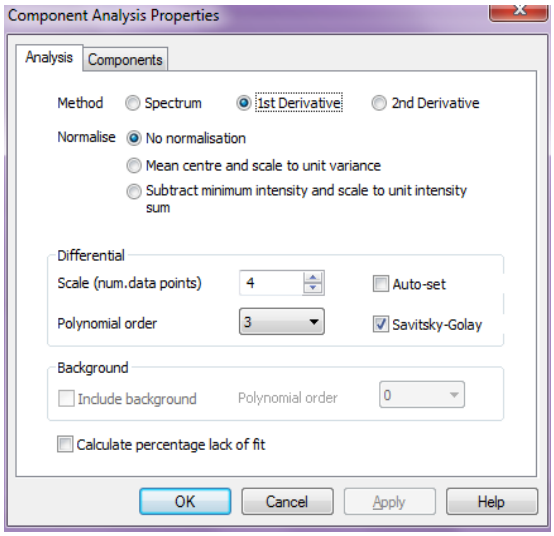

Figure 5.33 Illustration of the variables adjusted for optimisation of DCLS analysis.

The reference spectrum was normalised to a maximum value of 1. By selecting the option of no normalisation in the DCLS analysis, the result values will then be approximately the signal intensity - specifically the intensity of the largest peak in the reference signal. The results obtained from these "average component intensity" (ACI) calculations at varying DCLS parameters are outlined in Table 5.1.

Table 5.1 ACI values observed from uninfected 4 % pfa fixed cerebral tissue in the absence of nanoparticles recorded using excitation at a) 514.5 nm and b) 632.8 nm.

a)

Scale \ Polynomial order	3°	4°	5°	6°	7°
+1	-	7.78	-	8.3	8.05
+2	7.78	-	8.3	8.3	8.71
+3	-	6.65	-	6.75	8.71
+4	6.65	-	6.75	6.73	6.9

b)

Scale \ Polynomial order	3°	4°	5°	6°	7°
+1	-	2.07	1.96	2.1	2.08
+2	2.07	2.06	2.1	2.08	2.1
+3	2.06	1.98	2.08	2.04	2.08
+4	1.98	1.96	2.04	2.03	2.08

The ACI values reported across the range of DCLS parameters were similar, however the average result was higher using a 514.5 nm excitation wavelength. This was attributed to increased background fluorescence at shorter excitation wavelengths. Some of the combinations considered did not prove compatible with the script used to determine the average result value.

ACI calculations were also performed, under the aforementioned parameters, on SERS maps from ECM infected tissues incubated with etanercept functionalised nanoparticles. These positive results were divided by the respective negative values in Table 5.1; the positive: negative ratios of ACI values at the considered DCLS parameters are defined in Table 5.2.

Table 5.2 Positive: negative ACI comparison calculated by DCLS analysis at the indicated parameters. Results determined from SERS maps of cerebral tissue using excitation at a) 514.5 nm and b) 632.8 nm.

a)

Scale \ *Polynomial order*	**3°**	**4°**	**5°**	**6°**	**7°**
+1	-	15.47	-	13.99	14.65
+2	15.47	-	13.99	13.99	13.02
+3	-	20.01	-	19.12	13.02
+4	20.01	-	19.12	19.17	18.25

b)

Scale \ *Polynomial order*	**3°**	**4°**	**5°**	**6°**	**7°**
+1	-	18.30	19.40	18.02	18.21
+2	18.30	18.40	18.02	18.20	18.01
+3	18.40	19.20	18.20	18.60	18.19
+4	19.20	19.40	18.60	18.70	18.23

Higher positive:negative ACI ratios indicated DCLS parameters that provided greater discrimination between pixels corresponding to the bound SERS probes and those from biological tissue (where no probes were present). From Table 5.2, using a 514.5 nm excitation wavelength, DCLS comparison to the reference spectrum using the 1st derivative of a 3rd order polynomial with 7 data points or a 4th order polynomial with 7 data points offered the greatest discriminations. Using a 632.8 nm excitation wavelength, DCLS comparison to the reference spectrum using the 1st derivative of a 4th order polynomial with 8 data points presented the greatest discrimination.

These optimised parameters where employed in the analysis of ECM infected and uninfected cerebral tissue samples.

5.4.2 Average component intensity calculations of ECM infected and uninfected samples

Cerebral tissue samples obtained from ECM infected mice and uninfected mice were incubated with etanercept functionalised SERS active silver / silica nanoparticles using a 632.8 nm excitation wavelength. The maps were compared visually in Figure 5.34 using previously employed DCLS comparison and LUT values (LUT limits set at $0.7 \leq x \leq 0.9$).

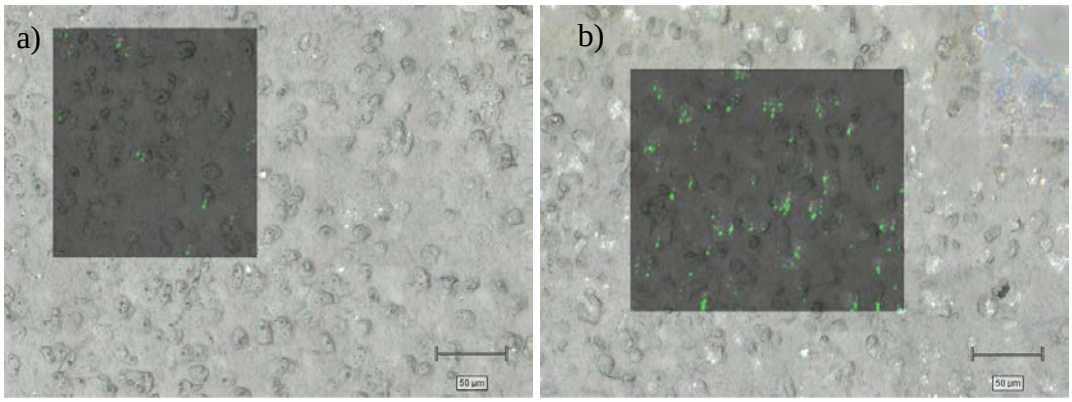

Figure 5.34 Visual comparison of SERS maps recorded, using a 632.8 nm excitation wavelength, from a) uninfected and b) ECM infected cerebral tissue samples incubated with etanercept functionalised silver /silica nanoparticles, fabricated from BT-SiO_2.

Visual discrimination between the infected and uninfected samples was possible. The average component intensity was calculated to semi-quantitatively compared the maps. The average ACI values (± one standard deviation) of 3 maps from one tissue sample are reported in Table 5.3.

Table 5.3 ACI comparison of SERS maps, recorded using a 632.8 nm excitation wavelength, from ECM infected and uninfected cerebral tissue samples incubated with etanercept functionalised silver / silica nanoparticle, fabricated from BT-SiO_2. ACI was calculated by DCLS comparison with reference spectrum using the 1st derivative of a 4th order polynomial with 8 data points.

Sample	ACI (a.u.)
Uninfected tissue	12.09 ± 6.37
ECM infected tissue	49.58 ± 15.45

Semi-quantitative comparison of the average ACI value provides discrimination between ECM infected and uninfected cerebral tissue samples, incubated with etanercept functionalised silver / silica nanoparticles, using a 632.8 nm excitation wavelength. These results indicated that increased levels of TNF were detected in mice suffering from cerebral malaria.

Similar investigations were performed using a shorter excitation wavelength. The visual comparison of infected and uninfected cerebral tissue samples using a 514.5 nm excitation wavelength is illustrated in Figure 5.35

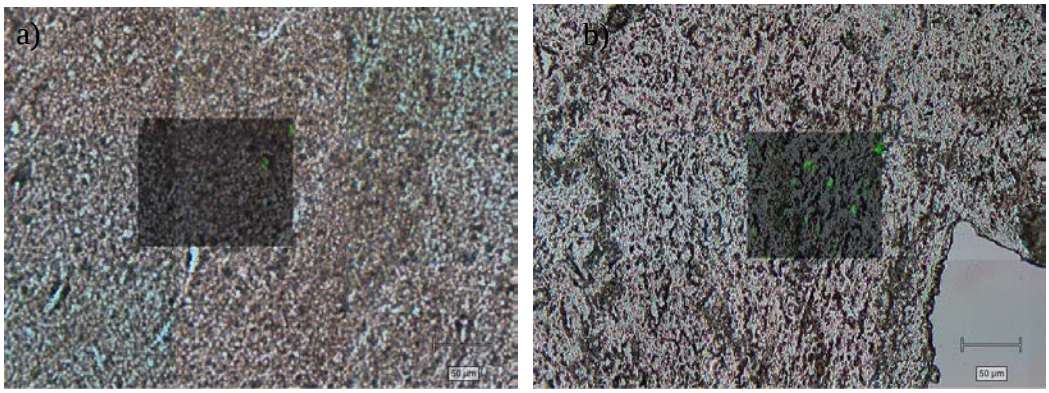

Figure 5.35 Visual comparison of SERS maps recorded, using a 514.5 nm excitation wavelength, from a) uninfected and b) ECM infected cerebral tissue samples incubated with etanercept functionalised silver /silica nanoparticles, fabricated from BT-SiO_2.

Visual discrimination between the infected and uninfected samples was possible using a 514.5 nm excitation wavelength. The average ACI value (± one standard deviation) of 3 maps from one tissue sample is reported in
Table 5.4.

Table 5.4 ACI comparison of SERS maps, recorded using a 514.5 nm excitation wavelength, from ECM infected and uninfected cerebral tissue samples incubated with etanercept functionalised silver / silica nanoparticle, fabricated from BT-SiO_2. ACI calculated by DCLS comparison with reference spectrum using the 1st derivative of a 4th order polynomial with 7 data points.

Sample	**ACI (a.u.)**
Uninfected tissue	4.93 ± 4.52
ECM infected tissue	12.27 ± 4.03

The distinction in ACI values of infected and uninfected cerebral tissue samples using a 514.5 nm excitation wavelength was diminished compared to the results at 632.8 nm. This was attributed to increased interference from background fluorescence commonly encountered at shorter excitation wavelengths.

Semi-quantitative analysis was also performed on splenic samples recovered from ECM infected and uninfected mice. In spite of the lack of specificity in the binding of etanercept functionalised nanoparticles to splenic samples, ACI values were calculated using 514.5 nm and 632.8 nm excitation wavelengths. These were compared to the cerebral samples previously discussed.

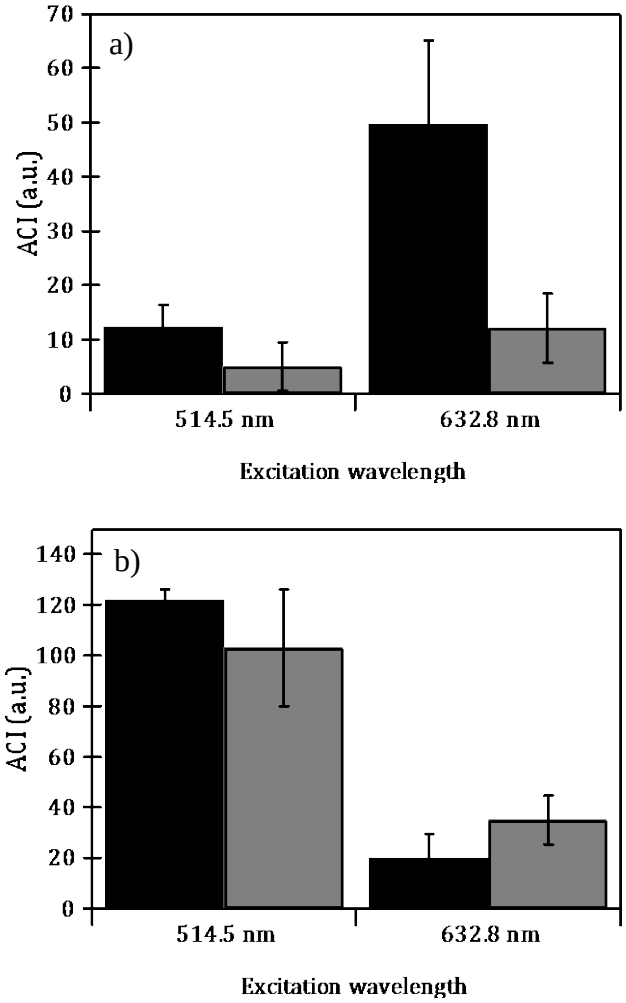

Figure 5.36 ACI comparison of ECM infected (black) and uninfected (grey) a) cerebral and b) splenic tissue samples. SERS maps recorded using 514.5 nm and 632.8 nm excitation wavelengths.

The average value calculated using a 514.5 nm excitation wavelength was significantly larger than the cerebral analogue, no discrimination could be made between ECM infected and uninfected samples. These results supported the proposition that ECM infection in mice, as suggested by increased levels of TNF, cannot be detected in splenic tissue samples.

5.5 Conclusions

Successful detection of SERS probes in a biological matrix using 632.8 and 514.5 nm excitation wavelengths was achieved. The particle size distribution of the silver / silica nanoparticles was determined to be positively correlated with the level of detected signal. A relative composition of ≥ 25 % dimeric species afforded sufficient SERS detectability from mapped cell populations.

Attenuation of the employed laser power was required to maintain the integrity of the spectral resolution, especially at shorter excitation wavelengths. 10 % laser output provided acceptable signal to noise ratios whilst maintaining the veracity of the SERS spectrum. Accumulation time was experimentally determined to exert less influence on the recorded spectra.

The signal observed post incubation with cell targeting silver / silica nanoparticles, functionalised with etanercept, appeared to be localised over the cells. This may have been due to a reduction in extinction of the nanoparticles and thus depletion of overall signal. A comparison with non-targeting protein functionalised nanoparticles would help establish the specificity of the recorded signal. Furthermore 3D mapping or 2D mapping through the z-plane of the samples would indicated if the signal from the functionalised nanoparticles is originating from within or on top of the cell i.e. whether the nanoparticles are membrane bound or internalised.

The presence of the silica shell did not afford stabilisation of the nanoparticles over a period of 1 month post incubation. Diminished response from mapped population of the same sample over time suggested oxidation of the silver nanoparticle core. Further work is necessary to determine if bio-functionalisation of the nanoparticles would preclude said oxidation.

Elevated serum levels of TNF are believed to be correlated to inflammatory signalling pathways, including ECM. Etanercept functionalised silver / silica nanoparticles were incubated with cerebral and splenic tissue samples from mice

infected with ECM. The SERS output, established by DCLS analysis with a reference spectrum, was compared to that of uninfected tissue samples.

Preventative measures were required to reduce non-specific binding of the functionalised nanoparticles; SecureSeal™ hybridisation chambers were employed to minimise evaporation effects. When the activated cerebral tissue sections were blocked using soluble etanercept, the etanercept functionalised nanoparticles exhibited reduced binding to the tissue surface. It was therefore proposed that the adhesion of etanercept functionalised nanoparticles to cerebral tissue sections is a result of TNF-etanercept binding.

Perfuse-fixing of cerebral tissue using pfa, in comparison to acetone, was shown to improve the morphological integrity of the tissue slices. Samples perfuse-fixed with pfa also exhibited increased SERS output, suggesting improved chemical stability.

SERS mapping of cerebral tissue samples was compared using 514.5 and 632.8 nm excitation wavelengths. Increased output was reported using a 514.5 nm excitation wavelength. The density of signal, not deemed to be a result of precipitation or non-specific binding, and was reduced at shorter incubation periods. This improved the localisation of signal on the mapped area.

Splenic tissue samples were also collected from mice infected with ECM. SERS signal was detected from samples incubated with etanercept functionalised nanoparticles using 514.5 and 632.8 nm excitation wavelengths. However, the specificity of signal, as determined *via* blocking with soluble etanercept, could not be established. Additionally, extended incubation periods improved the SERS output at 632.8 nm but had no significant effect at 514.5 nm. It was proposed that diagnosis of ECM in mice, as identified by increased levels of TNF, may not be possible using splenic tissue samples.

A method for semi-quantitative analysis of tissue samples was developed using DCLS analysis. A 1st order differential was introduced to reduce the contribution

from the tissue background. The resulting technique gave a positive value (proportional to intensity) from pixels where the reference spectrum was observed and effectively zero contribution from elsewhere in the mapped region. Dividing the summation of these values by the number of pixels provided an average value per pixel – the average component intensity (ACI).

Visual and semi-quantitative discrimination of ECM infected and uninfected tissue samples were achieved using a 632.8 nm excitation wavelength. This distinction was reduced using a 514.5 nm excitation wavelength, mostly likely due to the increased background fluorescence.

Semi-quantitative analysis was also performed on splenic tissue samples. No discrimination was observed between ECM infected and uninfected sections. This supported the proposition that ECM infection in mice, as suggested by increased levels of TNF, cannot be detected in splenic tissue samples.

5.6 Future work

The cerebral and splenic tissue samples analysed in chapter 5 where extracted from mice on day 6 of induced ECM infection. Due to the semi-quantitative results obtained, it may be possible to monitor the TNF expression as a function of time from infection. Retrieving tissue samples prior to and after day 6 may provide additional information on the secretion of TNF in inflammatory signalling pathways.

Additionally, due to narrow bands of spectral output observed in SERS mapping, more than one biomarker may be simultaneously targeted. BT-NH_2 and BT-SiO_2 have similar Raman cross section and produce spectrally distinct SERS read-outs. However, efforts to further increase the SERS intensities of silver / silica nanoparticles fabricated using the BT-NH_2 precursor would be required. Bio-functionalisation of BT-NH_2 based silver / silica particles with anti ICAM-1 could be used, in parallel with etanercept functionalised BT-SiO_2 analogues. The

simultaneous detection of these inflammatory biomarkers would improve the validity of this SERS based technique.

6 Conclusions

Four tri-functional molecules have been synthesised to stabilise a silver nanoparticle core, act as a Raman reporter and provide a suitable precursor for an integrated network of silica polymers via Stöber condensation. The use of a silane precursor was found to be unnecessary however use of a suitable site of growth for the silica greatly enhanced the reproducibility of both the synthesis and the SERS. This has resulted in the synthesis of reproducible SERS detectable silver / silica, core / shell nanoparticles which will find use in a wide range of applications where gold has previously been used, but offering the alternative optical properties of silver.

To render the fabricated particles suitable for bio-analysis, the SERS activity for use within a biologically relevant window was assessed. Protein molecules were tethered to the silica surface *via* covalent coupling silanes. This afforded greater stabilisation when compared to electrostatic association of the proteins to the nanoparticle surface. The presence of protein on the surface was confirmed by gel electrophoresis though further work is needed to evaluate the activity of the surface bound protein molecules.

Anti-TNF functionalised nanoparticles were incubated with tissue samples believed to over-express TNF. The SERS output from inflamed (positive) and uninflamed (negative) samples exhibited good discrimination visually. A semi-quantitative method for comparing the detectable SERS signal from each tissue samples was developed and further confirmed the discrimination between the samples.

These preliminary results suggest that bio-functionalised, SERS detectable, silver / silica nanoparticles are capable of imaging target molecules in a biologically meaningful environment. This offers an alternative optical reagent where gold / silica hybrids have commonly been employed.

7 Future work

The presence of a silica shell did not afford substantial stabilisation to silver nanoparticle cores. Preliminary TEM images indicated that the radius of silica shell was no more 5 nm. Increasing the thickness of the silica shell may improve the robustness of the core / shell particles. A kinetic study of reactions occurring at the nanoparticle core as a function of shell thickness could be performed.

The presence of protein on the nanoparticle surface was confirmed by gel electrophoresis, however further investigation into the activity of the surface bound protein is required. This may be achieved by circular dichroism or an immunoassay technique. Additionally, further characterisation of the average number of (biologically active) proteins molecules conjugated to the silica shell should be carried out.

The semi-quantitative analysis, enabled by ACI calculations, could be extended to assess the levels of pro-inflammatory cytokines secreted at various time intervals during infections. This would require cerebral tissue sections to be removed from mice at increasing time periods from point of induced infection. While discrimination between infected and uninfected splenic tissue samples was not possible on day 6 of ECM infection, differences may be observed earlier or later in the inflammation process.

The ability to detect more than 1 biomarker simultaneously using nanoparticles has the potential to increase the sensitivity of screening methods. The narrow bands of information rich spectral output from Raman spectroscopy highlight the multiplexing capabilities of this technique, making it ideal for multiple biomarker detection. BT-SiO_2 and BT-NH_2 precursors were used to synthesis silver / silica nanoparticles with SERS detectability in the red. The Raman cross sections of these precursor molecules are similar, and their SERS output spectrally distinct, making them ideal reporters for multiplex analysis. Dual imaging of TNF and the associated biomarker ICAM-1 would provide a greater indication of inflammation in tissues samples.[206]

A direct comparison between silica encapsulated gold and silver cores would be interesting. TNF may not be a suitable target for this investigation. Oxidation of the silver core would result in increased reactive oxygen species (ROS), activating oxygen sensitive signalling pathways that stimulate inflammation events. This would elicit the secretion of pro-inflammatory cytokines such as TNF. While it has been established that the silica shell is not impermeable, it is hoped that additional stability and protection is afforded by the tethered proteins. If not, false amplification of signal from inflamed tissue sections may be observed on incubation with silver / silica core / shell nanoparticles.

8 Experimental

8.1 Preparation of silver colloids

All glassware was soaked for a period of at least 2 hours in a 3:1 mixture of hydrochloric acid and nitric acid (*aqua regia*) and rinsed thoroughly with distilled water before being used to prepare silver colloids.

8.1.1 Preparation of borohydride reduced, citrate stabilised silver nanoparticles

Borohydride reduced, citrate stabilised silver nanoparticles (BRCS AgNP) of approximately 10 nm diameter were prepared using a previously described method.[64] Briefly, a 396 mL solution of sodium citrate (0.30 mM) and sodium borohydride (1 mM) was vigorously stirred on an ice bath for 30 minutes. Silver perchlorate monohydrate, $AgClO_4.H_2O$, (4 mL, 0.01 M) was rapidly added to the solution and stirring was continued for a further 30 minutes, to enhance the monodispersity of the resulting colloid.

8.1.2 Preparation of EDTA reduced silver nanoparticles

Ethylenediaminetetraacetic acid reduced silver nanoparticles (EDTA AgNP) of approximately 40 nm diameter where synthesised according to the previously published method by Fabrikanos *et al.*[25] Briefly, sodium hydroxide (10 mL, 0.40 M) was injected to a boiling solution of EDTA (1 L, 1.62×10^{-4} M). Silver nitrate (0.026M, 10 mL) was added to the boiling solution in 2.5 mL aliquots and the solution was heated for a further 15 minutes. Stirring was maintained throughout.

8.2 Silica encapsulation of silver nanoparticles

8.2.1 Silica encapsulation *via* Kobayashi method[164]

This method was based on a modification of the Stöber method.[164] 4 mL ethanol was added to BRCS AgNP (1 mL, 1.8×10^{-5} M) followed by tetraethylorthosilicate, TEOS, (8.9 µL) and trimethylamine, TMA, (1 µL, 0.6 M). The reaction mixture was stirred vigorously for 15 minutes and left to stand overnight. The samples were centrifuged at 7000 rpm for 20mins and resuspended in 10 mL dH_2O.

8.2.2 Silica encapsulation *via* Ung method[64]

Silica encapsulated silver nanoparticles were prepared according to the method outlined by Ung *et al.*[64] A solution of BRCS AgNP (5 mL, 7.7×10^{-5} M) was adjusted to pH 5. Aminopropyltrimethoxysilane (APTMS, 5 mL, 2×10^{-6} M) was added and stirred for 15 minutes to activate the colloid, rendering the surface vitreophillic. The colloid was adjusted to approx. pH 11.5 using the mild hindered amine base 2,6 lutidine before the addition of active silica (5 mL, 0.0154%). The solution was agitated overnight. Ice-cold ethanol was slowly added to the solution until a 4:1 v/v ratio of ethanol: water was achieved. Samples were centrifuged at 7000 rpm for 20 minutes and resuspended in dH_2O.

8.2.3 Silica encapsulation *via* modified Stöber method

The colloid surface was rendered vitreophillic by the addition of APTMS (135 µL, 0.5 mM) to 1 mL aliquots of AgNP and agitation for 15 min. The nanoparticle conjugates were washed (centrifugation at 7000 rpm, 20 min) and resuspended in 1 mL dH_2O. Ethanol was added to 1:4 v/v dH_2O:ethanol ratio to assist the growth of silica via Stöber condensation. TEOS (22.25 µL) and TMA (125 µL) were added, the solution was stirred for 15 min. and allowed to stand for approximately 12 hr.

Samples were centrifuged through 50% glycerol to remove excess silica particles and washed in dH_2O before being resuspended in 1 mL dH_2O.

8.3 Silica encapsulation of SERS "active" silver nanoparticles

8.3.1 Synthesis of BT-COOH (Figure 3.10)

3,5-Dimethoxyanaline (2.000 g, 1 equiv, 13.06 mmol) and acrylic acid (0.941 g, 1 equiv, 13.06 mmol) were dissolved in toluene (60 mL). The reaction mixture was refluxed at 110 °C for 48 hours under an inert atmosphere. Compound A was purified by column chromatography.

5-aminobenzotriazole (0.327 g, 1.1 equiv, 1.9 mmol) was dissolved in hydrochloric acid (5 mL, 50% (v/v)) and diazotized by the drop wise addition of sodium nitrite (0.184 g, 1.2 equiv, in 1 mL H_2O) at 0 °C with stirring over 30 minutes. Compound A (0.500 g, 1 equiv, 1.7 mmol) was dissolved in sodium acetate buffer (1.0 M, 5 mL, pH 6.0). This was added to the diazotized solution drop wise and stirred overnight. Solid BT-COOH was purified by gravimetric filtration and washed with water.

Yield = 0.534 g, 65.53 %,

δ_H[400 MHz, $(CD_3)_2SO$]2.73 (2 H, t, *J* 6.0, -NHCH$_2$C*H*$_2$), 3.50 (2 H, t, *J* 6.0, -NHC*H*$_2$), 3.81 (6 H, s, -OC*H*$_3$), 5.45 (2H, s, H-2,6), 7.25 (1 H, d, *J* 8.0, H-5'), 7.33 (1 H, s, H-2'), 7.54 (1 H, d, *J* 8.0 H-6'); FAB MS : *m/z* 371.33 [(M^+ + H. $C_{17}H_{18}N_6O_4$ requires 371.14)]

8.3.2 Synthesis of BT-SiO_2 (Figure 3.10)

BT-COOH (0.050 g, 1 equiv, 0.135 mmol) and 1,1-carbonyldiimidazole (0.034 g, 1.558 equiv, 0.210 mmol) were dissolved in anhydrous dimethylformamide (DMF) (2 mL) and heated for 5 minutes at 40 °C under an inert atmosphere. When the solution reached room temperature, APTMS (0.024 mL, 1 equiv, 0.135 mmol) was added and stirred for 2 hours.

Attempts to purify $BTSiO_2$ by column chromatography were unsuccessful and so the crude product was used as a precursor for silica encapsulation via Stöber condensation.

FAB MS: *m/z* 490.27 [(M^+ + H. $C_{20}H_{27}N_7O_6Si$ requires 490.56]

8.3.3 Silica encapsulation using rationally designed precursors

The dye precursors illustrated in Figure 3.10 were added to EDTA AgNP (1 mL, 100 pM) to an optimised final concentration (section 3.3.2) and agitated for 30 min. prior to centrifugation (7000 rpm, 20 min.) and resuspension (500 µL dH_2O). The nanoparticle – dye conjugates were made up to 1mL with the slow addition of ice-cold ethanol. Silica growth was initiated by the addition of triethylamine (10 µL, 1 % v/v in ethanol) and the sequential addition of TEOS (10 µL, 4 % v/v in ethanol) and over a three hour period until the final concentration of TEOS reached 5.4 mM.

8.4 Bio-functionalisation of silica encapsulated nanoparticles

8.4.1 Conjugation of Etanercept to silica surface

Based on the original NP concentration, the core / shell nanoparticles were functionalised with approx. 1000 fold molar excess of etanercept. This was achieved by reacting 10 equivalents of triethoxysilylpropyl isocyanate (10 mg/mL, dimethyl sulfoxide, DMSO) with 1 equivalents of etanercept in $NaHCO_3$ buffer (0.1 M at pH

9) at 4°C overnight. The "silanised" molecules were added to unwashed core / shell nanoparticles and agitated prior to centrifugation (7000 rpm, 20 min.) and resuspension (500 μL dH_2O).

8.4.2 Gel Electrophoresis of bio-functionalised nanoparticles

Tris Borate EDTA buffer (TBE) was purchased from Sigma Aldrich at 10x concentrate. Agarose was dissolved in 1x TBE to from a 1% w/v solution. The gel was cooled to approx. 60 °C, poured and allowed to set. 1x TBE buffer was used to cover the gel. 10 μL of sample was mixed with 5 μL loading buffer (6x) and 5 μL of this was added to the wells. 120 V was applied and the gel was run for approx. 45 min.

8.5 Cell Studies

8.5.1 Cell preparation

HeLa cells were routinely grown in eagle minimum essential (EMEM) with heat-inactivated foetal bovine serum (10 %), L-glutamine (200 mM, 1 % v/v), penicillin (1 % v/v, 10.000 IU mL^{-1}) and streptomycin (10 mg mL^{-1}) at 37 ^{o}C in a humidified 5 % CO_2 atmosphere. After reaching confluence, cells were harvested and seeded at $2x10^5$ cells per well in a 24-well sterile tissue culture plate to which 13 mm round glass cover-slips had been previously applied. The cells were incubated overnight at 37 $^{\circ}C$, 5 % CO_2 in order to allow the cells to adhere to the cover-slips. Etanercept functionalised silver / silica, core / shell nanoparticles were added to the cells and incubated for 1 hr. Following incubation and in order to remove any extracellular matrix, the cells were washed four times with phosphate buffered saline (PBS) before fixation with paraformaldehyde (4 %). After 15 min. the cover-slips were washed consecutively with PBS and dH_2O. After fixation the cover-slips were air dried for approx. 2 hr. before being mounted on labelled slides using distyrene-plasticiser-xylene (DPX) mountant.

8.5.2 Analysis of cell slides

Cell slides were mapped according to the standard protocol described in M8 – StreamLine™ imaging technical note using a Renishaw inVia Raman Microscope / Leica DMI 5000 M spectrometer (632.8 nm line focus, 100x LWD 0.75 N.A., centred at 1500 cm^{-1}, 100 % laser power – 13 mW, acquisition time, 5 sec.). Component Direct Classical Least Squares (DCLS) Raman map images were derived according to the standard protocol described in M10 – multivariate data analysis technical note. Component DCLS is typically used when reference spectra are available for all the components in the multiplex. The DCLS method involves fitting the unknown data (collected during mapping) to a linear combination of the specified component spectra (standard solution spectra). Each reference spectrum is used to create separate images with look up table (LUT) values between 0 and 1. Values close to 1 indicate areas within the image most similar in shape to that of the reference spectrum.

8.6 Tissue Studies

8.6.1 Tissue preparation

Tissue preparation was provided by Tovah Shaw, University of Glasgow. Tissue samples were collected from the brain and spleen of uninfected mice and mice infected with experimental cerebral malaria (ECM). Immunohistochemistry was performed on 15 μm tissue sections. The tissues were perfuse-fixed with acetone, cryopreserved in 30% sucrose, embedded in Tissue-Tek® OCT™ (Miles Inc. Diagnostic Division, Elkhart, USA) and frozen in liquid Nitrogen and cryopreserved at −70 °C. 4 % paraformaldehyde (pfa) was also considered as a fixation agent. 15 μm tissue sections were cut using a cryostat, mounted onto glass slides and washed with bovine serum albumin (3 % in PBS).

8.6.2 Antigen Retrieval

Tissue sections were incubated for twenty minutes at 96°C in a water bath in 100ml Tris EDTA buffer (10mM EDTA, 0.25mM Tris) pH 9. All antigen retrieval steps are followed by a twenty minute cool down period. Silver / silica, core / shell nanoparticles were incubated under a number of conditions (discussed in chapter 5) and the slides washed in buffer (0.1 M phosphate buffer, 0.1 % bovine serum albumin, 0.05 % sodium azide, 0.05 % Tween) prior to analysis.

8.6.3 Analysis of tissue samples

Tissue samples were analysed using the cell analysis method outlined in 8.5.2.

8.7 Instrumentation

8.7.1 Extinction spectroscopy

Colloidal suspensions were characterised using UV-visible spectroscopy. Aqueous suspensions of silver nanoparticles with an approx. diameters 20 nm and 100 nm have surface plasmonic peaks at approximately 370 nm and 600 nm respectively.[207] Increasing λ_{max} and peak broadening are two indicators of increased polydispersity (broad distribution of particle size) within the sample.

Extinction readings were taken within the range of 300 - 800 nm using a Cary Eclipse extinction spectrophotometer. Silver nanoparticle and their precursor-conjugate spectra (chapter 3) were baseline corrected using dH_2O as a blank. Bio-functionalised silica nanoparticle SERS spectra (chapters 4-5) were baseline corrected using appropriate buffer (25 mM HEPES buffer pH 7.5, 20 mM KCl or 10 mM phosphate buffer pH 7.5) as a blank.

8.7.2 Raman analysis of solution samples

514.5 nm: SERS was recorded using a *Renishaw Probe* spectrometer with an Argon ion laser (514.5 nm) equipped with a 20x / 0.4 long working objective. The inelastically scattered light was collected for an accumulation time of 1 sec and analysed using a grating of 1800 line/ mm centred at 1600 cm^{-1}. Unfocused laser power at sample was approximately 5 mW.

632.8 nm: A Leica DM/ LM microscope equipped with an Olympus 20x / 0.4 long-working-distance objective was used to collect 180^{o} backscattered light from a cuvette using the 632.8 nm line of a helium-neon laser coupled to a *Renishaw Radarscope System 2000*. The inelastically scattered light was collected for an accumulation time of 1 sec and analysed using a 1200 lines/ mm grating centred at 1600 cm^{-1}. Unfocused laser power at sample was approximately 6 mW.

784.6 nm: SERS was recorded using a *Renishaw InVia* Raman inverted microscope system equipped with a 20x /0.4 long working distance objective using a 784.6 nm diode laser and 1 sec. accumulation. A grating of 1200 line/ mm was used with a *RenCam* CCD optimized for near infrared wavelengths. Unfocused laser power at sample was approximately 150 mW.

8.7.3 Dynamic Light Scattering

Nanoparticle diameter and particle size distribution data were determined *via* dynamic light scattering using a Malvern Zetasizer Nano ZS. 1 mL samples were analysed using standard disposable cuvettes.

8.7.4 Zeta Potential

Laser Doppler Micro-electrophoresis is used to measure zeta potential of colloids. 1 mL samples were analysed using standard disposable cuvettes on a Malvern Zetasizer NanoZS.

8.7.5 Scanning Electron Microscopy

Scanning electron microscopy (SEM) was carried out on silica encapsulated nanoparticles deposited onto poly(diallyldimethylammonium) (PDDA) coated silicon wafers. Following cleaning with methanol and oxygen plasma (Diener electronic femto oxygen plasma cleaner, 72 cm^3 / min. gas flow), silicon wafers were coated with a 10 mg/mL PDDA solution in 1 nM NaCl for 30 minutes. The coated wafers were then rinsed with deionised water and dried with N_2. 10 mL of colloidal suspensions were deposited on individual wafers and allowed to sit for 25 minutes, after which the samples were removed. The sample coated wafers were then washed with deionised water and dried using N_2. SEM imaging was carried out using a Sirion 200 Schottky field-emission electron microscope operating at an accelerating voltage of 5 kV.

9 References

1. E. Smith and G. Dent, *Modern Raman spectroscopy : a practical approach*, J. Wiley, Hoboken, NJ, 2005.
2. J. R. Ferraro and K. Nakamoto, *Introductory Raman spectroscopy*, Academic Press, Boston, 1994.
3. P. Pagsberg, R. Wilbrandt, K. B. Hansen and K. V. Weisberg, *Chem. Phys. Lett.*, 1976, **39**, 538-541.
4. J.-X. Cheng and X. S. Xie, *The Journal of Physical Chemistry B*, 2003, **108**, 827-840.
5. W. Kiefer and H. J. Bernstein, *Appl. Spectrosc.*, 1971, **25**, 500-501.
6. M. J. Tauber, R. A. Mathies, X. Chen and S. E. Bradforth, *Rev. Sci. Instrum.*, 2003, **74**, 4958-4960.
7. T. G. Spiro, *Accounts Chem. Res.*, 1974, **7**, 339-344.
8. B. Kustner, C. Schmuck, P. Wich, C. Jehn, S. K. Srivastava and S. Schlucker, *Phys. Chem. Chem. Phys.*, 2007, **9**, 4598-4603.
9. M. Fleischmann, P. J. Hendra and A. J. McQuillan, *Chem. Phys. Lett.*, 1974, **26**, 163-166.
10. M. G. Albrecht and J. A. Creighton, *J. Am. Chem. Soc.*, 1977, **99**, 5215-5217.
11. D. L. Jeanmaire and R. P. Van Duyne, *J. Electroanal. Chem.*, 1977, **84**, 1-20.
12. M. Moskovits, *J. Chem. Phys.*, 1978, **69**, 4159-4161.
13. K. Faulds, R. P. Barbagallo, J. T. Keer, W. E. Smith and D. Graham, *Analyst*, 2004, **129**, 567-568.
14. G. Sabatte, R. Keir, M. Lawlor, M. Black, D. Graham and W. E. Smith, *Anal. Chem.*, 2008, **80**, 2351-2356.
15. M. Quinten, *Z. Phys. D: At. Mol. Clusters*, 1995, **35**, 217-224.
16. A. Moores and F. Goettmann, *New J. Chem.*, 2006, **30**, 1121-1132.
17. L. M. Liz-Marzán, *Mater. Today*, 2004, **7**, 26-31.
18. M. Faraday, *Phil. Trans. R. Soc. Lond.*, 1857, **147**, 145-181.
19. J. Turkevich, P. C. Stevenson and J. Hillier, *Discuss. Faraday Soc.*, 1951, **11**, 55-75.
20. B. V. Enustun and J. Turkevich, *J. Am. Chem. Soc.*, 1963, **85**, 3317-3328.
21. G. Frens, *Nat. Phys. Sci.*, 1973, **241**, 20-22.
22. M. Brust, M. Walker, D. Bethell, D. J. Schiffrin and R. Whyman, *J. Chem. Soc. Chem. Comm*, 1994, 801-802.
23. P. C. Lee and D. Meisel, *J. Phys. Chem.*, 1982, **86**, 3391-3395.
24. C. H. Munro, W. E. Smith, M. Garner, J. Clarkson and P. C. White, *Langmuir*, 1995, **11**, 3712-3720.
25. V. Fabrikanos, S. Athanassiou and K. Leiser, *Z. Naturforsch. B: Chem. Sci.*, 1963, **18**, 612-617.
26. G. Mie, *Ann. Phys. (Leipzig)* 1908, **25**, 377.
27. R. Desai, V. Mankad, S. K. Gupta and P. K. Jha, *Nanosci. Nanotechnol. Lett.*, 2012, **4**, 30-34.
28. M.-C. Daniel and D. Astruc, *Chem. Rev.*, 2003, **104**, 293-346.
29. S. E. J. Bell and N. M. S. Sirimuthu, *J. Am. Chem. Soc.*, 2006, **128**, 15580-15581.
30. L. H. Eng, V. Schlegel, D. Wang, H. Y. Neujahr, M. T. Stankovich and T. Cotton, *Langmuir*, 1996, **12**, 3055-3059.
31. J. Kneipp, H. Kneipp, M. McLaughlin, D. Brown and K. Kneipp, *Nano Lett.*, 2006, **6**, 2225-2231.
32. K. Faulds, W. E. Smith, D. Graham and R. J. Lacey, *Analyst*, 2002, **127**,

282-286.
33. Y. C. Cao, R. Jin, J.-M. Nam, C. S. Thaxton and C. A. Mirkin, *J. Am. Chem. Soc.*, 2003, **125**, 14676-14677.
34. S. P. Xu, X. H. Ji, W. Q. Xu, X. L. Li, L. Y. Wang, Y. B. Bai, B. Zhao and Y. Ozaki, *Analyst*, 2004, **129**, 63-68.
35. G. Wang, H.-Y. Park, R. J. Lipert and M. D. Porter, *Anal. Chem.*, 2009, **81**, 9643-9650.
36. D. Graham, G. McAnally, J. C. Jones and W. Ewen Smith, *Chem. Commun.*, 1998, 1187-1188.
37. D. Graham, R. Brown and W. Ewen Smith, *Chem. Commun.*, 2001, 1002-1003.
38. G. McAnally, C. McLaughlin, R. Brown, D. C. Robson, K. Faulds, D. R. Tackley, W. E. Smith and D. Graham, *Analyst*, 2002, **127**, 838-841.
39. A. Enright, L. Fruk, A. Grondin, C. J. McHugh, W. E. Smith and D. Graham, *Analyst*, 2004, **129**, 975-978.
40. C. J. McHugh, F. T. Docherty, D. Graham and W. E. Smith, *Analyst*, 2004, **129**, 69-72.
41. D. Graham, K. Faulds and W. E. Smith, *Chem. Commun.*, 2006, 4363-4371.
42. R. J. Stokes, A. Ingram, J. Gallagher, D. R. Armstrong, W. E. Smith and D. Graham, *Chem. Commun.*, 2008, 567-569.
43. R. J. Stokes, A. Macaskill, P. J. Lundahl, W. E. Smith, K. Faulds and D. Graham, *Small*, 2007, **3**, 1593-1601.
44. K. Kneipp, R. R. Dasari and Y. Wang, *Appl. Spectrosc.*, 1994, **48**, 951-955.
45. B. Küstner, M. Gellner, M. Schütz, F. Schöppler, A. Marx, P. Ströbel, P. Adam, C. Schmuck and S. Schlücker, *Angew. Chem. Int. Ed.*, 2009, **48**, 1950-1953.
46. M. A. Palladino, F. R. Bahjat, E. A. Theodorakis and L. L. Moldawer, *Nat Rev Drug Discov*, 2003, **2**, 736-746.
47. P. J. Anderson, *Semin. Arthritis Rheu.*, 2005, **34**, 19-22.
48. H. Xu, J. Aizpurua, M. Käll and P. Apell, *Phys. Rev. E*, 2000, **62**, 4318.
49. H. Xu, E. J. Bjerneld, M. Käll and L. Börjesson, *Phys. Rev. Lett.*, 1999, **83**, 4357-4360.
50. J. C. Cook, C. M. P. Cuypers, B. J. Kip, R. J. Meier and E. Koglin, *J. Raman Spectrosc.*, 1993, **24**, 609-619.
51. D. Graham, W. E. Smith, A. M. T. Linacre, C. H. Munro, N. D. Watson and P. C. White, *Anal. Chem.*, 1997, **69**, 4703-4707.
52. D. G. Thompson, K. Faulds, W. E. Smith and D. Graham, *The Journal of Physical Chemistry C*, 2009, **114**, 7384-7389.
53. A. F. Robson, T. R. Hupp, F. Lickiss, K. L. Ball, K. Faulds and D. Graham, *Proc. Natl. Acad. Sci. U. S. A.*, 2012, **109**, 8073-8078.
54. C. L. Zavaleta, B. R. Smith, I. Walton, W. Doering, G. Davis, B. Shojaei, M. J. Natan and S. S. Gambhir, *Proc. Natl. Acad. Sci. U. S. A.*, 2009, **106**, 13511-13516.
55. X. H. Gao, Y. Y. Cui, R. M. Levenson, L. W. K. Chung and S. M. Nie, *Nat. Biotechnol.*, 2004, **22**, 969-976.
56. X. M. Qian, X. H. Peng, D. O. Ansari, Q. Yin-Goen, G. Z. Chen, D. M. Shin, L. Yang, A. N. Young, M. D. Wang and S. M. Nie, *Nat. Biotechnol.*, 2008, **26**, 83-90.
57. J. Lahiri, L. Isaacs, J. Tien and G. M. Whitesides, *Anal. Chem.*, 1999, **71**, 777-790.
58. K. L. Prime and G. M. Whitesides, *J. Am. Chem. Soc.*, 1993, **115**, 10714-10721.
59. M. Zheng, Z. G. Li and X. Y. Huang, *Langmuir*, 2004, **20**, 4226-4235.
60. X. D. Zhang, D. Wu, X. Shen, P. X. Liu, N. Yang, B. Zhao, H. Zhang, Y.

M. Sun, L. A. Zhang and F. Y. Fan, *Int J Nanomedicine*, 2011, **6**, 2071-2081.
61. W. D. James, L. R. Hirsch, J. L. West, P. D. O'Neal and J. D. Payne, *J. Radioanal. Nucl. Chem.*, 2007, **271**, 455-459.
62. H. Otsuka, Y. Nagasaki and K. Kataoka, *Adv. Drug Deliv. Rev.*, 2003, **55**, 403-419.
63. L. Maus, J. P. Spatz and R. Fiammengo, *Langmuir*, 2009, **25**, 7910-7917.
64. T. Ung, L. M. Liz-Marzan and P. Mulvaney, *Langmuir*, 1998, **14**, 3740-3748.
65. P. D. Lickiss, in *Advances in Inorganic Chemistry*, ed. A. G. Sykes, Academic Press, 1995, vol. Volume 42, pp. 147-262.
66. W. Stöber, A. Fink and E. Bohn, *J. Colloid Interface Sci.*, 1968, **26**, 62-69.
67. C. J. Brinker, *J. Non-Cryst. Solids*, 1988, **100**, 31-50.
68. S. P. Mulvaney, M. D. Musick, C. D. Keating and M. J. Natan, *Langmuir*, 2003, **19**, 4784-4790.
69. L. M. LizMarzan, M. Giersig and P. Mulvaney, *Langmuir*, 1996, **12**, 4329-4335.
70. C. Fernandez-Lopez, C. Mateo-Mateo, R. A. Alvarez-Puebla, J. Perez-Juste, I. Pastoriza-Santos and L. M. Liz-Marzan, *Langmuir*, 2009.
71. S. Shibata, K. Aoki, T. Yano and M. Yamane, *J. Sol-Gel Sci. Techn.*, 1998, **11**, 279-287.
72. S. G. Kim, N. Hagura, F. Iskandar and K. Okuyama, *Adv, Powder Technol.*, 2009, **20**, 94-100.
73. Y. Han, J. Jiang, S. S. Lee and J. Y. Ying, *Langmuir*, 2008, **24**, 5842-5848.
74. W. E. Doering and S. M. Nie, *Anal. Chem.*, 2003, **75**, 6171-6176.
75. J. L. Gong, J. H. Jiang, H. F. Yang, G. L. Shen, R. Q. Yu and Y. Ozaki, *Anal. Chim. Acta*, 2006, **564**, 151-157.
76. J. F. Bringley, T. L. Penner, R. Z. Wang, J. F. Harder, W. J. Harrison and L. Buonemani, *J. Colloid Interface Sci.*, 2008, **320**, 132-139.
77. L. O. Brown and S. K. Doorn, *Langmuir*, 2008, **24**, 2277-2280.
78. L. O. Brown and S. K. Doorn, *Langmuir*, 2008, **24**, 2178-2185.
79. M. E. Aubin-Tam and K. Hamad-Schifferli, *Biomed. Mater.*, 2008, **3**, 034001.
80. N. Michael Green, in *Methods in Enzymology*, eds. W. Meir and A. B. Edward, Academic Press, 1990, vol. Volume 184, pp. 51-67.
81. N. Frascione, V. Pinto and B. Daniel, *Anal. Bioanal. Chem.*, 2012, **404**, 23-28.
82. J. M. Prober, G. L. Trainor, R. J. Dam, F. W. Hobbs, C. W. Robertson, R. J. Zagursky, A. J. Cocuzza, M. A. Jensen and K. Baumeister, *Science (New York, N.Y.)*, 1987, **238**, 336-341.
83. H. Kobayashi, M. Ogawa, R. Alford, P. L. Choyke and Y. Urano, *Chem. Rev.*, 2009, **110**, 2620-2640.
84. X. Michalet, A. N. Kapanidis, T. Laurence, F. Pinaud, S. Doose, M. Pflughoefft and S. Weiss, *Annu. Rev. Biophys. Biomolec. Struct.*, 2003, **32**, 161-182.
85. J. R. Lakowicz, *Principles of fluorescence spectroscopy*, Springer, New York, 2006.
86. A. Müller-Taubenberger, M. J. Vos, A. Böttger, M. Lasi, F. P. L. Lai, M. Fischer and K. Rottner, *Eur. J. Cell Biol.*, 2006, **85**, 1119-1129.
87. R. M. Hoffman, *Acta Histochem.*, 2004, **106**, 77-87.
88. Y. Yan and G. Marriott, *Curr. Opin. Chem. Biol.*, 2003, **7**, 635-640.
89. A. Miyawaki, *Curr. Opin. Neurobiol.*, 2003, **13**, 591-596.
90. A. M. Cedergren, S. D. Miklasz and E. W. Voss, *Mol. Immunol.*, **33**, 711-723.
91. H. J. Zambarakji, D. J. Keegan, T. M. Holmes, A. S. Halfyard, M. P.

Villegas-Perez, D. G. Charteris, F. W. Fitzke, J. Greenwood and R. D. Lund, *Exp. Eye Res.*, 2006, **82**, 164-171.
92. P. Alivisatos, *Nat. Biotechnol.*, 2004, **22**, 47-52.
93. A. Hoshino, K.-i. Hanaki, K. Suzuki and K. Yamamoto, *Biochem. Bioph. Res. Co,*, 2004, **314**, 46-53.
94. M. Bruchez, Jr., M. Moronne, P. Gin, S. Weiss and A. P. Alivisatos, *Science*, 1998, **281**, 2013-2016.
95. X. Wu, H. Liu, J. Liu, K. N. Haley, J. A. Treadway, J. P. Larson, N. Ge, F. Peale and M. P. Bruchez, *Nat. Biotechnol.*, 2003, **21**, 41-46.
96. X. Michalet, F. F. Pinaud, L. A. Bentolila, J. M. Tsay, S. Doose, J. J. Li, G. Sundaresan, A. M. Wu, S. S. Gambhir and S. Weiss, *Science*, 2005, **307**, 538-544.
97. M. Vibin, R. Vinayakan, A. John, C. S. Rejiya, V. Raji and A. Abraham, *J. Colloid Interface Sci.*, 2011, **357**, 366-371.
98. W. C. W. Chan and S. M. Nie, *Science*, 1998, **281**, 2016-2018.
99. W. Cai and X. Chen, *Nat Protoc*, 2008, **3**, 89-96.
100. E. R. Goldman, G. P. Anderson, P. T. Tran, H. Mattoussi, P. T. Charles and J. M. Mauro, *Anal. Chem.*, 2002, **74**, 841-847.
101. H. Mattoussi, J. M. Mauro, E. R. Goldman, G. P. Anderson, V. C. Sundar, F. V. Mikulec and M. G. Bawendi, *J. Am. Chem. Soc.*, 2000, **122**, 12142-12150.
102. L. Liotta and E. Petricoin, *Nat Rev Genet*, 2000, **1**, 48-56.
103. X. Gao and S. Nie, *Trends Biotechnol*, 2003, **21**, 371-373.
104. X. Gao, L. Yang, J. A. Petros, F. F. Marshall, J. W. Simons and S. Nie, *Curr. Opin. Biotech.*, 2005, **16**, 63-72.
105. B. Dubertret, P. Skourides, D. J. Norris, V. Noireaux, A. H. Brivanlou and A. Libchaber, *Science*, 2002, **298**, 1759-1762.
106. M. Dahan, T. Laurence, F. Pinaud, D. S. Chemla, A. P. Alivisatos, M. Sauer and S. Weiss, *Opt. Lett.*, 2001, **26**, 825-827.
107. S. Pathak, S.-K. Choi, N. Arnheim and M. E. Thompson, *J. Am. Chem. Soc.*, 2001, **123**, 4103-4104.
108. R. Weissleder, *Nat. Biotechnol.*, 2001, **19**, 316-317.
109. S. Kim, Y. T. Lim, E. G. Soltesz, A. M. De Grand, J. Lee, A. Nakayama, J. A. Parker, T. Mihaljevic, R. G. Laurence, D. M. Dor, L. H. Cohn, M. G. Bawendi and J. V. Frangioni, *Nat. Biotechnol.*, 2004, **22**, 93-97.
110. A. M. Smith, H. Duan, A. M. Mohs and S. Nie, *Adv. Drug Deliv. Rev.*, 2008, **60**, 1226-1240.
111. C. H. L. R. Alfano, W.L. Sha, H.R. Zhu, A.L. Akins, J. Cleary, R. Prundente and E. Cellmer, *Lasers Life Sci.*, 1991, **4**, 23-28.
112. P. Matousek and N. Stone, *Analyst*, 2009, **134**, 1058-1066.
113. P. Matousek, I. P. Clark, E. R. C. Draper, M. D. Morris, A. E. Goodship, N. Everall, M. Towrie, W. F. Finney and A. W. Parker, *Appl. Spectrosc.*, 2005, **59**, 393-400.
114. C. Krafft, B. Dietzek and J. Popp, *Analyst*, 2009, **134**, 1046-1057.
115. B. R. Wood, A. Hermelink, P. Lasch, K. R. Bambery, G. T. Webster, M. A. Khiavi, B. M. Cooke, S. Deed, D. Naumann and D. McNaughton, *Analyst*, 2009, **134**, 1119-1125.
116. G. T. Webster, L. Tilley, S. Deed, D. McNaughton and B. R. Wood, *FEBS letters*, 2008, **582**, 1087-1092.
117. K. Kneipp, Y. Wang, H. Kneipp, L. T. Perelman, I. Itzkan, R. Dasari and M. S. Feld, *Phys. Rev. Lett.*, 1997, **78**, 1667-1670.
118. S. M. Nie and S. R. Emery, *Science*, 1997, **275**, 1102-1106.
119. K. Kneipp, H. Kneipp and J. Kneipp, *Accounts Chem. Res.*, 2006, **39**, 443-450.
120. S. Schlucker, *Chemphyschem*, 2009, **10**, 1344-1354.
121. J. Kneipp, H. Kneipp, B. Wittig and K. Kneipp, *Nano Lett.*, 2007, **7**, 2819-

2823.
122. J. Kneipp, H. Kneipp, B. Wittig and K. Kneipp, *The Journal of Physical Chemistry C*, 2010, **114**, 7421-7426.
123. N. L. Rosi and C. A. Mirkin, *Chem. Rev.*, 2005, **105**, 1547-1562.
124. S. Lee, H. Chon, M. Lee, J. Choo, S. Y. Shin, Y. H. Lee, I. J. Rhyu, S. W. Son and C. H. Oh, *Biosens. Bioelectron.*, 2009, **24**, 2260-2263.
125. J. H. Kim, J. S. Kim, H. Choi, S. M. Lee, B. H. Jun, K. N. Yu, E. Kuk, Y. K. Kim, D. H. Jeong, M. H. Cho and Y. S. Lee, *Anal. Chem.*, 2006, **78**, 6967-6973.
126. M. J. Natan, *Faraday Discuss.*, 2006, **132**, 321-328.
127. N. Lewinski, V. Colvin and R. Drezek, *Small*, 2008, **4**, 26-49.
128. K. K. Maiti, U. S. Dinish, C. Y. Fu, J.-J. Lee, K.-S. Soh, S.-W. Yun, R. Bhuvaneswari, M. Olivo and Y.-T. Chang, *Biosens. Bioelectron.*, 2010, **26**, 398-403.
129. F. McKenzie, A. Ingram, R. Stokes and D. Graham, *Analyst*, 2009, **134**, 549-556.
130. N. Stone, K. Faulds, D. Graham and P. Matousek, *Anal. Chem.*, 2010, **82**, 3969-3973.
131. K. K. Maiti, U. S. Dinish, A. Samanta, M. Vendrell, K.-S. Soh, S.-J. Park, M. Olivo and Y.-T. Chang, *Nano Today*, 2012, **7**, 85-93.
132. M. Y. Sha, H. Xu, M. J. Natan and R. Cromer, *J. Am. Chem. Soc.*, 2008, **130**, 17214-17215.
133. A. Young, M. Amin, J. Petros, M. Natan, S. Nie and M. Wang, *Conf Proc IEEE Eng Med Biol Soc*, 2005, **1**, 723-726.
134. S. Keren, C. Zavaleta, Z. Cheng, A. de la Zerda, O. Gheysens and S. S. Gambhir, *Proc. Natl. Acad. Sci. U. S. A.*, 2008, **105**, 5844-5849.
135. M. Feldmann, F. M. Brennan and R. N. Maini, *Annu. Rev. Immunol.*, 1996, **14**, 397-440.
136. P. C. Heinrich, I. Behrmann, S. Haan, H. M. Hermanns, G. Muller-Newen and F. Schaper, *Biochem. J.*, 2003, **374**, 1-20.
137. E. T. Andreakos, B. M. Foxwell, F. M. Brennan, R. N. Maini and M. Feldmann, *Cytokine Growth F. R.*, **13**, 299-313.
138. E. Y. Kim and K. D. Moudgil, *Immunol. Lett.*, 2008, **120**, 1-5.
139. P. Tang, M.-C. Hung and J. Klostergaard, *Biochemistry*, 1996, **35**, 8216-8225.
140. R. A. Black, *Int. J. Biochem. Cell B.*, 2002, **34**, 1-5.
141. S. Mocellin, C. R. Rossi, P. Pilati and D. Nitti, *Cytokine Growth F. R.*, 2005, **16**, 35-53.
142. P. H. Carter, P. A. Scherle, J. A. Muckelbauer, M. E. Voss, R. Q. Liu, L. A. Thompson, A. J. Tebben, K. A. Solomon, Y. C. Lo, Z. Li, P. Strzemienski, G. J. Yang, N. Falahatpisheh, M. Xu, Z. R. Wu, N. A. Farrow, K. Ramnarayan, J. Wang, D. Rideout, V. Yalamoori, P. Domaille, D. J. Underwood, J. M. Trzaskos, S. M. Friedman, R. C. Newton and C. P. Decicco, *Proc. Natl. Acad. Sci. U. S. A.*, 2001, **98**, 11879-11884.
143. L. A. Tartaglia, D. Pennica and D. V. Goeddel, *J. Biol. Chem.*, 1993, **268**, 18542-18548.
144. Y. Mukai, T. Nakamura, M. Yoshikawa, Y. Yoshioka, S. Tsunoda, S. Nakagawa, Y. Yamagata and Y. Tsutsumi, *Sci Signal*, 2010, **3**, ra83.
145. M. Feldmann and R. N. Maini, *Nat. Med.*, 2003, **9**, 1245-1250.
146. P. F. Piguet, G. E. Grau, C. Vesin, H. Loetscher, R. Gentz and W. Lesslauer, *Immunology*, 1992, **77**, 510-514.
147. P. H. Wooley, J. Dutcher, M. B. Widmer and S. Gillis, *J. Immunol.*, 1993, **151**, 6602-6607.
148. G. J. Thorbecke, R. Shah, C. H. Leu, A. P. Kuruvilla, A. M. Hardison and M. A. Palladino, *Proc. Natl. Acad. Sci. U. S. A.*, 1992, **89**, 7375-7379.
149. F. C. Breedveld, *The Lancet*, 2000, **355**, 735-740.

150. P. Tugwell, *Rheumatology*, 2000, **39**, 43-47.
151. M. J. Elliott, R. N. Maini, M. Feldmann, A. Longfox, P. Charles, P. Katsikis, F. M. Brennan, J. Walker, H. Bijl, J. Ghrayeb and J. N. Woody, *Arthritis Rheum.*, 1993, **36**, 1681-1690.
152. L. Jespers, A. Roberts, S. Mahler, G. Winter and H. Hoogenboom, *Biotechnology*, 1994, **12**, 899-903.
153. W. Y. K. Hwang and J. Foote, *Methods*, 2005, **36**, 3-10.
154. H. Engelmann, D. Aderka, M. Rubinstein, D. Rotman and D. Wallach, *J. Biol. Chem.*, 1989, **264**, 11974-11980.
155. W. Lesslauer, H. Tabuchi, R. Gentz, M. Brockhaus, E. J. Schlaeger, G. Grau, P. F. Piguet, P. Pointaire, P. Vassalli and H. Loetscher, *Eur. J. Immunol.*, 1991, **21**, 2883-2886.
156. K. M. Mohler, D. S. Torrance, C. A. Smith, R. G. Goodwin, K. E. Stremler, V. P. Fung, H. Madani and M. B. Widmer, *J. Immunol.*, 1993, **151**, 1548-1561.
157. R. McQueenie, R. Stevenson, R. Benson, N. MacRitchie, I. McInnes, P. Maffia, K. Faulds, D. Graham, J. Brewer and P. Garside, *Anal. Chem.*, 2012, **84**, 5968-5975.
158. L. L. Hench and J. K. West, *Chem. Rev.*, 1990, **90**, 33-72.
159. T. Nann and P. Mulvaney, *Angew. Chem. Int. Ed,*, 2004, **43**, 5393-5396.
160. G. A. van Ewijk, G. J. Vroege and A. P. Philipse, *J. Magn. Magn. Mater.*, 1999, **201**, 31-33.
161. L. M. Liz-Marzán and A. P. Philipse, *J. Colloid Interface Sci.*, 1995, **176**, 459-466.
162. C. Graf, D. L. J. Vossen, A. Imhof and A. van Blaaderen, *Langmuir*, 2003, **19**, 6693-6700.
163. I. Pastoriza-Santos, J. Pérez-Juste and L. M. Liz-Marzán, *Chem. Mater.*, 2006, **18**, 2465-2467.
164. Y. Kobayashi, H. Katakami, E. Mine, D. Nagao, M. Konno and L. M. Liz-Marzan, *J. Colloid Interface Sci.*, 2005, **283**, 392-396.
165. T. Pal, T. K. Sau and N. R. Jana, *Langmuir*, 1997, **13**, 1481-1485.
166. Plueddem.Ep, *J. Adhes.*, 1970, **2**, 184-&.
167. F. J. Boerio, L. Armogan and S. Y. Cheng, *J. Colloid Interface Sci.*, 1980, **73**, 416-424.
168. C. J. Brinker, K. D. Keefer, D. W. Schaefer and C. S. Ashley, *J. Non-Cryst. Solids*, 1982, **48**, 47-64.
169. R. Aelion, A. Loebel and F. Eirich, *J. Am. Chem. Soc.*, 1950, **72**, 5705-5712.
170. R. Keir, D. Sadler and W. E. Smith, *Appl. Spectrosc.*, 2002, **56**, 551-559.
171. R. J. Hunter, *Zeta Potential in Colloid Science: Principles and Applications*, Academic Press, 1988.
172. W. E. Doering, M. E. Piotti, M. J. Natan and R. G. Freeman, *Advanced Materials*, 2007, **19**, 3100-3108.
173. *United States Pat.*, 2003.
174. M. Schütz, B. Küstner, M. Bauer, C. Schmuck and S. Schlücker, *Small*, 2010, **6**, 733-737.
175. K. Faulds, R. E. Littleford, D. Graham, G. Dent and W. E. Smith, *Anal. Chem.*, 2003, **76**, 592-598.
176. A. Van Blaaderen, J. Van Geest and A. Vrij, *J. Colloid Interface Sci.*, 1992, **154**, 481-501.
177. E. Allahyarov, E. Zaccarelli, F. Sciortino, P. Tartaglia and H. Löwen, *EPL-Europhys. Lett.*, 2007, **78**, 38002.
178. E. C. Le Ru, M. Dalley and P. G. Etchegoin, *Curr. Appl. Phys.*, 2006, **6**, 411-414.
179. K. A. Huynh and K. L. Chen, *Environ. Sci. Technol.*, 2011, **45**, 5564-5571.

180. T. Vo-Dinh, H.-N. Wang and J. Scaffidi, *J. Biophotonics*, 2010, **3**, 89-102.
181. D. Graham and K. Faulds, *Chem. Soc. Rev.*, 2008, **37**, 1042-1051.
182. X. Han, B. Zhao and Y. Ozaki, *Anal. Bioanal. Chem.*, 2009, **394**, 1719-1727.
183. M. A. Markowitz, P. R. Kust, J. Klaehn, G. Deng and B. P. Gaber, *Anal. Chim. Acta*, 2001, **435**, 177-185.
184. H. Izutsu, F. Mizukami, T. Sashida, K. Maeda, Y. Kiyozumi and Y. Akiyama, *J. Non-Cryst. Solids*, 1997, **212**, 40-48.
185. G. Deng, M. A. Markowitz, P. R. Kust and B. P. Gaber, *Mat. Sci. Eng. C - Biomim*, 2000, **11**, 165-172.
186. L. Stebounova, E. Guio and V. Grassian, *J Nanopart Res*, 2011, **13**, 233-244.
187. S. Luo, E. Zhang, Y. Su, T. Cheng and C. Shi, *Biomaterials*, 2011, **32**, 7127-7138.
188. J. O. Escobedo, O. Rusin, S. Lim and R. M. Strongin, *Curr Opin Chem Biol*, 2010, **14**, 64-70.
189. C. Amiot, S. Xu, S. Liang, L. Pan and J. Zhao, *Sensors*, 2008, **8**, 3082-3105.
190. G. Raspoet, M. T. Nguyen, M. McGarraghy and A. F. Hegarty, *J. Org. Chem*, 1998, **63**, 6867-6877.
191. M. Hanauer, S. Pierrat, I. Zins, A. Lotz and C. Sönnichsen, *Nano Lett.*, 2007, **7**, 2881-2885.
192. D. Zanchet, C. M. Micheel, W. J. Parak, D. Gerion and A. P. Alivisatos, *Nano Lett.*, 2000, **1**, 32-35.
193. M. Zheng, F. Davidson and X. Huang, *J. Am. Chem. Soc.*, 2003, **125**, 7790-7791.
194. D. R. Porterfield and A. Campion, *J. Am. Chem. Soc.*, 1988, **110**, 408-410.
195. J. J. Baraga, M. S. Feld and R. P. Rava, *Appl. Spectrosc.*, 1992, **46**, 187-190.
196. Z. Kaymakcalan, P. Sakorafas, S. Bose, S. Scesney, L. Xiong, D. K. Hanzatian, J. Salfeld and E. H. Sasso, *Clin. Immunol.*, 2009, **131**, 308-316.
197. K. C. Bantz, A. F. Meyer, N. J. Wittenberg, H. Im, O. Kurtulus, S. H. Lee, N. C. Lindquist, S.-H. Oh and C. L. Haynes, *Phys. Chem. Chem. Phys.*, 2011, **13**, 11551-11567.
198. W. Xie, L. Su, A. Shen, A. Materny and J. Hu, *J. Raman Spectrosc.*, 2011, **42**, 1248-1254.
199. S.-i. Harashima, T. Horiuchi, N. Hatta, C. Morita, M. Higuchi, T. Sawabe, H. Tsukamoto, T. Tahira, K. Hayashi, S. Fujita and Y. Niho, *The Journal of Immunology*, 2001, **166**, 130-136.
200. F. Roelofs and W. Vogelsberger, *The Journal of Physical Chemistry B*, 2004, **108**, 11308-11316.
201. E. Mahon, D. R. Hristov and K. A. Dawson, *Chem. Commun.*, 2012, **48**, 7970-7972.
202. J. R. Bradley, *J. Pathol.*, 2008, **214**, 149-160.
203. D. Kwiatkowski, A. V. Hill, I. Sambou, P. Twumasi, J. Castracane, K. R. Manogue, A. Cerami, D. R. Brewster and B. M. Greenwood, *Lancet*, 1990, **336**, 1201-1204.
204. T. Robak, A. Gladalska and H. Stepien, *Eur Cytokine Netw*, 1998, **9**, 145-154.
205. J. D. Bancroft and M. Gamble, *Theory and Practice of Histological Techniques*, Churchill Livingstone, 2008.
206. V. H. Fingar, S. W. Taber, W. C. Buschemeyer, A. ten Tije, P. B. Cerrito, M. Tseng, H. Guo, M. N. Johnston and T. J. Wieman, *Microvas. Res.*, 1997, **54**, 135-144.
207. T. Jensen, L. Kelly, A. Lazarides and G. C. Schatz, *J. Clust. Sci.*, 1999, **10**, 295-317.

Appendix I

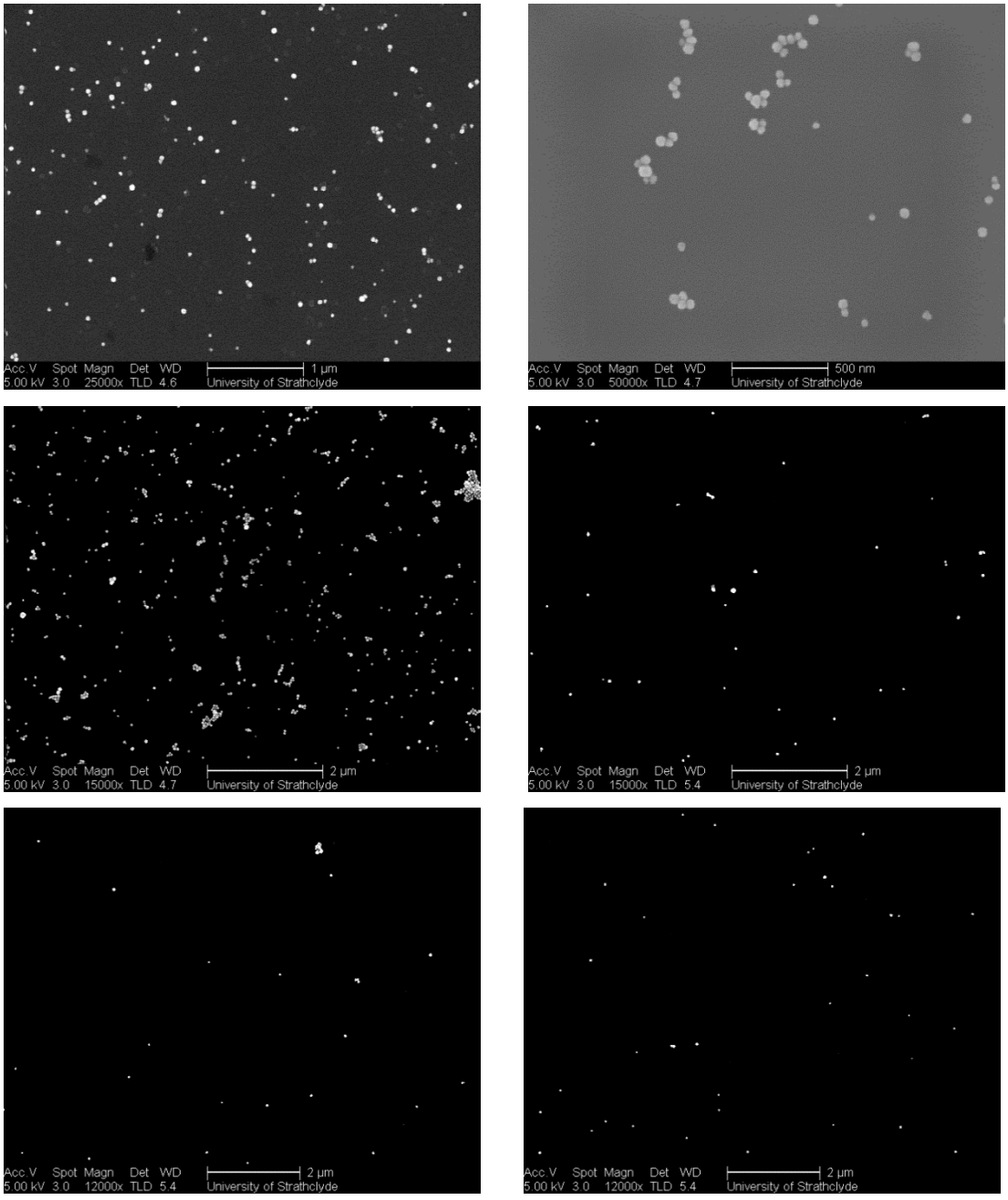

Figure 1 SEM images of silver / silica core / shell nanoparticles constructed from BT-SiO_2

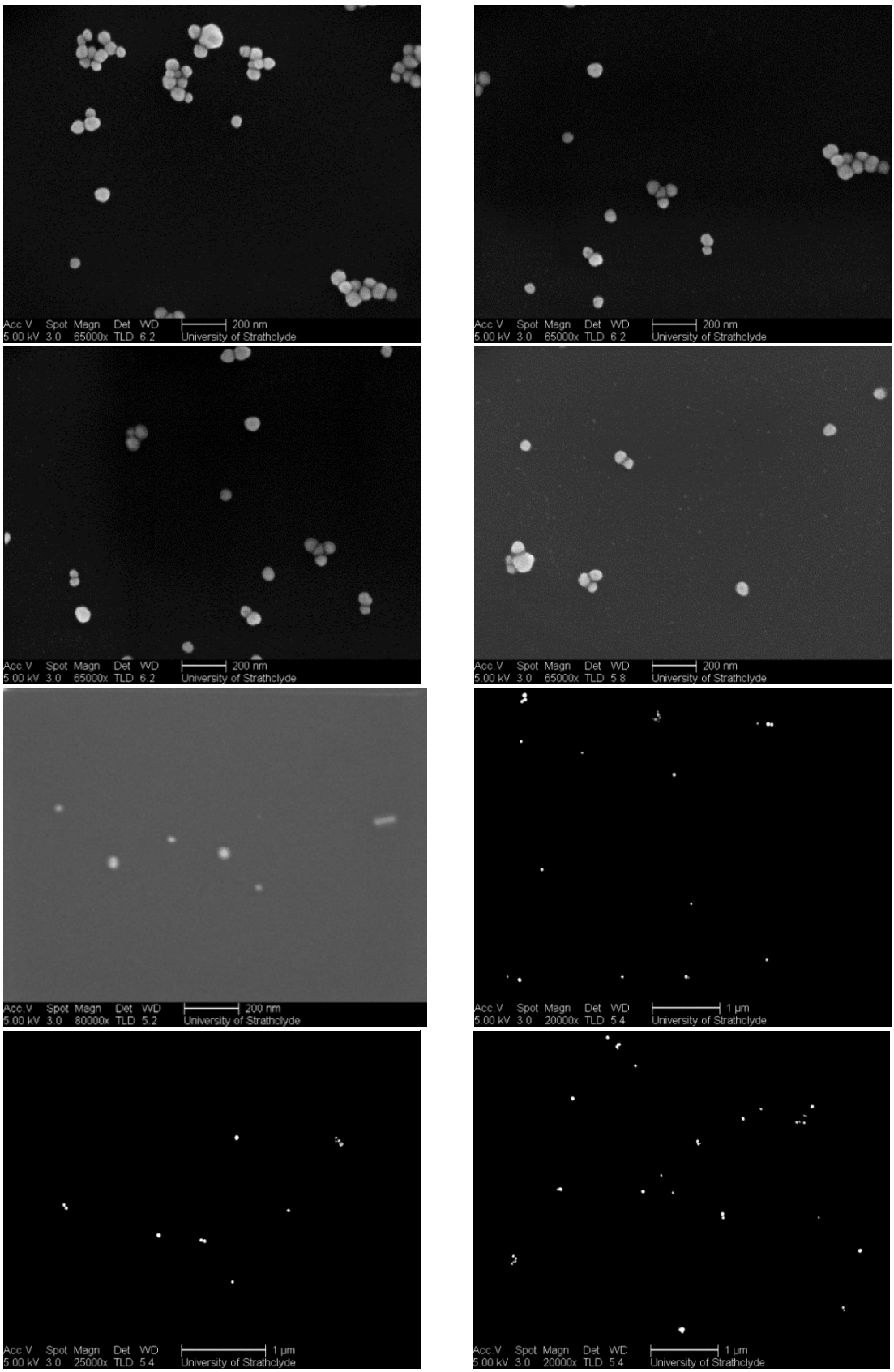

Figure 2 SEM images of silver / silica core / shell nanoparticles constructed from BT-COOH

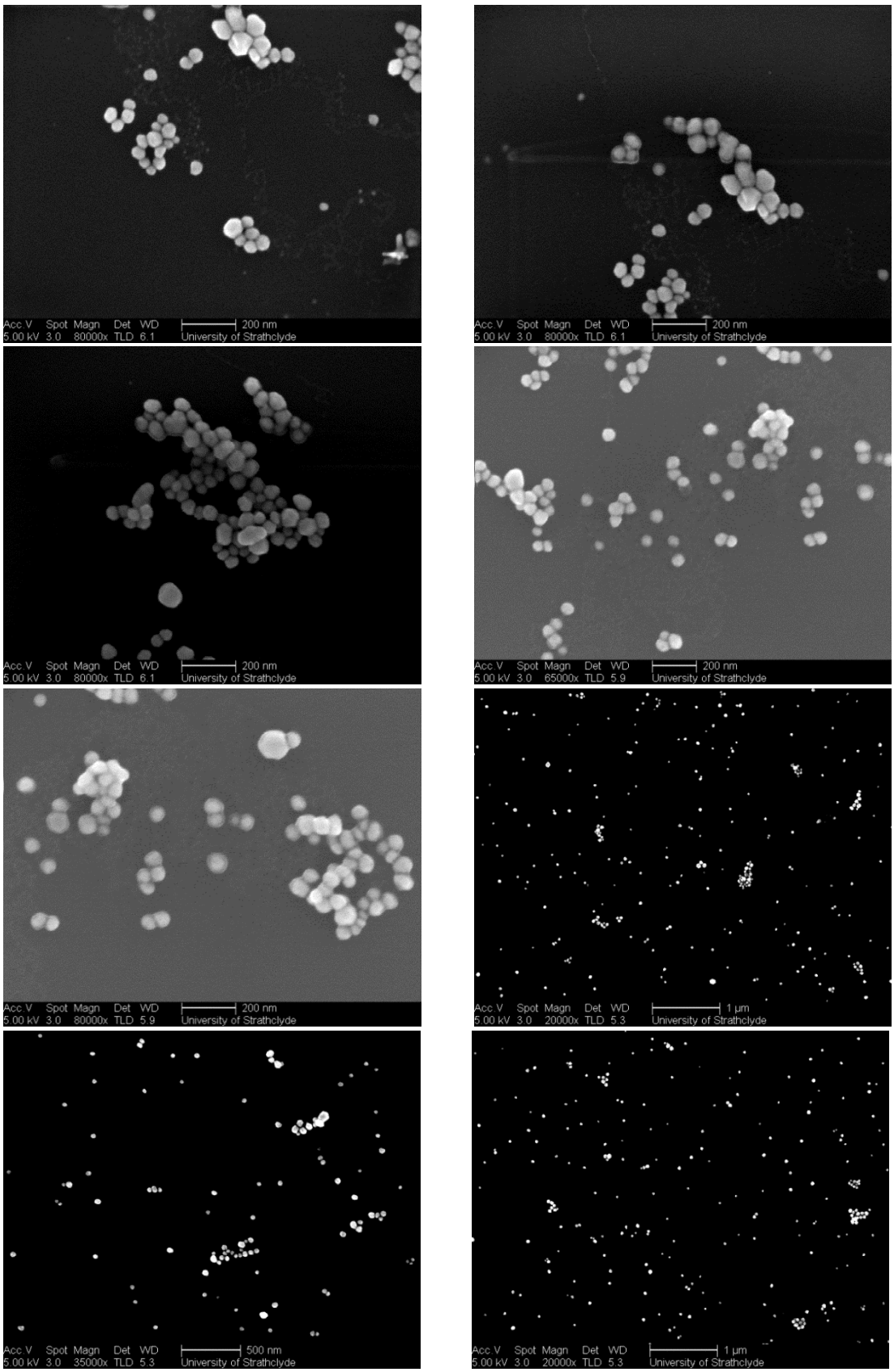

Figure 3 SEM images of silver / silica core / shell nanoparticles constructed from BT-NH_2

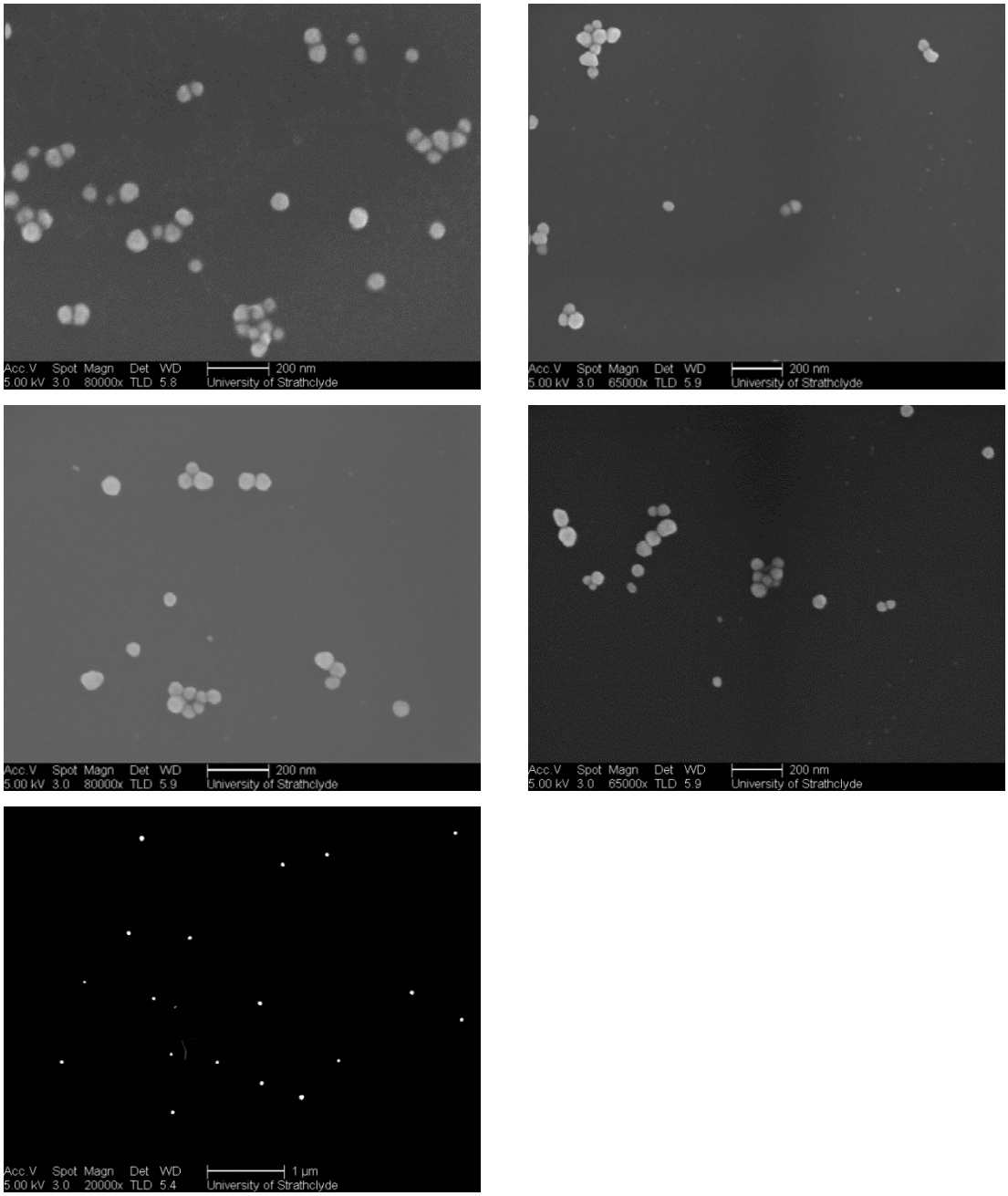

Figure 4 SEM images of silver / silica core / shell nanoparticles constructed from BT-OH.

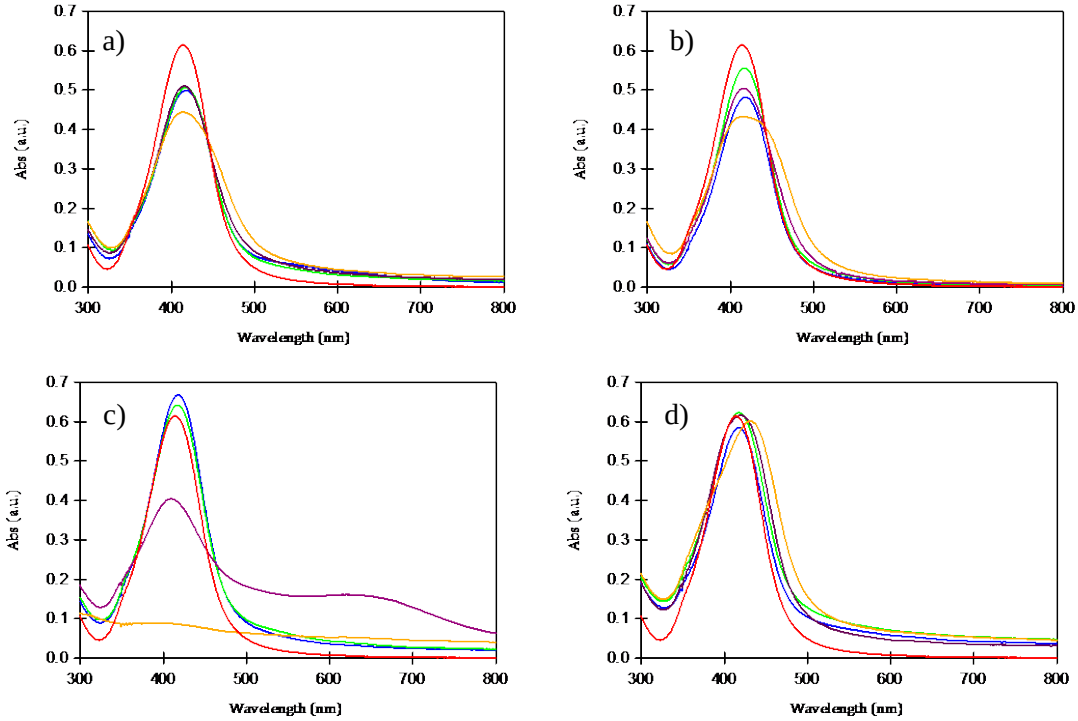

Figure 5 Extinction spectra of AgNP with final concentration of a) BT-SiO_2, b)BT-COOH, c) BT-NH_2 and d) BT-OH dye at 0 M (red), 10^{-8} M (blue), 10^{-7} M (green), 10^{-6} M (purple) and 10^{-5} M (orange) in 1 mL colloidal suspensions.

Table 1 Assignment of Raman bands associated with BTCOOH at 514.5 nm excitation

Theoretical (DFT)	Experimental	Assignments
1078	1123	benzotriazole C-H bends, N-H bends and some C-N azo stretches.
1131	1189	methoxy C-O stretch, C-H bend, triazole N-H stretch and some dimethoxyphenyl C displacement
1251	1274	benzotriazole and C-N azo stretches
1330	1345	dimethoxyphenyl ring breathing including C-C, C-N amine bends and some methoxy hydrogen
1364	1385	azo stretch
1410	1450	C-C stretch, C-H methoxy
1433	1499	C-C, C-O stretches
1594	1547	dimethoxyphenyl C-C stretch, C-H bend and amine N-H bend
1609	1619	benzotriazole quadrant and amine stretch

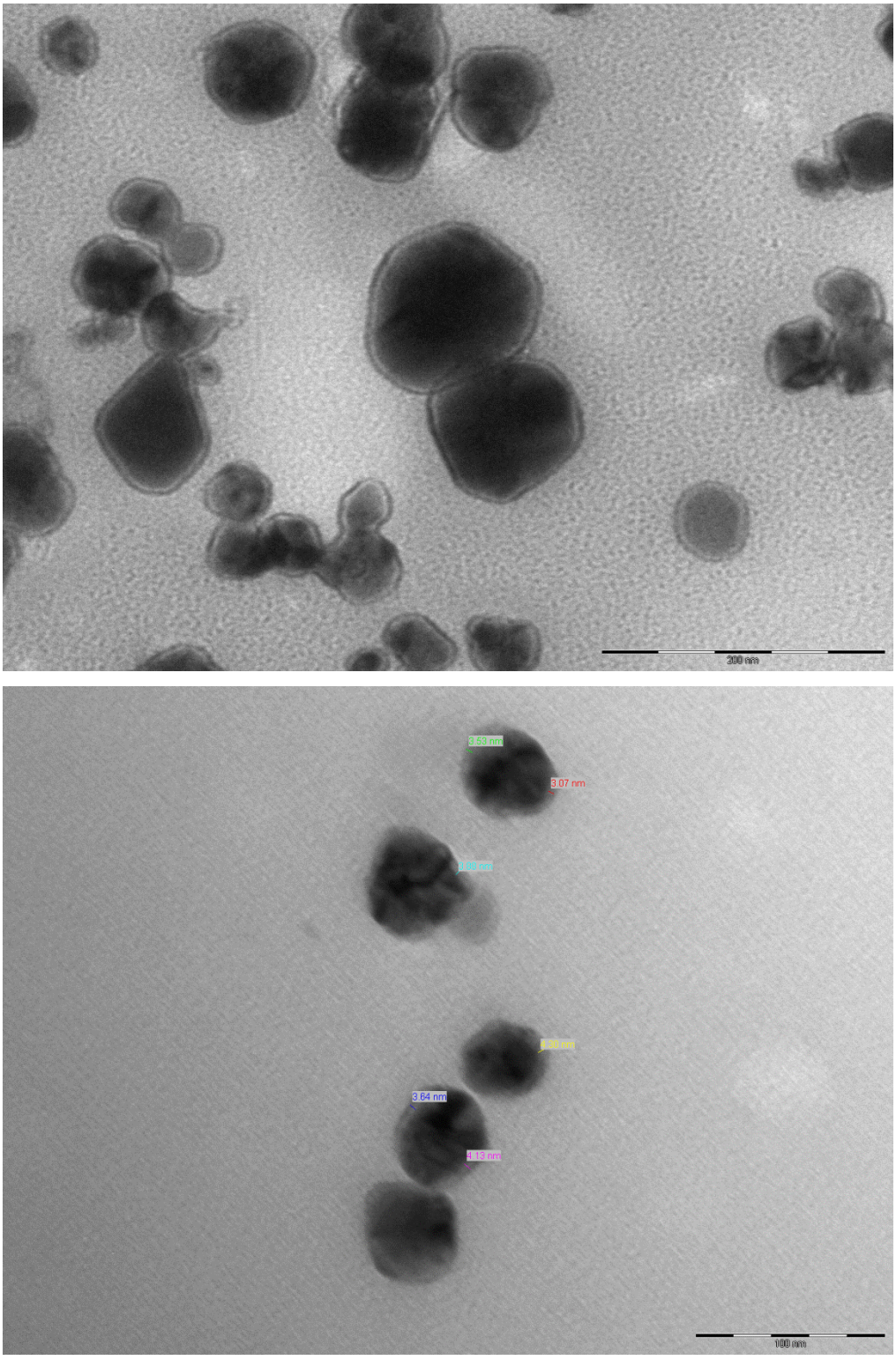

Figure 6 TEM images of silver / silica core / shell nanoparticles constructed from BT-COOH.

ChemComm

View Online
Dynamic Article Links

Cite this: DOI: 10.1039/c0cc05338d

www.rsc.org/chemcomm

COMMUNICATION

Rationally designed SERS active silica coated silver nanoparticles†‡

Louise Rocks, Karen Faulds and Duncan Graham*

Received 2nd December 2010, Accepted 22nd February 2011
DOI: 10.1039/c0cc05338d

A reproducible method for the successful silica coating of silver nanoparticles is reported. A selection of tri-functional reporter molecules were designed to allow controlled synthesis of silica shelled, dye coded, SERS active silver nanoparticles.

Surface enhanced Raman scattering (SERS) has been employed in the development and improvement of numerous biological detection systems.[1,2] The output consists of narrow spectral bands highlighting the multiplexing capabilities of this technique.[3] One approach that can be exploited to improve the sensitivity of this technique is to make use of the resonance contribution from a dye molecule which has an electronic transition close to the excitation frequency. This is known as surface enhanced resonance Raman scattering (SERRS). Sensitivity of this detection system is excellent and in some cases can rival that of fluorescence.[4,5]

Metallic nanoparticles, especially the coinage metals, have proven to be useful substrates for SE(R)RS analysis. Decreasing the size of the particles to the nanometre range results in significant absorption in the UV/visible range which can influence the optical properties in both near and far field.[6]

The vast majority of biological cellular SE(R)RS analysis has utilised gold nanoparticles, due to the biocompatible nature of the material, their mobility and versatility.[7] Whilst the SERS enhancement of silver nanoparticles is typically greater than that observed with gold analogues,[8] there has been some concern regarding the cytotoxic properties of silver and as such their biocompatibility.[9] The requirement for aqueous compatible nanoparticles for use within a biological environment has led to the development of core-shell systems to isolate the inner metal core from the outer biological environment. The use of nanoparticle cores, both metallic and semi-conductor, functionalised with polyethylene glycol (PEG) shells has been shown to be widely applicable to cellular analysis.[10,11] Similarly, silica is being used increasingly for the shelling of nanoparticles to provide a robust substrate with consistent surface chemistry.

Centre for Molecular Nanometrology, WestCHEM, Department of Pure and Applied Chemistry, University of Strathclyde, 295 Cathedral Street, Glasgow, UK. E-mail: duncan.graham@strath.ac.uk; Tel: +44 1415484701

† This article is part of a ChemComm web-based themed issue on Surface Enhanced Raman Spectroscopy.

‡ Electronic supplementary information (ESI) available: SEM images, UV-visible experimental procedures. See DOI: 10.1039/c0cc05338d

The silica shell is considered to "physically sequester" the nanoparticle core allowing exploitation of the optical, electrical, and catalytic properties of the core.[12] Silica growth can be achieved using Stöber synthesis.[13] This involves ammonium hydroxide-catalysed hydrolysis and condensation of alkoxysilanes in low molecular-weight alcohols. The main limitation to the silica coating of metallic nanostructures is the inherent vitreophobic nature of noble metals. The relative chemical instability of silver, in comparison to gold, poses an additional obstacle in the silica coating of silver nanoparticles. Ammonium hydroxide readily oxidises silver to form soluble complex ions resulting in the formation of excess core-free silica particles.[14] Furthermore, transferring metallic nanoparticles into an alcohol/water solution, as per the Stöber method, may result in multiple silver cores within the silica shell due to the reduction in dielectric constant. For this reason vitreophilising agents, namely mercapto and amino functionalised silane coupling agents, have been employed to facilitate the silica-coating of both silver and gold nanoparticles.[12,15] Self assembled monolayer coverage of the silane coupling agents enhances the stability of the core in the harsh conditions necessary for silica growth and provides a vitreophilic surface for the growth of a silica shell *via* alkoxysilane condensation.

Raman reporter molecules such as fluorescein isothiocyante have previously been incorporated into the silica coated nanoparticles to produce SERS active probes for biological applications.[16] These methods often employ mixed monolayer coverage of Raman active molecules and vitreophilising precursors. Competition for surface binding of the aforementioned molecules can result in reduced reproducibility of SERS signal, since the amount of reporter molecules per nanoparticle may not be homogenous. Successful silica encapsulation of gold nanospheres has been achieved *via* covalent attachment of silane precursors to complete monolayers of Raman reporters[17] and also monolayer coverage of terminal alkoxysilane Raman reporters.[18] Similarly, a resonant molecule capable of providing a vitreophillic surface should provide a suitable precursor for silver/ silica core/shell nanotags with increased sensitivity.

A series of tri-functional linkers based on benzotriazole dyes were synthesised for conjugation to the surface of silver nanoparticles (Fig. 1).[19] Benzotriazole dyes have previously been synthesised and designed specifically to complex directly to the surface of silver nanoparticles through the benzotriazole moiety.[20] Alkoxy silane functionality can be introduced to the dyes (Dye 1) to provide a vitreophillic surface. Thus, they can

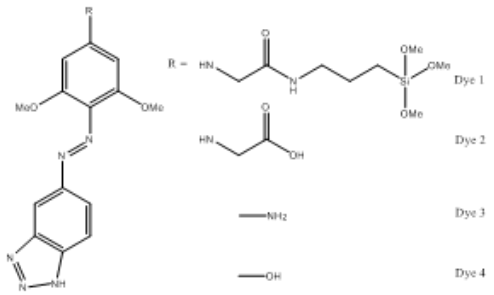

Fig. 1 Tri-functional benzotriazole dyes designed as precursors for silica encapsulation of silver nanoparticles.

be considered to act as precursors for the development of an integrated network of siloxane linkages *via* the Stöber method.

Silver nanoparticles (AgNP) were synthesised according to the previously published method by Fabrinkos *et al.*[21] Dye 1 was added to colloidal suspensions to a final concentration of 1×10^{-7} M. Silica coating was achieved using a modified Stöber method (see supporting information‡). Due to the oxidizing capabilities of ammonium hydroxide, a more sterically hindered amine base, triethylamine, was used as a catalyst. Previous work has indicated that even one methyl substitute on ammonium hydroxide is enough to reduce the rate of oxidation of silver nanoparticles.[22] Tetraethyl orthosilicate (TEOS) was introduced to the nanoparticle–precursor conjugates in small aliquots over a three hour period until a final concentration of 5.4 mM was achieved. Continuous agitation of the samples was employed throughout the shelling process. Silica coating was successful using the alkoxysilyl functional Dye 1, however the formation of multiple silver cores was evident (ESI, Fig. S1‡).

Dyes 2–4 also possess functional groups capable of undergoing condensation with TEOS. These dyes were added to colloidal suspensions of AgNP to a final concentration of 1×10^{-7} M prior to silica coating *via* the outlined modified Stöber method (see supporting information‡). The resulting AgNP@SiO_2 (core@shell) "nanotags" were washed and analysed by UV visible spectroscopy (Fig. 2a and b). The data was normalised to take into account the variation in nanoparticle concentration within the samples. Conjugates prepared from Dye 2 did not exhibit significant aggregation of the AgNP. Dampening of the surface plasmon and increased absorbance at longer wavelengths were observed in the nanotags prepared from Dyes 1 and 3. This suggests aggregation of the nanoparticle cores has occurred. Nanotags prepared using Dye 4 exhibited minimal agglomeration of the nanoparticle cores.

The SE(R)RS properties of the four tri-functional precursors were investigated, post-silica coating of the silver nanoparticles, using 3 excitation wavelengths (Fig. 2c). The intensity of the peak at 1615 cm^{-1} was standardized against cyclohexane intensity at 800 cm^{-1}. No significant peaks were observed from any of the samples using 785 nm excitation.

The SERS enhancement was found to be greater for the nanotags synthesised from Dyes 1 and 3 (with alkoxysilyl and amino functionality) which is most likely due to formation of multiple cores within the sample. In the case of Dye 1, this is most likely due to premature siloxane bridging between adjacent nanoparticle-dye conjugates in the alkaline alcohol solution prior to addition of TEOS. Dye 3 was observed to induce aggregation of nanoparticles in an aqueous environment prior to silica coating (ESI, Fig. S2‡). This is most likely a result of electrostatic interactions between the protonated primary amine of Dye 3 with the bare silver nanoparticles. The UV visible data illustrated in Fig. 2a and b indicates Dyes 2 and 4, with carboxyl and hydroxyl functionality, respectively, have increased reproducibility with respect to monodispersity of the nanotags.

SEM images of Ag@SiO_2 nanotags synthesised from Dyes 2–4 illustrate that shelling of the silver nanoparticles was successful using the tri-functional precursors (ESI, Fig. S3‡). The samples synthesised from Dye 3 exhibited numerous nanoparticle cores within the silica shell. The nanotags synthesised from Dyes 2 and 4 showed evidence of monomers and smaller aggregates within shells. This is in agreement with the data observed in Fig. 2. All four rationally designed dyes are capable of initiating silica shelling of silver nanoparticles, however Dyes 2 and 4 produce nanotags with reduced polydispersity. The SERS intensity of nanotags synthesised from Dye 2 is approximately twice that observed from the Dye 4 analogues. Thus the carboxyl functionalised benzotriazole dye is determined to be the optimal dye for silica coating of silver nanoparticles. Similarly, non resonant Raman reporters with terminal carboxyl groups should prove to be equally effective precursors.

Earlier work in this field has employed mixed monolayers of vitreophilising precursors and dye molecules to synthesise SE(R)RS active nanotags. We have demonstrated that certain dyes can act as both a resonant molecule for SERRS and a precursor for the silica shelling of silver nanoparticles.

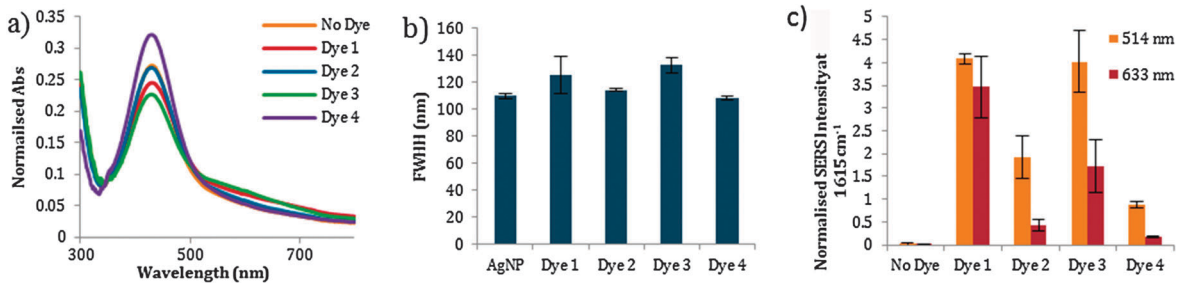

Fig. 2 A comparison of the (a) UV visible (b) full width at half height measurements and (c) SERRS spectra observed at 2 wavelengths from nanotags synthesised using the 4 benzotriazole dyes identified in Fig. 1. Spectra are the average of triplicate samples (the error bars are ±1 standard deviation).

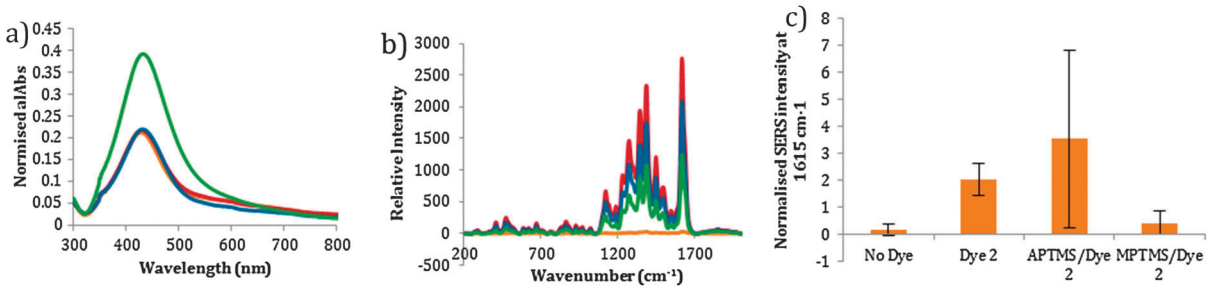

Fig. 3 A comparison of the (a) UV visible and (b) SERRS spectra observed (514 nm excitation) from AgNP (yellow), nanotags synthesised from full monolayer of Dye 2 (red), mixed monolayer APTMS/Dye 2 (blue) and mixed monolayer MPTMS/Dye 2 (green). Spectra are an average of triplicate samples.

To highlight the increased reproducibility of the SERS enhancement of nanotags synthesised from monolayers of the rationally designed dyes in comparison to mixed monolayers, vitreophilising precursors 3-aminopropyl trimethoxysilane (APTMS) and 3-mercaptopropyl trimethoxysilane (MPTMS) were added to the silver colloidal suspension to a final concentration of 1×10^{-6} M. The samples were agitated for a period of 0, 15 or 60 min prior to addition of Dye 2 to a final concentration of 1×10^{-7} M.

Irreversible aggregation of the silver nanoparticles was induced in samples incubated with the silane precursors for 15 and 60 min (ESI, Fig. S4a and b‡). Addition of Dye 2 simultaneously with the silane precursors did not induce significant aggregation of the silver nanoparticles, however variation between sample replicates was significantly increased (ESI, Fig. S4c‡). Raman measurements were also obtained from all conjugates pre-silica coating at 514 nm excitation (ESI, Fig. S5‡). The significant variation in SERS intensity observed in the samples incubated with APTMS/MPTMS for a period of 15 or 60 min can largely be attributed to the aggregation as observed in the UV visible spectra. When APTMS and Dye 2 were added simultaneously, the SERS intensity was 2.75 times greater than in the absence of a silane precursor. However, the relative standard deviation of the sample replicates increased from 14.6% to 62.7%. When MPTMS and Dye 2 were added simultaneously, the preferential binding of sulfur to the silver surface results in minimal binding of Dye 2 and thus the SERS intensity was depleted.

The resulting AgNP@SiO_2 "nanotags" were washed and analysed by UV visible and Raman spectroscopy (Fig. 3). While the greatest enhancement is observed from nanotags prepared from an APTMS/Dye 2 mixed monolayer, the relative standard deviation of the SERS intensity is 3 times greater than in the absence of a silane precursor (92.5% *cf.* 28.3%). Samples prepared using a mixed monolayer coverage of dye and MPTMS had reduced SERS intensity but increased variation in SERS intensity at 1615 cm^{-1} when compared to samples prepared in the absence of a silane precursor (102.1% *cf.* 28.3%).

Four tri-functional molecules have been synthesised to stabilise a silver nanoparticle core, act as a Raman reporter and provide a suitable precursor for an integrated network of silica polymers *via* Stöber condensation. The use of a silane precursor was found to be unnecessary, however use of a suitable site of growth for the silica greatly enhanced the reproducibility of both the synthesis and the SERS. This has resulted in the synthesis of reproducible SERS active silver/silica, core/shell nanotags which will find use in a wide range of applications where gold has previously been used but offering the alternative optical properties of silver.

Notes and references

1 D. Graham and K. Faulds, *Chem. Soc. Rev.*, 2008, **37**, 1042.
2 X. Han, B. Zhao and Y. Ozaki, *Anal. Bioanal. Chem.*, 2009, **394**, 1719.
3 K. Faulds, F. McKenzie, W. E. Smith and D. Graham, *Angew. Chem.*, 2007, **119**, 1861.
4 G. Sabatte, R. Keir, M. Lawlor, M. Black, D. Graham and W. E. Smith, *Anal. Chem.*, 2008, **80**, 2351.
5 K. Faulds, R. P. Barbagallo, J. T. Keer, W. E. Smith and D. Graham, *Analyst*, 2004, **129**, 567.
6 M. Quinten, *Z. Phys. D: At., Mol. Clusters*, 1995, **35**, 217.
7 J. Kneipp, H. Kneipp, M. McLaughlin, D. Brown and K. Kneipp, *Nano Lett.*, 2006, **6**, 2225.
8 R. J. Stokes, A. Macaskill, P. J. Lundahl, W. E. Smith, K. Faulds and D. Graham, *Small*, 2007, **3**, 1593.
9 P. V. AshaRani, G. Low Kah Mun, M. P. Hande and S. Valiyaveettil, *ACS Nano*, 2008, **3**, 279.
10 X. H. Gao, Y. Y. Cui, R. M. Levenson, L. W. K. Chung and S. M. Nie, *Nat. Biotechnol.*, 2004, **22**, 969.
11 X. M. Qian, X. H. Peng, D. O. Ansari, Q. Yin-Goen, G. Z. Chen, D. M. Shin, L. Yang, A. N. Young, M. D. Wang and S. M. Nie, *Nat. Biotechnol.*, 2008, **26**, 83.
12 S. P. Mulvaney, M. D. Musick, C. D. Keating and M. J. Natan, *Langmuir*, 2003, **19**, 4784.
13 W. Stöber, A. Fink and E. Bohn, *J. Colloid Interface Sci.*, 1968, **26**, 62.
14 T. Ung, L. M. Liz-Marzan and P. Mulvaney, *Langmuir*, 1998, **14**, 3740.
15 L. M. LizMarzan, M. Giersig and P. Mulvaney, *Langmuir*, 1996, **12**, 4329.
16 X. Liu, M. Knauer, N. P. Ivleva, R. Niessner and C. Haisch, *Anal. Chem.*, 2009, **82**, 441.
17 B. Küstner, M. Gellner, M. Schütz, F. Schöppler, A. Marx, P. Ströbel, P. Adam, C. Schmuck and S. Schlücker, *Angew. Chem., Int. Ed.*, 2009, **48**, 1950.
18 M. Schütz, B. Küstner, M. Bauer, C. Schmuck and S. Schlücker, *Small*, 2010, **6**, 733.
19 G. McAnally, C. McLaughlin, R. Brown, D. C. Robson, K. Faulds, D. R. Tackley, W. E. Smith and D. Graham, *Analyst*, 2002, **127**, 838.
20 D. Graham, G. McAnally, J. C. Jones and W. Ewen Smith, *Chem. Commun.*, 1998, 1187.
21 V. Fabrikanos, S. Athanassiou and K. Leiser, *Z. Naturforsch. B: Chem. Sci.*, 1963, **18**, 612.
22 Y. Kobayashi, H. Katakami, E. Mine, D. Nagao, M. Konno and L. M. Liz-Marzan, *J. Colloid Interface Sci.*, 2005, **283**, 392.